**Contract No:**

This document was prepared in conjunction with work accomplished under Contract No. DE-AC09-08SR22470 with the U.S. Department of Energy (DOE) Office of Environmental Management (EM).

Savannah River National Laboratory

# 2019 LDRD Annual Report

LEGACY WASTE CLEANUP

NUCLEAR MATERIALS THREAT REDUCTION

NUCLEAR DETERRENT

SECURE ENERGY & MANUFACTURING

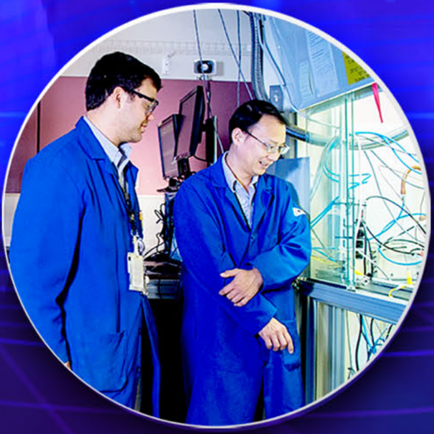

Savannah River National Laboratory®

OPERATED BY SAVANNAH RIVER NUCLEAR SOLUTIONS

## Disclaimer

“This report was prepared by Savannah River Nuclear Solutions, LLC (SRNS) for the United States Department of Energy under Contract No. DE-AC09-08SR22470 and is an account of work performed under that contract. Neither the United States Government nor any agency thereof, nor any of their employees, not any of their contractors, subcontractors or their employees assume any legal liability or responsibility for any third party’s use of the results of such use of any information, apparatus, product, or process disclosed, or represent that its use would not infringe privately owned rights. Reference herein to any specific commercial product, process or services by trademark, name, manufacturer or otherwise does not necessarily constitute or imply endorsement recommendation, or favoring of same by SRNS or the United States Government or any agency thereof.”

**SRNL-STI-2020-00118**

# CONTENTS

# MESSAGE FROM THE LABORATORY DIRECTOR

The Laboratory Directed Research and Development (LDRD) Program at Savannah River National Laboratory (SRNL) serves as a key driver for incubating novel concepts and positioning the laboratory for growth in key mission areas as well as exploring new areas of opportunity. The LDRD program advances innovative ideas to pursue our strategic goals in the areas of legacy waste cleanup, nuclear deterrent, nuclear material threat reduction, and secure energy and manufacturing. By developing and adapting science and technology for the Department of Energy (DOE), the FY19 LDRD program included a focus on future mission enablers that will position SRNL for future growth in key areas. These future mission enablers include cyber-physical security protocols, smart manufacturing, remote systems, process intensification, and nuclear materials processing.

LDRD also plays an impactful role cultivating staff excellence by providing the opportunity to further develop existing and emerging core competencies. In addition, the LDRD program builds the framework to create and strengthen strategic partnerships with other national labs, universities and commercial companies. SRNL's university partnerships are valuable as they not only allow for rewarding collaborative efforts, but also provide a direct connection with the next generation of scientists and engineers as students and post-doctoral researchers working on innovative R&D programs.

This report reflects the execution of our LDRD program within the objectives and guidelines outlined by the DOE through the DOE Order 413.2C. The projects described herein reflect the innovation required to fulfill SRNL's strategic vision and program plans, and they provide great value to the DOE and the nation. The diversity exhibited in the research and development projects underscores the DOE Office of Environmental Management (DOE-EM) and National Nuclear Security Administration (NNSA) missions and enhances these missions by developing the technical capabilities and human capital necessary to support future national needs.

On behalf of the SRNL Senior Management team, I would like to congratulate those members of the SRNL staff and their collaborators for their achievements and the excellence of their work. Their efforts reflect the importance of SRNL's creative ideas and competencies to our nation.

Dr. Vahid Majidi
Laboratory Director
Savannah River National Laboratory

# Savannah River National Laboratory (SRNL)
# Laboratory Directed Research and Development Program (LDRD)

Fiscal Year (FY) 2019 marked the fourteenth year of Savannah River National Laboratory's (SRNL's) Laboratory Directed Research and Development (LDRD) program. When the program began in FY06, just two years after SRNL becoming the DOE's 17th national laboratory, it began with a modest authorized collection rate of just under 1.5%. It grew from there each year, reaching 5% in FY17. The authorized collection rate was maintained at 5% in FY19. The increase in collection rates experienced over the years evidences the value placed on this important program, which provides the discretionary funding needed to develop ideas for future programmatic growth in our key business areas as well as develop and maintain our core competencies. The LDRD program leverages the unique capabilities of SRNL to yield foundational scientific research and development (R&D) essential to our core business areas, while aligning optimally and continuously with SRNL's Strategic Plan and providing long-term benefits to DOE and the National Nuclear Security Administration (NNSA), other customers, and stakeholders. As can be seen in the "By the Numbers" summary, this program also plays an important role in sustaining staff excellence with high participation by students, post-docs, and early-career staff. Nearly 70% of the projects in FY19 included contributions from early-career or post-doctoral staff.

## FY19 LDRD Program Focus Areas:

The FY19 LDRD Program included focus areas designed to align with our strategic goals in the areas of legacy waste cleanup, nuclear deterent, nuclear material threat reduction, and secury energy and manufacturing. In addition several future mission enablers were identified and projects were encouraged to incorporate the these tools into their projects.

- **LEGACY WASTE CLEANUP**

  Unique concepts that lead to new approaches and options for critical EM risk reduction challenges and also reduce the life cycle in processing high activity liquid waste and nuclear materials, remediating contaminated soil, groundwater and facilities, as well as validating long-term remediation strategies.

- **NUCLEAR DETERRENT**

  Unique concepts that ensure a sustainable tritirum supply to meet current and future stockpile needs, including gas transfer systems, chemical processing and purification and incoporation of process intensification and advanced manufacturing concepts to the tritium supply chain.

- **NUCLEAR MATERIALS THREAT REDUCTION**

  Innovative process technologies to convert excess nuclear materials into useful products or waste forms. Enchancements to the Nation's capabilties to detect, characterize, assess, and track nuclear materials and processes across the globe.

- **SECURE ENERGY & MANUFACTURING**

  Advanced research in the development, demonstration, and deployment of secure energy and manufacturing technologies. Development of innovative solutions to increase electrical network security, reliability, and resiliency.

## FUTURE MISSION ENABLERS

- Cyber-Physical Security Protocols
- Smart Manufacturing
- Remote Systems
- Process Intensification
- Nuclear Materials Processing

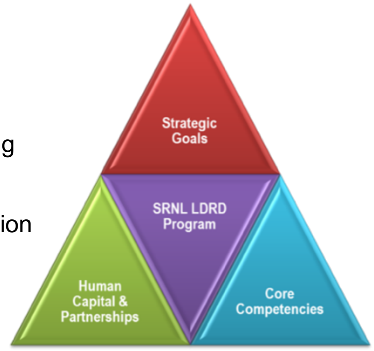

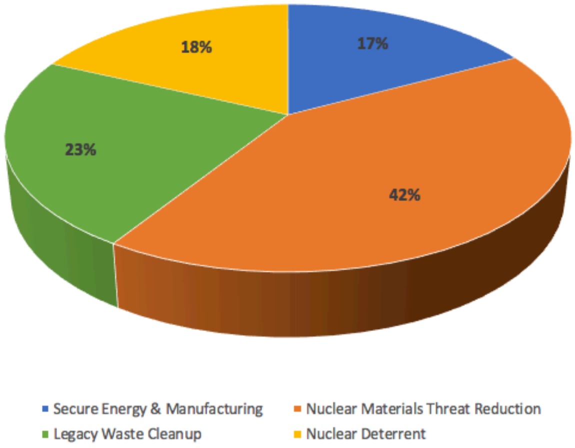

*The pie chart shows the distribution of FY19 projects, both new starts and continuation projects, among the four program areas.*

# LDRD BY THE NUMBERS

**4**

**# PATENTS GRANTED FROM PRIOR YEAR LDRD EFFORTS**

**6**

**# INVENTION DISCLOSURES SUBMITTED**

**19**

**# PUBLICATIONS IN PEER REVIEWED JOURNALS**

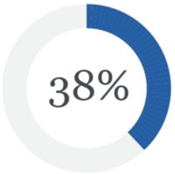

**% OF PROJECT LED BY EARLY CAREER STAFF**

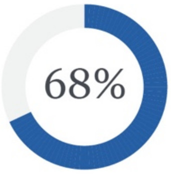

**% OF PROJECT INVOLVING EARLY CAREER STAFF OR POST-DOCS**

**$8.5M**

**TOTAL PROGRAM COST**

**39**

**TOTAL NUMBER OF PROJECTS**

**$203K**

**AVERAGE COST PER PROJECT**

**8**

**NUMBER OF POST-DOCS INVOLVED IN LDRD PROJECTS**

**3**

**NUMBER OF POST-DOCS PERFORMING RESEARCH AT SRNL**

**23**

**NUMBER OF STUDENTS INVOLVED IN LDRD PROJECTS**

**9**

**NUMBER OF STUDENTS PERFORMING RESEARCH AT SRNL**

## Collaborations

**25 TOTAL COLLABORATIONS**

**WITH 13 DIFFERENT UNIVERSITIES AND 3 COMPANIES**

### UNIVERSITIES

- Auburn University
- California State University, Northridge
- Claflin University
- Clemson University
- Fayetteville State University
- Florida State University
- Georgia Institute of Technology
- Jacobs University
- Soochow University
- University of Cambridge
- University of Georgia
- University of South Carolina
- Western Carolina University

### COMPANIES

- JEOL USA
- Savannah River Consulting
- United States Army Cyber School

# LEGACY WASTE CLEANUP

# Metal-Organic-Framework Glasses as Rad Contaminant Sequesters and Nuclear Waste Forms

**Project Team:** Dien Li (Primary),
Natalia Shustova (U of South Carolina),
Kathryn Taylor-Pashow,
Daniel I. Kaplan, Jake Amoroso,
Tom Bennett (U of Cambridge, UK),
Shuao Wang (Soochow U, China)

**Subcontractor**:
University of South Carolina

**Thrust Area**: Legacy Waste Cleanup

**Project Start Date:** October 1, 2017

**Project End Date:** September 30, 2020

*Remediation of Tc remains an unresolved problem at SRS and other DOE sites. The objective of this project was to develop novel metal organic framework (MOF) glasses for radioactive contaminant sequestration and stabilization from aqueous media. During FY19, we synthesized, characterized and evaluated cetyl trimethylammonium bromide (CTAB)-functionalized and* $F^-$*,* $Cl^-$*,* $I^-$*,* $CF_3SO_3^-$ *-exchanged MIL-101. MIL-101-CTAB was demonstrated to have high* $ReO_4^-$ *removal capacity (~130 mg/g sorbent) from artificial groundwater (AGW). Re chemical speciation and binding mechanism on MIL-101-CTAB were also studied by synchrotron X-ray absorption spectroscopy.* $ReO_4^-$ *was demonstrated as being in the pore structure with slightly larger Re-O bond distances than those in* $NaReO_4$*. In addition, a new Ni-TIPA MOF was demonstrated to be very stable, selective and effective for* $TcO_4^-$ *removal from the SRS tank waste stream (~90% removal). This research may provide a highly applicable platform for solving critical DOE and industrial problems related to nuclear environmental stewardship and nuclear power production.*

## Objectives

- Synthesize and characterize CTAB-functionalized, and $F^-$, $Cl^-$, $I^-$, $CF_3SO_3^-$-exchanged MIL-101.
- Evaluate these MOFs for $TcO_4^-$ surrogate (i.e., $ReO_4^-$) removal from AGW.
- Investigate a new Ni-TIPA MOF for Tc removal from the SRS tank waste stream.
- Develop methods for vitrifying the crystalline MOFs.

## Introduction

$^{99}$Tc is a major long-lived fission product created during nuclear power generation. Over the years, Tc has been inadvertently introduced into the environment from leaks at waste storage facilities. $^{99}$Tc currently is one of the key risk drivers at the Savannah River Site (SRS) and other DOE environmental management sites (most notably the Hanford Site, Paducah Gaseous Diffusion Plant, and Oak Ridge National Laboratory). The most common chemical form of Tc in liquid nuclear wastes and in the environment is anionic pertechnetate ($TcO_4^-$). $TcO_4^-$ displays limited adsorption onto common sediment minerals and is highly mobile making it difficult to capture or to be immobilized [1]. As the stockpile of $^{99}$Tc-bearing nuclear waste continues to increase rapidly, novel sequestration technologies are needed to reduce its potential contamination of the environmental and living organisms.

With current technologies, quaternary amine-based resins have been used to remove aqueous Tc [2]. However, these resins are expensive and have only modest $TcO_4^-$ loading capacities from the raffinate waste streams. Chemical reductants (e.g., $Fe_3S_4$, soluble or structural Fe(II)) [3] and some bacteria [4] can reduce Tc(VII) to the sparingly soluble Tc(IV). However, the resulting $Tc(IV)O_2 \cdot 1.6H_2O$ has a solubility of $1.5\times10^{-8}$ M in groundwater [5], which greatly exceeds the EPA's maximum contaminant level of $5\times10^{-10}$ M, and is readily re-oxidized and re-mobilized under most environmental conditions [6]. Tc reduction to form sulfides (e.g., $Tc_2S_7$) [7] or embedding into other sulfide phases [8] or iron oxide waste forms [9] have also been investigated. However, these methods are not practical for many applications. There are currently no demonstrated technologies that are highly efficient and cost-effective for separation of Tc-containing nuclear waste streams and remediation of aqueous Tc in the contaminated sites.

## The overarching objective of this project was to develop novel metal organic framework (MOF) glasses as radioactive contaminant sequesters and nuclear waste forms.

During FY18, MIL-101-Cr was identified as being most effective for Tc removal from AGW. During FY19, we continued to develop, characterize and evaluate MIL-101-Cr based MOFs for $TcO_4^-$ and $ReO_4^-$ sequestration from AGW and highly acidic solutions, while we were also developing new MOF materials of higher alkaline stability, selectivity, and capacity, as well as vitrification technology.

## Approach

During FY19, we prepared CTAB-functionalized, and $F^-$, $Cl^-$, $I^-$, $CF_3SO_3^-$-exchanged MIL-101-Cr, which were expected to have higher Tc capacity and improved stability. Powder X-ray diffraction (XRD), BET surface area measurement, thermogravimetric analysis (TGA), energy dispersive X-ray spectroscopy (EDS), and Fourier transform infrared (FTIR) spectroscopy were used for MOF characterization, while synchrotron radiation X-ray absorption spectroscopy was applied to studying Tc or Re chemical speciation and molecular binding mechanisms after the sequestration by MOFs. In addition, we investigated a new Ni-TIPA MOF for Tc removal from the SRS tank waste stream, while we also tried to develop methods for vitrifying the crystalline MOFs for stabilization of Tc and other contaminants in the MIL-101-Cr and Ni-TIPA MOF glass waste forms.

## Results/Discussion

### 1. Synthesis of modified MIL-101 MOFs

**1.1. MIL-101-Cr-$NO_3$.** Chromium(III) nitrate nonahydrate (0.800 g, $2.00\times10^{-3}$ mol) and terepthalic acid (0.328 g, $1.97\times10^{-3}$ mol) were placed in a Teflon-lined autoclave followed by the addition of 4.6 mL deionized water and 0.4 mL of $HNO_3$ (5.0 M, 2.0 mmol). The autoclave was then sealed and placed in an oven at 210 °C for 8 hours. Upon cooling, the resulting green solid was centrifuged and washed three times with DMF, water and ethanol for 12 h at 80 °C, respectively.[10]

**1.2. MIL-101-Cr-$NO_3$-CTAB.** Under a nitrogen atmosphere, (Cr)MIL-101 (0.200 g), CTAB (0.300 g), and chloroform (10 mL) were added to a 75 mL heavy-wall pressure flask. The flask was sealed and heated at 110 °C while stirring. The resulting green solid was centrifuged and washed three times with chloroform (20 mL) and then dried under vacuum for 3 h.

**1.3. MIL-101-Cr-F.** Chromium(III) nitrate nonahydrate (0.400 g, $1.00\times10^{-3}$ mol) was dissolved in 4.8 mL of deionized water, then placed in a Teflon-lined autoclave. Terephthalic acid (0.164 g, $9.87\times10^{-4}$ mol) was then added followed by the addition of 0.2 mL of HF (5.00 M, $1.00\times10^{-3}$ mol). The autoclave was then sealed and placed in an oven at 220 °C for 8 hours. Upon cooling, the resulting green solid was centrifuged to collect the precipitate and solvent exchanged with DMF (3×10 mL) with centrifugation between each exchange. The product was then washed three times with DMF, water and ethanol, respectively, and dried for 12 h at 80 °C.

**1.4. MIL-101-Cr-Cl.** An aqueous aluminum(III) chloride hexahydrate solution (15 mL, 30 mM) was added to a 20 mL vial containing 30 mg of (Cr)MIL-101-F. The vial was then placed in a preheated oven at 90 °C for 18 h. Upon cooling, the resulting green solid was filtered and washed with water (3×50 mL) and ethanol (3×50 mL).

**1.5. MIL-101-Cr-I.** An aqueous aluminum(III) iodide solution (15 mL, 30 mM) was added to a 20 mL vial containing 30 mg of (Cr)MIL-101-F. The vial was then placed in a preheated oven at 90 °C for 18 h. Upon cooling, the resulting green solid was filtered and washed with water (3 × 50 mL) and ethanol (3 × 50 mL).

**1.6. MIL-101-Cr-OTf (OTf = trifluoromethanesulfonate).** An aqueous aluminum(III) triflate solution (15 mL, 30 mM) was added to a 20 mL vial containing 30 mg of (Cr)MIL-101-F. The vial was then placed in a preheated oven at 90 °C for 18 h. Upon cooling, the resulting green solid was filtered and washed with water (3 × 50 mL) and ethanol (3 × 50 mL).

## 2. Characterization of modified MIL-101 MOFs

The crystal structure of MIL-101-Cr-$NO_3^-$ is shown in Figure 1. The CTAB-functionalized, and $F^-$, $Cl^-$, $I^-$, $CF_3SO_3^-$-exchanged MIL-101-Cr MOFs were characterized by powder XRD, TGA, EDS and FTIR to confirm the known crystal structure, exchanged anion incorporation, and CTAB functionalization. The powder XRD patterns of the new MIL-101 materials are shown in Figure 2, in comparison with that of original MIL-101-Cr-$NO_3^-$. The similar powder XRD patterns confirmed the correct identity of MIL-101-Cr. The TGA traces of these new MIL-101-Cr materials are shown in Figure 3, in comparison with that of MIL-101-Cr-$NO_3^-$. The thermal behavior of the anion-exchanged MIL-101-Cr were very similar to that of MIL-101-Cr-$NO_3^-$, while MIL-101-Cr-CTAB appears to show less mass loss below 200 °C, which indicated less water or solvent present due to CTAB functionalization.

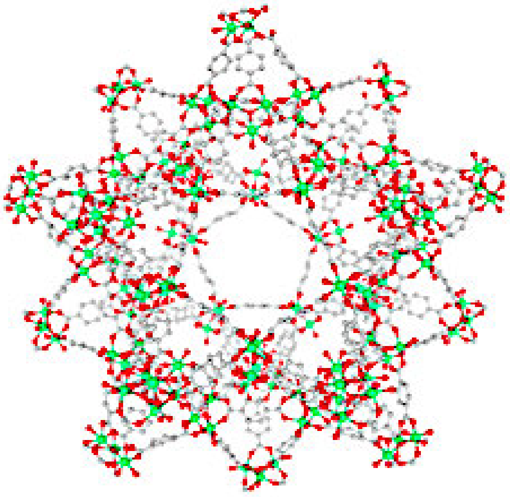

**Figure 1.** Crystal structure of MIL-101-Cr-$NO_3$ [10]

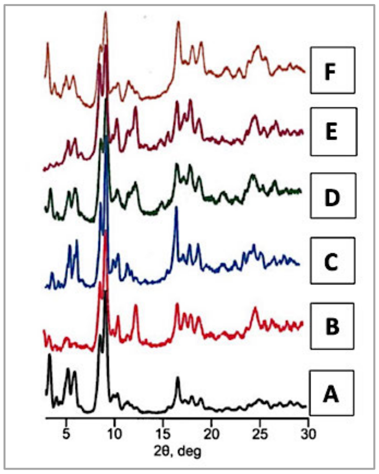

**Figure 2. (above)** Powder XRD patterns of MIL-101-Cr-NO3 **(A),** MIL-101-Cr-F **(B),** MIL-101-Cr-Cl **(C),** MIL-101-Cr-I (D), MIL-101-Cr-OTf **(E),** and MIL-101-Cr-CTAB **(F).** (OTF=trifluoromethanesulfonate, $CF_3SO_3$-);

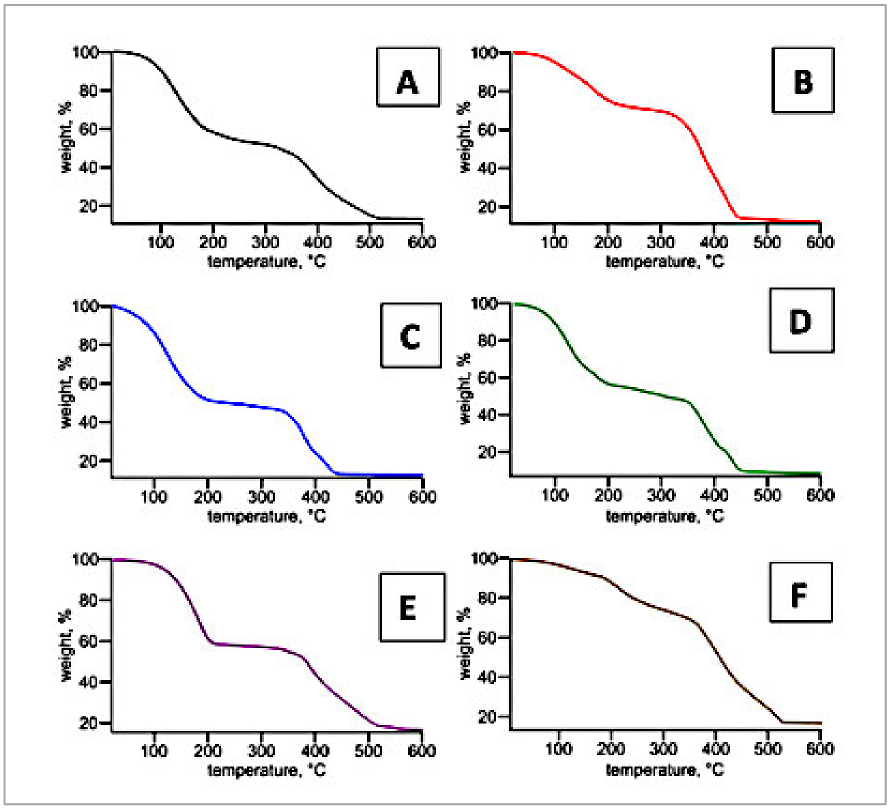

**Figure 3. (right)** TGA traces of MIL-101-Cr-NO3 **(A),** MIL-101-Cr-F **(B),** MIL-101-Cr-Cl **(C),** MIL-101-Cr-I **(D),** MIL-101-Cr-OTf **(E),** and MIL-101-Cr-CTAB **(F).**

The EDS of the anion-exchanged MIL-101 are shown in Figure 4, which demonstrated that the anions (i.e., $F^-$, $Cl^-$, $I^-$, and $CF_3SO_3^-$) were exchanged into the MIL-101-Cr material. In addition, the FTIR spectra of CTAB-functionalized MIL-101-Cr-$NO_3^-$ made from different batches are shown in Figure 5. The FTIR peaks characteristic of CTAB at 2918, 2850 and 1470 $cm^{-1}$ (the shoulder in the spectra) demonstrated the success of CTAB functionalization onto MIL-101-Cr-$NO_3^-$.

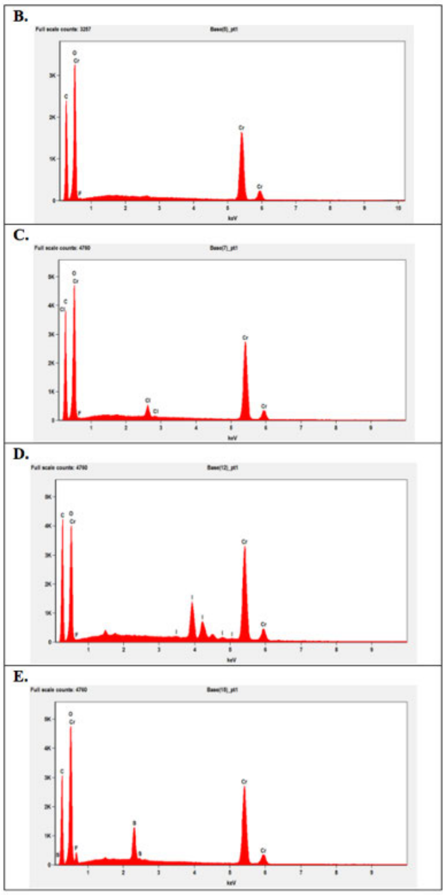

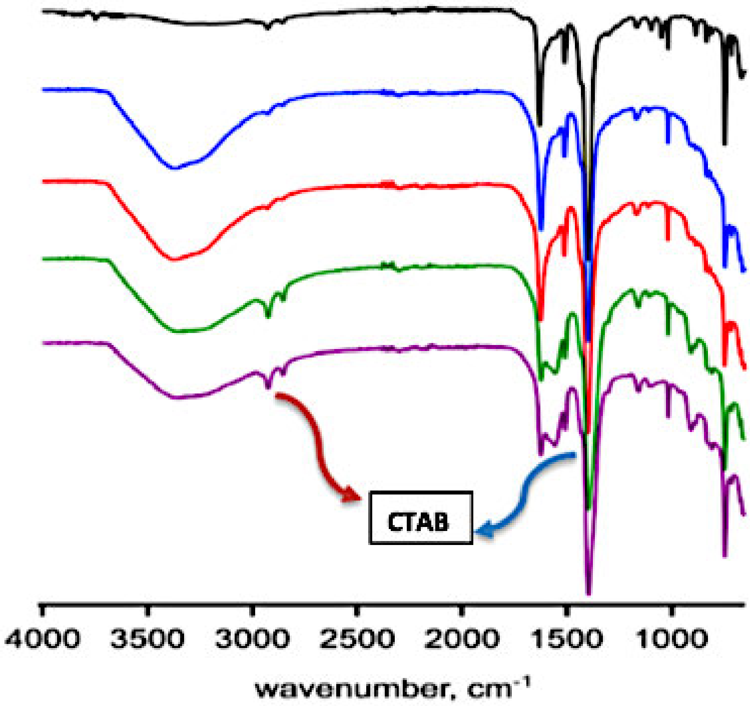

**Figure 4 (left).** EDS of MIL-101-Cr-F (B), MIL-101-Cr-Cl **(C),** MIL-101-Cr-I (D), and MIL-101-Cr-OTf (E).

**Figure 5. (above)** FTIR spectra of MIL-101-Cr-CTAB from different batches: as synthesized **(black),** MIL-101-Cr-CTAB-1 **(blue),** MIL-101-Cr-CTAB-2G **(red),** MIL-101-Cr-CTAB-3 **(green),** and MIL-101-Cr-CTAB-4G **(purple).**

### 3. New MIL-101-Cr for $ReO_4^-$ sequestration from AGW

The CTAB-functionalized and $F^-$, $Cl^-$, $I^-$ and $CF_3SO_3^-$ exchanged MIL-101-Cr MOFs were evaluated for non-radioactive surrogate of $TcO_4^-$ (i.e., $ReO_4^-$) sequestration from AGW under atmospheric ($P_{CO2}$ = $10^{-3.5}$ atm) conditions. The equilibrium sorption capacity ($q_e$, mg/g) were calculated using formula 1:

$$q_e = \frac{(C_0 - C_e) \times V}{M} \qquad (1)$$

where $C_0$ and $C_e$ were Re concentrations before and after adsorption, respectively, V was the total volume of liquid phase (i.e., AGW), and M was the mass of the solid material.

The experimental results are shown in Figure 6. As noted, MIL-101-Cr was identified as the most effective for $ReO_4^-$ removal from AGW among eleven MOFs of known crystal structure and chemistry tested during FY18, with a saturation capacity of ~55 mg $ReO_4^-$/g sorbent (Figure 6A). With CTAB functionalization to MIL-101-Cr, the Re saturation capacity further increased to ~130 mg $ReO_4^-$/g sorbent (Figure 6A). The Re adsorption reaction toward these two MOFs was fast and completed within 30 minutes for MIL-101-Cr and 10 minutes for MIL-101-Cr-CTAB (Figure 6B). With the presence of competing anions (i.e., $NO_3^-$, $CO_3^{2-}$, $SO_4^{2-}$ and $Cl^-$) in de-ionized water, when the competing anion concentration was 100 times as high as that for $ReO_4^-$, $NO_3^-$, $CO_3^{2-}$ and $Cl^-$ decreased the Re removal capacity of MIL-101-Cr by 20-30%, while $SO_4^{2-}$ decreased the Re removal capacity of MIL-101-Cr by ~85% (Figure 6C). In contrast, with the presence of

$NO_3^-$, $CO_3^{2-}$ and $Cl^-$ in de-ionized water, the Re removal capacity of MIL-101-Cr-CTAB remained little changed within the batch experimental uncertainty, while $SO_4^{2-}$ decreased the Re removal capacity of MIL-101-Cr-CTAB by ~15% (Figure 6C). These results demonstrated that with CTAB functionalization, the selectivity of MIL-101-Cr for $ReO_4^-$ or $TcO_4^-$, as expected, was significantly improved.

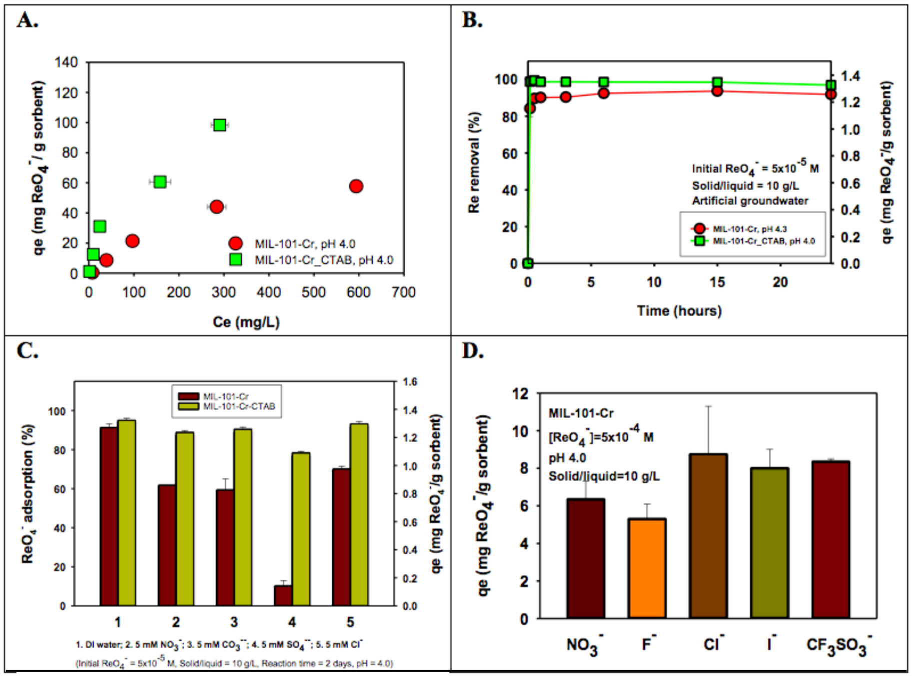

**Figure 6.** $ReO_4^-$ removal from AGW by new MIL-101-Cr MOFs.

- **A.** Isotherms and $ReO_4^-$ removal capacity of MIL-101-Cr and MIL-101-Cr-CTAB.
- **B.** $ReO_4^-$ adsorption versus time for MIL-101-Cr and MIL-101-Cr-CTAB.
- **C.** Effects of competing anions on $ReO_4^-$ adsorption by MIL-101-Cr and MIL-101-Cr-CTAB. It is noted that this batch experiment was conducted using de-ionized water without or with single anion.
- **D.** $ReO_4^-$ removal capacity of anion-exchanged MIL-101-Cr.

In addition, we also evaluated the $F^-$, $Cl^-$, $I^-$ and $CF_3SO_3^-$ exchanged MIL-101-Cr MOFs for $ReO_4^-$ removal from AGW. As shown in Figure 6D, the $Cl^-$, $I^-$ and $CF_3SO_3^-$ exchanged MIL-101-Cr MOFs were more effective at $ReO_4^-$ removal than MIL-101-Cr-$NO_3^-$, probably because the bonding of these anions with the framework is weaker than that for $NO_3^-$, so that $ReO_4^-$ was more efficiently exchanged into the pore structure of these new MIL-101-Cr MOFs.

In order to understand Re chemical speciation and molecular binding mechanisms in MIL-101-Cr and MIL-101-Cr-CTAB MOFs that were exposed to $ReO_4^-$ in AGW, Re $L_3$-edge synchrotron X-ray absorption spectra of these MOF samples were collected using the Canadian Light Source BioXAS beamline. The Re $L_3$-edge X-ray absorption near-edge structure (XANES) spectra are shown in Figure 7A, while the Re $L_3$-edge extended X-ray absorption fine structure (EXAFS) spectra in k space and R magnitude are shown in Figure 7B and 7C, respectively. The spectra of two model compounds, $ReO_2$ and $NaReO_4$, were also included in Figure 7 for comparison. The results indicated that the Re chemical speciation in these MOFs was $ReO_4^-$, but the Re-O bond distances were slightly larger than those in $NaReO_4$. It is likely that $ReO_4^-$ was located in the large pore structure of MIL-101-Cr, and its bonding environment can be further understood through detailed EXAFS data fitting which is currently under way.

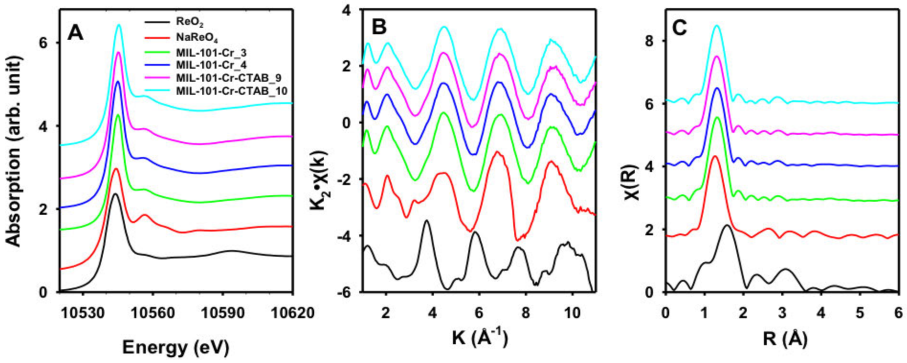

**Figure 7.** Re L3-edge X-ray absorption spectra of MIL-101-Cr and MIL-101-Cr-CTAB exposed $ReO_4^-$ in AGW, in comparison with two model compounds, $ReO_2$ and $NaReO_4$.

- **A.** Re $L_3$-edge XANES.
- **B.** Re $L_3$-edge EXAFS in k space.
- **C.** Re $L_3$-edge EXAFS in R magnitude.

### 4. Ni-TIPA MOF for $TcO_4^-$ removal from the SRS tank waste

A Ni-TIPA MOF was acquired from Soochow University. The crystal structure of Ni-TIPA is shown in Figure 8. It has a large pore size of 10.43×16.11 Å. Ni-TIPA was demonstrated to have high stability in aqueous media across a broad pH range, up to a pH value of 14, as well as high capacity and selectivity toward $ReO_4^-$ removal from aqueous media.

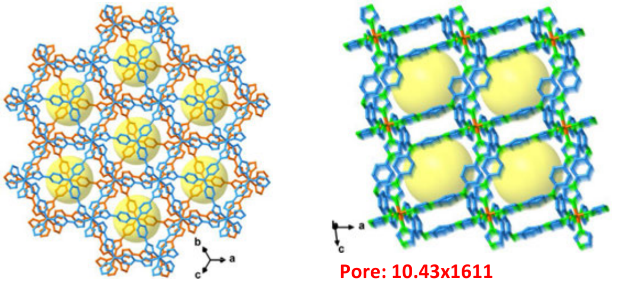

**Figure 8.** Crystal structure of Ni-TIPA MOF

A series of batch contact experiments to test this Ni-TIPA MOF were performed utilizing a sample of actual SRS tank waste.[11] Samples of Ni-TIPA MOF were added to 15-mL conical bottom polypropylene tubes in amounts ranging from 0.004 to 0.16 g. To each tube was then added 4 mL of the SRS tank waste solution to yield experiments with phase ratios ranging from 1 mg/mL to 40 mg/mL. A tube containing only the SRS tank waste solution (no Ni-TIPA) was also run in parallel as a control sample. The tubes were then mounted on a Thermo Scientific® Labquake® tube rotator and were tumbled for 3 hours. At the end of the 3-hour experiment, the tubes were removed from the rotator. The supernatant from each tube was then decanted and filtered through a 0.1-µm PVDF syringe filter. The filtrate was analyzed for $^{99}$Tc activity by liquid scintillation counting (LSC).

The batch contact test results are shown Figure 9. The percent removal of $^{99}$Tc increased as the phase ratio increased. At the highest phase ratio tested, 90% of the $^{99}$Tc was removed from the SRS tank waste solution in 3 hours, in good agreement with experimental results performed using the simulated SRS tank waste (Shen et al., in preparation).

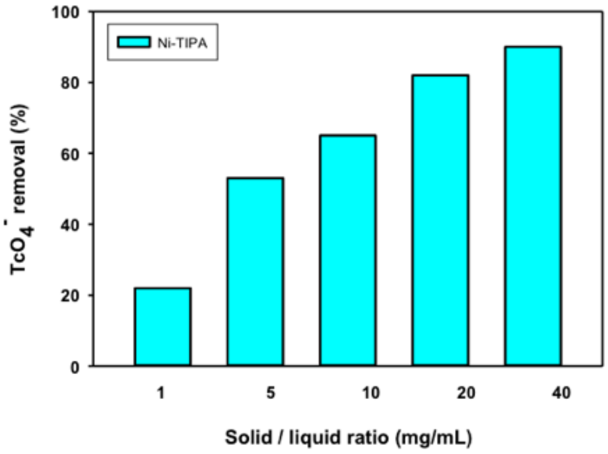

**Figure 9.** $TcO_4^-$ removal percentage from the SRS tank waste stream by Ni-TIPA MOF.

### 5. Potential for economical vitrification

Thermogravimetric analyses of selected MOFs were conducted (Figure 3). The results indicated that these MOFs may be vitrified using economic methods, like heating under 300 °C. In addition, pressure-induced vitrification technology may be developed for these MOFs that are demonstrated to have high capacity for $TcO_4^-$ removal and improved stability in aqueous media. The MOF glasses can be used as potential nuclear waste forms for Tc stabilization.

## FY2019 Accomplishments

- Synthesized and characterized five new versions of MIL-101-Cr MOFs (CTAB-functionalized and $F^-$, $Cl^-$, $I^-$ and $CF_3SO_3^-$ exchanged).
- Completed batch experiments to evaluate these MIL-101-Cr MOFs for $ReO_4^-$ removal from AGW, including adsorption capacity, kinetics, effects of competing anions. The CTAB-functionalized MIL-101-Cr had the highest capacity of ~130 mg $ReO_4^-$/g sorbent. The adsorption reactions were fast and completed within 30 minutes for MIL-101-Cr and 10 minutes for MIL-101-Cr-CTAB.
- Investigated Re chemical speciation and molecular interaction with MIL-101-Cr through synchrotron X-ray absorption spectroscopy. $ReO_4^-$ was demonstrated as being in the pore structure with slightly larger Re-O bond distances than those in $NaReO_4$.
- Studied a new Ni-TIPA MOF for Tc removal from the SRS tank waste stream. The Ni-TIPA MOF was demonstrated to be very stable and selective. The removal percentage of 99Tc increased as the Ni-TIPA/liquid ratio increased, it can remove 90% of $TcO_4^-$ from the SRS tank waste stream at the Ni-TIPA/liquid ratio of 40 mg/mL.

## Future Directions

- Continue developing new MOFs for higher $TcO_4^-$ removal capacity and improved stability, especially under alkaline conditions.
- Develop methods for vitrifying these MOFs as nuclear waste forms so that the entrapped contaminants are stabilized without leaching out.
- Prepare proposals to DOE EM Soil & Groundwater Remediation Program, International Program, and DOE Nuclear Energy program.

### *Publications/Presentations*

1. Dien Li, Natalia B. Shustova, Kathryn M. Taylor-Pashow, Daniel I. Kaplan, Jake W. Amoroso, Thomas D. Bennett, CTAB-functionalized MIL-101-Cr for $TcO_4^-$ and $ReO_4^-$ sequestration from AGW: Capacity and molecular binding mechanisms, **2019**, in preparation.
2. Nannan Shen, Shuao Wang, Kathryn M. Taylor-Pashow, Dien Li, Mechanism unravelling for ultrafast and selective $^{99}TcO_4^-$ uptake from nuclear waste streams by Ni-TIPA metal organic framework: A combined radiological experiment and molecular dynamics simulation study, **2019**, in preparation.

### *References*

1. J.P. Icenhower, N.P. Qafoku, J.M. Zachara, W.J. Martin, The biogeochemistry of technetium: A review of the behavior of an artificial element in the natural environemnt, American Journal of Science, 310 (2010) 721-752.
2. L.Y. Liang, B.H. Gu, X.P. Yin, Removal of technetium-99 from contaminated groundwater with sorbents and reductive materials, Separations Technology, 6 (1996) 111-122.
3. T. Peretyazhko, J.M. Zachara, S.M. Heald, B.H. Jeon, R.K. Kukkadapu, C. Liu, D. Moore, C.T. Resch, Heterogeneous reduction of Tc(VII) by Fe(II) at the solid-water interface, Geochimica Et Cosmochimica Acta, 72 (2008) 1521-1539.
4. A.E. Plymale, J.K. Fredrickson, J.M. Zachara, A.C. Dohnalkova, S.M. Heald, D.A. Moore, D.W. Kennedy, M.J. Marshall, C.M. Wang, C.T. Resch, P. Nachimuthu, Competitive reduction of pertechnetate (($TcO_4^-$)-Tc-99) by dissimilatory metal reducing bacteria and biogenic Fe(II), Environmental Science & Technology, 45 (2011) 951-957.
5. D. Li, D.I. Kaplan, Solubility of Technetium Dioxides ($TcO_2$-c, $TcO_2 \cdot 1.6H_2O$ and $TcO_2 \cdot 2H_2O$) in Reducing Cementitious Material Leachates: A Thermodynamic Calculation, Savannah River National Laboratory, Aiken, SC 20908, 2013.
6. J.K. Fredrickson, J.M. Zachara, A.E. Plymale, S.M. Heald, J.P. McKinley, D.W. Kennedy, C.X. Liu, P. Nachimuthu, Oxidative dissolution potential of biogenic and abiogenic TcO2 in subsurface sediments, Geochimica Et Cosmochimica Acta, 73 (2009) 2299-2313.
7. Y. Liu, J. Terry, S. Jurisson, Pertechnetate immobilization in aqueous media with hydrogen sulfide under anaerobic and aerobic environments, Radiochimica Acta, 95 (2007) 717-725.
8. D.M. Fan, R.P. Anitori, B.M. Tebo, P.G. Tratnyek, J.S.L. Pacheco, R.K. Kukkadapu, M.H. Engelhard, M.E. Bowden, L. Kovarik, B.W. Arey, Reductive sequestration of pertechnetate (($TcO_4^-$)-Tc-99) by nano zerovalent iron (nZVI) transformed by abiotic sulfide, Environmental Science & Technology, 47 (2013) 5302-5310.
9. W. Um, H.S. Chang, J.P. Icenhower, W.W. Lukens, R.J. Serne, N.P. Qafoku, J.H. Westsik, E.C. Buck, S.C. Smith, Immobilization of 99-technetium (VII) by Fe(II)-goethite and limited reoxidation, Environmental Science & Technology, 45 (2011) 4904-4913.
10. I.Y. Skobelev, A.B. Sorokin, K.A. Kovalenko, V.P. Fedin, O.A. Kholdeeva, Solvent-free allylic oxidation of alkenes with O-2 mediated by Fe- and Cr-MIL-101, Journal of Catalysis, 298 (2013) 61-69.
11. C.L. Crawford, Results for the First Quarter Calendar Year 2019 Tank 50 Salt Solution Sample, SRNL-STI-2019-00184, Rev. 0, Savannah River National Laboratory, Aiken, SC 29808, 2019.

### *Acronyms*

| | |
|---|---|
| **AGW** | Artificial groundwater |
| **BET** | Brunauer-Emmett-Teller |
| **CTAB** | Cetyl trimethylammonium bromide |
| **DOE** | Department of Energy |
| **EDS** | Energy dispersive X-ray spectroscopy |
| **EXAFS** | Extended X-ray absorption fine structure |
| **FTIR** | Fourier transform infrared spectroscopy |
| **LSC** | Liquid scintillation counting |
| **MIL** | Materials Institute Lavoisier |
| **MOF** | Metal organic framework |
| **PVDF** | Polyvinylidene fluoride |
| **SRS** | Savannah River Site |
| **TGA** | Thermogravimetric analysis |
| **TIPA** | Tris(4-(1H-imidazol-1-yl)phenyl)amine |
| **XANES** | X-ray absorption near-edge structure |
| **XRD** | X-ray diffraction |

### *Total Number of Post-Doctoral Researchers*

One post-doctoral researcher involved through the subcontract with the University of South Carolina

# Synthesis and Characterization Of Novel Actinide Compounds

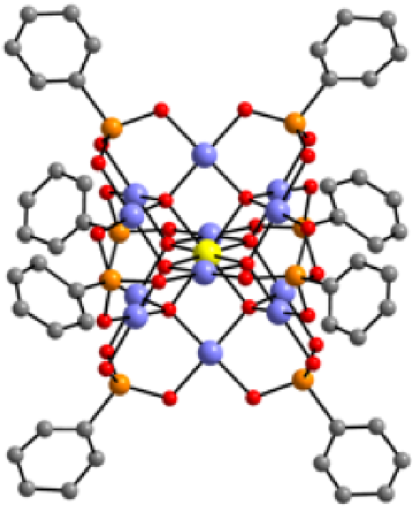

**Figure 1.** Molecular structure and packing arrangement of $[U^{III}Pd^{II}_{12}(AsPh)_8O_{32}]^{5-}$; the first uranium-based polyoxopalladate

**Project Team:** J. H. Christian (Primary),
T. C. Shehee (SRNL), U. Kortz (Jacobs University),
C. McMillen (Clemson), N. S. Dalal (FSU), J. Ling (Claflin)

**Thrust Area**: Legacy Waste Cleanup

**Project Start Date:** October 1, 2017

**Project Start Date:** September 30, 2019

*To develop new separation and environmental remediation tactics for heavy metals it is important to understand the chemical and electronic factors that distinguish lanthanides from actinides. In this LDRD, we attempted to synthesize new actinide-based polyoxometalates (POMs) using synthetic templates that have traditionally been used to develop lanthanide-based POMs. Our goal was to structurally characterize the actinide POMs so they could be compared to their lanthanide analogues. In FY 19, we were successful in the synthesis of the first uranium-based polyoxopalladate –* $[U^{III}Pd^{II}_{12}(AsPh)_8O_{32}]^{5-}$ *(Figure 1).*

## Objectives

- Develop and implement a robust synthesis method for generating high-purity $PuCl_3$
- Complete successful single-crystal syntheses of new uranium and plutonium POMs
- Use single-crystal X-ray diffractometry to elucidate the structures of newly synthesized actinide POMs
- Perform magnetic characterization of newly synthesized actinide POMs

## Introduction

A crucial challenge in achieving efficient separation of nuclear waste, spent nuclear fuel, and nuclear materials interacting with water, is the difficulty in separating trivalent actinides from lanthanides due to similarities in oxidation state, ionic radii, and some chemical properties.[1] Therefore, it is important to improve our understanding of the coordination chemistry of f-element complexes and the chemical differences between lanthanides and actinides in order to improve our understanding of the factors that contribute to extraction selectivity and the fate of heavy elements in the environment. Currently, about 95% of actinide structures in the Cambridge Structural Database (CSD) and Inorganic Crystal Structure Database (ICSD) databases are composed of thorium or uranium.[2] The lack of structural diversity in actinide chemistry is largely caused by experimental limitations due to a lack of licensing for possessing transuranic materials, limited radiological laboratory equipment, and an unfounded belief that thorium and uranium can be accurate surrogates for other actinides. These common limitations leave ample scholarly space for SRNL to conduct high throughput exploratory research involving synthesis of compounds containing uranium and transuranic elements.

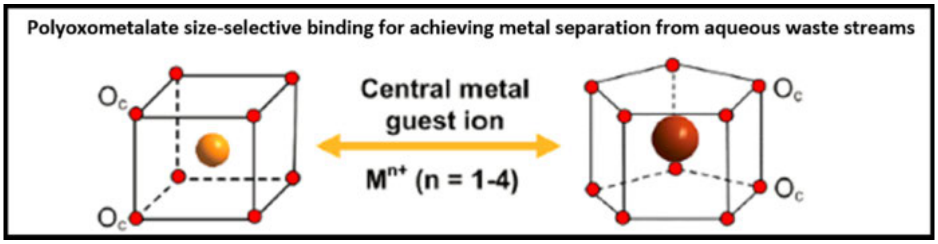

**Figure 2.** Polyoxometalates can accommodate heavy metals in a variety of chemical coordinations.

Polyoxometalates (POMs) are an interesting class of compounds that can accommodate actinide ions (Figure 2). POMs have a general composition of $[X_xM_mO_y]^{n-}$ in which X are positive-valent elements, and M are hosted metals. We believe the utility of polyoxoanions for novel actinide compound development is three-fold: **(1)** there is an abundance of existing POM structures in the literature; many of which accommodate lanthanide or early-actinide ions. Therefore, these POMs could accommodate many transuranic elements while also providing the lanthanide analogs needed to directly compare bonding behavior between the Ln and Ac structures. **(2)** Many existing POMs encapsulate metals in well-defined coordination environments, thus making them ideal candidates for magnetic (EPR, SQUID) and spectroscopic (XPS, UV-vis, IR) characterization. **(3)** The well-defined coordination environments of POMs should facilitate our construction of accurate computation models aimed at further elucidating the electronic structure and bonding behavior of new actinide compounds.

To synthesize novel uranium and plutonium POMS for this LDRD, we focused our synthetic efforts on the use of polyoxopalladate ligands, a family of metal oxide nanoclusters containing a palladium backbone that has been shown to accommodate all $Ln^{3+}$ ions.[3]

## Approach

To generate new actinide compounds, we utilized existing polyoxometalate synthetic templates but substituted Pu and U as the metal cations instead of lanthanides. We narrowed our synthetic focus to a class of heteropolyoxopalladates that were recently shown to be very effective at incorporating small, medium, and also large lanthanide(III) ions into the center of the palladate ligand.[3] These previous results suggested that the $Pd^{III}_{12}O_{32}$ shell can adjust to the coordination requirements of the encapsulated guest cation, which we postulated would prove useful at stabilizing U and Pu.

Typical synthesis involved a one-pot self-assembly reaction of $Pd(CH_3COO)_2$, phenylarsonic acid, and the respective metal$^{3+}$ cation in 0.5 M aqueous sodium acetate solution with strict control over solution pH. Uranyl nitrate was used for uranium-based reactions while $Pu(NO_3)_3$ was used for plutonium-based reactions. The low pH of $Pu(NO_3)_3$ was incompatible with our reactions. Thus, at the end of FY19, we developed a robust technique for generating $PuCl_3$; a water soluble, neutral inorganic salt.

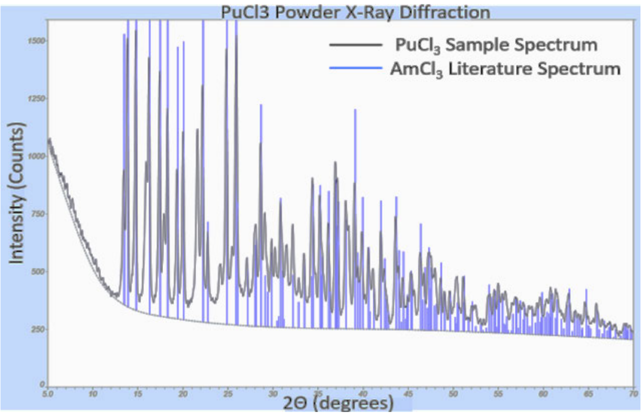

**Figure 3.** Powder X-ray diffraction spectrum of synthesize $PuCl_3$ (black) is shown with an overlay of the published $AmCl_3$ spectrum (blue). The synthesize $PuCl_3$ spectrum is an excellent match with $AmCl_3$ indicating the synthesized powder is high-purity.

To generate $PuCl_3$, plutonium nitrate (~0.00156 moles) was reduced using twice the moles of ascorbic acid (~0.00312 moles). Plutonium$^{3+}$ oxalate was then precipitated according to the following reaction: $2\ Pu(NO_3)_3 + 3\ H_2C_2O_4 \rightarrow Pu_2(C_2O_4)_3$. Plutonium$^{3+}$ oxalate was then filtered and air dried. The oxalate powder and a magnetic stirrer were then added to a round bottom flask equipped with an air reflux condenser and a thermometer. A molar excess (>1 moles $C_3Cl_6$ : 1 mole Pu) of $C_3Cl_6$ was added to the flask. The molar ratio was not important for the reaction as long as the ratio was >1 and there was sufficient volume of $C_3Cl_6$ to induce vigorous stirring. The solution was heated and vigorously stirred between 180 – 190 °C for 18 hours. The solution was then cooled to room temperature and filtered. The collected solid was rinsed several times with carbon tetrachloride ($CCl_4$). Successful synthesis of $PuCl_3$ was confirmed via powder X-ray diffraction (Figure 3) and visual inspection.

## Results/Discussion

In FY18, we set up our lab for performing POM actinide synthesis work, we purified actinide precursor compounds, and we were successful in growing $Ln^{3+}$ versions of several polyoxometalates. In FY19, we applied our synthetic techniques towards U and Pu-based reactions. No Pu reactions were successful when using $Pu(NO_3)_3$ as our metal source. We believe the low pH of our Pu solution was the primary factor inhibiting growth of stable compounds. We attempted to adjust the pH of our Pu solution, but insoluble Pu hydroxide forms readily as the solution approaches neutral pH. Thus, we worked to develop a synthetic plan for generating $PuCl_3$; a very soluble and neutral inorganic salt.

$PuCl_3$ was synthesized by reaction of $Pu_2(C_2O_4)_3$ with $C_3Cl_6$ between 180 – 190 $^{o}C$ for 18 hours. The light blue-green powder is very water soluble, but oxidizes within a few days if not stored under an inert environment. Unfortunately, we were not able to use our $PuCl_3$ to synthesize Pu POMs before the end of FY19. We were however able to synthesize the first uranium-based polyoxopalladate - $U^{III}[Pd^{II}_{12}(AsPh)_8O_{32}]_5$. The structure of this new compound was thoroughly characterized using single crystal X-ray diffraction. The new compound has 12 palladium$^{2+}$ ions surrounding the central $[XO_8]$ fragment. The oxygen atoms of the inner $[XO_8]$ cube are coordinated to $U^{3+}$ and three palladiums placed on a trigonal side of the cuboctahedron. Each of the twelve $Pd^{2+}$ ions exhibits square-planar coordination. The polyanions form a hexagonal-packing framework with channels along the a axis. This structure is very similar its $Ln^{3+}$ analogues.

## FY2019 Accomplishments

- Successfully synthesized the first uranium-based polyoxopalladate.
- Successfully synthesized $PuCl_3$ for use with future plutonium-based reactions.
- Completed successful single-crystal syntheses of POM lanthanide analogues.

## Future Directions

- Synthesize new plutonium-based POM compounds using $PuCl_3$
- Determine whether newly synthesized structures have a binding preference for U or Pu
- Analyze the magnetic properties of all newly synthesized compounds

### Publications/Presentations

1. Synthesis and Characterization of the First Heterooxypalladate Coordinated with Uranium $U^{III}[Pd^{II}_{12}(AsPh)_8O_{32}]_5$. – *Manuscript in Preparation.*

### References

1. A. E. V. Gorden, M. A. DeVore and B. A. Maynard, *Inorganic Chemistry*, **2012**, 52, 3445-3458
2. The Cambridge Structural Database (CSD), https://www.ccdc.cam.ac.uk/solutions/csd-system/components/csd/
3. M. Barsukova, N. V. Izarova, R. N. Biboum, B. Keita, L. Nadjo, V. Ramachandran, N. S. Dalal, N. S. Antonova, J. J. Carbó, J. M. Poblet and U. Kortz, *Chemistry – A European Journal*, **2010**, 16, 9076-9085.

### Acronyms

| | |
|---|---|
| **CSD** | Cambridge Structural Database |
| **EPR** | Electron paramagnetic resonance |
| **ICSD** | Inorganic Crystal Structure Database |
| **POM** | Polyoxometalate |
| **SQUID** | superconducting quantum interference device |
| **XPS** | X-ray photoelectron spectroscopy |

# Gamma-Ray Raster Imaging

**Project Team:** Tim Aucott, Willie Wells, Tad Whiteside

**Thrust Area**: Legacy Waste Cleanup

**Project Start Date:** October 1, 2017

**Project End Date:** September 30, 2019

*This project has developed an alternative imaging capability for imaging and quantifying radioactive materials in situ. This approach uses a robotic-mounted gamma-ray detector which can move around an area of interest, sampling the space at a high frequency. By rastering across the area, an image can be created with no collimation and a high efficiency.*

*An open-source robotic platform was programed to search an open area, collecting gamma-ray spectra every second. Informative path planning was used to direct the robot to areas of higher dose. Finally, a Bayesian particle filter was used to locate the source with minimal counting statistics.*

*The use of a robotic mount allows data collection for long periods of time unattended, and it will also eliminate uncertainties in positioning typically introduced by personnel. This approach will be particularly relevant for gloveboxes, shielded cells, or process piping which may have complex, non-uniform distributions of material.*

## Objectives

- Implement simultaneous localization and mapping (SLAM) in real time while robotic platform is travelling
- Calibrate detector response in 3D
- Develop Bayesian particle filter analysis
- Integrate informative path planning algorithms onto the platform, including real-time communication with the robotic operating system (ROS)
- Evaluate the system’s performance in a number of test configurations

## Introduction

Gamma-ray assays and images are a key tool for holdup characterization in a facility. Images can be used to create radiation maps, which can be used for establishing procedures, assist decontamination and aid radiological control. This project uses a small gamma-ray detector on a robotic platform to sample an area at high frequency in order to create an image.

This approach is:

- Lightweight: requiring little to no lead shielding
- Autonomous: requiring minimal operator time and input
- Precise: relying on camera, LIDAR, and software to map out the space

In addition, this work integrates state-of-the-art robotics developments to improve the acquisition of gamma-ray data. Informative Path Planning (IPP) is used to design a path for a robotic sensor platform to gather the most information about the radiation distribution while operating under the set of constraints given by the dynamics of the robot and other requirements such as minimizing the overall mission time.

Ideally, such a system would couple multiple layers of decisions:

- Select the locations where a robot should take samples
- Produce paths for the robot to use when travelling from one location to the next
- Generate a radiation map using some reconstruction algorithm

Given a robot equipped with a basic gamma detector and LIDAR sensor, how can we efficiently explore an unknown environment in such a way that we can satisfy the robot's constraints while simultaneously maximizing the accuracy of the map and minimizing the total runtime?

There are existing approaches which use directional sensors [1, 2] to gain further information about where a radiation source might be. In this work, an omnidirectional gamma sensor is utilized, meaning that the origination of the radiation when measuring at a location is not known. This greatly lowers the cost of the equipment needed but increases the complexity of localization. The use of Gaussian process regression (GPR) and an associated utility function has been proposed by several authors [3, 4]. This project also explored the use of a Bayesian particle filter [5, 6] to localize and quantify the source. Informative path planning algorithms were developed [7] to direct the sampling locations closer to areas of higher dose.

## Approach

A gamma-ray detection system, in this case a cadmium zinc telluride (CZT) semiconductor detector from Kromek, is mounted to a remote-controlled platform. The CZT provides excellent energy resolution in an extremely small package, keeping the payload light. The detector is controlled by an Intel Joule single-board computer, which in turn talks wirelessly to a laptop. Experiments were also carried out on a Turtlebot Waffle, which comes equipped with a laser detection system (LDS) and a light detection and ranging (LIDAR) system (shown in Figure 1). Gamma-ray spectra are saved along with LIDAR scans and positioning information.

The detector was calibrated in three dimensions as a function of energy, distance, and angle using a Ho-166m calibration source. This calibration was used as the input to a Bayesian particle filter. A particle filter is a form of maximum likelihood estimation (MLE) which utilizes a large, finite number of hypotheses to approximate an unknown source distribution.

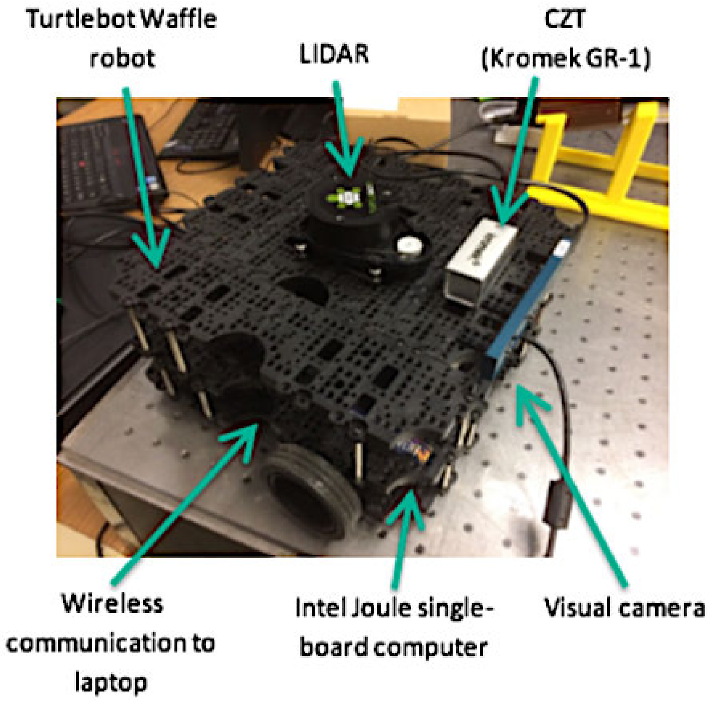

**Figure 1.** The Turtlebot Waffle robot, with important components and sensors

## Results/Discussion

The robot was tested with a Cs-137 10 µCi source, placed in a large paint can-sized container for improved response from the robot's LIDAR to help prevent collision. The can was placed at a location of (1.58 m, -1.1 m) relative to the starting point of the robot, which is treated as the origin (0 m, 0 m). The robot's navigation consisted of near-random waypoints to traverse, in which locations which had experienced higher detector count responses were more favored than location which received fewer counts. A few main points about the test should be noted:

- The robot covered only half of the total quartered-off area in which it could survey
- The robot, for most of the test, never moved behind the source (i.e., it was always to one side of the source during the test; a full 360-degree coverage was not obtained, only 180 degrees)
- The source was located at the center of the test area

The collection of all data stored from the robot's various sensors and other programs was stored in a .bag file, commonly used to record robot sensor data in ROS. These ROS .bag files were converted into .csv files for easy manipulation. Position, orientation, and radiation count data were pulled from the .csv files and processed as such: position data on the millisecond level was averaged to generate an average position per second, angle of orientation was converted from standard quaternion to angle (in degrees), and radiation counts were arranged into a set of spectra with 4096 channels.

The algorithm ran for a total of 140 times on a data set of the Cs-137 10 µCi source test, each time with a different distribution of particles and positions selected randomly within the test area. The predicted $x$ and $y$-coordinates and predicted activity, $A$, of each test was recorded. Because of the low efficiency of the CZT detector, the entire gamma-ray spectrum (not just the unscattered photopeak) was used for the analysis. As a result, although activity is predicted, it is dominated by down-scatter in the environment and did not accurately determine the source activity. The distribution of particles with position and activity (in color) is shown in Figure 2.

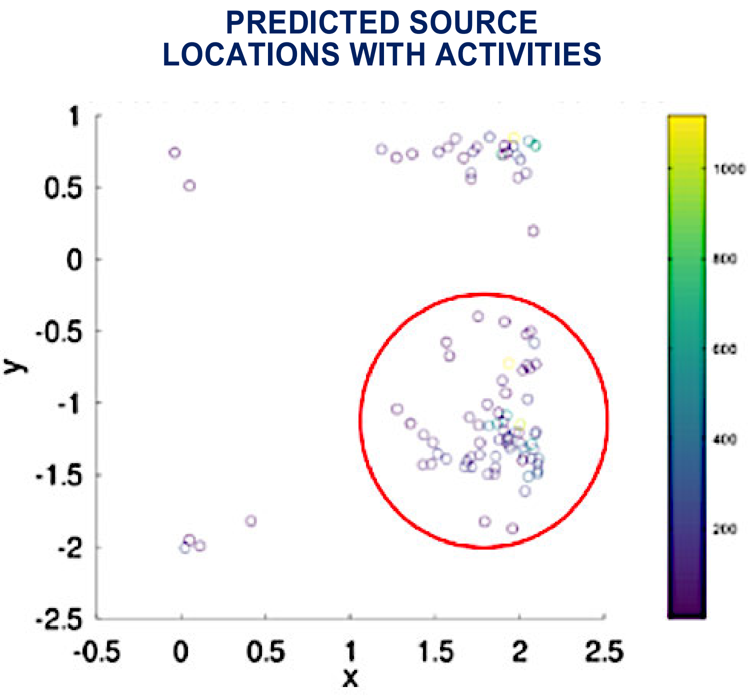
PREDICTED SOURCE LOCATIONS WITH ACTIVITIES

**Figure 2.** Distribution of most likely predicted source locations from 140 runs of particle filter algorithm.

**The mean (µ ± 1σ) of the $x$ and $y$-coordinates are: 1.76 ± 0.437 meters and -0.809 ± 0.851 meters.**

**Focusing on the highlighted cluster localized around (2 m, -1 m), the mean $x$ and $y$ positions, respectively, are: 1.86 ± 0.210 meters and -1.19 ± 0.296 meters.**

## FY2019 Accomplishments

- Robotic platform was successfully programmed to integrate the CZT data acquisition into the robotic operating system.
- Bayesian particle filter was successfully used to localize sources in an environment. This algorithm succeeded with minimal counting statistics and only a partial coverage of the search area.
- Informative path planning algorithm was successfully implemented, allowing for feedback between the CZT count rate and the robot's search path.

## The Future Work

- Design system for use in real facilities: Some obstacles included the use of wireless communications, as well as limited battery life. These logistical concerns would need to be addressed prior to deployment, especially given the advantage of long survey times.
- Increased count times could compensate for the low efficiency of the CZT detector. Alternatively, a larger detector or multiple small detectors could be added to increase the efficiency. This would allow the system to accurately quantify activities by measuring a calibrated photopeak.

### Publications/Presentations

1. S. Zanlongo, Y. Tan, T. Aucott, "Informative Path Planning for Mapping Radiation," ANS Winter 2018 Meeting, November 2018.
2. B. Quiter, R. Pavlovsky, J. Cates, T. Aucott, IEEE Nuclear Science Symposium, Scheduled November 2019.
3. SRNL-L4540-2019-00002, "Gamma Ray Raster Imaging," September 2019.
4. SRNL-L4120-2019-00028, "Bayesian Particle Filter for Robotic Gamma-Ray System," August 2019.
5. W. Wells, T. Aucott, "Gamma Ray Raster Imaging," Nuclear News, December 2019.

### References

1. K. Vetter, R. Barnowksi, A. Haefner, T. H. Y. Joshi, R. Pavlovsky, and B. J. Quiter, "A Gamma-Ray imaging for nuclear security and safety: Towards 3-D gamma-ray vision," Nucl. Inst. Methods Phys. Res. A, vol. 878, pp. 159–168, 2018.
2. M. Lee, M. Hanczor, J. Chu, Z. He, N. Michael, and R. Whittaker, "3-D Volumetric Gamma-ray Imaging and Source Localization with a Mobile Robot," Waste Management Symposia 2018.
3. R. Marchant and F. Ramos, "Bayesian Optimisation for informative continuous path planning," Proc. - IEEE Int. Conf. Robot. Autom., pp. 6136–6143, 2014.
4. G. Hitz, A. Gotovos, F. Pomerleau, M. É. Garneau, C. Pradalier, A. Krause, and R. Y. Siegwart, "Fully autonomous focused exploration for robotic environmental monitoring," Proc. - IEEE Int. Conf. Robot. Autom., pp. 2658–2664, 2014.
5. S. Thrun, W. Burgard, and D. Fox, *Probabilistic Robotics*, MIT Press, Aug. 2005
6. J. Towler, B. Krawiec, and K. Kochersberger, "Terrain and Radiation Mapping in Post-Disaster Environments Using an Autonomous Helicopter," Remote Sensing, vol. 4, p. 1995-2015.
7. B. Ristic, M. Morelande, and A. Gunatilaka, "Information driven search for point sources of gamma radiation," Signal Processing, vol. 90, p. 1225-1239, Oct. 2009.

### Acronyms

| | |
|---|---|
| **CZT** | Cadmium Zinc Telluride |
| **GPR** | Gaussian Process Regression |
| **IPP** | Informative Path Planning |
| **LDS** | Laser Detection System |
| **LIDAR** | LIght Detection And Ranging |
| **MLE** | Maximum Likelihood Estimation |
| **RMSE** | Root Mean Square Error |
| **ROS** | Robotic Operating System |
| **SLAM** | Simultaneous Localization And Mapping |

### Total Number of Post-Doctoral Researchers

One – Sabastian Zanlongo / On Site

### Total Number of Student Reserachers

Two – Aimee Gonzales and Mustafa Siddiqi / On Site

# Hyperspectral Raman Imaging using a Spatial Heterodyne Spectrometer (SHS)

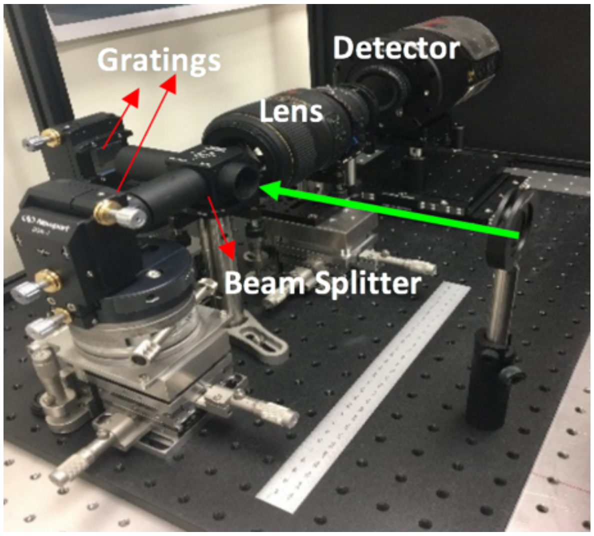

SHRS built at SRNL. Green Arrow indicates incoming light.

**Project Team:** K. A. S. Fessler, R. Lascola, P. O'Rourke, S. Serkiz

**Subcontractor**: S. M. Angel, M. L. Myrick (University of South Carolina)

**Thrust Area**: Legacy Waste Cleanup

**Project Start Date:** October 1, 2017

**Project End Date:** September 30, 2020

*SRNL, and the larger community, has limited chemical-specific imaging (CHI) capabilities, which would be beneficial for remote detection of threat chemicals or use in inaccessible/harsh environments, as well as in-line process monitoring. CHI is underdeveloped due to issues of sensitivity, stable alignment and calibration, and ease of operation associated with most optical instruments. The project objective is to develop a novel, rugged, highly sensitive spectrometer to support real-time, CHI using hyperspectral Raman spectroscopy. Raman spectroscopic analysis will provide chemical specificity and using a spatial heterodyne spectrometer (SHS) will increase the sensitivity due to the high light throughput design. The SHS design does not require moving parts allowing for a very stable system, reducing alignment and calibration issues. The instrument will be assembled and initially applied to Raman gas detection of the Saltstone disposal unit headspace gas concentrations. Raman gas analysis is the most impacted by sensitivity issues and will be used to demonstrate the increased light collection capability of the SHS over a conventional dispersive spectrometer. The system will be later modified to image spectral information in a spatial domain to provide information on the spatial distribution of a sample scene.*

## Objectives

- Instrumentation assembly and demonstration for Raman gas analysis
    - Demonstrate ability to measure gas samples with a SHS and compare results to a conventional Raman spectrometer.
- Optimization of SHS system for Saltstone headspace application and demonstrate lab-scale measurements
    - Lab measurements to demonstrate Raman as a useful technique for Saltstone samples at relevant concentrations (~100s ppm) and to identify potential implementation issues and solutions.
    - Streamlining data acquisition and developing data processing.
- Adaptation of system for hyperspectral measurements and optimization
    - Determine the components and arrangement needed to allow for hyperspectral measurements
    - Demonstrate ability to collect hyperspectral Raman images with a SHS

## Introduction

The Spatial Heterodyne Spectrometer (SHS) is a recently developed technology for optical spectroscopy that promises enhanced sensitivity and new opportunities for process and field measurements compared to conventional spectrometers. Sensitivity gains of 10-100x are obtained through light collection over a wide field-of-view and measurement across a two-dimensional detector array. The SHS may provide a faster response time to facilitate process controls and reactions to emerging off-normal conditions, as might be used when monitoring dissolver headspaces for flammability concerns. With no moving parts, a SHS can support the use of typically delicate laboratory instrumentation in a field environment. More novel measurement applications take advantage of the 2D nature of the detection for obtaining images of the scene. One dimension can be used to provide spatial information at the sample, permitting chemically sensitive imaging that can provide real-time determination of chemical distributions. Examples where such information would be valuable include imaging chemical concentration gradients in a process vessel and rapid detection of "residues of interest" across a wide area. With sufficient development, temporal information may also be obtained, permitting tracking of rapidly evolving chemical reactions.

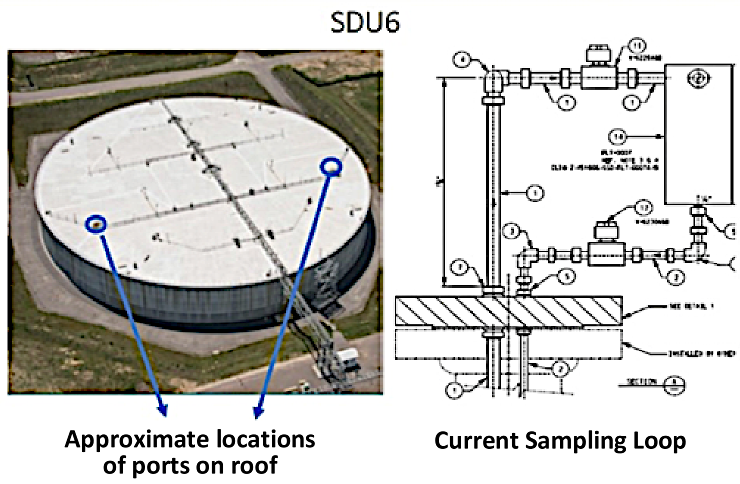

**Figure 1.** Saltstone Disposal Unit 6 and Sampling Loop

Saltstone disposal unit 6 (SDU6) requires controls to ensure the flammable gas concentration limit for a list of chemicals is not exceeded, left image in Figure 1. Calculated estimates of gas concentrations are very conservative and experimental measurements are needed to provide accurate gas concentrations to fill the tank with the appropriate amount of waste without exceeding the concentration limits. In-situ measurements are ideal to provide real-time analysis of the conditions within the tank. However, the current tests require pulling a sample and the sampling loop does not work as intended, right image in Figure 1.

## Approach

Raman spectroscopy is an optical scattering technique which provides a molecular "fingerprint" of compounds in the solid, liquid, or gas phase. Raman scattering is an inherently weak technique with only 1 in 108 photons Raman scattered, and increasing the irradiance, the number of molecules excited, or the collection efficiency are ways to improve signal strength. Of these methods, irradiance is often limited by sample photodegradation, and gases have the lowest molecular density of all sample phases which cannot be improved without pre-concentration. Increasing collection efficiency has historically had several challenges. Conventional dispersive spectrometers typically exchange spectral resolution for higher collection efficiency due to the slit-based spectrometer design. Michelson interferometeric spectrometers offer large collection efficiency, yet wavelength separation is achieved via a moving mirror which must travel large distances (ultraviolet) or in an extremely stable environment (mid-infrared) for high resolution. Both conditions provide challenges for operation in a process or field environment.

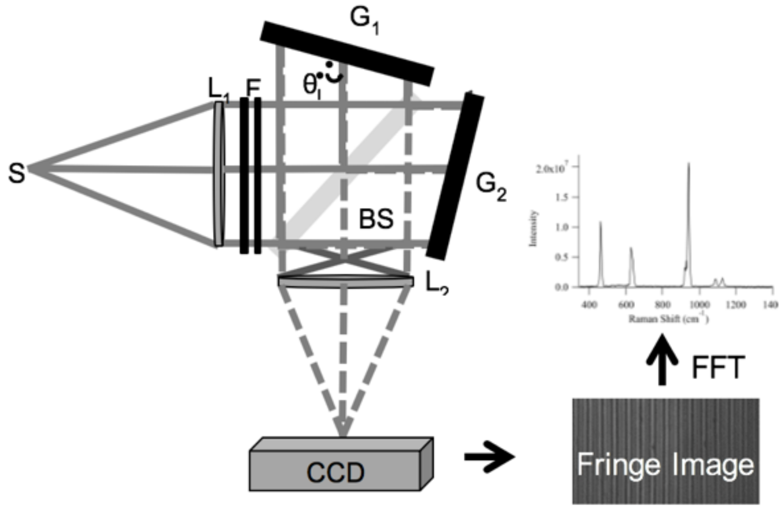

**Figure 2.** SHRS schematic; fringe image, and Raman spectrum from fast Fourier transform of fringe image

A new type of interferometric spectrometer, the spatial heterodyne spectrometer (SHS), has recently been adapted for Raman spectroscopic analysis, Figure 2.[1-6] The instrument offers large collection efficiency and high resolution in a system with no moving parts. With no moving parts, the SHS design promises the ruggedness and stability required for instrumentation being placed in a facility or used in the field. The spectrometer design also allows for monolithic units to be engineered for specific wavelength ranges. As stated above, increasing the collection efficiency is an approach to improve the sensitivity of a Raman measurement technique, and the SHS is a spectrometer that offers large collection efficiencies without compromising resolution or instrument size and stability. We propose to investigate the collection efficiency improvements for gas samples in a backscattering (180°) or perpendicular (90°) sampling arrangement when using an SHS. Depending on the optical set up, we expect to achieve a collection efficiency 10-100 times larger when using a SHS. The corresponding increases in sensitivity would make Raman spectroscopy a more attractive option for gas monitoring applications such as the SDU headspace analysis for flammable species. Sensitivity improvements could be used to lower detection limits, increase the speed of detection and response, or a combination of the two. The first year of the project focused on building an SHS and assembling a gas sample cell measurement scheme. The collection efficiency study, to compare the SHS to a conventional dispersive spectrometer, was delayed due to issues with measuring Raman spectra. Year two of this project began with troubleshooting the instrument and Raman measurement set-up to determine and fix any issues preventing the collection of Raman spectra followed by optimization of instrument and collection parameters, as well as acquiring first Raman gas phase measurements with the SHS.

## Results/Discussion

The SHS specifications were determined based on the SDU application, which is required to measure the flammable gases off-gassed during pouring of the Saltstone, $H_2$ and $NH_3$. The SHS was built to operate in the visible electro-magnetic spectrum using a commercially of the shelf (COTS) laser at 532 nm to take advantage of the increased Raman efficiency at shorter wavelengths. A spectral resolution of 30 cm$^{-1}$ is more than adequate for discriminating the Raman bands of $H_2$ (540, 655, and 4160 cm$^{-1}$) and $NH_3$ (934, 967, 3340, and 3659 cm$^{-1}$).[7-9] Therefore, the 150 gr/mm gratings were replaced with 50 gr/mm gratings to increase the spectral range to cover the entire Raman fingerprint region 0 - 4200 cm$^{-1}$. The new gratings also decreased the resolution to ~30 cm$^{-1}$, which is adequate to resolve the peaks of interest. With the new gratings, the rotational and vibrational lines of $H_2$ could be measured simultaneously without any scanning mechanisms.

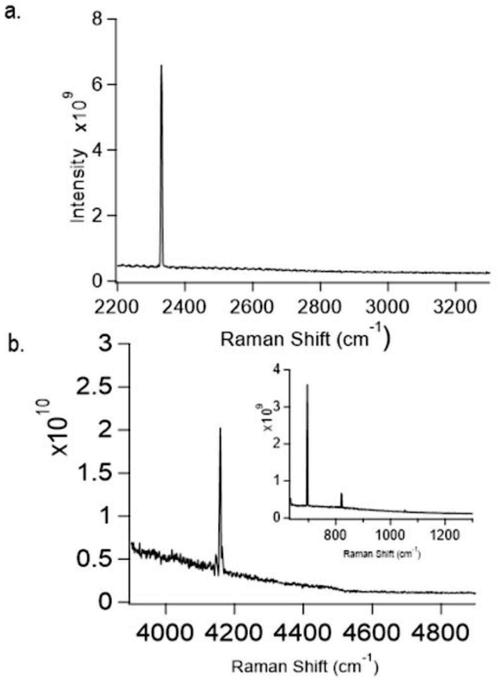

**Figure 3.** Raman spectra of **a)** nitrogen in air and **b)** hydrogen in cell measured using a SHRS. **(Inset)** Rotational spectrum of $H_2$.

Through our collaboration with USC, significant progress in instrument operation has been accomplished. Using Dr. Angel's SHS system, our first Raman gas measurements were made in his laboratory, and their work demonstrated a fluorescence issue with the COTS gas cell. Initially, gaseous nitrogen in the air was measured for 10 minutes using 532 nm at 295 mW to demonstrate a Raman gas measurement, Figure 3a. The detection limit of hydrogen was calculated using the known cross-section values for nitrogen and hydrogen and was determined to be <0.4%. A Raman spectrum of gaseous hydrogen was also measured, at an unknown concentration, to demonstrate the capability, Figure 3b. Due to the fluorescence issue with the gas cell, further hydrogen measurements were postponed until a new cell was obtained. Working with Dr. Angel's group, the optimal optical filtering was determined to improve the signal-to-noise ratio (SNR) to allow for Raman spectral gas measurements. Dr. Angel's student also visited our laboratory to provide technical advice to improve our SHS system. Dr. Myrick has greatly increased our measurement efficiency by providing a software script that can process the spectral data in less than one second and generates real-time spectral data. He also began investigating how to improve the data processing by building onto the basic processing techniques being used previously.

As mentioned above, several instrument issues had to be addressed to enable Raman measurements. Vibrational isolation of the SHS from the detector was found to be necessary due to the cooling fan in the detector vibrating the gratings and blurring the fringe pattern. The detector alignment also required improvement and was accomplished through the development of a precision mount designed and manufactured by SRNL, Figure 4. These two improvements, along with optimizing the detector settings, made Raman measurements possible. The COTS gas cell proved to fluoresce under 532 nm excitation, therefore a new gas cell as was designed and manufactured by SRNL as well, Figure 5. With the new cell, Raman gas measurements of hydrogen at known concentrations can be investigated and the comparison to a commercial spectrometer can be conducted.

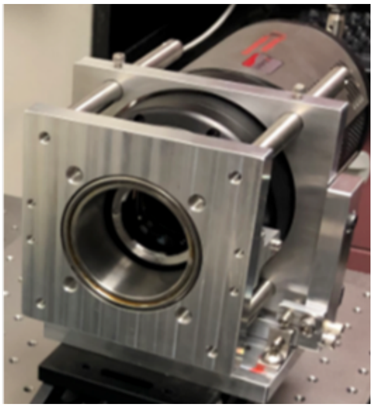

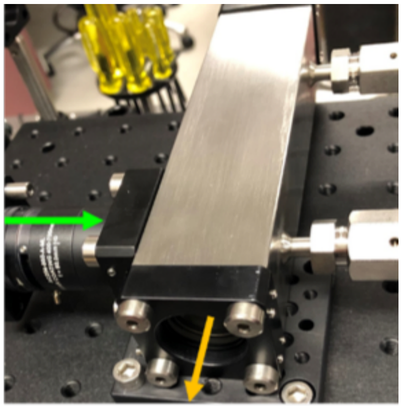

**Figure 4. (left)** SRNL designed detector mount

**Figure 5.** Raman gas cell built at SRNL. Arrows indicate incoming (green) and outgoing (orange) light.

## FY2019 Accomplishments

- Performed system troubleshooting and corrected several issues which were preventing Raman spectral measurements: vibration isolation of SHS from detector, optimized detector settings, designed new detector mount to provide precision adjustments, and designed new gas cell to eliminate fluorescence observed in COTS gas cell.
- Measured Raman spectra of $N_2$ and $H_2$ gases using the SHS, which has yet to be demonstrated in open literature.
- Increased spectral range of instrument to monitor entire fingerprint region (Raman shift 0 - 4200 $cm^{-1}$).
- Optimized filtering to improve SNR of gas measurements.
- Developed a data acquisition program to streamline spectral processing which decreased processing time by several orders of magnitude (10 minutes to <1 second).
- Set-up two contracts with professors S. Michael Angel and Michael L. Myrick, both at the University of South Carolina. Dr. Angel has provided technical advice, as well as conducted some of the experiments using his graduate students. Dr. Myrick has provided spectroscopic data analysis expertise and developed the software mentioned above.

## Future Directions

- Instrumentation assembly and demonstration for Raman gas analysis
  - Compare SHS results to a conventional Raman spectrometer.
- Optimization of SHS system for Saltstone headspace application and demonstrate lab-scale measurements
  - Lab measurements to demonstrate Raman as a useful technique for Saltstone samples at relevant concentrations (~100s ppm) and to identify potential implementation issues and solutions.
  - Continue developing data processing.
- Adaptation of system for hyperspectral measurements and optimization
  - Demonstrate ability to collect hyperspectral Raman images with a SHS.
- Demonstrating laser stability on UAV
  - Investigate the ability to mount a COTS laser onto a UAV and measure laser pointing stability.

## Publications/Presentations

1. SciX Conference oral presentation; October 22, 2018; Atlanta, GA.
2. SERMACS Conference oral presentation; November 1, 2018; Augusta, GA.

## References

1. Gomer, N.R.; Gordon, C.M.; Lucey, P.; Sharma, S.K.; Carter, J.C.; Angel, S.M. “Raman Spectroscopy using a Spatial Heterodyne Spectrometer: Proof of Concept.” Appl. Spectrosc. 2011. 65(8):849-857.
2. Lamsal, N.; Angel, S.M. “Deep-Ultraviolet Raman Measurements using a Spatial Heterodyne Raman Spectrometer (SHS).” Appl. Spectrosc. 2015. 69(5):525-534.
3. Barnett, P.D.; Angel, S.M. “Miniature Spatial Heterodyne Raman Spectrometer with a Cell Phone Camera Detector.” Appl. Spectrosc. 2017. 71(5): 988-995.
4. Barnett, P.D.; Strange, K.A.; Angel, S.M. “Improving Spectral Results through Row-by-Row Fourier Transform of Spatial Heterodyne Raman Spectrometer Interferogram.” Appl. Spectrosc. 2017. 71(6):1380-1386.
5. Strange, K.A.; Angel, S.M. “Characterization of a Visible Spatial Heterodyne Raman Spectrometer for Standoff Detection” Appl. Spectrosc. In preparation.
6. Strange, K.A.; Paul, K.C.; Angel, S.M. “Transmission Raman Measurements using a Spatial Heterodyne Raman Spectrometer.” Appl. Spectrosc. 2017. 71(2):250-257.
7. Tuschel, D. “Headspace Raman Spectroscopy.” Spectrosc. 2014. 29(9):1-6.
8. Teal, G.K.; MacWood, G.E. “The Raman Spectra of the Isotopic Molecules $H_2$, HD, and $D_2$.” J. Chem. Phys. 1935. 3(12):760-764.
9. De Groot, W.A. “The Use of Spontaneous Raman Scattering for Hydrogen Leak Detection.” 30th Joint Propulsion Conference, Indianapolis, IN. 1994. Pg.1-11.

## Acronyms

| | |
|---|---|
| **CHI** | Chemical-Specific Imaging |
| **SciX** | The Great Scientific Exchange |
| **SDU** | Saltstone Disposal Unit |
| **SERMACS** | Southeastern Regional Meeting for American Chemical Society |
| **SHS** | Spatial Heterodyne Spectrometer |
| **SHRS** | Spatial Heterodyne Raman Spectrometer |
| **SNR** | Signal-to-Noise Ratio |
| **SRNL** | Savannah River National Laboratory |

## Intellectual Property

**SRS-19-008:** Static Electric Field Detection Using Raman Spectroscopy to Measure the Depolarization Ratio of Gas Molecules Influenced by Dielectrophoretic Forces

**SRS-19-011:** Detector Mount of Plane Arrays in Optical Spectroscopic Measurement Systems

## Total Number of Student Researchers

Two graduate research students in Dr. Angel’s group were partially supported by this project. Both students worked at their university lab and one student visited the SRNL lab to provide technical advice.

# Extraction of Mercury Utilizing 3D Printed Media - Mercury Extraction Coalescer (MEC)

**Project Team:** M. S. Williams (Primary), J. Bobbitt, D. Lambert

**Subcontractor**: C. Huffman (Western Carolina University)

**Thrust Area**: Legacy Waste Cleanup

**Project Start Date:** October 1, 2018

**Project End Date:** September 30, 2019

*Mercury is a persistent environmental hazard that is strictly regulated. The design of a 3D printed coalescer was proposed to facilitate segregation and/or adsorption of elemental mercury from aqueous solutions. 3D printing techniques were employed to generate designed surfaces and internal geometries that would otherwise be very difficult to near impossible through traditional manufacturing processes.*

*The proposed coalescer was designed to take advantage of advancements in 3D printing to incorporate surface sub-structures and material compositions targeted specifically at mercury adsorption. The initial phase of research targeted the design of physical structures that could assit with adsorption or segregation of mercury from acidic condensate, rendering it isolated and preventing recirculation back into the chemical process, as well as implementation into standard environmental remediation techniques for contaminated aqueous solutions. Future work was to focus on formulating reactive coalescers to improve chemisorption along with physisorption.*

## Objectives

- Design 3D printable components with microstructures targeted at mercury segregation
- Print 3D components from various compositions (plastic, ceramic, metal)
- Integrate designs into current technology so as to minimize disruption of current processes
- Evaluate various designs at nominal testing conditions to determine operability and compare efficiency

## Introduction

Mercury is a known neurotoxin and its release to the environment is strongly regulated by the EPA.[1] Removal of mercury from aqueous systems is of high importance to environmental management and remediation entities. This proposal sought to improve the current technology by increasing the segregation of elemental mercury from acidic condensate. Surface structures, sub-structures, and chemistries have been shown to produce tunable interactions with liquids. The experimental approach of this project was to utilize 3D printing techniques to generate internal geometries, surface microstructures, and component chemistries sufficient to provide segregation of mercury from acidic aqueous media.

The initial phase of this project utilized a UV-curable resin printer to produce intricate 3D printed components that advanced from simple isolation to more advanced micro-structured segregation. Initial designs have been integrated into the current equipment utilized for simulated high-level waste chemical processing experiments performed at the Savannah River National Laboratory. Other 3D designs have been produced that have more advanced internal geometries or are composed of alternate materials.

The current state of the project has shown the initial success of integration of 3D printed components into the current process technology without disruption of processing and enhancement of the segregation of elemental mercury from the acidic condensate recycle stream.

## Approach

There were two stages to the first phase of this research: stage one was the design and printing of coalescers, stage two was the integration of printed components into equipment and testing.

To accomplish the design and printing of practical devices, literature concerning surface structures and sub-structures that aid in liquid-liquid separations was reviewed and utilized to influence the design of micro-features. The printer equipment selection was based on the ability of the FormLabs Form2 printer to produce fine details into the micron scale and the ability to utilize different printing material compositions. The ability to use multiple materials or even modify existing materials makes the FormLabs platforms ideal for R&D activities. We could quickly transition between printing media with no down-time between modifications.

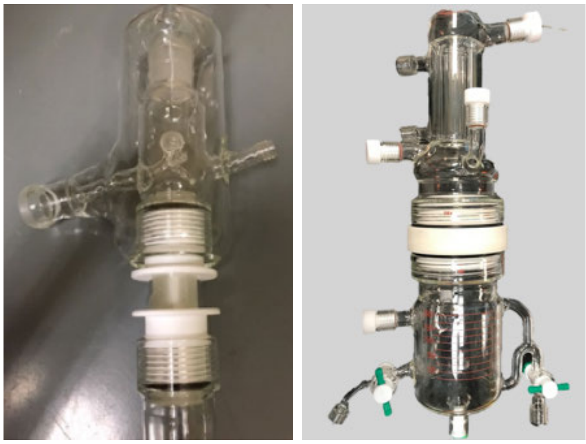

**Figure 1. (left)** 1 in. adapter and **(right)** 3 in. adapter designs for the integration of coalescers between the SRAT/SME condenser connector **(top)** and Mercury Water Wash Tank **(MWWT, bottom).**

The integration of the printed components into current testing equipment (Figure 1) was a necessary proof-of-concept for the broader application goal due to the fact that larger facilities that would require this addition are typically difficult to modify. For example, to make any changes in the Defense Waste Processing Facility (DWPF) at the Savannah River Site (SRS), a majority of interactions with equipment must be performed remotely with a crane making any modification difficult at best. By designing to integrate into current testing equipment, flexibility of the component and manufacture process may be highlighted. The use of 3D printing allowed rapid, cost-effective modification to component designs to evaluate various integration schemes. Once integrated, the coalescer testing was combined with other simulated waste reprocessing testing due to the scale of required preparation and oversight. To ensure the efficiency of the steam stripping process, the mercury must be suspended in solution as relatively small droplets and distributed near the surface. This suspension/distribution process is aided by the inclusion of insoluble solids such as sludge solids. To accommodate these necessary additions to the process, testing was combined with simulated Sludge Receipt and Adjustment Tank (SRAT) and Slurry Mix Evaporator (SME) tank chemical processing being performed concurrently to examine alternative antifoams. Initial tests were performed with a high-level waste sludge simulant that was designed to foam significantly during reprocessing so as to represent a worst-case-scenario for the antifoam. This testing has little impact on the mercury steam stripping process and the extraction of mercury from the process has little impact on the evaluation of the antifoam, so the combined tests were ideally suited to run concurrently. A coalescer was placed in-line with the acidic condensate and condensing mercury. To accommodate the coalescer, an adapter was designed to fit between the condenser and the traditional Mercury Water Wash Tank (MWWT). Once testing was completed, the used coalescer and any trapped liquid or material was removed from the setup and analyzed for mercury by Inductively Coupled Plasma – Atomic Emission Spectroscopy (ICP-AES).

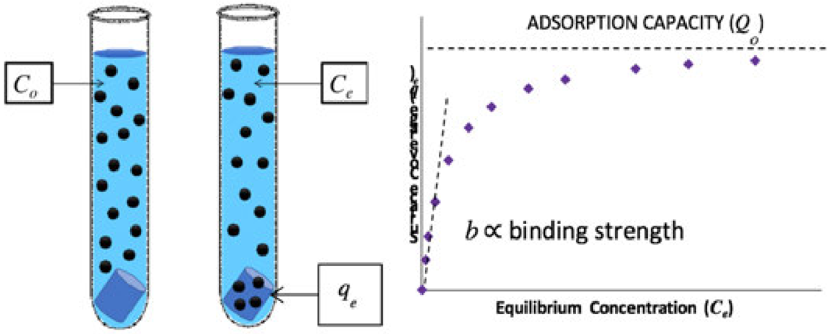

**Figure 2.** Adsorption capability ($Q_o$) can be calculated using the equilibrium concentration ($C_e$), the surface coverage ($q_e$), and the binding strength ($b$) by fitting the data to the Langmuir equation:

$$\boxed{q_e = \frac{bQ_oC_e}{1 + bC_e}}$$

For environmental remediation scenario testing, coalescers were provided to Dr. Carmen Huffman's research group at Western Carolina University to integrate into their setup. The preliminary examination was performed with a single coalescer sectioned into approx. 1 in. sections and placed in solutions of varying concentrations of aqueous contaminants. The metal concentration was allowed to come to equilibrium between the aqueous phase and the coalescer and an adsorption capacity will be calculated (Figure 2).

## Results/Discussion

After some initial complications associated with the learning curves on the printing process and the 3D design software, a variety of coalescer designs were produced and printed in various materials.

The first designs were printed in plastic and at a diameter of 3 in. to examine feasibility of printing the concepts as well as to fit the initial integration scheme involving a 3 in. Teflon bushing to be placed between two components of the typical SRAT/SME offgas stream. Successive plastic designs were scaled down to a 1 in. diameter and set up to fit into a modified adapter between the condenser and MWWT involving two separate Teflon fittings and a glass tube. The move to utilize a glass tube was closer to what could be anticipated as the available space in a chemical processing facility, such as DWPF: a process pipe responsible for transporting material. We were able to show that, first, the 3D printing method gives us the capability to modify designs quickly with little to no impact to the component manufacturing process (unlike traditional injection molding processes) and, second, that components could be designed and manufactured to fit within the available confines of typical processing environments with minimal impacts to process equipment. Whereas the simulated equipment required some minor modifications, full-scale process pipes would require minimal updates to accommodate such an addition.

Following the initial simple designs, more complexity was bred into the coalescers as the 3D design and printing process was further explored. After overcoming small learning curves associated with the design software and the necessary intricacies associated with transitioning from digital design to physical print, smaller and more complex microstructures were explored.

To expand on functionality, attempts to print in additional material compositions were made and also proved to be successful after another small learning curve to understand the printing process changes required to accommodate the differences in material.

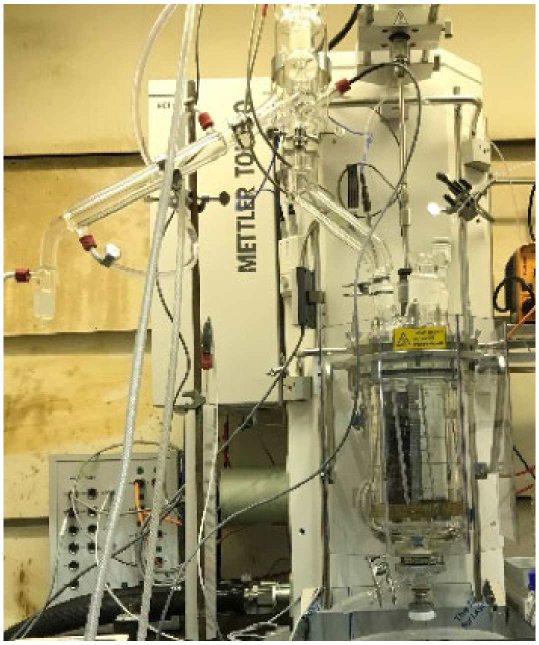

**Figure 3.** Reaction calorimeter, RC1, from Mettler Toledo.

With successfully printed components, testing was conducted to examine, one, the impacts to other processing parameters from the incorporation of the restricted path and, two, the enhancement of mercury removal, if any. The simplest design at a diameter of 1 in. and utilizing the two Teflon bushings connected by a glass tube was inserted into SRAT/SME testing for a new antifoam with our new equipment from Mettler Toledo: the RC1 (Figure 3). Day-shift only testing was performed, and steam-stripping steps were shortened due to testing constraints, but the concept was efficiently examined. An addition of 7.0336 grams of mercury (II) oxide was made to the simulant sludge with a theoretical product of 6.514 grams of elemental mercury. Of this theoretical amount, approximately 1.55 grams of mercury was recovered in the coalescer. This was determined based on soaking the coalescer in an aqua regia solution, diluting to a set volume, and analyzing the mercury concentration within the solution via ICP-AES. Even with the abbreviated testing and the simplest design, the coalescer segregated nearly 25% of the mercury from the process.

Testing in the environmental remediation protocols utilized by Dr. Carmen Huffman at Western Carolina University is on-going.

## FY2019 Accomplishments

- 3D printed increasingly complex coalescer components in decreasing sizes and increasing surface sub-structure complexity.
- Printed components in multiple materials, examining manufacturing parameter changes and inherent finished material limitations.
- Integrated 3D printed component into prototypical SRAT/SME testing with minimal impact to currently engineered components and operating parameters/procedures.
- Integrated 3D printed component into environmental remediation testing through university subcontract (Dr. Carmen Huffman, Western Carolina University).

## Future Directions

- Increase complexity of surface sub-structures and internal geometries to improve physisorption and chemisorption.
- Examine additional printing media to increase chemisorption alongside physisorption.
- Potential to patent material combinations, printed components, and/or improved methodology.

### *References*

1. A. F. Gruss, R. Rodriguez, D. W. Mazyck,"Mercury Oxidation by UV Irradiation: Effect of Contact Time, UV Wavelength, and Moisture Content", Ind. Eng. Chem. Res., 56, 6131-6135, **(2017).**
2. Y. Yoon, D. Kim, J-B Lee,"Hierarchical micro/nano structures for super-hydrophobic surfaces and super-lyophobic surfaces against liquid metal", Micro and Nano Systems Letters, 2, **(2014).**

### *Acronyms*

| | |
|---|---|
| **DWPF** | Defense Waste Processing Facility |
| **ICP-AES** | Inductively Coupled Plasma – Atomic Emission Spectroscopy |
| **MEC** | Mercury Extraction Coalescer |
| **MWWT** | Mercury Water Wash Tank |
| **NDA** | Non-Disclosure Agreement |
| **SME** | Slurry Mix Evaporator |
| **SRAT** | Sludge Receipt and Adjustment Tank |
| **SRNL** | Savannah River National Laboratory |
| **SRS** | Savannah River Site |
| **WCU** | Western Carolina University |

### *Intellectual Property*

A non-disclosure agreement (NDA) was entered between Dr. Huffman (WCU) and SRNL to protect the potential patentability of the device concept, designs, modifications, and uses.

### *Total Number of Student Researchers*

One student researcher was a part of Dr. Huffman's researcher group at WCU; all of their work was performed off-site at the university. Two undergraduate summer interns performed work on-site and provided hands-on manipulation of the 3D printed components and some design consultation.

# Large Area Contamination Monitoring

*Current decontamination and decommissioning (D&D) operations at Hanford have demonstrated a flaw in the current state of the art capability of defining airborne contamination boundaries. Rapid analysis of large volumes of air to more accurately measure airborne contamination could reduce personnel risk and speed D&D activities across the DOE complex and beyond. This work meshes with the DOE-EM mission to safely conduct radiological clean-up operations.*

*This project's overall goal was to study the feasibility of rapidly determining airborne alpha contamination using inexpensive high-volume household air purifiers. As opposed to conventional continuous alpha monitors which deposit alpha activity on simple filter papers, these air-purifiers deposit activity on large complex HEPA filter surfaces. This project has explored the feasibility of using various detectors and scintillators to rapidly analyze these large, complex samples for alpha contamination. This included using a CCD-based camera to detect scintillations caused by alpha-particles interacting with ZnS(Ag) plates, ZnS(Cu) powder, and multiple organic scintillators. It also included evaluating multiple X-ray spectrometers to examine the sensitivity of these instruments with this complex sample type. A study of the distribution of radon and its progeny onto these media was conducted. This work outlined an approach for analyzing CCD-based image data into actionable information.*

**Project Team:** D. P. DiPrete (Primary), K. M. Fenker, T. S. Whiteside, A. Brand, A. Jolie

**Thrust Area**: Legacy Waste Cleanup

**Project Start Date:** October 1, 2018

**Project End Date:** September 30, 2019

## Objectives

- Develop a cost-effective method to screen large volumes of air for actinide airborne contamination.
- Evaluate activated carbon and HEPA filters for radon removal from air volume samples.
- Determine how quickly and easily various detection systems can determine the presence of actinide contamination on the filters.
- Evaluate X-ray spectrometers (NaI and $SrI_2$) and compare to U-LEGE.
- Evaluated sensitivities of scintillation systems measured by light vs what conventional solid state alpha spectrometers and ZnS gross alpha scalars can do.
- Gather data for which system or systems will work best in an array to rapidly analyze filters.
- Determine depth particles penetrate the HEPA filter.

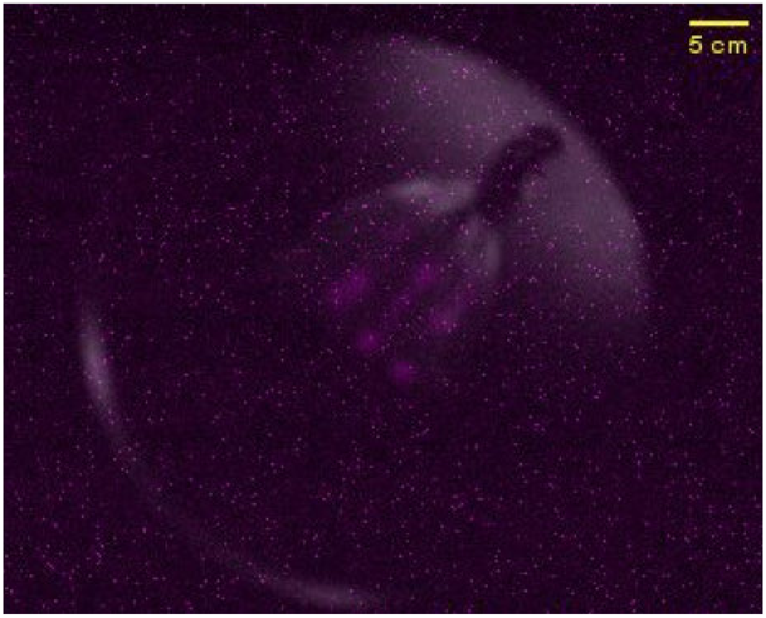

**Figure 1.** 3x3 array of Pu-238 particles buried in folds of a section of HEPA filter.

## Introduction

Decontamination and decommissioning (D&D) activities at the Hanford Pu Finishing Plant were significantly set back by the inability of the contractor to protect the workforce when faced with an unusual dispersion of airborne activity combined with the environmental conditions found at the Hanford Site. The Department of Energy (DOE) reached out to SRNL as well as across the complex for help with the airborne monitoring effort, but technologies weren't available to significantly bolster the efforts that were currently underway. The event was controlled eventually by numerous applications of chemical fixative on the source term, but all D&D activities were suspended for a significant period of time. Providing solutions to such situations is a perfect fit for SRNL, DOE's EM National Laboratory. The situation at Hanford will likely have repercussions across the DOE complex in other situations where DOE faces D&D challenges. Finding enhancements to technologies in the toolbox that the DOE community currently has for airborne monitoring in challenging situations will augment SRNL's reputation as a National Laboratory capable of providing technical solutions to DOE's radiological clean-up efforts. Challenges facing Hanford in D&Ding its plutonium legacy facilities will be challenges SRS will share as it tackles the D&D challenges of its F-Area Plutonium legacy facilities. Upon successful completion of this scoping effort, additional funding opportunities will be sought from funding sources such as the Hanford Grand Challenges program, or DOE programs such as NNSA NA-22 or 241.

## Approach

At the project onset, it was determined the most promising approach to rapidly screen large surface area samples for alpha activity would be to contact the surface of the media with a scintillator but provide an offset from the light collection and the actual scintillator. So rather than pursue the approach of using photomultiplier tubes or multiple avalanche photodiodes, a ThorLabs Scientific-Grade Digital Camera Model 8051Mwas procured and evaluated. In the early stages of the project, a small light-tight box to enclose the camera and a scintillating sample was put together. The system was first evaluated with scintillating paint to ensure functionality.

Plates of ZnS phosphor, bound onto a plastic light pipe backing were procured. Such plates are what are connected to photomultiplier tubes in the SRS hand-held alpha survey meters. High activity plates of Pu-238 (~1E7 dpm) were prepared in the Nuclear Measurements radiochemistry labs and sealed in contact with a piece of ZnS(Ag) plate. The Pu-238 activated ZnS(Ag) plates were then measured in the light-tight box to successfully establish proof-of-principle.

A sensitivity study was then conducted to establish whether this technology was practical. A series of stainless steel planchets ranging from 1E2 to 1E5 dpm were prepared. Each planchet was sealed with a piece of ZnS plate in contact and measured with the light-tight box. Algorithms were generated to sum multiple exposures with the camera to increase the sensitivity of the system. Numerous improvements with the light-tight box were carried out before it could successfully measure the 1E2 dpm sample.

The design of a light-tight container that could hold both a HEPA filter in a drawer slide and the mounted digital camera was contracted out to be constructed. Construction of the light-tight container took roughly 5 months, and numerous additions were made over the next couple of months to make the box light-tight. The box was then evaluated using the standards prepared initially for the small protype box. Once sensitivity was established, experiments were conducted to evaluate other scintillator systems.

The ZnS(Ag) plates were evaluated against ZnS(Cu) powder, PerkinElmer Enhance, and Utlima Gold AB liquid scintillation cocktail. ZnS(Cu) is a similar scintillator to what was on the plates. It has a Cu activator, not a Ag activator, so it emits light at a slightly different wavelength. However, this system is a powder, not a plate, so it can be applied to uneven surfaces and be in direct contact with the alpha emitters, as opposed to the ZnS(Ag) plates, which would be separated from the alpha activity by some distance on complex surface structures such as a HEPA filter. That distance through air would heavily attenuate alpha emissions prior to reaching the scintillator. A third scintillating media studied was PerkinElmer Enhance. PerkinElmer Enhance is a spray-on scintillator used in the medical research community to study the behaviors of biological systems labeled with various beta emitters. The fluors in this system are POPOP (1,4-bis(5-phenyloxazol-2-yl) benzene) and PPO (2,5-diphenyloxazole), the classic organic scintillators of historical liquid scintillation cocktails. The final scintillation system studied was the environmentally friendly liquid scintillation cocktail PerkinElmer Ultima Gold AB used heavily by the Nuclear Measurements Group's radiochemistry team.

Three different activities of Pu-238, 1E5, 1E4, and 1E3 dpm, were prepared for each scintillation system and were evaluated by the camera system.

Of all the scintillation systems studied, only the PerkinElmer Enhance system completely failed. A final study was undertaken where 4"x4" portions of the Air Purifying Units' HEPA filters were cut out. For each section, KimWipes were compressed into small balls and were each spiked with Pu-238 at ~1E5 dpm. The Pu-238 was dried onto the KimWipe balls, and the balls were inserted into the folds of the HEPA filter in a 3 by 3 pattern. One section had a ZnS(Ag) plate affixed to the surface. One section was dusted with ZnS(Cu) powder. One section had Ultima Gold AB Liquid scintillation cocktail applied to each area containing a KimWipe.

Concurrent to the scintillation studies a feasibility study was conducted looking at the potential for X-ray emissions for the detection of alpha activity. A couple of configurations were considered. A single X-ray spectrometer fixed above the HEPA filter in the manner of the camera was deemed not practical. The solid angle would be so large at a distance sufficient to measure the entire filter by one spectrometer that it would be too insensitive for any practical measurements. To load a device with a large number of spectrometers closely coupled with each section of the HEPA filter would be cost prohibitive. One detector put into a robotic system where it is used to scan across the entire surface area of the HEPA filter would be too time intensive. A compromise system was envisioned where one spectrometer was centered over each quadrant so having 4 spectrometers in total. A Monte Carlo N-Particle mathematical model was built to study the counting efficiencies of such a system, and how those efficiencies changed for a particle buried in different areas of the quadrant. Several detection systems were looked at, a thin windowed $SrI_2$ detector, a thin windowed NaI detector, and a high resolution HPGe thin windowed planar spectrometer. In addition to the X-ray detector study, a series of plates of various plutonium isotopes were prepared and analyzed in an attempt to add to the lack of knowledge in the available Nuclear Datasets on actinide X-ray emissions, namely those for Pu-238, Pu-239 and Pu-240.

The final area of study was a short look on where radon and it's progeny were depositing in the high volume Whirlpool Whispure Air Purifiers purchased for this project. The Whirlpool Whispure Air Purifiers have a HEPA that is particularly suitable for this project, being flat not round, relatively thin at 1", and not too large at 2"x2". In addition to the HEPA particle filters the Air Purifiers have a thin activated charcoal mesh designed to remove household odors. A short study was conducted seeing where alpha activity showed up in this system when the air purifiers were run in non-radiological areas. The alpha activity was measured using a hand-held alpha spectrometer. A HPGe spectrometer was also deployed in an attempt to get some radiological isotope identification as well.

## Results/Discussion

Results of the radon study indicated radon or more likely its progeny deposited on the activated charcoal odor screen, not the HEPA filter itself. These measurements were made using the hand-held alpha spectrometer. Identification of the isotopes captured using a HPGe detector were unsuccessful due to the high ambient background of the natural decay products that the attempt was being made to measure. An algorithm was developed to address radon rejection by decaying measured light over a number of pictures summed in time to see if excess light would remain. This algorithm is addressed in reference SRNL-STI-2019-00599.

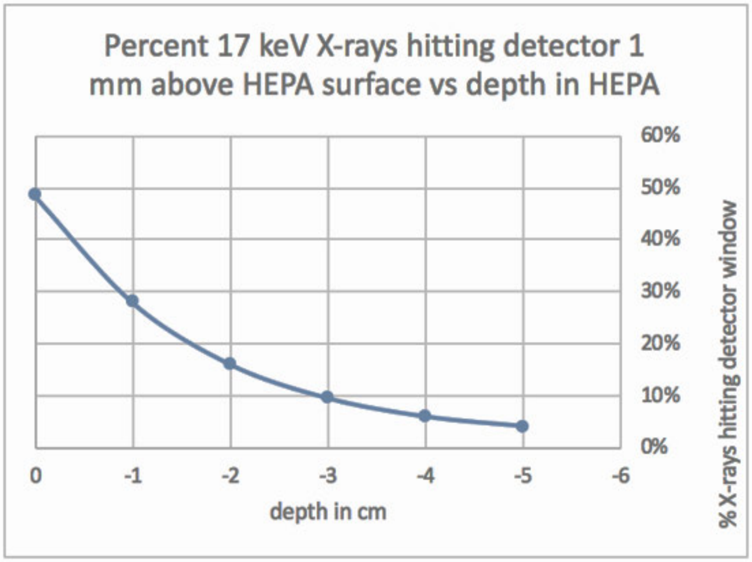

**Figure 2.** MCNP Model of X-rays Reaching Detector Window from HEPA Surface

The X-ray studies generated less promise than the scintillation studies. The MCNP analysis looked at the percentage of 17 keV X-rays that would reach a spectrometer set 1 mm above the HEPA, looking at only ¼ of the entire HEPA filter. The model showed that even with 4 detectors in place in a system, the counting efficiencies would preclude this approach leading to a rapid, highly sensitive alpha analysis of a HEPA filter system. More than 4 detectors would lead to a cost prohibitive system. The results of the MCNP model are provided in Figure 2. The X-ray studies did provide some nuclear data on X-ray emissions of a number of actinides that may be publishable and are still being evaluated and will be addressed further in SRNL-STI-2019-00598.

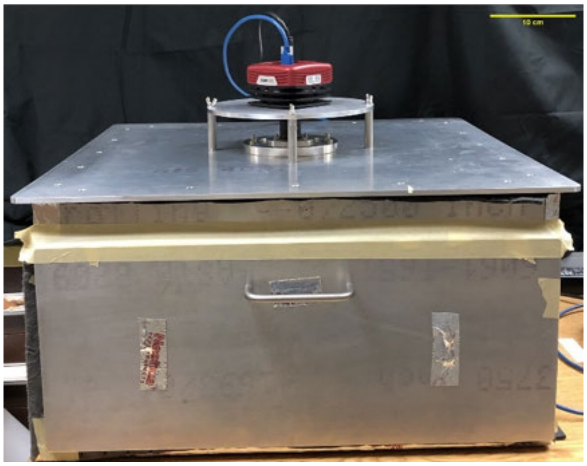

**Figure 3.** Light-tight box with camera and lens mounted on top. Box is sized to be able to image area of 19 in x 19 in. Max distance between camera lens and sample is 7 in.

The scintillation system did show promise for making this a real-world system, and although we made many measurements there is still some substantial work remaining to bring this to fruition. Figure 3 has a picture of the HEPA assay device prototype fabricated for this project.

We were able to image Pu-238 at various activities (E7-E3 dpm) using a solid sheet of ZnS(Ag) scintillator and the CCD-based digital camera. These images can distinguish the location of the Pu-238 on the substrate where they are deposited. Figure 4 provides an example of some of the sensitivity measurements where an array of plutonium plates from 1E5 to 1E2 dpm were placed inside the assay system and measured.

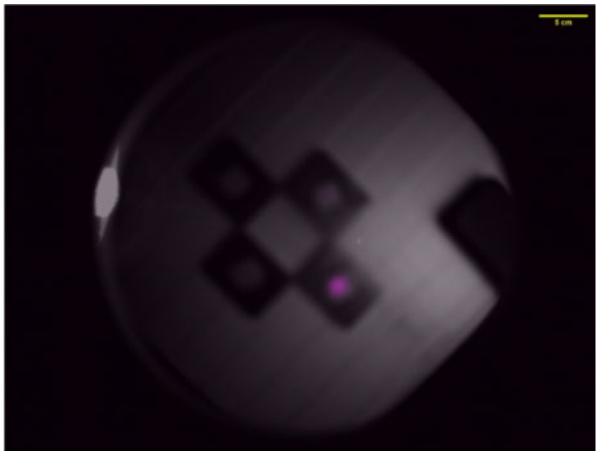

**Figure 4.** Solid Zn(S) on top of plates on top of filter, activities range from 1E5, 1E4, 1E3, 1E2 dpm (counter-clockwise from bottom right), 1x1 binning. Scintillation shown in magenta.

To increase sensitivity of the system, an algorithm was developed to sum a number of exposures. To acquire images, a ThorLabs Scientific-Grade Digital Camera Model 8051M was used, with a Kowa LM5JC10M Lens. Unfortunately, this lens has a 2/3" optical format while the camera has a 4/3" optical format, this causes vignetting, which is when a dark ring appears around the borders of the image in Figure 4. While not ideal, this did provide a constant "no-information" background against which to compare the dark current. To connect the lens to the camera the installed IR filter on the camera was removed. This camera has a peak quantum efficiency of 51% near 450 nm. This corresponds well with the Zn(S) emission spectra, which also peaks near 450 nm.

The camera was set up using methods commonly used for astrophotography.[1] First the black-level offset was set by taking a bias frame (the lens cap was in place and the exposure time was 0 ms) and then finding the minimum value of the 16-bit greyscale value of all the pixels in the image (0 is black and 65,535 is white). The black-level offset was changed to ensure the minimum value in this image was greater than 100 and less than 1000. For this camera it works out be a black-level offset value of 135. The appropriate gain for this camera was determined by taking a picture of the room ceiling and examining the maximum value in the image. If it was well below 65k, the gain was increased. If it was at 65k, the gain was decreased. For this camera, at all bin-levels except 1x1 a gain setting of 0 caused a "bunch-up" of pixels in the histogram at 65k. This "bunch-up" is where the pixels are hitting full-well capacity (maximum number of electrons stored). When the camera's binning was set to 1 by 1, the gain needed to be increased to 35 to cause the pixels to hit full-well capacity.

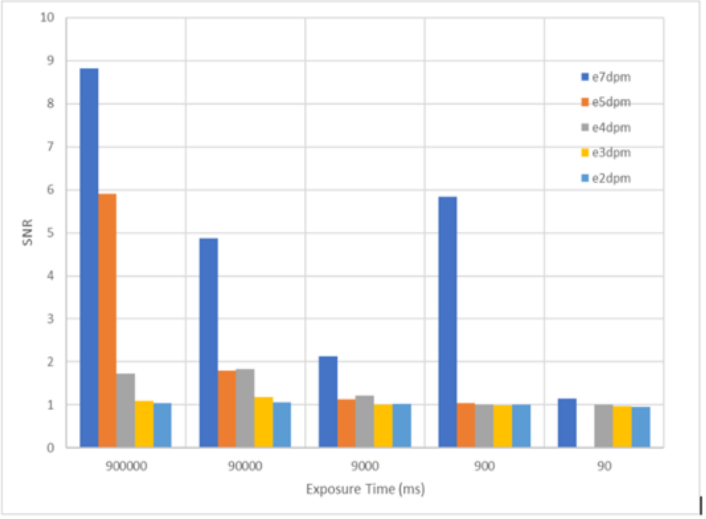

**Figure 5.** Signal to Noise Ratio (SNR) compared to sub-exposure time

With the camera's gain and black-level set up the sensitivity of the camera was evaluated through the binning process. When pixels are binned, their values are combined. For example in 2x2 binning, 2 vertical and 2 horizontal adjacent pixels are combined into 1 pixel. In 3x3 binning 3 vertical and 3 horizontal pixels are combined, etc. This camera has binning levels from 1 to 10 in both the horizontal and vertical axis. The vertical axis is binned in the hardware and the horizontal axis is binned in the software. For simplicity's sake, when we binned the camera, we changed both the horizontal and vertical bins by the same amount. The science images acquired in this work were taken at 5x5 binning. Using these techniques an idea of the sensitivity of the system and the number of time intervals binned is provided in Figure 5.

Different scintillating materials were evaluated. Solid sheets of ZnS(Ag) were the brightest. This may be because the plastic coating on the back acted as a light pipe (See Figure 6). It is not clear if the activity imaging is being washed out from the light pipe properties of the plastic coating.

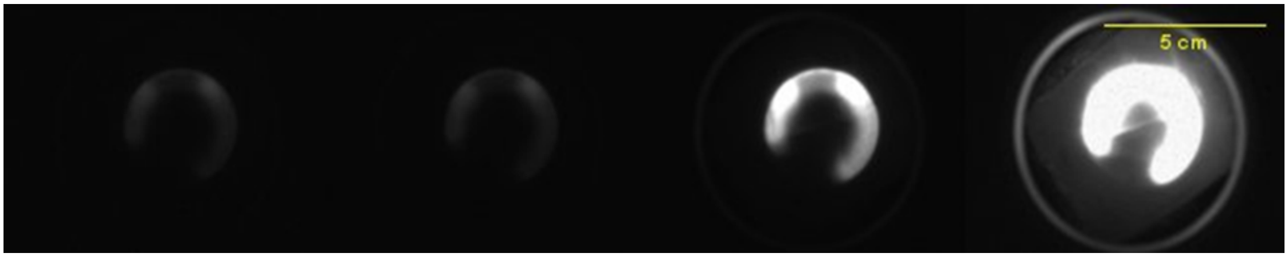

**Figure 6.** Pu-238 with 1E7 dpm underneath Zn(S) scintillator at sub-exposure times of 900, 9000, 90000, and 900000 ms.

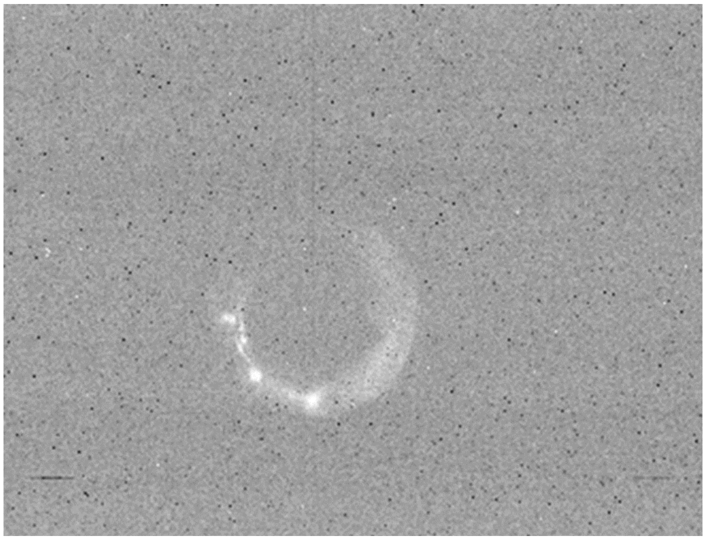

Powdered ZnS(Cu) was also evaluated and by using it, were able to possibly locate large particles of Pu-238 at specific locations on the substrate. See Figure 7.

PerkinElmer's Ultima-Gold Liquid Scintillation Cocktail (LSC) was also reactive enough to show activity. With the LSC and with solid ZnS, Pu-238 deposited within the actual HEPA filters was imaged (see Figures 8, 9, and 10). With an improved powder deposition technique, the ZnS powder would also probably work to image alpha emitters deposited on a filter.

**Figure 7.** Powdered Zn(S) over 106 dpm Plutonium-238 plate, 60 second sub-exposure time, 10x10 binning

**Figure 8.** Filter containing Pu-238 and LSC cocktail

**Figure 9.** LSC cocktail on top of 106 dpm plutonium in 9 locations in filter, 60 second sub-exposure time, 10x10 binning

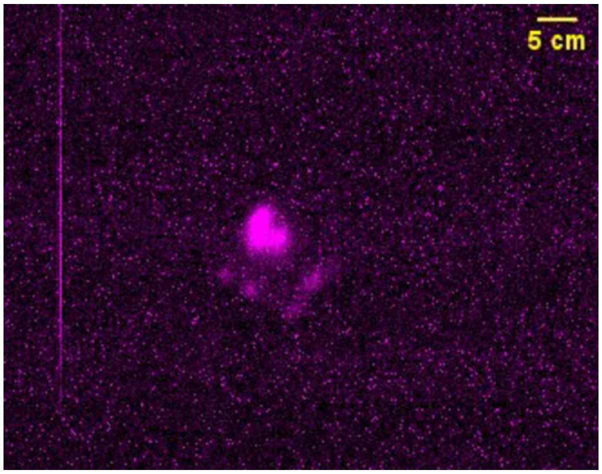

**Figure 10.** Solid Zn(S) on top of 106 dpm plutonium in 9 locations in filter, 60 second sub-exposure time, 10x10 binning

While imaging contamination on the filters was achieved, there is more work needed to be done to improve the resolution and sensitivity of the imaging. It is suspected that while they are the brightest, the ZnS(Ag) sheets are losing resolution because the plastic sheet substrate is acting as a light pipe. Perhaps a ZnS(Ag) laid down on a fractured substrate would provide improved resolution. The most inexpensive of these scintillators was the liquid scintillation cocktail. Work needs to be done to evaluate the most efficient way to apply the cocktail, and how much needs to be applied to work. Several different activated ZnS compounds exist, a study of the various scintillators to see which shows the most promise is needed. Finally the system needs to be applied to some real-world samples taken in contamination areas to access the effectiveness of this system.

## FY2019 Accomplishments

- Built an alpha imager which can be used for this project or others
- Determined sheet of ZnS or LSC spray will work to image contamination on and within air filter, and with improvements to the technique, ZnS powder could also be used.
- We can directly see where hotspots of Pu are located on the media.
- Light-tight media holder created and method to acquire good photos developed.
- Evaluated distribution of radon and progeny on this Air Purifier system.
- Acquired nuclear data on X-ray emissions of a number of actinides which could be of value to the Nuclear Data literature.

## Future Directions

- Study current scintillation agents’ properties further to determine if sensitivity limits can be extended
- Study more scintillating agents to refine properties of imager
- Study scintillation agent delivery systems
- Deploy air purifiers in- and collect filters from- an airborne radiation contaminated area
- Evaluate results of assay system vs dissection of real world air filters to see where contamination located
- Develop algorithm to turn image data into quantifiable “action” data: How much activity is on the filter, when is alpha (not Radon) contamination found.
- Use technique developed to precisely locate deposition of alpha emitting material on samples, for QA/QC purposes.

## Publications/Presentations

1. 2nd International Conference on Radioanalytical and Nuclear Chemistry (RANC 2019)
2. SRNL-STI-2019-00596 Imaging plutonium activity with a CCD-based camera
3. SRNL-STI-2019-00597 Scintillator evaluation using a CCD-based camera
4. SRNL-STI-2019-00598 Comparison of X-ray emissions of Pu-238 samples
5. SRNL-STI-2019-00599 Theoretical approach to Large Area Airborne Contamination Monitoring using a CCD-based camera
6. SERMACS2019 - Large Area Airborne Contamination Monitoring, Savannah, GA 10/20
7. Seminar at UNC-Charlotte - The Savannah River Site: Nuclear Measurements around the DOE Complex, 11/25

## References

1. Gain/Offset: http://www.stark-labs.com/help/blog/files/GainAndOffset.php

## Acronyms

| | |
|---|---|
| **CCD** | charged coupled device |
| **D&D** | deactivation and decommisioning |
| **DOE-EM** | Department of Energy Environmental Management |
| **DOE-NNSA** | Department of Energy National Nuclear Security Administration |
| **HEPA** | high efficiency particulate air |
| **HPGe** | high purity germanium |
| **MCNP** | Monte Carlo N-Particle |
| **SRS** | Savannah River Site |
| **SRNL** | Savannah River National Laboratory |
| **U-LEGE** | Ultra-Low Germanium Detector |

## Total Number of Interns/Summer Students

One – Adam Judy

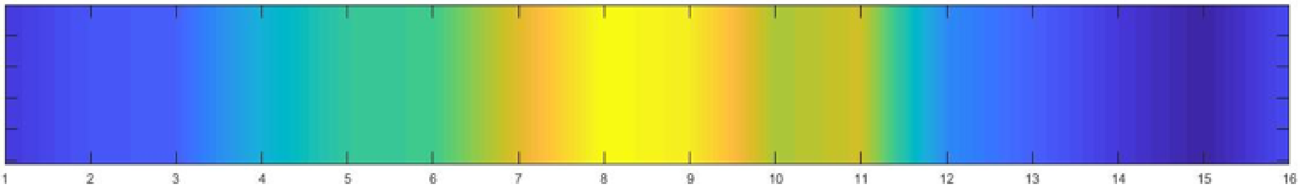

**(Left)** 1-D sensor array composed of 16 JFETs. **(Above)** Electric field image taken by the sensor shown on left. The image above is stretched to imitate 2-D.

# Electric Field Imager Project

**Project Team:** V. Ceyssens (Primary), N. Deroller, J. Nicholson, S. Branney

**Thrust Area**: Legacy Waste Cleanup

**Project Start Date:** October 1, 2018

**Project End Date:** September 30, 2019

*The proceeding document discusses research into the imaging of electric fields. Measurement of electric fields is done using junction field effect transistors (JFETs) as sensors in a 1-D array configuration. Research focuses on verifying, and then building off Dr. Generazio's work at NASA in this field.*

## Objectives

- Verify that junction field effect transistors (JFETs) can detect & measure electric fields
- Mimic Dr. Generazio's experiments to ensure viability
- Build 1-D array prototype of JFETs with LEDs to show measurement and field strength
- Design and manufacture a printed circuit board (PCB) of 1-D array prototype
- Verify that PCB prototype works as well as previous prototype
- Use measurement data to create an image of field strength using Matlab
- Build 2-D array prototype using PCBs
- Conduct testing of best prototype using Van de Graff generator for generation of strong electric fields

## Introduction

Although other researchers have attempted to measure electric fields, Dr. Generazio's approach, as described in [1], has paved the way not only for more in-depth research but also for potential practical applications. In his 2015 paper, Dr. Generazio details how his own patented configuration of a JFET could both detect field strength variations using an array and negatively image objects that lay between a field source and the sensor array. This negative imaging is possible because of the different triboelectric constants of materials, whereby materials effect electric fields differently [1]. The goal of this LDRD research is to confirm as far as possible that Dr. Generazio's work can be repeated, and then to venture beyond what is discussed in the literature.

The research conducted is significant for the advancement of science. Currently, there is no easily available way of measuring electric fields or imaging field strength. A breakthrough in this research will translate to several commercial applications, as well as scientific applications. Two examples include security check point imaging and checking integrity of electrical wires.

## Approach

The approach for this research was twofold: focus on Dr. Generazio's work first, and then begin researching other aspects of electric field imaging not discussed in the doctor's papers. Previous literature from Dr. Generazio (patents, presentation slides, the referenced document) were evaluated to understand what had been done and what should be replicated as part of this project. From there it was a matter of practical application and research into how to conduct different experiments, learning a new integrated development environment (IDE) and microcontroller to conduct said experiments, and building prototypes used for the experiments. After showing that the research had promise, there was a shift into PCB prototypes. This shift had a primary and secondary goal. The primary goal was to create prototypes that were easier to build and exactly replicable. The secondary goal was to show that non-wooden boards could function as sensor arrays, something Dr. Generazio did not try in his papers. With the creation of working PCB prototypes, the focus became testing the capabilities of the sensors as well as imaging an object.

## Results/Discussion

At the beginning of this project, the big question was whether this had merit; whether electric fields could be measured in this fashion. Initial results showed that it was possible to image electric fields. A charged rubber mat's proximity could be detected, and its movements could be discerned. The best PCB prototype could also detect the tapping of feet on the floor. On top of these, a test was conducted using a van de Graff generator as a strong electric field source. This test showed that there is potential for negative imaging using a field source, but the sensor array needs some adjustment before that is viable.

In Dr. Generazio's research, he stressed using wood for the construction of sensors because it interfered the least with electric fields. However, our prototypes showed that a good sensor could be built both on a breadboard and on a PCB. This confirmation is incredibly important because it allows for ease of assembly for future prototypes, and it means they can be mass produced later if that becomes necessary/desirable.

## FY2019 Accomplishments

- Confirmed that JFETs can be used to measure electric fields
- Built working breadboard and PCB prototypes showing that non-wood materials can be used for sensor construction
- Created image of an object using sensor and Matlab
- Ran Van de Graff generator test, showing potential for imaging objects

## Future Directions

- Conduct research into sensor arrays which are more production friendly
- Research the ability to distinguish between objects of different materials
- Contact Dr. Generazio to discuss his research and investigate the equilibrium reversing gate field effect transistor (ergFET)
- Attempt to increase sensitivity of sensor arrays
- Build standalone PCB without microcontroller board

### *References*

1. Generazio, Ed. "Electric Potential and Electric Field Imaging with Applications." Semanticscholar.org, Nov. 2015, pdfs.semanticscholar.org/6998/05fca8db1b78a2a95d107d6bfc616ce924c0.pdf.

### *Acronyms*

| | |
|---|---|
| **ergFET** | equilibrium reversing gate field effect transistor |
| **LED** | light emitting diode |
| **JFET** | junction field effect transistor |
| **PCB** | printed circuit board |

# Concrete Inpection in Remote Areas With Robotic Arms

**Project Team:** Jean Plummer (PI), William Wells, Karl Harrar, Christine Langton, Mike Serrato, Jane Carter, Eric Skidmore, Andrew Duncan, Jason Corley

**Thrust Area**: Legacy Waste Cleanup

**Project Start Date:** June 27, 2019

**Project End Date:** September 30, 2019

*The goal of this project is to develop state of the art techniques to evaluate conditions of inaccessible concrete structures. Focus is on the examination of remote concrete structures typically found in DOE EM facilities. This seedling included the development of a test bed consisting of a robotic arm capable of deploying concrete non-destructive examination (NDE) instruments to examine custom concrete forms with known defects. Concrete forms simulating the rough concrete surfaces, strength, composition and potential structural defects that can be found at our DOE EM facilities were designed and built for examination. Two state of the art concrete NDE instruments were identified to be tested and characterized as to their ability to provide desired NDE data on the developed test beams and slabs. A collaborative robot arm is being used as they are designed with built in features allowing them to safely operate alongside employees. A test bed was built to develop and evaluate deployment techniques of the NDE instruments with a robotic arm, Figure 1.*

## Objectives

- Setup Robotic Arm Concrete Inspection Test Bed
- Build concrete forms designed to simulate DOE aged facilities
- Test ability of the instruments of interest to collect desired non-destructive examination (NDE) data from test forms
    - Baseline performance with hand deployment
    - Test ability to obtain baseline performance using robotic arm

## Introduction

Remote concrete NDE technologies were identified as having broad applicability and high value across the DOE complex by the DOE EM Technology Development Office (TDO). At the Savannah River Site, H-Canyon Exhaust Tunnel (H-CAEX) stakeholders identified remote concrete NDE as the highest priority technology inspection goal to enhance bi-annual Structural Integrity (SI) evaluation of the tunnel. The H-CAEX tunnel is located below grade and does not allow human entry due to its hazardous environment. Current inspections collect visual information using cameras mounted on robotic crawlers, Figure 2. It is desired to have a more quantitative examination of the concrete structure.

This goal of this seedling was to develop and build a test bed to support the evaluation of using a robotic arm to perform remote inspections using concrete NDE instruments. Concrete test forms simulating the rough concrete surfaces, strength, composition and potential structural defects that can be found at our DOE EM facilities were built for examination and use in the test bed.

**Figure 1.** Test Bed deploying concrete inspection instruments on custom designed Concrete Tests forms

**Figure 2.** Human denied H-CAEX tunnel interior view

The test bed can be used as follows:

- to develop techniques and software to perform NDE examination with instruments mounted on a robotic arm
- to design and test custom robotic arm instrument mounts
- to characterize and evaluate state of the art NDE instruments
- to evaluate the ability to acquire desired NDE data
- to evaluate the quality of the acquired data

If the ability to collect the desired data supporting a more thorough SI evaluation can be developed and demonstrated using a robotic arm, the system could be mounted on a crawler for future enhanced remote inspections.

## Approach

The LDRD implementing team included SRNL R&D Engineering staff, SRNL subject matter experts (SMEs) in concrete science and inspection technologies and H-CAEX SI stakeholders to optimize the approach and desired results. Two promising state of the art NDE instruments were identified to be included for evaluation and characterization, the Pundit Live Array and the Proceq GPR, Figure 3. In addition to providing stakeholder identified desired data, the instrument technologies employed were thought to potentially work better on the rough concrete surfaces sometimes found in the remote hazardous environments.

**Figure 3.** State of the Art NDE Instruments of Interest

The basic LDRD approach is as follows:

1. Build the test bed which would include a robotic arm with custom end effector mounts to hold the NDE instruments.
2. Design and build concrete forms simulating the rough concrete surfaces, strength, composition and potential structural defects for testing.
3. Collect instrument data on the test beams using traditional manual hand-held methods, then collect the data using the developed test bed robotic arm system.
    a. Data would include instrument performance on smooth, mildly rough and very rough concrete surfaces.

## Results/Discussion

**TEST BED.** A test bed employing the collaborative UR5 robot arm was designed and built, Figure 4; collaborative robotic arms are designed with features to safely operate alongside people. An end effector mount was design and printed to attach the Pundit Live Array instrument to the robotic arm. Software and rudimentary techniques were developed and the ability to collect data from the Pundit Live Array instrument was demonstrated. The Proceq GPR unit was ordered in early July and was not received until late September, so this system was not tested with the robotic arm. More advanced techniques are needed to facilitate readings of rough concrete surfaces.

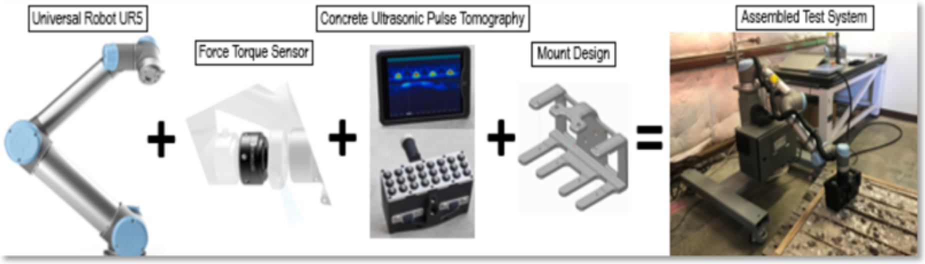

**Figure 4.** Test Bed Assembly with Pundit Live Array Instrument mounted

**CONCRETE TEST BEAMS.** Concrete test beams and forms simulating the rough concrete surfaces, strength, composition and potential structural defects were designed and built for testing. The form design included rebar location and compressive strengths similar to H-CAEX, however the designs were deemed to be universally useful, Figure 5. The test forms and beams were built in N-Area by the System One group, Figure 6.

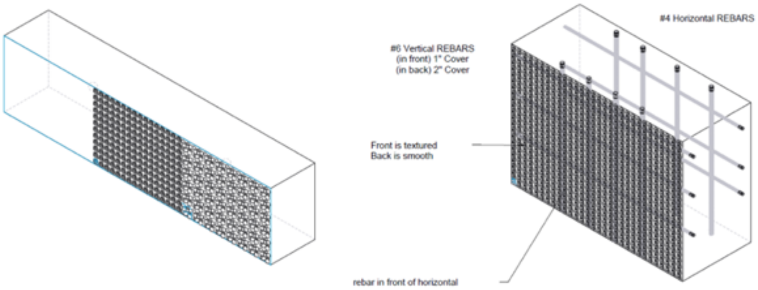

**Figure 5.** Concrete Beam **(left)** and Form **(right)** Design with varying surface textures and rebar

**DATA COLLECTION.** Initial instrument hand held test data was collected on the concrete forms in N-Area, Figure 7.

## FY2019 Accomplishments

- Built a Test Bed for evaluating the ability to perform remote concrete NDE inspections using a robotic arm
- Developed software and a methodology for evaluating the performance of state-of-the-art instruments
- Designed and built custom concrete test forms and beams simulating typical DOE facility concrete structures
- Ordered and received the Proceq GPR

## Future Directions

- Completion of this LDRD objectives to include the characterization of the identified promising NDE instruments to collect desired data from custom test forms
- Development of additional software and deployment technologies if required
- Development of lessons learned and recommendation for field deployment with team

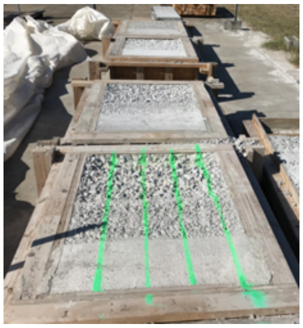

**Figure 6.** Test Forms with varying compressive strengths: 2000 psi, 3000 psi and 5000 psi

**Figure 7.** Collection of hand-held instrument data in field on test beam with multiple surface roughness

### Publications/Presentation

An abstract has been submitted for Oral Presentation at the 2020 Waste Management Symposia (WM2020) International Conference.

### Acronyms

| | |
|---|---|
| **GPR** | Ground Penetrating Radar |
| **H-CAEX** | H-Canyon Exhaust Tunnel |
| **MSIPP** | Minority Serving Institution Partnership Program |
| **NDE** | Non-Destructive Examination |
| **SI** | Structural Integrity |

### Total Number of Student Researchers

One – Jeffrey Kim, Undergraduate SRNL Summer Intern / MSIPP Program

# 3D Printable Encapsulated Scintillators For Radiological Applications

**Project Team:** Donald Benza (PI), Dr. Kenneth Gibbs, Bernadine Daichendt (SULI Intern), Dr. Aaron Washington, Dr. Khai Nguyen, Rick Minichan

**Thrust Area**: Legacy Waste Cleanup

**Project Start Date:** June 1, 2019

**Project End Date:** September 30, 2019

*3D printable X-ray scintillators/phosphors could have high utility at SRS. There are multiple and varied uses for radiation detection/imaging which ranges from dosimetry to X-ray computed tomography (CT) inspections. Multiple scintillators which emit red, green, and blue light respectively were filamentized and printed with good success. Filament feedstock is developed with a Filabot, a low-cost filament extruder. Scintillator powders are mixed with clear polyethylene terephthalate glycol (PETG) pellets at an approximate 5% by weight mixture. Initial testing was performed using both X-ray CT booths in addition to radioactive sources.*

## Objectives

- Develop 3D printable X-ray scintillator feedstock
- Determine X-ray energy response curves of chosen scintillators
- Test initial X-ray scintillator feedstock with radioactive sources

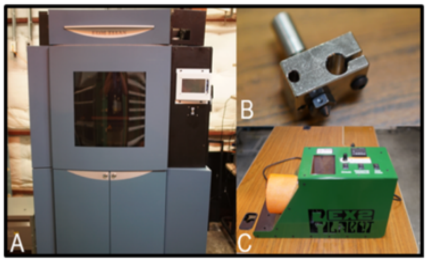

**Figure 1. A-** SRNL Modified Stratasys Titan 3D printer. **B-** SRNL 3D Printer Nozzle ecosystem (4 Nozzles) **C-** Filabot

## Introduction

This seedling was funded in June 2019 with proposed scope occurring in FY19. Despite a limited amount of time in FY19 available, much progress was made towards the objectives. The SRNL upgraded Stratasys Titan was identified as an excellent development tool due to its speed, versatility, and control of process parameters. This allowed test samples to be made in a timely manner. Before samples could be prepared, feedstock needed to be developed. Filaments were created out of clear PETG pellets and X-ray scintillator powder. Scintillators explored are europium doped yttrium oxide, terbium doped gadolinium oxysulfide, europium doped barium magnesium aluminate, copper doped zinc sulfide, and silver doped zinc sulfide. Samples were tested under X-ray irradiation in CT booths as well as with radioactive sources.

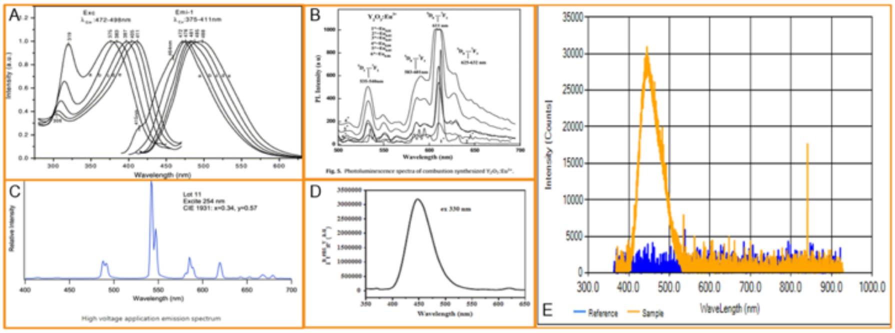

**Figure 2.** Emission spectra for **A** - ZnS:Cu (Ref1), **B** - $Y_2O_3$:Eu (Ref3), **C** - $Gd_2O_2S$:Tb (Ref4), **D** - $BaMgAl_{10}O_{17}$:$Eu^{2+}$ (Ref2), and **E** - ZnS:Ag

## Approach

Filament feedstock was prepared by coating clear PETG pellets with a scintillator powder. The pellets were loaded into a Filabot, a low-cost filament extruder, and transformed into a wire to be fed into any commonly available 3D printer. The SRNL upgraded Stratasys Titan was chosen to perform the work due to being open source with excellent control over process parameters. Samples were printed in various geometries and thicknesses for testing. Radioactive sources as well as X-ray CT booths were used to begin characterizing the materials.

## FY2019 Accomplishments

- Development of X-ray Scintillator Filament, Figure 3. This completed objective has generated great interest for other projects which will pursue funding. Filaments appear to be homogeneous but need to be further tested to ensure that is the case. 3 Patent disclosures were submitted as a result of this work. Data collected also provides opportunities for publishable papers.

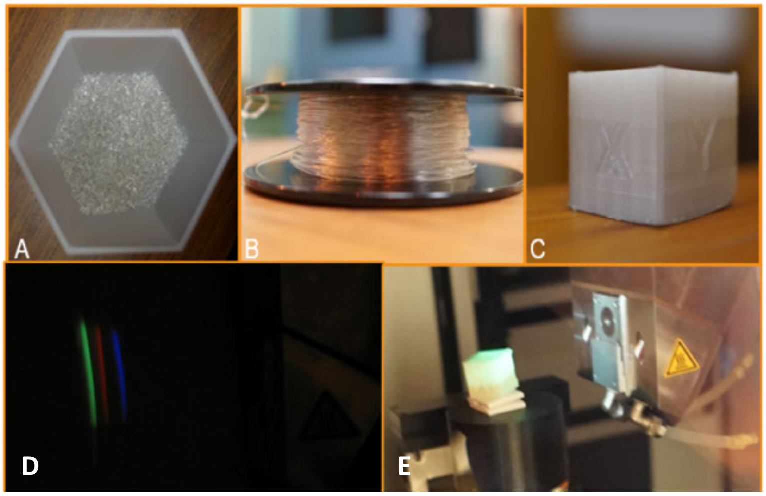

**Figure 3. A** - PETG pellets, **B** - PETG made filament, **C** - PETG cube printed part with Stratasys Titan, **D** -$Y_2O_3$:Eu (Red), $Gd_2O_2S$:Tb (Green), and ZnS:Ag (Blue) filaments under X-Ray irradiation, **E** - ZnS:Cu cube under X-Ray irradiation (Ref4).

- Determine X-ray energy response curves of chosen scintillators, Figure 4. This objective has begun testing but no conclusions can be made yet. A line detector which discriminates photon energies is arranged in front of a 150 KeV X-ray source. Background is taken and then scintillator samples are placed in front of the detector. A transmission curve is generated from this data. There are concerns that the setup is not yet fully perfected. It is also possible that the scintillators have similar response for the range of energies and more separation may occur at higher energy. A 400 KeV X-ray source is available but time did not allow for testing.

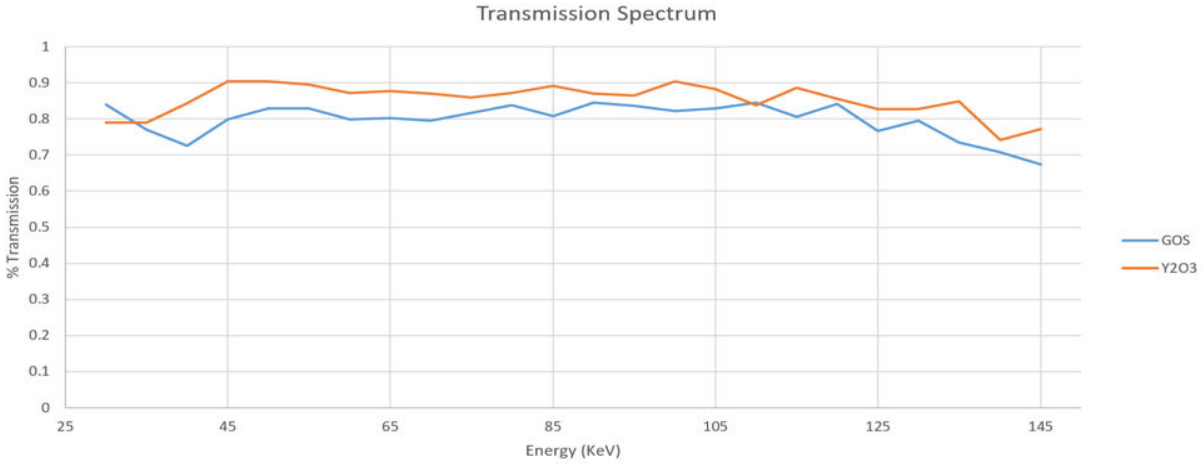

**Figure 4.** Transmission Spectrum for gadolinium oxysulfide and yttrium oxide

- Test Initial printed samples with radioactive sources, Figures 5 and 6. A checkerboard of 3 scintillators (gadolinium oxysulfide, ytrrium oxide, and zinc sulfide) was developed for testing. The checkerboard was imaged under irradiation from Am-241 (59.6 KeV), Cs-137 (662 keV), and Co-60 (1.1 MeV). After testing, it is possible that only gadolinium oxysulfide strongly illuminates under excitation from Cs-137. This is in contrast with Am-241 when all 3 scintillators are excited to luminesce. This can be an early indication of energy discrimination, but the setup needs to improve significantly to make reasonable conclusions. There was high noise in the camera due to high energy photons interacting with the CCD chip, making any conclusions difficult.

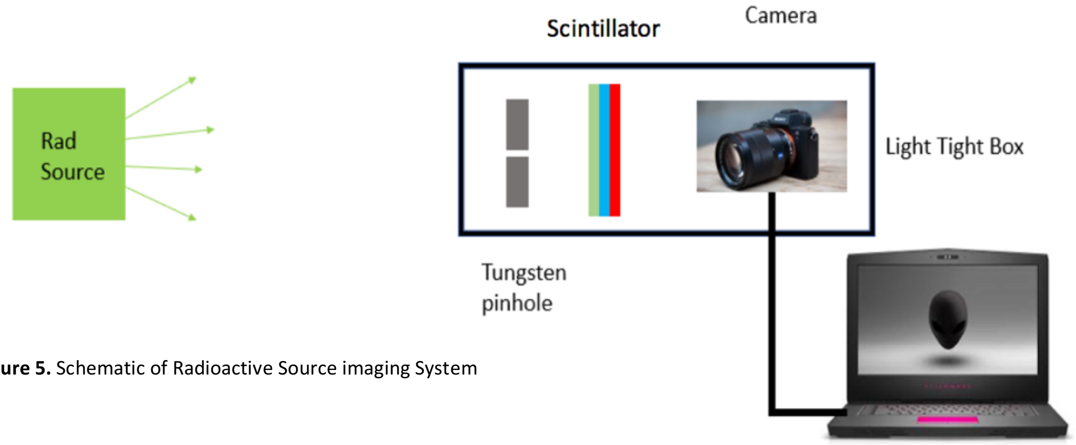

**Figure 5.** Schematic of Radioactive Source imaging System

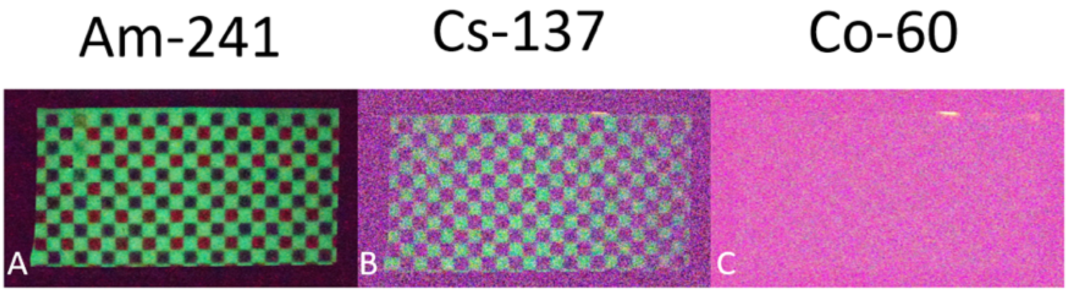

**Figure 6.** Printed checkerboard of $Y_2O_3$:Eu, $Gd_2O_2S$:Tb and ZnS:Ag under irradiation from **A-** Am-241 (Low Energy), **B-** Cs-137 (Mid Energy), and **C-** Co-60 (High Energy). Images taken with a Sony AS7ii DSLR Camera.

## Future Directions

- Engineer scintillators with desirable properties.
- Make quantifiable measurements of scintillator light output.
- Perform full characterization and calibration testing.

### References

1. K Manzoor, S.R Vadera, N Kumar, T.R.N Kutty. Synthesis and photoluminescent properties of ZnS nanocrystals doped with copper and halogen. Materials Chemistry and Physics. Volume 82. Issue 3. 2003. Pages 718-725. ISSN 0254-0584. https://doi.org/10.1016/S0254-0584(03)00366-3
2. Jeet, Suninder & Sharma, Manoj & Pandey, O. (2015). Synthesis and optical study of barium magnesium aluminate blue phosphors. AIP Conference Proceedings. 1661. 100005. 10.1063/1.4915440
3. J.R. Jayaramaiah, B.N. Lakshminarasappa, B.M. Nagabhushana. Luminescence studies of europium doped yttrium oxide nano phosphor. Sensors and Actuators B: Chemical. Volume 173. 2012. Pages 234-238. ISSN 0925-4005. https://doi.org/10.1016/j.snb.2012.06.092.
4. "New Process Higher Efficiency Terbium Doped Gadolinium Oxysulfide: Lorad Chemical Corporation." New Process Higher Efficiency Terbium Doped Gadolinium Oxysulfide | Lorad Chemical Corporation, Lorad Chemical Corporation, 2018, loradchemical.com/news/new-process-higher-efficiency-terbium-doped-gadolinium-oxysulfide.

### Acronyms

| | |
|---|---|
| **CCD** | charged coupled device |
| **CT** | computed tomography |
| **FDM** | Fused Deposition Modeling |
| **PETG** | polyethylene terephthalate glycol |

### Total Number of Student Researchers

One - Bernadine Daichendt, Clemson University SULI Intern

### Intellectual Property

1. SRS-19-013, Incident Photon Energy Discriminating X-ray Panel
2. SRS-19-014, Trace Impregnation of Additives into Additively Manufactured (AM) Parts for Anti Tampering
3. SRS-19-015, Fabrication of Unmanned Systems Using 3D Printed Components Using Materials Sensitive to Radiation

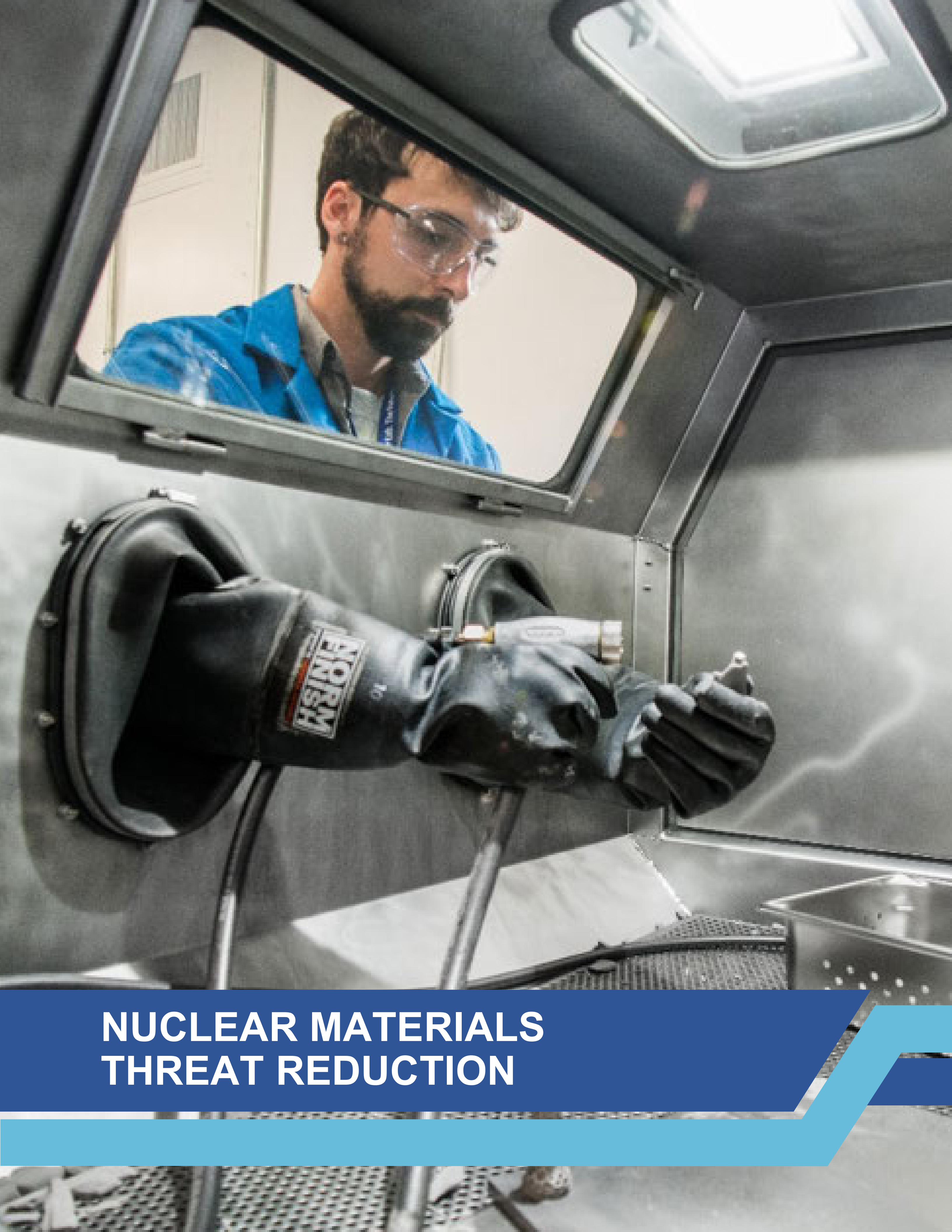

# NUCLEAR MATERIALS THREAT REDUCTION

# Synchrotron Based Microstructural Characterization Method Development for Pu Oxides

**Project Team:** M.A. DeVore II, J. Venzie, M. Wellons, J. Fortner, L. Schuller-Nickels, B. Powell

**Thrust Area**: Nuclear Materials Threat Reduction

**Project Start Date:** October 1, 2017

**Project End Date:** September 30, 2019

*Analysis was performed on the data collected from the APS experiments. Analysis included XRF and XANES to determine oxidation state, and EXAFS to determine bonding distances and coordination numbers. The oxidation state for most samples was the +4 as expected for $PuO_2$. Other measurements indicated that there could be +5 oxidation state. The bonding distances for typical $PuO_2$ are Pu–O of 2.33 and Pu–Pu of 3.81 Å. In evaluation of some measurements of EXAFS, there appears to be a shorter Pu–O distance of approximately 1.81 Å. This would be typical of plutonium in the +5 or +6 oxidation state with a -yl oxygen. Further analysis needs to be performed to ascertain exact distances.*

## Objectives

- Data analysis of X-ray Absorption Spectroscopy (XAS) data from APS beamline
- Return of samples and waste handling

## Introduction

The pre-detonation technical nuclear forensic (TNF) community is investing in the research, development, and exploitation of new non-isotopic forensic signatures of plutonium oxide. The community is interested in it as an intermediate form in the fuel and weapons cycle, and as the most common storage form for plutonium. Isotopic signatures, while useful, only provide limited information about the provenance of plutonium oxide. The TNF community is interested in exploring chemical and morphological characteristics to better understand the type of flowsheet used, scale of facilities, expertise of operators, etc. Detailed material science studies of plutonium oxide are needed to advance the understanding of the crystalline properties and their relationships to macro-scale signatures.

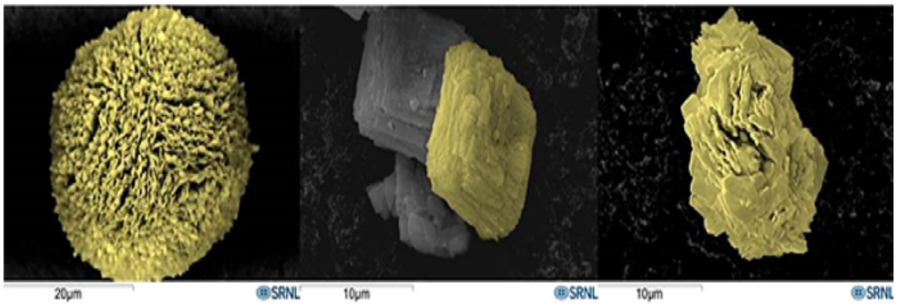

**Figure 1.** Three microcrystalline morphologies of $PuO_2$ observed in a single production batch.

The process by which particles grow is dependent on their crystal structures, grain size, and orientation of grains within a particle. Variations in density and microstructure of $PuO_2$ powder have led to differing particle sizes and morphologies (Figure 1). The microstructure is controlled by calcination temperature and the physicochemical conditions of precipitation, including shape of mixing tank, valance of plutonium, mixing sequence of plutonium and oxalic acid, precipitation temperature, and molar concentrations of oxalic acid, plutonium, and nitrate. Calcination has little effect on overall size of particle, but a great effect on surface roughness and particle morphology.

Nondestructive analysis of individual $PuO_2$ particles requires the use of bright sources of X-rays produced by synchrotron sources such as those produce at the Advance Photon Source (APS) at Argonne National Laboratory. The light source can reveal higher resolution crystallographic mapping, more sensitive chemical analysis, and higher fidelity morphological information than any methods currently available to SRNL. APS will allow the ability to simultaneously map X-ray diffraction (XRD) and X-ray fluorescence (XRF) grains on a particle. These allow the measure of grain sizes, shapes, and orientations for investigation. Further analysis of the data includes interrogation of oxidation states via X-ray Absorption Near Edge Spectroscopy (XANES), XRD pattern matching, and analyzing particle morphology to X-Ray absorption spectroscopy (XAS) spectra.

## Approach

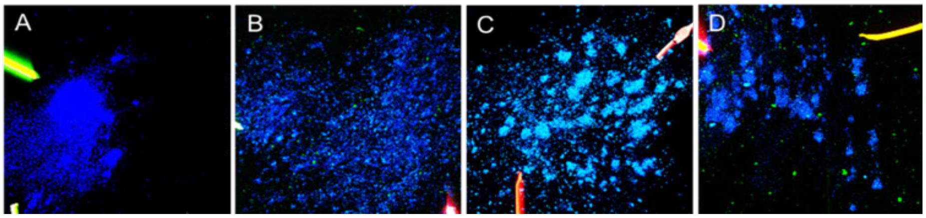

**Figure 2.** XRF maps of individual samples **A)** Lab synthesized clean $PuO_2$, **B)** AFS-2 production $PuO_2$, **C)** Lab synthesized $PuO_2$ with U contaminant, **D)** Lab synthesized $PuO_2$ with Fe contaminant. **Blue** – plutonium particles, **green** – Fe containing particles, **bars** – fiducial wires.

The final year of this project was used to perform analysis of the XAS data collected at the APS at Argonne National Laboratory. The analysis consists of XANES and Extended X-ray Absorption Fine Structure (EXAFS) with modelling to determine oxidation state, and modelled bond distances such as Pu–O and Pu–Pu distances that reveals information about coordination number and crystallographic unit cell.

## Results/Discussion

Synchrotron radiation analysis of the data taken in late FY18 was evaluated in FY19. Two types of X-ray absorption spectroscopy data were taken, X-ray Absorption Near Edge Spectroscopy (XANES) and Extended X-ray Absorption Fine Structure (EXAFS). XANES is best used to determine the oxidation state of the plutonium in the samples, while EXAFS is used for bond distances and coordination numbers. Fluorescence mapping was also undertaken to locate particles and determine if any contaminants make it through the precipitation process.

Since the samples were first prepared in a glovebox, the exact location of the particles in the samples were unknown. This was revealed by the XRF mapping shown in Figure 2. The blue areas are plutonium, and the green is iron. Typical fluorescence spectrum of four samples is shown in Figure 3. Each sample has the characteristic plutonium fluorescence line. Interestingly, AFS-2 material has both plutonium only regions, and plutonium/iron regions. The plutonium with iron addition sample is very similar to AFS-2 materials in the fluorescence. For Pu/U, there appears to be a small uranium fluorescence peak at the La1 line but is unconfirmed.

Figure 4 shows the typical full spectrum of XAS. The near edge region between the pre-edge and first peak determines the oxidation state. There appears to be little difference in the near edge region, but there are some small differences in the EXAFS that can only be revealed with fitting of the spectra.

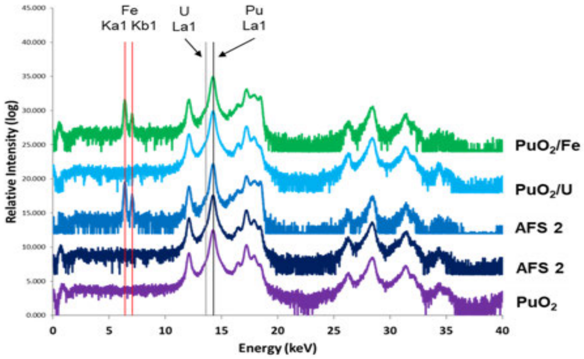

**Figure 3.** Typical XRF spectra of 4 samples. AFS-2 can have both iron and plutonium. The fluorescence lines listed are the major lines, others may be used.

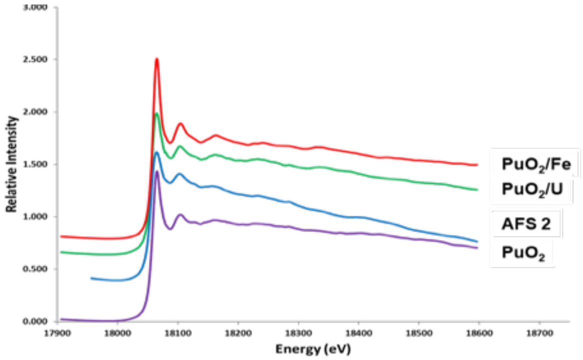

**Figure 4.** XAS spectrum of samples characterized at APS.

EXAFS was analyzed by fitting computed X-ray scattering paths based on the crystal structure of $PuO_2$, and absorber to nearest neighbor distances for Fe/O, U(IV, VI)/O, Pu(III, IV, V, VI)/O. All fitting calculations were performed in Artemis EXAFS software to determine the bands described in Figure 5. Pu-Pu distances of 3.80 Å are observed in each spectrum, with small shifts away from it, likely due to sample quality and preparation. Pu–O distances of 2.33 Å are very consistent across all the samples. AFS-2 $PuO_2$ is listed twice, the blue shows just plutonium in the XRF, while the green shows iron in the XRF with Pu. It is unclear at this time if the bands located below the 2.33 Å bands are related to a different oxidation state Pu, or a contribution from iron oxide. The small shoulder in the red spectrum is likely related to the same idea, but with uranium instead of plutonium.

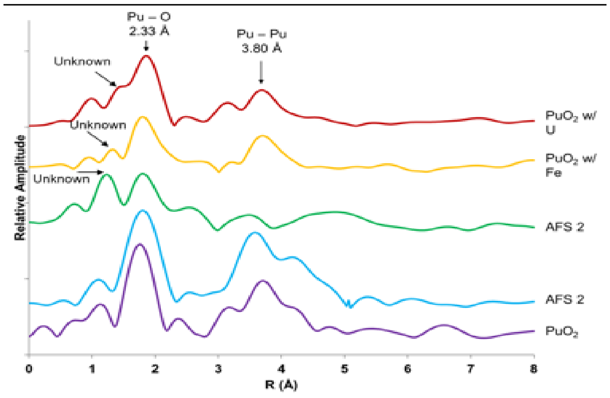

**Figure 5.** EXAFS of lab synthesized $PuO_2$, AFS-2, AFS-2 with Fe in XRF, $PuO_2$ with Fe contamination, and $PuO_2$ with U contamination. Bands are shifted, and determined by fitting the first and second shell nearest neighbors.

## FY2019 Accomplishments

- Attended an XAS workshop that allowed for better understanding of the synchrotron data. Data modelling techniques from the workshop show that there could be short Pu-O bonds indicative of other oxidation states of plutonium present in some characterized samples.
- Return of samples in a timely order.
- Waste treatment of returned samples.

## Future Directions

The future direction should be a refinement of the techniques and data processing of actinide samples. There were quite a few things learned, such as having oxidation state standards when determining XANES, taking XAS class before trying to process data, or having a better particle encapsulation technique to locate individual particles. There is still a concern over safety at APS and any new encapsulation techniques will need to be evaluated against their safety standards.

### *Publications/Presentations*

1. American Chemical Society Sci-Mix invited poster presentation, ACS Fall National Meeting San Diego, August 26, 2019.
2. American Chemical Society, Inorganic Chemistry Division, Actinides and Lanthanides subsection, ACS Fall National Meeting, San Diego, August 27, 2019
3. In preparation – Publication for Minerals special issue, Nuclear Forensic Applications in Geoscience and Radiochemistry.

### *Acronyms*

| | |
|---|---|
| **APS** | Advanced Photon Source |
| **XAS** | X-Ray absorption spectroscopy |
| **EXAFS** | Extended X-Ray Absorption Fine Structure |
| **TNF** | technical nuclear forensic |
| **XANES** | X-Ray Absorption Near Edge Spectroscopy |
| **XRD** | X-ray diffraction |
| **XRF** | X-ray fluorescence |

### *Total Number of Post-Doctoral Researchers*

One

# Development of Direct Injection/Ionization Mass Spectrometry Methods for Whole Molecule Characterization

**Project Team:** M. Wellons (Primary), K. Lawrence, A. Swindle, D. Mannion, R. Smith, J. Mannion, C. Shick, J. Dunbar, W. Kuhne

**Collaborators:** C. Cody (JEOL USA Inc.)

**Thrust Area:** Nuclear Materials Threat Reduction

**Project Start Date:** October 1, 2018

**Project End Date:** September 30, 2019

*Soft ionization methods for mass spectrometry allow the detection of partial or whole molecular species to enable rapid, unambigious indentification of species relevant to environmental remediation and nuclear safeguards challenges. In this project, various soft ionization methods were developed for the trace detection of whole molecule inorganic and organic species. Whole molecule uranyl complexes, including uranyl acetate, uranyl nitrate, uranyl chloride, uranyl oxalate and uranyl-tributylphosphate were successfully detected using paper spray mass spectroscopy (PSI-MS) and matrix-assisted ionization in vacuum (MAIV). PSI-MS of uranium, strontium, and cerium species led to nanogram limits of detection (LOD) with fast measurement times and no sample preparation. Finally, the detection and characterization of explosive compounds were carried out using standards for RDX and TNT to develop and optimize methods for concentrating samples swiped from surfaces. This work has demonstrated a new characterization modality for convenient and rapid analysis with little to no sample preparation.*

## Objectives

- Completion of PSI-MS analysis for inorganic elements and uranium complexes collected on cotton swipe substrates
- Development of matrix-assisted ionization in vacuum techniques for uranium complexes
- Sr and Ce species optimization using ESI-MS and PSI-MS; limit of detection characterization
- Development of AMS methods for explosive material detection and characterization.

## Introduction

The rapid characterization of the molecular and isotopic information for actinides and other inorganic samples is of paramount importance for a litany of applications, including forensics, medical diagnostics, environmental monitoring, and more. For nuclear safeguards applications, the determination of uranium isotopic and concentration information from environmental samples typically involves extensive chemical and physical processing prior to analysis. Harsh sample preparation results in the loss of the original uranium chemical speciation (i.e. what the uranium was bonded to/with when found in the environment) as well as the mixing of anthropogenic uranium with background material contained within the collection media (e.g. a swipe or soil). The objective of this work is to adapt ambient mass spectrometry (AMS) techniques,

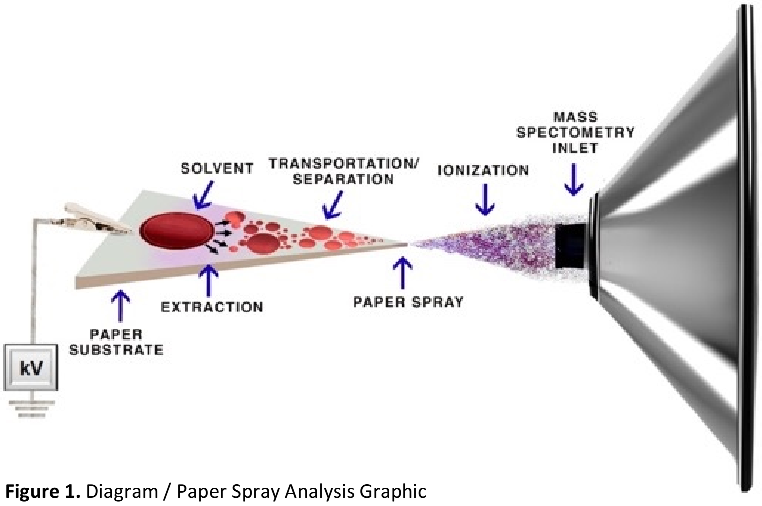

**Figure 1.** Diagram / Paper Spray Analysis Graphic

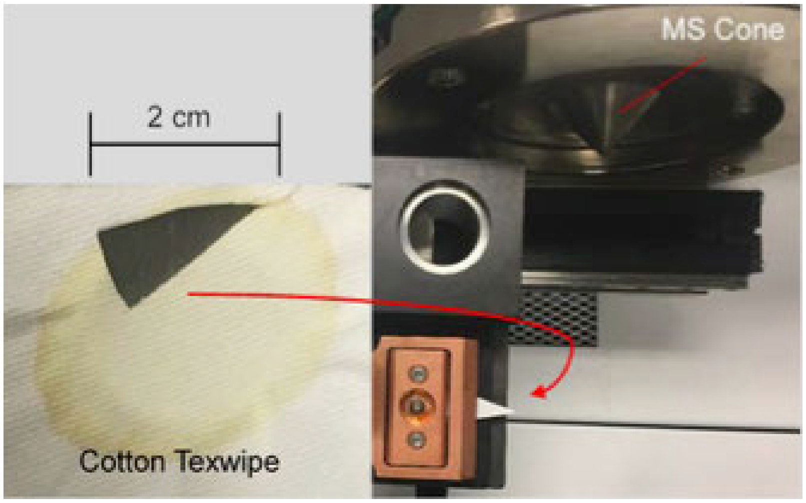

**Figure 2.** Cotton Texwip with uranyl doping that has been sectioned and loaded into a paper spray ionization source.

including paper spray ionization mass spectrometry (PSI-MS), matrix assisted ionization in vacuum (MAIV), and electrospray ionization (ESI-MS) for the rapid analysis of intact uranium complexes. PSI-MS is a recently developed AMS technique that allows for rapid (<5 min) sample analysis with no sample preparation (Figure 1). PSI-MS has been utilized for the direct analysis of blood,[2-4] urine,[5-6] and environmentally collected chemical warfare agent simulants.[7] For PSI-MS, samples are collected on a swipe consisting of a small triangle of filter paper or other fibrous material. The particulate on the swipe is then extracted or solvated by the solvent, ionized via electrospray ionization mechanisms, and guided into the mass spectrometer by electric fields (Figure 2). This results in a mass spectrum that is representative of species present on the swipe. Despite the promising nature of PSI-MS, no studies have previously been reported regarding uranium analysis by PSI-MS.

The measurement of uranium complexes using matrix- assisted ionization in vacuum (MAIV) was successfully carried out in FY19. MAIV generates mass spectra similar to those generated using electrospray ionization methods; however, it does not require the use of photons, electron beams, high voltage or added heat to initiate ionization. Instead, it is dependent on the choice of matrix and vacuum conditions.[8] The actual mechanism by which MAIV enhances ionization is unknown and is often referred to as "magic ionization." MAIV is typically carried out by introducing solid 3-nitrobenzonitrole (3-NBN) crystals directly into vacuum; however the introduction of liquid solutions containing saturated 3-NBN concentrations has yielded rapid results for inorganic species.[9] This method was employed for uranium complexes, including uranyl nitrate, uranyl chloride, uranyl acetate, and uranyl oxalate with LODs around 10 ppm for most species. Future investigations with other matrices could lower the LOD to levels more comparable to other AMS methods.

The fast analysis of trace inorganic molecules and complexes is important for forensic analysis, nuclear safeguards monitoring,[10,11] environmental monitoring[12,13] and geochronical measurements[14]. Method development and LOD was determined for various inorganics (Sr, Ce, and U) using ESI and PS-MS methods. Both species have LOD < ppm with the developed PSI-MS method in positive ion mode and allow isotopic species > 0.1 mole % to be detected reproducibly with internal standards. Stable isotopes of Sr were investigated as surrogate isotopes for the radioactive species $^{90}$Sr that is a legacy contaminant at DOE sites and is of concern to humans given its long half-life of 29 years. Additionally, scoping studies were performed to test ionization methods best suited for explosive material detection and characterization. Initial studies were begun in late FY19 for the detection and quantification of RDX and TNT.

## Approach

The overall project goal is to develop SRNL technical expertise in the arena of PSI-MS and MAIV for uranium detection, and develop expertise using PSI-MS and DART for inorganic species of Sr, Ce, Cd and explosive compounds. In FY19, activities for uranium characterization based on scoping measurements by the vendor JEOL for uranium compounds were carried out. SRNL work focused on determining if inorganics interfere with uranium detection and determining a LOD using PSI-MS. The detection and quantification of Sr and Ce was carried out using PSI-MS. No previous work has been reported using AMS for the detection of these two elements, which have significance to environmental radioactivity and nuclear forensics. The detection of RDX and TNT explosive standards using DART were also carried out in FY19. A literature review was performed to generate some reference operational settings for DART, but a strong effort was placed on method development for concentrating trace levels of sample material collected from surfaces.

ESI-MS was collected by placing the standard solutions into a syringe and attached to a syringe pump at flow rates of 33-50 µL/min. The solvent was run between samples to clean the orifice and reduce carryover. For PSI-MS, the filter paper wedges were mounted in the JEOL paper spray attachment and positioned ~1 mm from the skimmer cone entrance. A methanol/water mixture (95/5) with 1% $HNO_3$ was used to solvate the paper wedges and was applied dropwise at the back portion using a syringe pump set to 12.5 µL/min. Paper wedges were aligned manually during the first ~30 s of the run, using the total ion current chronogram (TICC) during the alignment process to maximize ion current into the mass spectrometer. Nanogram-level LODs were determined for the inorganic species through evaluation of serial dilutions of ppm and ppb (5-7 µL deposition volumes) level solutions. The solutions were prepared with an internal standard, however, in practice, internal standard would be contained in the solvent and metered solvent flow would be used to determine the mass quantities of internal standard applied to the swipe sample. Data extraction and analysis was performed using JEOL version 4 msAxel software for data acquisition, mass calibration, and to export spectrum data from regions of interest in the extracted ion current chromatogram (EICC). Peak deconvolution was carried out in OriginPro 2016 to obtain peak locations and intensities. For the calibration curves, the intensities were extracted from the raw data of each run using RStudio with MALDIquant and MALDIquantForeign packages.

## Results/Discussion

### *PSI-MS analysis for inorganic elements and complexes with uranium ions*

Mass spectra were collected on an atmospheric pressure ionization, high-resolution, mass spectrometer for solutions containing uranyl acetate, uranyl chloride, uranyl nitrate, and uranyl tri-n-buytl-phosphate (TBP) complexes. To demonstrate the ability to characterize inorganic contaminants in the presence of uranium, a multi-element inorganic standard containing U, Bi, Pb, Cd, Fe, and Zn was deposited onto cotton substrates and directly analyzed without purification (Figure 3). All species deposited on the swipe were detected with strong signal-to-noise ratios (S/N~1000 for $UO_2^+$) with µg levels of mass loading when estracted via solvent (80/20 MeOH/$H_2$0). High integrated intensities (>$10^5$ counts) from a collection period of approximately 1 min were obtained. The measured isotope abundances were in good agreement with natural abundances for most of the major isotopes characterized. The cotton swipes showed minor background constituents and produced stronger and more stable ion counts than the classic cellulose based filter paper substrates. These experiments were reproducing the experiments previously conducted under the vendor JEOL's guidance in FY18.

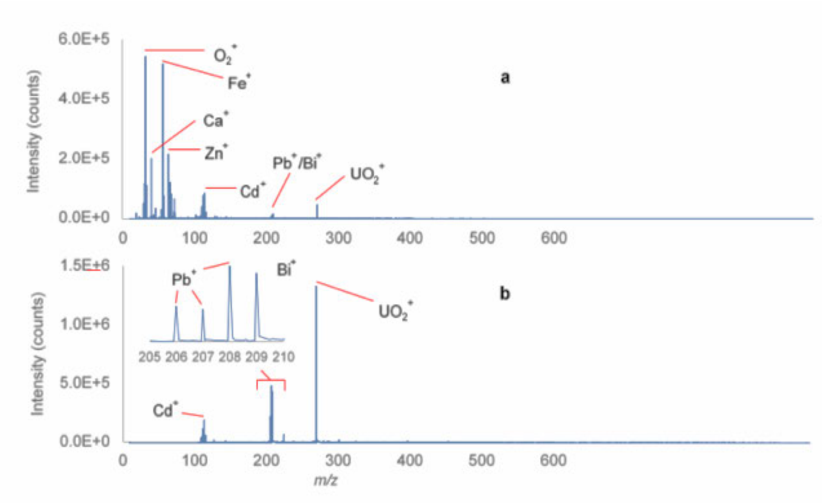

**Figure 3.** Positive ion mass spectra of a directly analyzed cotton Texwipe with mixed element doping in **a)** low mass and **b)** high mass operation modes and extracted via MeOH/$H_2$0. High mass mode can be used to increase sensitivity for species with mass-to-charge ratios >100 through modulation of the ion guide voltage; sensitivity for $UO_2$ increased by approximately one order of magnitude in high mass mode.

The quantification of U via the use of gadolinium nitrate as an internal standard was carried out using PSI- MS. The ratio of the measured $^{238}U^{16}O_2$ to $^{160}Gd^{16}O$ intensity was plotted against the deposited uranyl concentration to construct a calibration curve (Figure 4). The linear relationship between the $^{238}U^{16}O_2$ / $^{160}Gd^{16}O$ intensity ratio and the deposited uranyl concentration demonstrates that uranyl quantitation with PSI-MS is possible using an internal standard. LODs were determined to be approximately 94 ng for $UO_2^+$ and uranyl acetate through the measurement of ppb level solutions. Isotopic ratio measurements ($^{235}U/^{238}U$) were also investigated (Figure 4). Reproduction experiments confirm that low isotope ratio errors (<1% error) can be achieved with PSI-MS through adequate count rates (similarly to other mass spectrometry based analytical methods). Additionally, swipe limit of blank (LOB) for U is suspected to be lower for PSI-MS than other analytical methods as the swipe material is not digested for analysis by PSI-MS, preventing

U within the natural fibers from contributing to the background and distorting measured isotope ratio values. No major interfering species for U analysis were detected, and $UO_2^+$ was observed rather than atomic $U^+$.

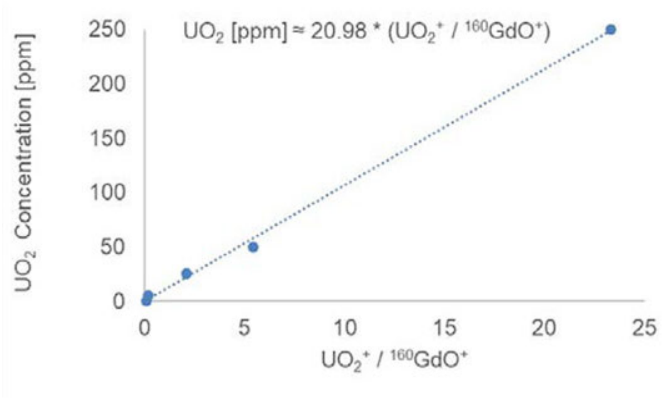

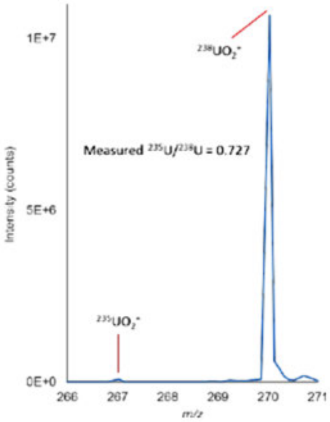

**Figure 4. (left)** Linear calibration curve constructed from trials with 50 ppm $Gd(NO_3)_3$ as an internal standard and varying concentrations of $UO_2Cl_2$ ($R^2=0.9944$), **(Right)** $^{235}U/^{238}U$ isotope ratio measurement via PSI-MS.

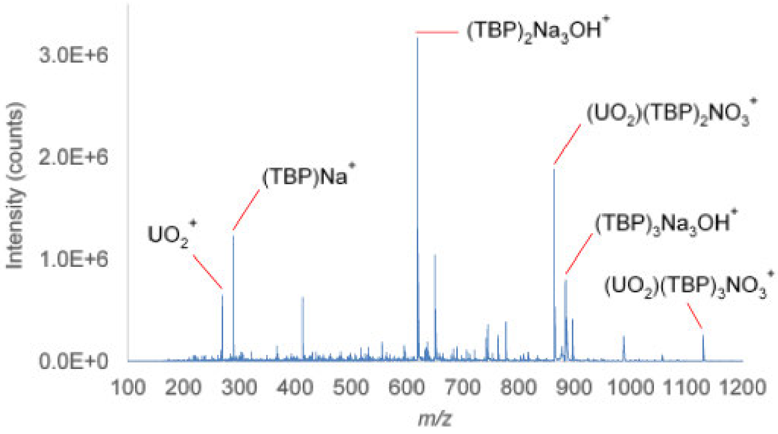

**Figure 5. (left)** Positive ion mass spectrum of 0.2 μM uranyl nitrate and 0.5 μM TBP deposited on (7 μL) on cellulosic filter paper. Complete identification of the observed species was tabulated separately.

The detection of uranyl tributylphosphate (TBP) was also carried out to demonstrate the ability for whole-molecule characterization using PSI- MS. U-TBP complexes were prepared by mixing TBP ligand and uranyl nitrate before drop casting onto the paper substrate. The 1:2 and 1:3 uranyl-TBP complexes were detected in positive ion mode alongside TBP-Na adducts and the uranyl cation (Figure 5). These finding are similar to those reported by PNNL for ESI- MS characterization of aqueous uranyl-TBP mixtures, however, several differences were observed, which warrant further investigation.[15] Soft-ionization, resulting from electrospray-like mechanisms, allows for the detection of intact uranyl complexes by preventing ion fragmentation. In addition to uranyl-TBP complexes, uranyl acetate was also successfully analyzed via PSI-MS.[16]

### *MAIV method development for uranium-bearing species*

The detection of uranium complexes (uranyl nitrate, uranyl chloride, uranyl acetate, and uranyl oxalate) in MAIV using a 3-NBN matrix was successfully carried out. Concentrations ranging from 0.1 to 500 ppm were saturated with the 3-NBN and directly injected into the orifice in negative ion mode. Analysis was performed in negative ion mode with the DART source retracted to allow access to Orifice 1. At the end of each analysis sequence, Fomblin Y was analyzed using DART(-) for exact mass calibration. Initial results show successful detection of the uranium complexes using MAIV (Figure 6). U speciation was identified using MAIV with mass loading as low as 25 nanograms for uranyl acetate. Lower LODs calculated for the various species were 0.25 ppm for uranyl nitrate, 11.6 ppm for uranyl chloride, 8.1 ppm for uranyl acetate, and 3.0 ppm for uranyl oxalate.

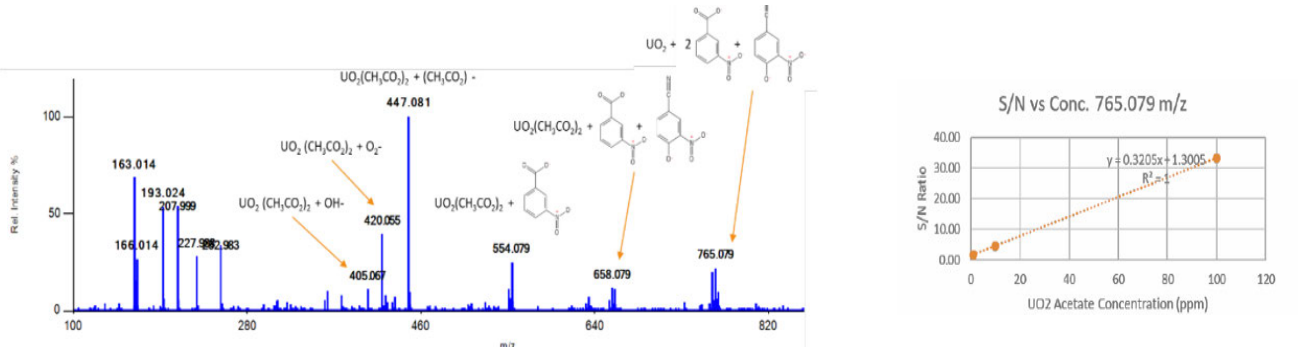

**Figure 6. (above left)** Example negative ion mass spectrum of 250 ppm uranyl acetate in water [$UO_2(CH_3CO_2)_2$] = 635 ng. **(above right)** Calibration curve for uranyl acetate using MAIV.

This work reveals that the 3-NBN matrix contributes to the ionization process by forming adducts with uranyl complexes with a net negative charge. This complexation occurs across a range of concentrations and with all uranyl complexes studied; however, the contribution of these uranyl complex-matrix ion adducts to the total analyte signal varied from one uranyl complex to the other. The uranyl complex ligand identity does seem to have an impact on LODs. When analyzing inorganics in a 3-NBN matrix, deprotonated matrix components either formed inorganic-matrix adducts or reacted to create positively charged complexes with the uranyl. Inorganic complexes with 3-nitrobenzoic acid (3-NBA) and 4-hydroxy-3-NBN were primarily detected, although other components of the matrix, such as picric acid, also formed adducts or complexes with uranyl. All species were detected as singly negatively charged complexes in the mass spectra, but it is unknown whether this reaction occurs in solution or during ionization in the gas phase. In the MAIV spectra of the matrix in the absence of inorganics, 3-NBA constituted a relatively minor part of the matrix but is the only matrix component that appears in all significant $UO_2$(ligand) + matrix ions.

Though our work indicates the main matrix constituents that are contributing to ionization are 3-NBA and 4-hydroxy-3-NBN, neither of these components have been investigated as candidates for MAIV previously. It is hypothesized that a tailor-made matrix "cocktail" containing higher concentrations of 3-NBA and 4- hydroxy-3-NBN would lead to higher ionization efficiencies, lower LODs, and smaller mass loading. If these matrix components initiate ionization in MAIV, it is possible they could perform better for organic analysis MAIV than the currently and widely used 3-NBN.

### *Sr and Ce Species detection using ESI-MS and PSI-MS*

The detection of trace levels of strontium and cerium species was developed for PSI-MS and ESI-MS. Strontium nitrate was measured using ESI-MS and PSI-MS, both in positive-ion mode. Strontium nitrate and cerium nitrate solutions were prepared with yttrium nitrate and gadolinium nitrate as internal standards, respectively. The ESI-MS spectrum of Sr produced single charged Sr and YO+ ions (Figure 7) and the measured m/z values for the different Sr species had less than 0.005% error compared to the exact species masses. Spectra collected using the PSI-MS method showed similar percent error in the measured m/z values and measured isotopic abundancies compared to ESI-MS but also measured the polysaccharide contamination ($[C_6H_{10}O_5+Na+H]^+$ inherent in the cellulosic filter paper used in the study (Figure 7).

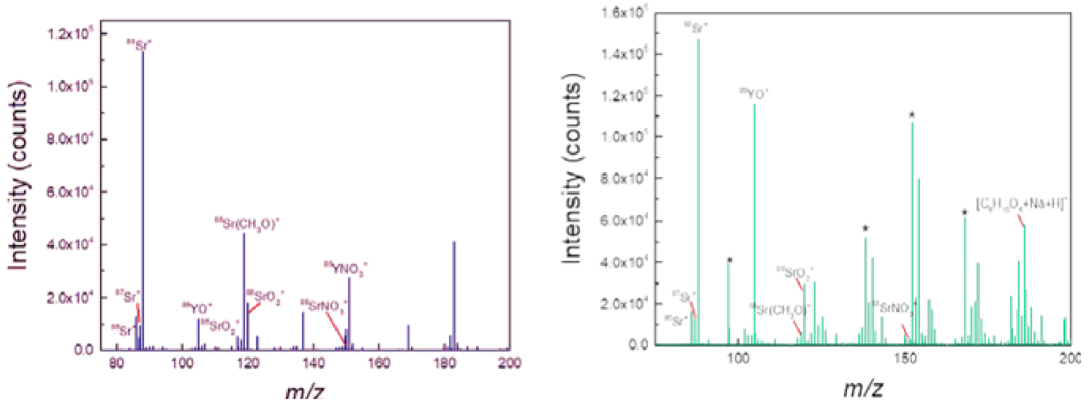

**Figure 7. (left)** 116 ppm $(SrNO_3)_2$ with 50 ppm $Y(NO_3)_3$ internal standard for ESI-MS; **(right)** 116 ppm $(SrNO_3)_2$ with 50 ppm $Y(NO_3)_3$ internal standard for PSI-MS.

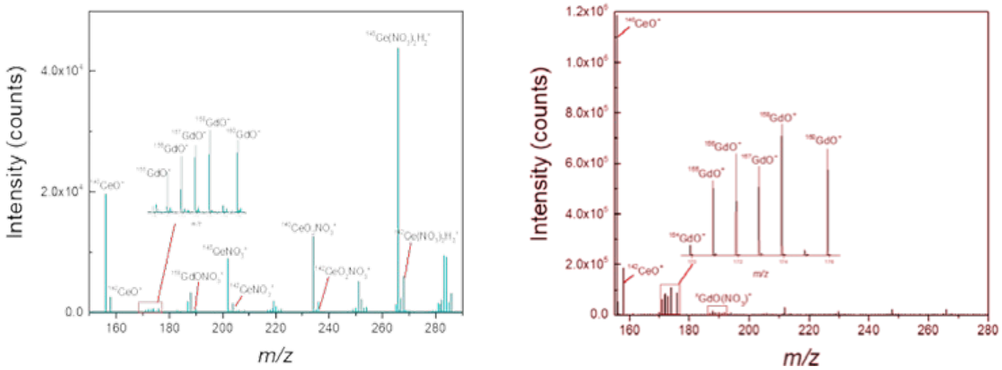

**Figure 8. (left)** 154 ppm $Ce(NO_3)_2$ with 50 ppm $Gd(NO_3)_3$ internal standard using ESI-MS; **(right)** 154 ppm $Ce(NO_3)_2$ with 50 ppm $Gd(NO_3)_3$ internal standard using PSI-MS.

Limit of detection determinations for Sr using ESI-MS compared to PSI-MS showed that ESI-MS was capable of slightly lower limits of detection. LODs were in the ppb range for ESI-MS (0.19±0.096 ppm) versus PSI-MS (1.9±0.7 ppm). Similar results were found for the detection of $Ce(NO_3)_3$ with a $Gd(NO_3)_3$ internal standard, where ESI-MS spectra produced singly charged $CeNO_3$ adducts as well as oxide adducts from Ce hydrolysis (Figure 8). For Ce detection, the percent error in the m/z measurements with ESI-MS were below 0.05%; however, the error in the isotopic abundancies were higher for the gadolinium adducts due to interferences between some of the $GdO^+$ isotopic adducts with cerium hydrolysis adducts, where the $^{140}CeO(OH)^+$ species has m/z value within m/z = 0.015 of $^{157}GdO$. Using PSI-MS, the less prevalent adducts, such as cerium nitrate, were not observed above the background levels of the spectra and led to a lower percent error for the calculated isotopic abundancies of $GdO^+$ adducts. The most common $[CeO]^+$ adduct was still observed for the two most abundant isotopes ($^{140}Ce$ and $^{142}Ce$) and was used for the calibration curves. Additionally, the nitrate oxide adducts of the different gadolinium species were also observed. The percent error in the m/z measurements for PSI-MS were slightly lower than for ESI-MS, below 0.01%, but there was an increase in the percent error for the measured isotopic abundancies for the cerium adducts. Overall, the LOD for cerium was lower for ESI-MS (0.12±0.03 ppm) compared to PSI-MS (0.32±0.07 ppm), consistent with Sr detection. The LODs were dependent on instrument settings such as the radiofrequency (RF) quadrupole ion guide voltage.

Overall the detection of strontium nitrate and cerium nitrate has been measured with low percent error and LODs in the ppm range while the different adducts, including the adducts for the original nitrate molecules, were observed.

### *RDX and TNT Explosives*

Spectra have been collected in the negative ion mode for ESI-MS and DART ionization methods for standards of RDX and TNT. The effect of solvents to promote ionization have been tested for methanol/water mixtures and acetonitrile. Data work is ongoing, and results will be presented in FY20.

## FY2019 Accomplishments

- Completion of the method development for the JEOL AccuTOF mass spectrometer and the direct analysis (i.e. no sample preparation) of uranyl containing and inorganic multi-element containing swipes. Nanogram level detection limits for uranyl were measured.
- Methods using ESI-MS and PSI-MS were developed for the direct analysis of inorganic Strontium and Cerium with ppm to ppb LODs.
- Successful analysis of intact organo-uranyl complexes using MAIV with the identification of potentially novel matrix components that can increase the ionization efficiencies of uranium molecules, leading to lower LODs.
- Method development for trace explosives in complex environmental matrices using DART-MS.

## Future Directions

- Development of method protocols for explosive compounds and leverage sample collection against planned site field exercise.

## Publications/Presentations

1. Inorganic molecular ion detection using Ambient Mass Spectrometry Techniques. Draft Manuscript in Preparation. *Rapid Communication in Mass Spectrometry, 2019.*
2. Matrix-assisted ionization in vacuum (MAIV) of whole molecule uranium compounds. Draft Manuscript in Preparation. *Rapid Communication in Mass Spectrometry, 2019.*
3. Coopersmith, K., Cody, RB., Mannion, J.M., Hewitt, J.T., Koby, S.B. and M.S. Wellons. (2019). Rapid paper spray mass spectrometry characterization of uranium and exemplar molecular species. *Rapid Communication in Mass Spectrometry.* DOI: 10.1002/rcm.8517.
4. Dunbar, D., Swindle, A., Lawrence, K., Kuhne, W., Wellons, M., Development of ambient mass spectrometry rapid analysis methods for trace inorganics, *SULI Intern Report,* Doc# SRNL-STI- 2019-0417.
5. Paper spray ionization mass spectrometry for rapid chemical and isotopic characterization of trace uranium samples. 70th Southeastern Regional Meeting American Chemical Society (SERMACS), Augusta, GA October 31-November 3, 2018. Abstract. Oral Presentation

## References

1. Ren, Y.; Wang, H.; Liu, J.; Zhang, Z.; McLuckey, M. N.; Ouyang, Z., Analysis of Biological Samples Using Paper Spray Mass Spectrometry: An Investigation of Impacts by the Substrates, Solvents and Elution Methods. *Chromatographia* **2013,** *76* (19), 1339-1346.
2. Espy, R. D.; Teunissen, S. F.; Manicke, N. E.; Ren, Y.; Ouyang, Z.; van Asten, A.; Cooks, R. G., Paper Spray and Extraction Spray Mass Spectrometry for the Direct and Simultaneous Quantification of Eight Drugs of Abuse in Whole Blood. *Anal. Chem.* **2014,** *86* (15), 7712-7718.
3. Shi, R.-Z.; El Gierari, E. T. M.; Manicke, N. E.; Faix, J. D., Rapid measurement of tacrolimus in whole blood by paper spray-tandem mass spectrometry (PS-MS/MS). *Clinica Chimica Acta* **2015,** *441,* 99-104.
4. Jett, R.; Skaggs, C.; Manicke, N. E., Drug screening method development for paper spray coupled to a triple quadrupole mass spectrometer. *Anal. Methods* **2017,** *9* (34), 5037-5043.
5. Michely, J. A.; Meyer, M. R.; Maurer, H. H., Paper Spray Ionization Coupled to High Resolution Tandem Mass Spectrometry for Comprehensive Urine Drug Testing in Comparison to Liquid Chromatography-Coupled Techniques after Urine Precipitation or Dried Urine Spot Workup. *Anal. Chem.* **2017,** *89* (21), 11779-11786.
6. Jeong, E. S.; Kim, K. H.; Cha, E.; Kwon, O.-S.; Cha, S.; Lee, J., Direct and rapid quantitation of ephedrines in human urine by paper spray ionization/high resolution mass spectrometry. *Journal of Chromatography B* **2016,** *1028,* 237-241.
7. Dhummakupt, E. S.; Mach, P. M.; Carmany, D.; Demond, P. S.; Moran, T. S.; Connell, T.; Wylie, H. S.; Manicke, N. E.; Nilles, J. M.; Glaros, T., Direct Analysis of Aerosolized Chemical Warfare Simulants Captured on a Modified Glass-Based Substrate by “Paper-Spray” *Ionization. Anal. Chem.* **2017,** *89* (20), 10866-10872.
8. Lee, C.; Inutan, E. D.; Chen, J. L.; Mukeku, M. M.; Weidner, S. M.; Trimpin, S.; Ni, C.-K., Toward understanding the ionization mechanism of matrix-assisted ionization using mass spectrometry experiment and theory. *Rapid Communications in Mass Spectrometry,* ***2019,*** *DOI: 10.1002/rcm.8382.*
9. Cody, R. B., Ambient Profiling of Phenolic Content in Tea Infusions by Matrix-Assisted Ionization in Vacuum. *J. Am. Soc. Mass Spectrom.* **2018,** *29* (8), 1594-1600.
10. Lamouroux, C.; Moulin, C.; Tabet, J. C.; Jankowski, C. K., Characterization of zirconium complexes of interest in spent nuclear fuel reprocessing by electrospray ionization mass spectrometry. *Rapid Communications in Mass Spectrometry* **2000,** *14* (19), 1869-1877.
11. Zheng, J.; Tagami, K.; Watanabe, Y.; Uchida, S.; Aono, T.; Ishii, N.; Yoshida, S.; Kubota, Y.; Fuma, S.; Ihara, S., Isotopic evidence of plutonium release into the environment from the Fukushima DNPP accident. *Scientific Reports* **2012,** *2* (304), 1-8.
12. Liu, W.; Dai, X.; Bai, Z.; Wang, Y.; Yang, Z.; Zhang, L.; Xu, L.; Chen, L.; Li, Y.; Gui, D.; Diwu, J.; Wang, J.; Zhou, R.; Chai, Z.; Wang, S., Highly Sensitive and Selective Uranium Detection in Natural Water Systems Using a Luminescent Mesoporous Metal–Organic Framework Equipped with Abundant Lewis Basic Sites: A Combined Batch, X-ray Absorption Spectroscopy, and First Principles Simulation Investigation. *Environmental Science & Technology* **2017,** *51* (7), 3911-3921.
13. Xiao, S. J.; Zuo, J.; Zhu, Z. Q.; Ouyang, Y. Z.; Zhang, X. L.; Chen, H. W.; Zhang, L., Highly sensitive DNAzyme sensor for selective detection of trace uranium in ore and natural water samples. *Sens. Actuators B* **2015,** *210*, 656-660.
14. Spano, T. L.; Simonetti, A.; Balboni, E.; Dorais, C.; Burns, P. C., Trace element and U isotope analysis of uraninite and ore concentrate: Applications for nuclear forensic investigations. *Applied Geochemistry* **2017,** *84,* 277-285.
15. McDonald, L. W.; Campbell, J. A.; Vercouter, T.; Clark, S. B., Characterization of Actinides Complexed to Nuclear Fuel Constituents Using ESI-MS. *Anal. Chem.* **2016,** *88* (5), 2614-2621.
16. Coopersmith, K.; Cody, R. B.; Mannion, J. M.; Hewitt, J. T.; Koby, S. B.; Wellons, M. S., Rapid paper spray mass spectrometry characterization of uranium and exemplar molecular species. *Rapid Communications in Mass Spectrometry* **2019***, 33* (22), 1695-1702.

## Acronyms

| | |
|---|---|
| **AMS** | Ambient Mass Spectrometry |
| **DART** | Direct analysis in real time |
| **ESI-MS** | Electrospray Ionization Mass Spectrometry |
| **LOD** | Limit of detection |
| **MAIV** | Matrix-assisted Ionization in Vacuum |
| **NBN** | Nitrobenzonitrile |
| **NBA** | 3-nitrobenzoic acid |
| **PSI-MS** | Paper Spray Ionization Mass Spectrometry |
| **S/N** | Signal to noise ratio |
| **TBP** | Tributylphosphate |

# Develop SRNL's ALGE3D Code for Use as National Response Asset

**Project Team:** G. M. Maze (Primary),
S. Aleman, A. Garrett, R. Buckley,
E. Viparelli, S. Sanders, T. Richardson

**Subcontractor:** University of
South Carolina

**Thrust Area:** Nuclear Materials
Threat Reduction

**Project Start Date:** October 1, 2017

**Project End Date:** September 30, 2019

*Currently, national emergency response agencies have well developed models to simulate the effects of hazardous contaminants in riverine systems primarily driven by one-dimensional flows; however, there is a gap in the support for more complex systems. While many models exist, none are capable of quick deployment in emergency situations that could support a variety of release situations including mixtures of both particulate and dissolved chemicals in a complex flow area, e.g., lakes, bays, and tidal estuaries. Adaptations of ALGE3D have been implemented to update and expand particulate tracer and sedimentation capabilities to allow for a more comprehensive model. Quick-deployment model inputs will also be developed for multiple high impact areas to aide in the timeliness of emergency response in key locations. The final product of ALGE3D allows for coupling of dissolved tracer concentrations, particulate tracer concentrations, and their associated sedimentation effects.*

## FY2019 Objectives

- Expand location library
- Develop particulate tracer module for ALGE3D
- Develop sedimentation module for ALGE3D
- Couple with atmospheric dispersion model
- Verification, testing and publication

## Introduction

On average North Americans live within ~3 km of a water body.[1] Of the top 10 most populated US cities from a 2015 US Census Bureau estimate, 7 of the cities are situated near the ocean, a bay, or on one of the Great Lakes. A contamination of the water ways in the United States could be devastating to the economy (through tourism and industries such as fishing), public health (from direct contact, or contaminated drinking water), and in some cases even infrastructure (water treatment plants). For example, Figure 1 shows two visible satellite images for Chesapeake Bay, the first on August 23, 2011 and the second on September 13, 2011. In the second image a large plume of suspended particles in the Bay can clearly be seen. In this case it was a sediment plume caused by a large storm system moving through, and the major impacts included mainly damage to the fishing and oyster industries that year along with beach and recreation area closures.[2,3] However, a similar plume containing radioactive or chemical material would have resulted in much costlier and wide spread consequences due to the associated human health impacts.

Current US emergency response capabilities for contamination to waterways, either from an accidental release or a planned attack, include the use of a one-dimensional transport model.[4,5] This works well for most riverine systems which have flow in primarily one (downstream) direction. However, in more complex systems, such as tidal estuaries, bays, or lakes, a more complex model is needed. SRNL will develop ALGE3D to fill this gap in technology for emergency response of multi-dimensional aqueous modeling of scales below the Rossby radius of deformation, where the forces associated with the rotation of the earth are negligible. A three-dimensional model with the capability to handle dissolved and particulate contaminants, model the associated sedimentation effects, and support quick-deployment will provide a unique capability that could support the US emergency response enterprise.

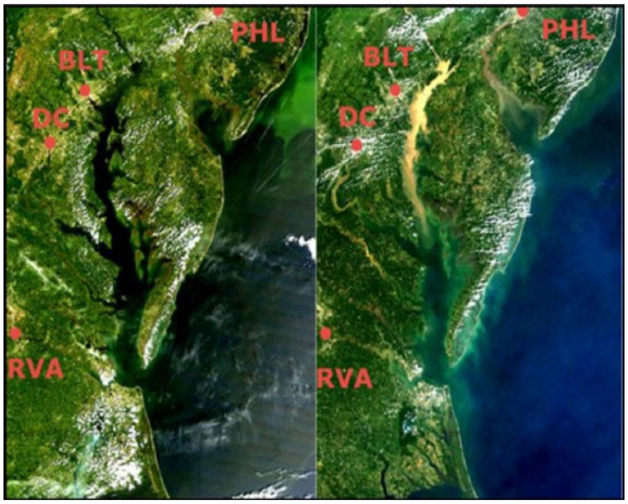

**Figure 1.** MODIS images of Chesapeake Bay Augusta 23, 2011 and September 12, 2011. Major population centers are labeled.

## Approach

ALGE3D is a 3-D hydrodynamic code developed by SRNL which solves the momentum, mass, and energy conservation equations to predict the movement and dissipation of thermal or dissolved chemical plumes discharged into cooling lakes, rivers, and estuaries.[6] The first portion of this project included data gathering for multiple highly populated bodies of water with multiple potential sources of accidental release. Data was gathered for Chesapeake Bay, Lake Michigan, Biscayne Bay, New York Harbor, Port of Houston, Port of Long Beach, Puget Sound, San Francisco Bay, Delaware Bay, Long Island Sound, Tampa Bay, the mouth of the Savannah River (port of Savannah), and the mouth of the Cape Fear River (port of Wilmington).

While data gathering was being accomplished a pre-processor graphical user interface (GUI) was developed. The highly structured format of the required input files can be limiting and provide an endless source of frustration for users, so to facilitate use in an emergency response situation a program was developed. This program guides the user through the selection of necessary data and generates the necessary input files in the proper format and verifies all required files are present based on the user's selections. Within the GUI each location has a preselected list of potential release locations or allows the user to input a custom release location. The GUI will also calculate the tidal forcing for each location that has tidal forcing based on the tidal harmonics present at each location as calculated by NOAA.[7] Each location was also run for 1 year to allow spin up time to set up the background salinity pattern in the area. This will allow for quicker modeling run times as the model does not need to be given time to set up the domain.

Code modifications were made to include suspended sediment, particulate species, and dissolved species transport. The dissolved species can be adsorbed onto or desorbed off of suspended sediment particles based on the chemical properties specified of the released material. Sedimentation effects, including erosion and deposition were also added into the code. In addition to the transport modules added, modifications were made to the code to reduce the amount of spin up time needed to obtain the physical properties (salinity and temperature) by adding an option to include an initial spatially varying field rather than one set initial value. This modification allows the code to be run in a more operational time frame.

Verification of the transport modules was conducted by running multiple validation cases. Simple settling column cases were run with and without dissolved species interactions for sand, silt, and clay sediment particles. The settling time of the material was compared to theoretical settling velocities from the Dietrich settling velocity equations.[8] Moving flume cases are still ongoing with varying fine sand sediment loads and will be compared to experiments conducted by Coleman et al.[9, 10]

**A simulation case was also run to show the models capability to use multiple types of material input sources.**

NARAC provided atmospheric surface deposition files for a FEMA exercise of a simulated dirty bomb release near New York. These atmospheric surface deposition files were used to create an input for the aqueous model.

## Results/Discussion

Simple settling column cases were compared with the theoretical settling depth estimated by using settling velocity as calculated by Dietrich 1982.[8] The settling depth in the model runs was determined to be the depth to which the concentration is measured as >1% of the surface concentration. After 60 seconds the sand theoretically settles 0.65 m but was modeled to a depth of 1 m, the silt theoretically settles 0.339 m but was modeled to a depth of 0.3m, and the clay theoretically settles <0.1 m and was modeled to <0.1 m. Figure 2 shows the settling depths of sand, silt and clay sediments after 1 minute, 1 hour, and 1 day of modeling, the figure also shows the particulate form of the dissolved species interacting with the sediments. The red line in each panel shows the theoretical settling depth. In each case there is some discrepancy in the theoretical and modeled settling depth. The model assumes spherical particles with no colloidal interactions, while the theoretical equations have been developed to account for the non-spherical nature of sediment particles.

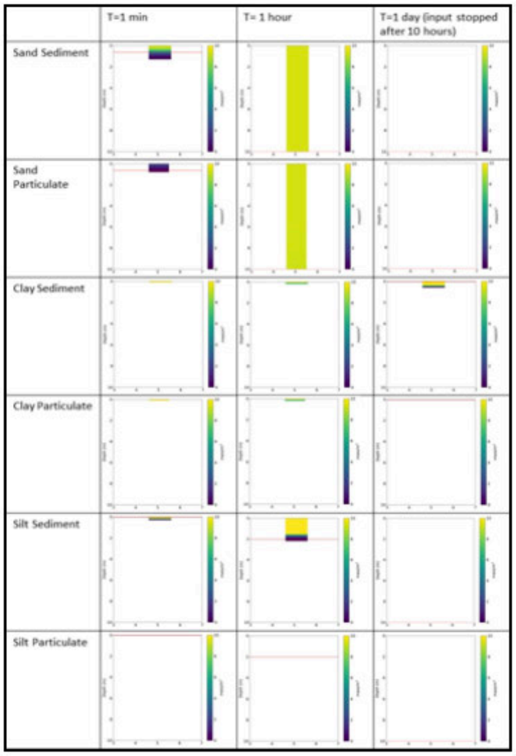

**Figure 2.** Concentration of suspended sediments and particulate sediments 1 minute, 60 minutes and 24 hours after release.

## FY2019 Accomplishments

- Developed bathymetric and identification grid for 13 locations.
- Developed and tested modules for dissolved, particulate, and sediment transport including interactions and half-life decay.
- Implemented GPU modeling to reduce model run time.
- Verification of particulate and sediment modules was performed using a stagnant water column simulation and moving flume simulations.
- Ability to use atmospheric surface deposition files as input to model was proven.

## Future Directions

- Refine pre- and post- processing GUI
- Validation and verification of simulations. Ongoing moving flume cases with varying fine sand sediment loads will be compared to experiments.
- Expand library of release locations
- Add library of potential release materials with the appropriate model inputs and critical values for analysis
- Inverse modeling
- Refine coupling with atmospheric dispersion models

## *Publications/Presentations*

1. Maze, Grace. (2017, December) ALGE3D: A Three-Dimensional Transport Model, Presented at the American Geophysical Union Fall Meeting, New Orleans, Louisiana.
2. Maze, Grace. (2018, February) ALGE3D: A Three-Dimensional Transport Model, Presented at Ocean Sciences Meeting, Portland, Oregon.
3. Maze, Grace. (2018, March) ALGE3D: Development as an Aqueous Emergency Response Model, Presented at the Palmetto Chapter of the American Meteorological Society Mini-Technical Conference, Columbia, South Carolina.
4. Maze, Grace. (2018, December) ALGE3D: A Three-Dimensional Transport Model, Presented at the American Geophysical Union Fall Meeting, Washington DC.
5. Maze, Grace. (2019, January) Expanding ALGE3D as an aqueous emergency response model, Presented at Annual American Meteorological Society Meeting, Phoenix, Arizona.
6. Maze, Grace (2019, February) Expanding ALGE3D as an Aqueous Emergency Response Model, Invited to present at the IMAAC working group quarterly meeting, Washington DC.
7. Maze, Grace. (2019, March) Expanding ALGE3D as an Aqueous Emergency Response Model, Presented at the Palmetto Chapter of the American Meteorological Society Mini-Technical Conference, Columbia, South Carolina.

## *References*

1. M. Kummu, H. de Moel, P. J. Ward and O. Varis, "How close do we live to water? A global analysisof population distance to freshwater bodies," PloS ONE, vol. 6, no. 6, June 2011.
2. D. Strain, "A 2011 storm walloped the Bay with sediment, study says," Sea Grant Maryland, 30 July 2013.
3. R. M. Hirsch, "Flux of Nitrogen, Phosphorus, and suspended sediemnt from the Susquehanna River Basin to the Chesapeake Bay during Tropical Storm Lee, September 2011, as an indicator of the effects of reservoir sedimentation on water quality," U.S. Department of the Interior, U.S. Geological Survey, Reston, Virginia, 2012.
4. R. Bahadur and W. B. Samuels, "Modeling the fate and tansport of a chemical spill in the Elk River, West Virigina," J. Environ. Eng., vol. 141, no. 7, 2005.
5. W. B. Samuels and D. Ryan, "ICWater: Incident command tool for protecting drinking water," in ESRI Internation User Conference, 2005.
6. J. Blanton, A. Garrett, J. Bollinger, D. Hayes, L. Koffman and J. Amft, "Transport and Dispersion of a conservative tracer in coastal waters with large intertidal areas," Estuaries and Coasts, vol. 32, no. 3, 2009.
7. NOAA, "Tides and Currents," [Online]. Available: https://tidesandcurrents.noaa.gov/.
8. W. E. Dietrich, "Settling Velocity of Natural Particles," Water Resources Research, vol. 18, no. 6, pp. 1615-1626, 1982.
9. N. L. Coleman, "Effects of Suspended Sediment on the Open-Channel Velocity Distribution," Water Resources Research, pp. 1377-1384, 1986.
10. N. L. Coleman, "Velocity Profiles with Suspended Sediment," Journal of Hydraulic Research , pp. 211-229, 1981.

## *Acronyms*

| | |
|---|---|
| **FEMA** | Federal Emergency Management Agency |
| **GPU** | graphics processing unit |
| **GUI** | graphical user interface |
| **NARAC** | National Atmospheric Release Advisory Center |
| **US** | United States |
| **USGS** | United States Geological Survey |
| **NOAA** | National Oceanographic and Atmospheric Administration |

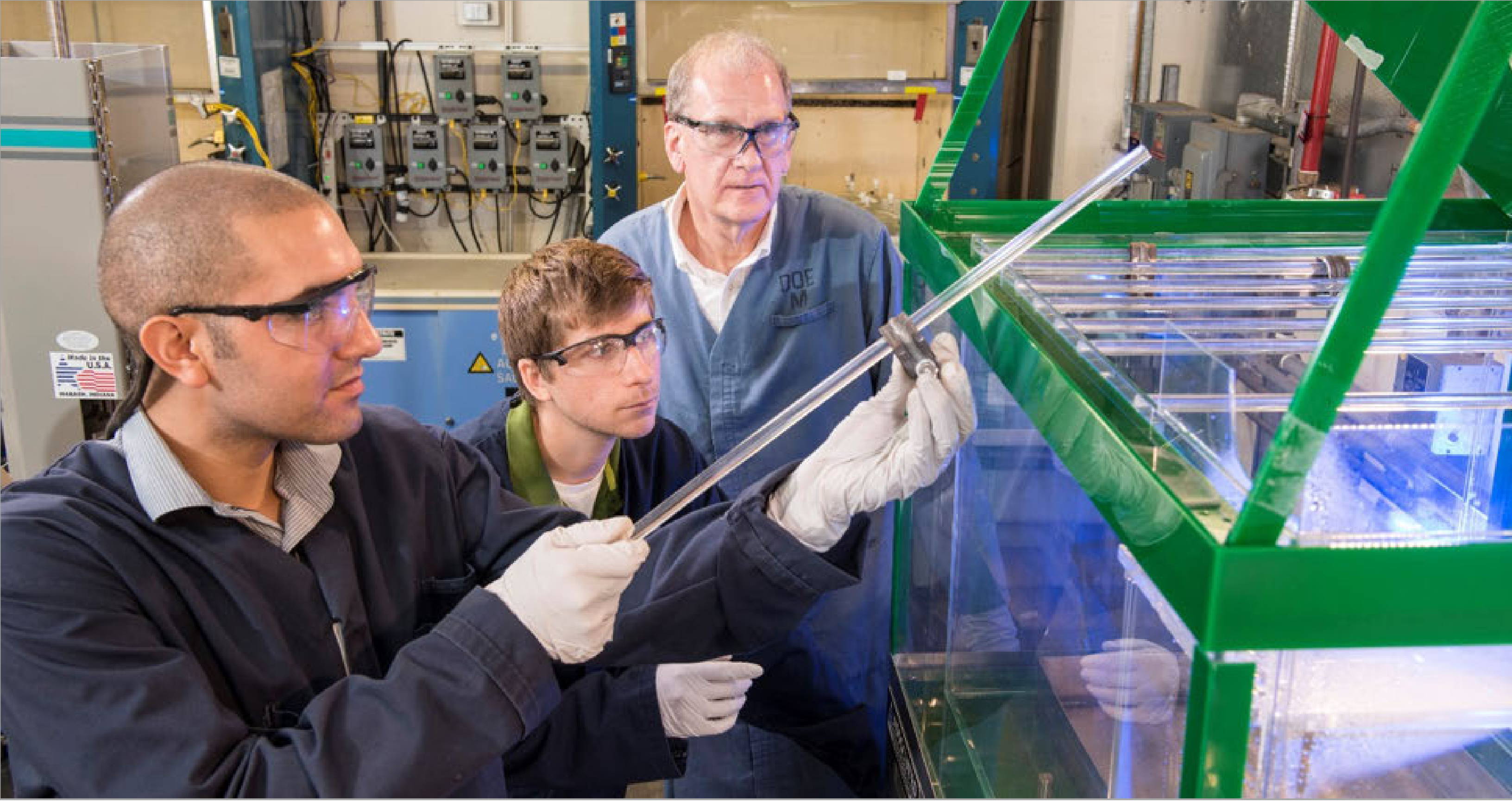

# Oxyhydroxides on Aluminum Spent Nuclear Fuel: Formation Studies and Removal Practices to Prevent Radiolytic Gas Production

**Project Team:** R.E. Fuentes (co-PI), A.L. d'Entremont (co-PI), C.G. Verst, C. Crawford, B.L. García-Díaz, R.L. Sindelar

**Collaborators:** T. Knight, M. Shalloo University of South Carolina

**Thrust Area:** Nuclear Materials Threat Reduction

**Project Start Date:** October 1, 2017

**Project End Date:** September 30, 2019

*Aluminum-clad Spent Nuclear Fuel (ASNF) forms hydrated oxides or (oxy)hydroxides on the cladding due to water exposure during irradiation and storage. This poses challenges to sealed (road-ready) dry storage due to risks of release of bound water and decomposition releasing hydrogen and/or oxygen. To assess the risks, it is necessary to understand the (oxy)hydroxides' growth/formation and morphology as the precursor state for drying and their gas generation from radiolysis. This will help determine safe (oxy)hydroxide loadings on dry-stored fuel as well as methods of removal. In this work, (oxy)hydroxides were grown on aluminum alloy substrates and the resulting layers studied for morphology and thickness; radiolysis studies were performed on powders to correlate morphology and particle size to gas generation, and drying studies were performed on powders and adherent oxide films. These experiments will be used to guide development of drying strategies for safe dry storage.*

## Objectives

- Grow thick and/or dense (oxy)hydroxide film surrogates more characteristic of those on actual ASNF for use in dehydration testing.
- Investigate thermal treatments to determine temperatures required for adsorbed water removal.
    - Perform thermal drying tests on (oxy)hydroxide powders to determine time and temperature requirements.
    - Perform thermal drying tests on adherent (oxy)hydroxide films on aluminum.

## Introduction

The aluminum cladding of research-reactor fuel undergoes general corrosion with resulting formation of adherent aluminum (oxy)hydroxide films during in-reactor and post-discharge exposure to water. These films have different crystalline structures and morphologies due to various conditions and temperatures while immersed in water (Figure 1). For extended dry storage of ASNF, (oxy)hydroxides pose challenges due to the risk of thermal or radiolytic decomposition releasing water and/or hydrogen and oxygen gases. For this study, laboratory experiments investigating formation of (oxy)hydroxides under exposure to water at various temperatures and durations were conducted. In addition, radiolytic yield of hydrogen from aluminum (oxy)hydroxide powders and thermal drying behavior of aluminum (oxy)hydroxides (in both powder and adherent film forms) were measured to identify approaches for reducing bound water on fuel cladding prior to sealed dry storage. Effective drying strategies for adherent (oxy)hydroxides on fuel cladding will improve the safety of dry storage by mitigating potential avenues for additional corrosion and/or generation of flammable gases inside the storage canister.

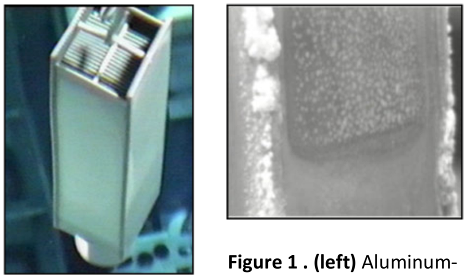

**Figure 1 . (left)** Aluminum-clad fuel assembly with intact, protective oxyhydroxide film after long-term wet storage in good-quality water; **(right)** trihydroxide deposits due additional corrosion during wet storage in poor water quality.

## Approach

The work this year continued to investigate aqueous corrosion of aluminum coupons to grow adherent (oxy)hydroxide films as surrogate oxides for drying tests, with an aim to obtain thicker and/or denser films. Changes from earlier testing included extended exposure durations (up to 16 weeks), a wider temperature range (down to room temperature for producing trihydroxides and up to 185°C, under pressure, for producing boehmite), and increased use of isothermal immersion tests after confirming no apparent differences between films formed under a heat flux versus those under isothermal conditions. Coupons were sanded with 600 grit on the target face for oxide growth in order to remove existing oxides that might impede formation of the (oxy)hydroxide.

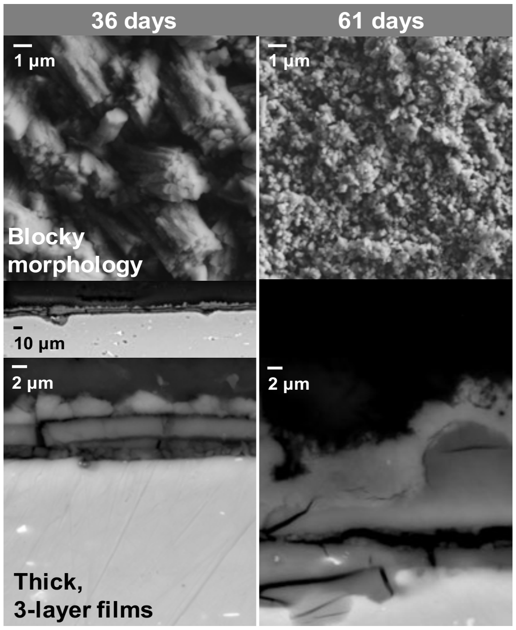

**Figure 2.** Hydroxide films formed by aqueous corrosion in room-temperature water for (left) 36 days and (right) 61 days. (Top) planview SEM, (middle and bottom) cross-section SEM.

Experiments were also conducted to investigate thermal dehydration of aluminum trihydroxides (bayerite and gibbsite) characteristic of low-temperature (< 80°C) corrosion in water and aluminum oxyhydroxide (boehmite) characteristic of high-temperature (> 80°C) corrosion in water. First, commercially produced (oxy)hydroxide powders (boehmite and gibbsite) were tested via thermogravimetric analysis (TGA) and differential scanning calorimetry (DSC). The effort aimed to identify or confirm key temperature ranges/thresholds for the thermal decomposition reactions, as well as impacts of ramp rate and hold times, for drying of isolated, high-surface-area (oxy)hydroxides. Powder tests were conducted up to 1000 °C to ensure capturing complete dehydration to alumina, and some tests were conducted with temperature holds of various temperatures and durations with the aim of isolating different phases of the drying behavior. The information gleaned from powder tests was used to guide subsequent drying tests on adherent (oxy)hydroxide films grown on aluminum alloy substrates. TGA was used to analyze small samples of the aluminum coupons with adherent (oxy)hydroxide films. The samples were tested at drying temperatures of 200, 220, 260, and 500 °C and were held at the test temperature for long durations with the aim to determine the maximum dehydration achievable at that temperature. Specimens were characterized both pre- and post-drying using X-ray diffraction (XRD) to determine the film composition and scanning electron microscopy (SEM) to determine its morphology in both planview and cross-section.

## Results/Discussion

Thick, blocky bayerite films (Figure 2) were found to form relatively rapidly on coupons in room-temperature water, more so than in 50 °C water. This was unexpected, as corrosion kinetics were expected to be accelerated by increasing water temperature. Literature sources [1] indicate that pseudoboehmite is the first phase to develop during formation of Al (oxy)hydroxides in water, and the transition point between formation of trihydroxides and boehmite is known to be near 80 °C, so it is hypothesized that the development of pseudoboehmite into the trihydroxide may occur more rapidly at temperatures further from this transition temperature. Exposure to room-temperature water for 36, 38, and 61 days produced three-layered films averaging about 8, 11, and 20 µm thick, respectively. XRD indicated that these films consisted predominantly of bayerite with some boehmite. The films produced roughly resemble those found on sampled ASNF materials stored wet in L-Basin after extended (i.e., decades) storage [2]. The 8-µm bayerite film was used for the initial drying tests.

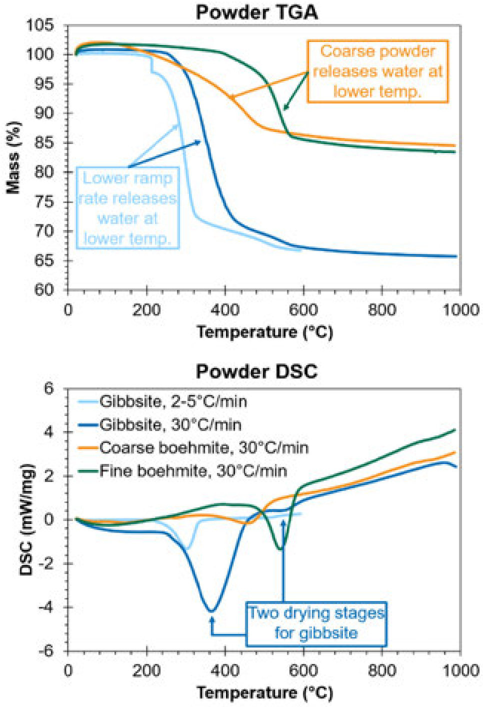

**Figure 3.** Representative TGA (top) and DSC (bottom) results for gibbsite and boehmite powders.

TGA/DSC tests of (oxy)hydroxide powders resulted in successful conversion of gibbsite powder to boehmite or alumina and of boehmite powders to alumina, depending on the maximum temperature reached. Figure 3 shows some representative TGA and DSC curves for the boehmite and gibbsite powders. At low ramp rates (≤5 °C/min), the conversion to boehmite occurred around 300 °C (210–340 °C). XRD confirmed that boehmite was the only phase detected after tests reaching 450 °C. The transition to alumina occurred around 510 °C (470–550 °C), with XRD detecting only alumina after tests reaching at least 600 °C. Boehmite powders dehydrated to alumina at about 400 °C (330–460 °C) for coarse (77-µm particle diameter) powder and about 490 °C (420–520 °C) for fine (0.7-µm particle diameter) powder. For all powders tested, the maximum percent mass loss after drying to high temperature slightly exceeded the theoretical mass loss for complete dehydration of the stoichiometric (oxy)hydroxide to alumina, which is likely attributable to physisorbed water in the powder.

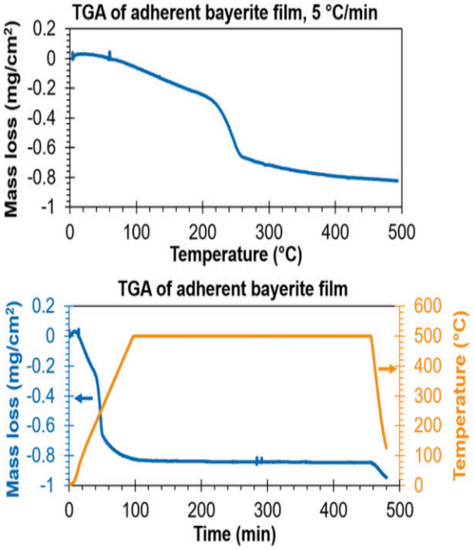

**Figure 4.** Example TGA results for ~8-µm-thick bayerite film, as a function of (top) temperature during ramp-up to 500°C and (bottom) time for the entire test.

For TGA of adherent (oxy)hydroxide films, the mass loss per unit surface area increased with increasing temperature for all temperatures tested (200, 220, 260, and 500 °C). The final mass losses per unit surface area were approximately 0.95 mg/cm$^2$ for 6 h at 500 °C, 0.84 mg/cm$^2$ for 4 h at 260 °C, 0.60 mg/cm$^2$ for 24 h at 220 °C, and 0.51 mg/cm$^2$ for 24 h at 200 °C. For a 500 °C, 6-h hold, the mass losses appeared to saturate after approximately 1 hour at temperature, suggesting full dehydration to alumina was reached. The mass losses also appeared to plateau before the end of the hold for 200 °C test and decreased to a very low rate for the other temperatures, suggesting that these values were likely close to the maximum achievable mass loss at that temperature. An example of the TGA results for a 500 °C test is shown in Figure 4. Here, the most rapid mass loss occurred within the range between about 220 and 250 °C, providing further evidence that temperatures ≤220 °C may be inherently too low to release much of the bound water. Drying resulted in a dramatic change in film morphology. Figure 5 shows planview SEM of post-drying samples for the same, originally ~8-µm-thick bayerite film shown in Figure 2. The initially continuous film cracked into sections on the order of 50 µm square and partially delaminated, with the outermost layer of the film completely flaked off in some regions. The layer exposed under the spalled oxide also displayed prominent cracking, with spacing on the order of 10 µm, but this surface layer appeared to remain completely adhered to the aluminum substrate.

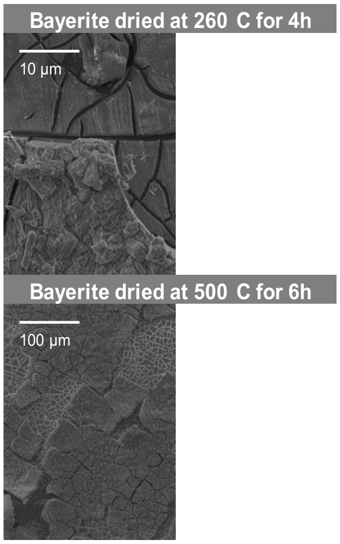

**Figure 5.** Planview SEM showing post-drying morphology of ~8-µm-thick bayerite films after TGA at (top) 260 °C and (bottom) 500 °C. Prominent cracking of the film occurred, and some of the oxide spalled off of the surface.

## FY2019 Accomplishments

- Thick (up to ~20 micron average), blocky trihydroxide films were produced for use in drying tests via room-temperature water exposure.
- Drying tests have been performed using simultaneous thermogravimetric analysis (TGA) and differential scanning calorimetry (DSC) on gibbsite and boehmite powders to identify or confirm key temperature ranges/thresholds for the thermal decomposition reactions and impacts of ramp rate and hold times for drying of isolated, high-surface-area (oxy)hydroxides. The results were used to inform drying of adherent (oxy)hydroxide films.
- Drying tests of adherent (oxy)hydroxide films have been performed. Small pieces of the aluminum specimens with adherent (oxy)hydroxides were cut and studied under TGA. Scanning electron microscopy (SEM) and X-ray diffraction (XRD) were used to examine the morphology and composition, respectively, both pre- and post-drying.

## Future Directions

- Radiolysis testing of boehmite films formed by thermal dehydration of trihydroxide films should be conducted to verify whether their gas generation is comparable to that of boehmite films formed directly from aluminum exposure in water at temperatures over 80 °C.
- Conclusions from drying behavior (thermal decomposition) and radiolytic yield obtained from investigations of surrogate oxides should be validated using samples cut from actual ASNF exposed to reactor conditions and wet storage (e.g., those sampled in Ref. [2]).

## Publications/Presentations

1. Anna L. d'Entremont, Roderick E. Fuentes, Luke C. Olson, Kathryn E. Metzger, Robert L. Sindelar, Oxide Growth and Validation for Aluminum Research Reactor Fuel, Proceedings of Waste Management Symposia 2019, #19422, Phoenix, Arizona. (Conference paper)
2. Anna L. d'Entremont, Roderick E. Fuentes, Luke C. Olson, Kathryn E. Metzger, Robert L. Sindelar, Oxide Growth and Validation for Aluminum Research Reactor Fuel, WM2019 Conference March 3-7, Phoenix, Arizona. (Contributed presentation)
3. Anna L. d'Entremont, Roderick E. Fuentes, Matthew G. Shalloo, Travis W. Knight, Robert L. Sindelar, Thermal Dehydration of Aluminum (Oxy)hydroxides on Fuel Cladding Material, Waste Management Symposia 2020, Phoenix, Arizona (Submitted for paper and presentation).

## References

1. K. Wefers and C. Misra, "Oxides and hydroxides of aluminum," Alcoa Laboratories Pittsburgh, PA Alcoa Technical Paper #19, 1987.
2. L. C. Olson, C. Verst, A. L. d'Entremont, R. E. Fuentes, and R. L. Sindelar, "Characterization of Oxide Films on Aluminum Materials following Reactor Exposure and Wet-Storage in the SRS L-Basin," Savannah River National Laboratory SRNL-STI-2019-00058, 2019.

## Acronyms

| | |
|---|---|
| **ASNF** | Aluminum Spent Nuclear Fuel |
| **DSC** | Differential Scanning Calorimetry |
| **NMM** | Nuclear Materials Management |
| **SEM** | Scanning Electron Microscopy |
| **STA** | Simultaneous Thermal Analyzer |
| **TGA** | Thermogravimetric Analysis |
| **XRD** | X-ray Diffraction |

## Total Number of Researchers

One Grad Student, Matt Shalloo who performed work at offsite at Univ. of SC

# An Improved Technique for Characterization of Actinide Isotopic Composition

**Project Team:** R.B. Thomas (Primary), M.A. Bernard, D. Diprete

**Thrust Area:** Nuclear Materials Threat Reduction

**Project Start Date:** October 1, 2018

**Project End Date:** September 30, 2019

*The focus of this project was to develop a tool for high resolution characterization of heavy actinides (e.g. americium, neptunium, and curium). This project supports the SRNL core competency for nuclear material detection, characterization and assessment. It also supports nuclear materials management programs for boutique processing missions, as a method by which to assure the customer is getting a quality product, or to characterize secondary products to make them more attractive to potential customers. These techniques have broader applications with the potential to support outside projects. Current methods for characterization of heavy actinides use a combination of inductively coupled plasma mass spectrometry and counting methods. These methods can have uncertainties ranging from 5-7%. The use of thermal ionization mass spectrometry could reduce these uncertainties for isotopic measurements and could contribute to the analytical methods offered by SRNL for the characterization of actinides.*

## Objectives

- Analyze/characterize Np analysis.
- Analyze/characterize Am analysis, determine uncertainty of measurement related to the precision of the measurement.

## Introduction

The analysis of actinides, other than U and Pu, have become of more interest as spent nuclear fuels are processed, recycled, and sent to waste. Current methods for analyzing these actinides, using a combination of counting methods and inductively coupled plasma mass spectrometry have relatively large uncertainties (5-7% at the 95% confidence interval). While these uncertainties are currently suitable for waste calculations and rough characterizations, there are cases where an improved technique for isotopic characterization would be advantageous. Thermal ionization mass spectrometry (TIMS) is a technique that is capable of achieving uncertainties of less than 0.5% at the 95% confidence interval.[1] SRNL has expertise in the analysis of U and Pu by TIMS. Uncertainties for U and Pu measurements by TIMS can be as low as 0.03% at the 95% confidence interval depending on the quality of reference materials used for traceability.

The majority of publications relating to the analysis of americium, curium, and neptunium are related to environmental samples, counting methods and inductively coupled plasma mass spectrometry (ICPMS).[1-5] Nuclear material samples, for example, process samples, accountability samples, waste samples, or nuclear criticality/safety samples have unique challenges for analysis, including the need for facilities that can handle all kinds of radioactive samples. For ICPMS analysis, isobaric compounds or isotopes can interfere with isotopes of interest (e.g. $^{241}$Pu and $^{241}$Am, $^{248}$Cm and $^{232}$Th$^{16}$O). Counting methods can be limited by the activity of the isotopes of interest and overlapping energies. TIMS is a mass spectrometry method that has fewer interferences than ICPMS and has a higher resolution for separation of isotopes.

As used nuclear fuels are processed, recycled, and sent to waste, there is an increased interest in the analysis of actinides, other than U and Pu. There will be a need for reference materials, as well as the capability to analyze samples containing these elements in order to meet varying needs of the nuclear community. The addition of TIMS analysis to counting techniques and ICPMS techniques would give SRNL a core analytical technique with lower uncertainties than current techniques which would be applicable to reference materials, safeguards and nuclear forensics as well as nuclear material accountability, nuclear safety and waste measurements.

## Approach

The objective of this research project is to develop an analytical tool that can be used to accurately and precisely characterize the isotopic composition of heavy-actinides, such as americium, curium, neptunium and californium by thermal ionization mass spectrometry (TIMS).

Some of the questions that were asked as part of this research are:

- Can each element be analyzed by TIMS?
- What sample size is required?
- What is the estimated uncertainty of the analysis?
- What are the primary sources of uncertainty?
- Are there limitations to the use of TIMS for isotopic characterization for each element?

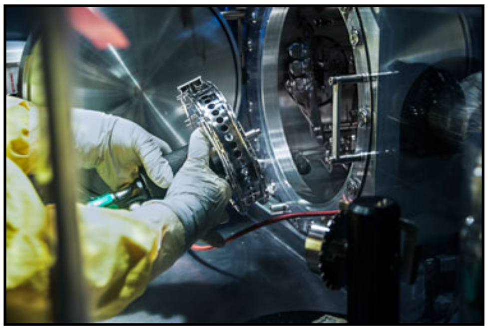

**Figure 1.** Sample wheel as it is loaded into the ion source for the TRITON™ thermal ionization mass spectrometer.

Test materials were made from legacy materials stored onsite or, in one case, a reference material used for counting techniques. All analyses were performed on SRNL Analytical Laboratories' TRITON™ thermal ionization mass spectrometer (Figure 1), using the total evaporation method to minimize effects of mass fractionation.

## Results/Discussion

### *Neptunium analysis.*

The Neptunium sample consisted of a legacy F-canyon material that was composed predominantly of $^{237}$Np. A method was developed for analyzing the neptunium by the total evaporation measurement. A limitation of TIMS is that it is optimized for the measurement of isotopic ratios, making it difficult to quantify the measurement at this point in time. Further work will be needed if SRNL acquires a TIMS with a different configuration (so that a larger isotopic ratio range can be analyzed) or if there are samples that contain multiple Np isotopes in quantities sufficient enough to be analyzed by the detectors on the mass spectrometer. This sample did contain significant organic material (assumed to be remnants of processing) and some evidence of U and Pu, which are assumed to be potential contamination (Figure 2). These observations emphasized the need for purification of samples prior to analysis of samples by sensitive methods like TIMS, and also the need to practice contamination control, since small amounts of contamination can be detected.

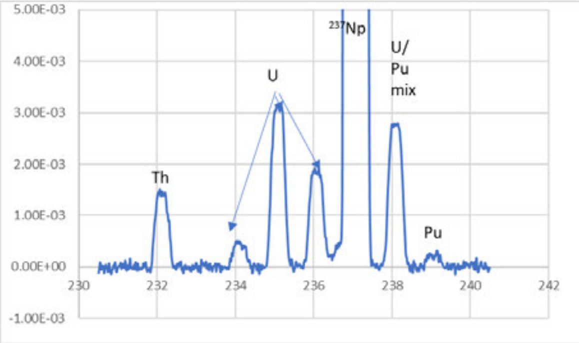

**Figure 2.** Mass scan for Np sample, showing other elements (contamination) in the sample. The $^{235}$U (largest non-Np peak) makes up ~0.15% of the sample.

### *Americium analysis.*

The first sample used to characterize the americium analysis was fairly pure $^{243}$Am. In order to have a two-isotope material, the legacy material was mixed with a $^{241}$Am gamma-counting standard that was available on-site to create a material with a $^{241}$Am/$^{243}$Am of about 0.0011. The method random uncertainty is comparable to the 2010 international target value for depleted uranium ($^{235}$U/$^{238}$U < 0.007%)[6], and the day-to-day variation is insignificant compared to the random uncertainty (Figure 3). A determination of systematic uncertainty was limited by a lack of low-uncertainty certified reference materials.

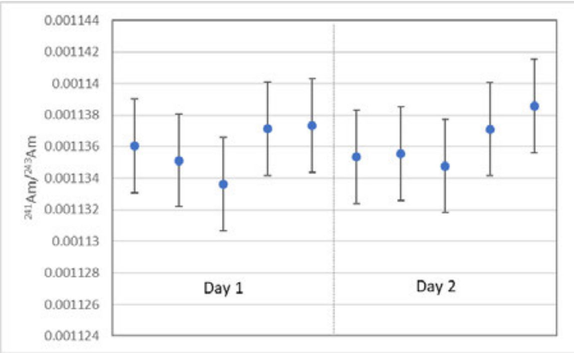

**Figure 3.** $^{241}$Am/$^{243}$Am measurements over two days.

## FY2019 Accomplishments

- Americium measurements using the total evaporation method were developed. Preliminary results exhibit a random uncertainty component of less than 0.30 percent at the 95% confidence interval and a day to day variance of less than 0.05% (insignificant compared to the uncertainty of the measurement).
- A similar method for neptunium was developed. Neptunium runs at higher temperatures than americium or plutonium. Since the sample contained only one isotope of neptunium, we were unable to determine the random uncertainty for the analysis. However, the method has been characterized so that when there is a material with two isotopes of neptunium SRNL will have a method that can be used.

## Future Directions

- Develop working reference materials for americium designed for nuclear material measurements using legacy materials available on-site.
- Finalize neptunium measurements with a two-isotope material or create and characterize such a material by mixing samples.
- Develop analytical methods for other actinide elements, such as curium or californium.

### References

1. Aggarwal, SK (2018) *A Review on the Mass Spectrometric Studies of Americium: Present Status and Future Perspective*; Mass Spec Reviews 37:43-56.
2. Becker, JS (2003) Review: Mass spectrometry of long-lived radionuclides; Spectrochimica Acta Part B 58:1757-1784.
3. Chartier et al. (1999) Determination of Am and Cm in spent nuclear fuels by isotope dilution inductively coupled plasma mass spectrometry and isotope dilution thermal ionization mass spectrometry after separation by high-performance liquid chromatography, Fresenius J Anal. Chem 364: 320-327.
4. Vajda, N and Kim, C-K (2011) Determination of Transuranium Isotopes (Pu, Np, Am) by Radiometric Techniques: A Review of Analytical Methodology; Anal. Chem. 83:4688-4719.
5. Goldstein et al (2018) Sequential chemical separations and multiple ion counting ICP-MS for $^{241}$Pu–$^{241}$Am–$^{237}$Np dating of environmental collections on a single aliquot; J Radioanal Nucl Chem 318: 695-701.
6. Zhao et al. (2010*) International Target Values 2010 for Measurement Uncertainties in Safeguarding Nuclear Materials*; IAEA STR-368.

### Acronyms

| | |
|---|---|
| **TIMS** | Thermal Ionization Mass Spectrometry |
| **ICPMS** | Inductively Coupled Plasma Mass Spectrometry |

# Process Image Analysis using Big Data, Machine Learning, and Computer Vision

**Project Team:** Bruce Hardy (PI), Anna d'Entremont, Lindsay Roy, Michael Martinez-Rodriguez, Brenda García-Díaz

Subcontractor: **Jason Bakos, Taylor Clingenpeel, Phil Moore, Ben Torkian, R. Doran (USC)**, A.J. Medfort (GT)

**Thrust Area:** Nuclear Materials Threat Reduction

**Project Start Date:** October 1, 2018

**Project End Date:** September 30, 2020

*The development of algorithms for machine learning and data analysis for the 3013 MIS corrosion surveillance program is a collaborative effort by SRNL, USC and GT. For corrosion detection, LCM image data is extracted from large binary files, with software written to convert the data to physical attributes (i.e., height, color and grayscale values; all as functions of a location in a plane projection). The user interface for the software permits selective downloading of binary data and interrogation of attributes. User input thresholds are used to flag attributes of interest. Machine learning algorithms, developed for this application, are used to determine whether the features are the result of corrosion. To address the fundamental mechanisms of corrosion, machine learning algorithms are being developed to derive interatomic potential force-fields from ab-initio DFT calculations. The goal is to apply molecular modeling on a large enough scale to guide the design of resistant materials.*

## Objectives

- Develop machine learning (ML) methods, based on computer vision, to analyze imaging data for corrosion
- Develop machine learning methods for molecular modeling of corrosion processes
- Identify 3013 data sets, and numerical methods, suitable for near-term development
- Determine preliminary set of attributes for training supervised ML algorithms
- Assemble training sets, train and test ML algorithms
- Classify features by size, quantity, density, and location
- Utilize computer vision to reduce amount of data needing manual analysis
- Identify additional data sets within SRNL that can be analyzed using the methodologies developed as part of this project
- Begin development of ML methodology for obtaining adaptive force-fields from ab-initio molecular models (MM) for corrosion

## Introduction

Halides contained in Pu-bearing material have been found and produce corrosion in the Inner Can Closure Weld Region (ICCWR) for the 3013 canister system used throughout the DOE complex. Inspections using a laser confocal microscope (LCM) produce immense amounts of image data: approximately 6000 images per can, having 786,432 pixels per image, with 8 layers of data for each pixel. There is currently a 5-year backlog of images, with approximately 5 canisters/year, that must be evaluated. Simplistic computer-aided image analysis can flag parameters, such as pit depth and cracking to guide manual examinations for corrosion. However, while this approach greatly improves the efficiency of the examination process compared to unaided manual screening, it is still excessively time consuming. A more sophisticated approach is to assess the data using machine learning (ML) algorithms to identify corrosion without manual intervention. As a complement to corrosion detection, molecular level analyses can yield a fundamental understanding of corrosion occurring in the ICCWR and guide the design of corrosion resistant materials, welding processes, and coatings. These 2 efforts comprise the research in this LDRD.

This 2-year LDRD project has 2 concurrent objectives: The first is the development of machine learning algorithms to identify the presence of corrosion from a very large set of images generated by LCM scanning of 3013 canisters used to store Pu oxides. This portion of the LDRD constitutes image analysis of a metal surface for the presence of corrosion. The image processing algorithms developed for this project will provide a suitable basis for analysis of other types of corrosion data, which can be produced in vast quantities using modern devices.

The second component of the LDRD consists of the development of machine learning algorithms that obtain molecular mechanics force-fields from ab-initio Density Functional Theory (DFT) calculations for corrosive attack by chlorides on 304L or 316L stainless steel. The goal of this latter component is to determine means for mitigating corrosion on a fundamental level, including coatings, welding methods, metal composition, etc. Force-field modeling is necessary for this endeavor because the incipience and progression of corrosion is governed by molecular structures, grain boundaries, dislocations and surface structures represented by large numbers of atoms. Although DFT calculations are extremely adept at describing molecular scale processes, they are computationally expensive making them ill-suited for calculations of more than several hundred atoms, especially for the repeated applications inherent in material design. Fortunately, force-field methods provide an avenue for viable molecular-scale calculations involving the numbers of atoms involved in corrosion processes. The accuracy of the force-field calculations depends strongly on the accuracy of the force-field model, which is extremely difficult and time-consuming to derive from either data or ab-initio calculations. The use of machine learning algorithms has the potential to make the calculation of force-fields much more efficient. However, the application of machine learning to force-field derivation has not been explored significantly for corrosion processes and, if shown viable, would have wide-ranging impact on design of corrosion-resistant materials and on the mitigation of corrosion in existing process systems.

## Approach

### *First Component – Image Analysis*

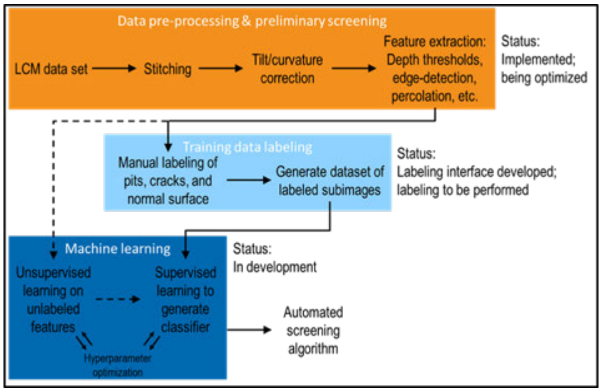

**Figure 1.** Data processing and implementation of machine learning

Corrosion is strongly, but not exclusively, associated with surface pitting and cracking, coloration, along with shapes and patterns of surface features. Conversely, not all pits and surface lesions are the result of corrosion: some are artifacts of fabrication, impact, scoring or other non-corrosion events. Corrosion is identified via the combined properties of pit depth, area, edge contour, color and clustering. Software was developed to extract these features from large binary files generated by the LCM. The individual images, which collectively span the ICCWR are stitched together and corrected to eliminate the effect of curvature on measurement of the local height. Various methods are applied to the data to best relate it to presence of corrosion. Mathematical operations invoked for computer vision and image interpretation include, but are not limited to: labeling, gradient methods, statistical characterization, correlations and filters.[1,2] The processed data is then input to ML algorithms; labeled data for training, and afterwards data for evaluation by the trained ML algorithm. The process is shown schematically in Figure 1.

### *Second Component – ML based FF Derivation from DFT Calculations*

The objective of second part of the LDRD project is to advance the fundamental understanding of corrosion by developing novel methods to simulate the complex chemistry and physics through coupling quantum mechanical and empirical force field methods. In corrosion science, sophisticated multiscale models beginning at the ab-initio level provide mechanistic insight into metal-environment interactions resulting in general corrosion, intergranular corrosion, and pitting corrosion.[3] Specifically, this research focuses on designing machine-learning algorithms to develop and train adaptive force fields for the study and prediction of corrosion behavior, specifically the metal-environment interface.[4] Accurately calculating the parameters for a robust force field, however, is a much more complicated than a simple regression fit, requiring more sophisticated data analytics.[5-7] Further, the functional form of standard force fields is often insufficient to capture the complex physics of a reactive interface, especially in the case of the complex electronic structure of magnetic metal oxides. While atomistic modeling techniques are well suited to study the chemical reactions occurring at the interface between a material and its environment, modeling corrosion is computationally slow because the models must be constructed to resolve both relevant reaction mechanisms and mass transport processes. By developing machine learning methods to obtain quantitative structure-activity relationships considering both molecular and bulk boundary conditions, researchers will be able to significantly advance knowledge by exploring more combinatorial spaces and nonlinear processes which are difficult using traditional approaches.

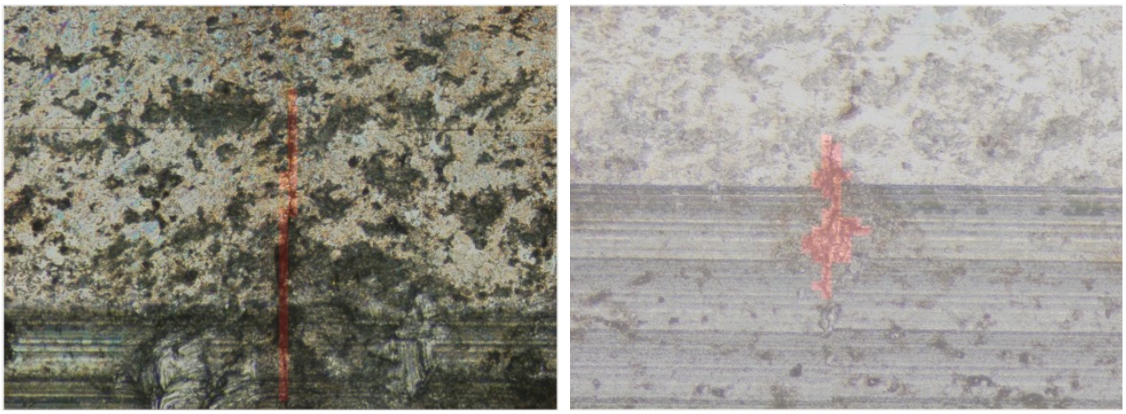

"Bellatrix": 2x2 stitch consisting of 1407x1930 pixels including mosaic overlap. Defect region highlighted in red, comprising 1.4% of total area.

**"Acrux":** 2x2 stitch consisting of 1407x1925 pixels including mosaic overlap. Defect region highlighted in red, comprising 1.7% of total area.

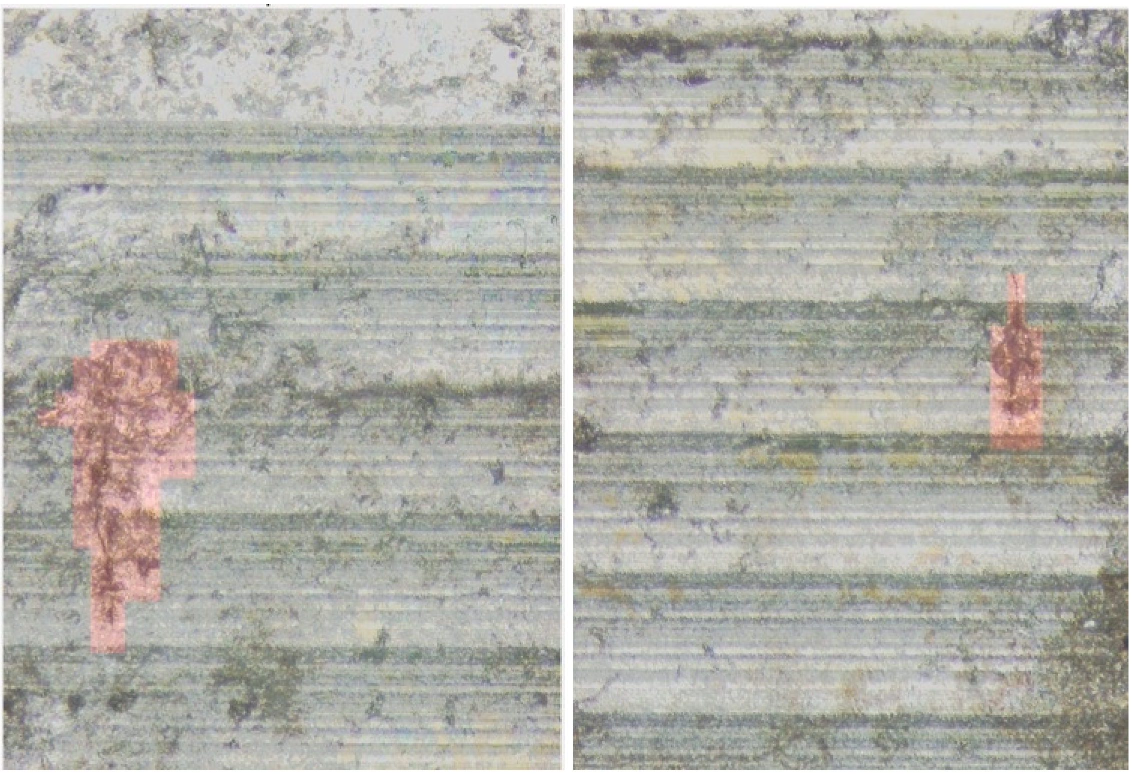

**"Cursa Major":** 2x1 stitch consisting of 1407x1024 pixels including mosaic overlap. Defect region highlighted in red, comprising 6.8% of total area**.**

**"Cursa Minor":** 1407x1024 pixels including mosaic overlap. Defect region highlighted in red, comprising 1.7% of total area.

**Figure 2.** Training Samples

## Results/Discussion

LCM image data taken for the MIS program was reviewed to obtain samples containing cracks, pits and other features characteristic of corrosion. The low incidence of corrosion in the actual ICCWR samples made it necessary to obtain more data for proper training of the ML algorithms that were developed for this program. Corrosion data from the 3013 canisters was therefore augmented with LCM images of coupons that were exposed to boiling MgCl. To provide an efficient means for handling large amounts of binary image data a GUI was developed to serve as an interface with the data files, manipulate and group images, label features for training the ML algorithm, group features with user defined thresholds, correct for sample tilt and curvature, and stitch images. The last of the GUI capabilities is extremely important as features of significance, especially cracks, can extend across many images or lie at the interface between them. Moreover, it was found that larger views, consisting of a composite of many images, are necessary for ML crack detection.

Cracks, pits and color patterns are all associated in various forms with corrosion. Pits can readily be detected using height data thresholds. Cracks, particularly "hairline" cracks do not always have a definitive height signature. Rather, crack identification is a combination of grayscale image intensity (pixel value) and height data. Initially, it was hoped that standard edge detection methods could be used with pixel values to extract crack edges. Methods considered included: erosion and dilation, blurring, Fourier and Gaussian filters, and gradient methods. Unfortunately, other surface features combined to create background noise that was similar in frequency to that associated with crack edges. To overcome this problem, Deep Neural Network (DNN) methods were developed and applied to identify cracks. Early in the development of this approach the training of the DNN algorithms suffered due to the small amount of crack data available. Training data was expanded by using synthetic images and will be further expanded using coupon data. After increasing the amount of labeled training data and adjusting the DNN algorithms, selection and recall for the crack identification was significantly improved. The most promising results were achieved by training classifiers using a training set consisting of four portions of scans that each contain one known defect. Each of these was decomposed into fixed-sized blocks, with each block that overlaps any part of a known defect region manually labeled as "defect" and all other blocks labeled as "normal". The blocks labeled as "defect" comprise only a small portion of the total number of blocks. Additional examples of blocks containing defects are generated using data augmentation techniques. The resulting labeled data is used to train a convolutional neural network classifier. As shown in Fig. 2, the scans surrounding four known crack-like defects, named "Bellatrix," "Acrux," "Cursa Major," and "Cursa Minor", serve as the training data. "Bellatrix" and "Acrux" are comprised of 2x2 data file mosaics, while "Cursa Major" and "Cursa Minor" are comprised of 2x1 mosaics. The defect areas are highlighted in red. Prior results indicate that classification performance improves when there are significantly more blocks labeled as "defect" than as "normal". For this, we apply an augmentation approach in which we apply small 2D spatial offsets to all blocks labeled as "defect" and add the resulting blocks back into the data set (except for those generated blocks where the offset places it outside the image boundary or no longer covering part of the original defect region). A 5-channel convolutional neural network was used to classify blocks as "defect" or "normal". The input channels include the red, green, and blue colors from the LCM "peak" image, as well as the height data after correcting for curvature, and laser intensity. Feature data for pits cracks and color will be used in a higher level ML algorithm for association with corrosion.

Development of FF methods for MD simulation began with DFT and MD training of neural networks using Gaussian descriptors to construct symmetry invariant features into the NN. Benchmark calculations included 100 DFT configurations with a target accuracy energy of 1 meV/atom and MD simulations utilizing a canonical ensemble for 500 MD steps at 300K with 0.5 fs integration timestep. The training set included a pristine Fe 111 surface examining the water/Fe interface. The validation set included 5-6 water layers with the Fe surface. The results indicate that even this relatively large number of DFT calculations is insufficient to capture the wide range of environments that will occur in a corrosion process, and the challenging electronic structure of the magnetic metal/water interface makes generating substantially larger datasets intractable. For this reason, a new strategy of "transfer learning" is being pursued. In this approach, inexpensive MD methods (EAM, TIP3P) are utilized to generate a large data set (10-100k images). These images are used to pre-train a DNN capable of reproducing the lower-level MD theory. Some intermediate layers of the network are then "frozen" by holding their weights constant, and the remaining layers will be re-trained to reproduce the DFT data. This approach is expected to drastically reduce the amount of DFT data needed to obtain accurate predictions, and also lead to force fields that are reliable even outside the training data regime.

## FY2019 Accomplishments

**Developed a pre-processing GUI using the Matlab© user interface**

- Easily used by investigators
- Reads LCM binary data in native vk4 format
- Stitches images, tested with 300 but can do many more
- Corrected jump discontinuity between images
- Corrected for tilt and curvature to get accurate local surface height data
- Can simultaneously view multiple features corresponding to different LCM channels
- Developed feature selection and labeling in the GUI
- Reduced time to identify features having significant thresholds by factor of 10-18

**Developed methods for processing data for machine learning algorithms**

- Improved edge detection for cracks and pits
- Developed preliminary machine learning algorithms for crack detection
- Algorithms for generating labeled data for training sets

**Generating baseline metal lattice configurations for FF training set**

- Calculated Fe/$H_2O$ interfaces using DFT and MD
- Developed preliminary machine learning algorithms for FF generation

## Future Directions

- L-basin corrosion analysis.
- Proposals for more complete development of ML applications for FF derivation form DFT calculations.
- Extension of image analysis to inclusions in articles produced by additive manufacturing.
- Application of AI methods to data analysis, particularly for corrosion and material degradation.
- Development of surrogate molecular models having reduced complexity but retaining a high degree of accuracy.
- Guided material synthesis based on empirical data with imposed physical constraints.
- Advanced process control, invoking reachability theory and fault tolerance.
- Test FF algorithm with validation set.
- Incorporate iron/iron oxide defects with different water phases.
- Replace water with halides for corrosion and reactivity.

### Publications/Presentations

1. Presented LDRD results at the 2019 AIChE spring meeting. Published associated paper in the Proceedings: 2019 AIChE Spring Meeting and 15th Global Congress on Process Safety.
2. Publication in progress on application of machine learning and edge detection methods in the image analysis for identification and interpretation of cracks, pits and other features related to corrosion.
3. Publication in progress for DFT baseline calculations for training supervised ML algorithm applied to derivation of FF's.

### References

1. Ian Goodfellow, Yoshua Bengio, and Aaron Courville. Deep Learning. MIT Press, Cambridge MA (2016)
2. Aurélien Géron. Hands-On Machine Learning with Scikit-Learn &Tensorflow. O'Reilly, Sebastapol, CA (10/12/2018).
3. Gunasegaram, D. R.; et al., Int. Mater. Rev. 2014, 59, 84.
4. Ghosh, S.; Suryanarayana, P. Comput. Phys. Commun. 2017, 216, 109.
5. Roy, L. E.; Jakubikova, E.; Guthrie, M. G.; Batista, E. R. J. Phys. Chem. A 2009, 113, 6745.
6. Joyce, J. J.; et al., Mater. Res. Soc. Symp. Proc. 2010, 1264, Z09-04.
7. Li, W.; Ando, Y. Physical Chemistry Chemical Physics 2018, 20, 30006.

### Acronyms

| | |
|---|---|
| **AI** | Artificial Intelligence |
| **DNN** | Deep Neural Network |
| **DOE** | Department of Energy |
| **DFT** | Density Functional Theory |
| **EAM** | Embedded Atom Model |
| **FF** | Molecular mechanics Force-Field |
| **GT** | Georgia Institute of Technology, Atlanta, GA |
| **ICCWR** | Inner Can Closure Weld Region |
| **LCM** | Laser Confocal Microscope |
| **MD** | Molecular Dynamics |
| **MIS** | Material Identification and Surveillance program |
| **ML** | Machine Learning |
| **MM** | Molecular Models |
| **NN** | Neural Network |

### Number of Post-Doctoral and Student Researchers

One – Post-doc at GT

Two – Undergrad Students at USC

One – Grad student at GT

One – MSIPP student at SRNL

# Collaboration with United States Army Cyber School (USACyS) For Signal Manipulation

**Project Team:** David Weir (Primary), Robert Barnett, Jon Dollan, Davis Shull

**Thrust Area**: Nuclear Materials Threat Reduction

**Project Start Date:** October 1, 2018

**Project End Date:** September 30, 2020

*Savannah River National Laboratory has been investing into its cybersecurity capabilities over the last few years. Cybersecurity has been a rapidly growing area for the CSRA in general and has included the consolidation of Cyber and Electronic Warfare units at Fort Gordon. This consolidation has been driven by the convergence of cyberwarfare and electronic warfare as the technologies behind both fields unify. This convergence, investment by SRNL into cybersecurity for critical infrastructure, and the desire for collaboration between the Army and SRNL has resulted in an opportunity for SRNL to develop R&D capabilities in electronic warfare that will complement SRNL's cybersecurity efforts. Discussions between SRNL and the U.S. Army Cyber School (USACyS) has identified a general gap in electronic warfare capability in which both entities could contribute to solve.*

## Objectives

- Meet with USACyS and determine methods of collaboration
- Sign a Memorandum of Understanding between SRNL and USACyS
- Procure necessary tools/equipment
- Bench test methods of signal manipulation

## Introduction

The Central Savannah River Area (CSRA) has seen a significant increase in investment into cybersecurity over the last few years. Fort Gordon has been designated as the location that the Army will be co-locating its Army Cyber School, Operations group, and Electronic Warfare groups. SRNL is in the process of investing into developing capabilities and personnel who can tackle high level R&D projects in cybersecurity. The lab's focus has been industrial control system (ICS) security, which more broadly is part of critical infrastructure. This area is of interest to the Army, as critical infrastructure is important for national defense, but also because electronic warfare techniques are becoming increasingly applicable to cyber-attacks on ICS as these systems become more dependent on advanced electronics and communication systems. The proximity of SRNL and Fort Gordon, and mutual interests in national security, inevitably resulted in dialogue between the two entities.

In FY19 a Memorandum of Understanding (MOU) was signed between USACyS and SRNL that will pave the way for personnel exchange that will be necessary for future collaborative work. The SRNL team also built up capabilities with software defined radios, refining the skills needed for bit-level manipulation.

## Approach

The technical approach for this project began with a series of planning meetings with USACyS to determine personnel appropriate for this project. This transitioned into meetings and tours to discuss the technologies in use and the current gaps in capabilities. An MOU was signed and an internship request was issued to USACyS. Bench-test equipment has been procured with guidance from USACyS. Lab space was also established where testing and evaluation of the hardware can occur.

Simulated industrial control systems developed by SRNL R&D Engineering (R&DE) will be used as a signal generation test bed. Personnel from USACyS will work with the lab team to identify signals of interest and develop a tool for bit-level manipulation of that signal. That tool will then be tested on the simulated systems.

**Figure 1.** A new and fruitful relationship between SRNL and USACyS.

## Results/Discussion

The project has contributed heavily toward the signing of an MOU between USACyS and SRNL. The team has been training on the new software defined radios in preparation for the intern from Fort Gordon. This project will be taking advantage of the new ICS simulation capabilities being developed by the R&DE department.

## FY2019 Accomplishments

- An MOU has been signed between USACyS and SRNL
    - This LDRD contributed heavily to this accomplishment.
    - The MOU has provisions specifically for collaborative opportunities.
    - USACyS is processing paperwork to have a student or instructor placed at SRNL for the purpose of collaborating on this LDRD.
    - SRNL has been invited to exercises and collaborative events supporting Cyber Initiatives.
- Software Defined Radios and Target Equipment have been purchased; lab space established.

## Future Directions

- Development of this initial prototype will open avenues for continued development of the technology and its capabilities. Further funding would be based on DoD interest in developing and supporting this technology.
- Collaboration with USACyS in exercises to demonstrate capability and evaluate equipment.
    - Training exchanges, and long-term research positions from Fort Gordon Cyber Officers.

### *Publications/Presentations*

Several presentations have been given to the Fort Gordon USACyS team and faculty as well as tours of SRNL facilities in the process of developing the MOU and working towards future collaborative opportunities. It was also briefed to the other commands present at Fort Gordon (Futures, Intelligence, Training, and Cyber) as well as in briefs to DHS, NNSA, and other DoD agencies.

### *Acronyms*

| | |
|---|---|
| **CSRA** | Central Savannah River Area |
| **ICS** | Industrial Control System |
| **MOU** | Memorandum of Agreement |
| **R&DE** | Research and Development Engineering |
| **SDR** | Software Defined Radio |
| **SOI** | Signal of Interest |
| **USACyS** | United States Army Cyber School |

# Development of Novel Solid-State Storage System for Plutonium Oxide Using Excess DOE Nickel

**Project Team:** P.S. Korinko, J. Bobbitt, Jr., A. Washington, T. Hubbard

**Thrust Area**: Nuclear Materials Threat Reduction

**Project Start Date:** October 1, 2018

**Project End Date:** September 30, 2020

*The objective of this project is to develop an alternative method for dispositioning plutonium oxide by dispersing it into a refractory metal matrix at a loading of 5 weight percent. This level of dispersion makes the waste form a level D attractiveness. The initial powder and powder blends were characterized using a newly acquired Malvern Morphologi 4. This instrument will facilitate basic understanding of the particle to particle interactions as well as providing information in determining how the particles interact with the electron beam. These interactions will be determined by characterizing the powder blends before and after processing in the Arcam A2X electron beam powder bed fusion equipment. When printed, the waste form may contain identifying marks for traceability until it is containerized. It will also be characterized to ensure that it meets the requirements for a special waste form.*

## Objectives

- Procure particle analysis tools to characterize the starting powders
- Procure nickel and hafnium oxide powders in the appropriate size fraction for using in the Arcam A2X electron beam powder bed fusion (E-PBF) system
- Characterize powder blends prior to processing them in the Arcam A2X
- Characterize the powders after processing in the A2X
- Develop the process parameters for consolidating the nickel – hafnia powders and develop the understanding of the electron beam / particle interactions on consolidation

## Introduction

This project advances the state of electron beam and nickel and hafnia beam interactions as it works to consolidate the ceramic metallic (cermet) composite powder blend. There has been little work published on the capability of producing cermets using electron beam melting (EBM) and this effort was groundbreaking for process development.

This project supports the disposition of plutonium oxide with a higher volume fraction than is achievable using a simple blend down approach. It accomplishes this by creating a special waste form that is more inert than simply mixing the powders and containerizing them. It encapsulates the plutonium oxide surrogate in a refractory metal matrix with good corrosion resistance. It would also enable the special waste form to be printed into shapes and simultaneously serialized for disposition.

## Approach

The approach that will be used to ascertain the suitability of electron beam melting (EBM) of the cermet will be to do the fundamental powder characterization using the Malvern Morphologi 4, Figure 1, to characterize the particle shapes, distribution of hafnia in the nickel, and the particle size distribution (PSD) before and after processing. Upon characterization of the powders, the powder blend will be consolidated into a dense block with up to 5% hafnia in the nickel matrix. Determining the effect of hafnia particle size and its interactions with the electron beam will facilitate the fundamental understanding for this process technique.

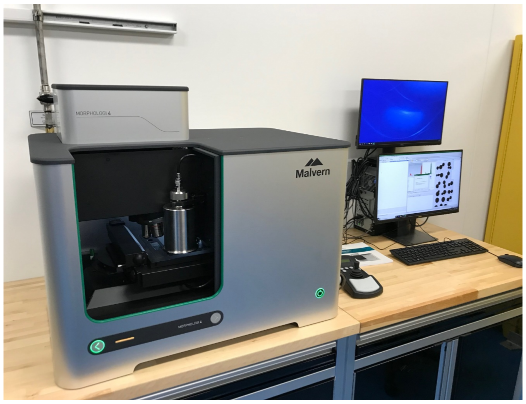

**Figure 1.** Malvern Morphologi4 installed in the Additive Manufacturing Development Laboratory.

## Results/Discussion

The Malvern Morphologi 4 was installed and the conditions required for various powder materials were determined. It was demonstrated that the small powders required higher energy to disperse and longer settling times to ensure that they were adequately dispersed and fully settled on the plate.

The nickel powders, with their larger particle size and generally spherical shape were suitable for lower energy dispersion conditions and shorter settling times. The generally spherical powders exhibit a number of different characteristics including some fine powder agglomerations, satellite particles, non-spherical shapes, etc., as shown in Figure 2.

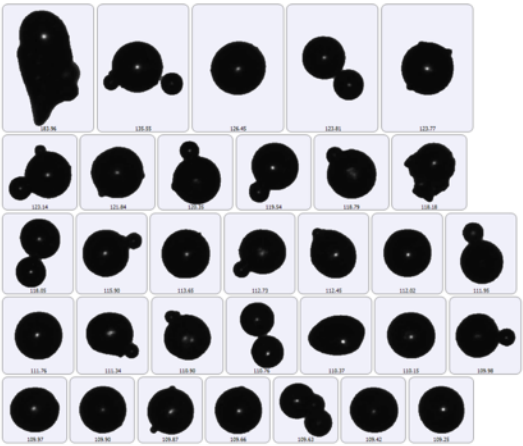

**Figure 2.** Malvern Morphologi4 particle shape analysis.

## FY2019 Accomplishments

- Procured and installed a new particle analysis tool that will enable SRNL to characterize both the powder shape and PSD using an automated tool
- Characterized the hafnia and nickel powders individually and as a powder blend and determined that the powders are likely to remain well dispersed if properly mixed prior to exposure to the A2X processing conditions.

## Future Directions

- Work with University of North Carolina on a workshop to consolidate the nickel and hafnia powders
- Characterize the used powders to determine effects of beam interactions on the powder blend
- Prepare a technical brief for joint presentation
- Develop alternative funding source for continued development of the materials science and engineering for processing

### *Acronyms*

| | |
|---|---|
| **E-PBF** | Electron Beam Powder Bed Fusion |
| **EBM** | Electron Beam Melting |
| **SRNL** | Savannah River National Laboratory |
| **PSD** | Particle Size Distribution |
| **Cermet** | Ceramic Metallic Composite |

# Development of a Simple, Robust Plutonium Waste Form

**Project Team:** J.H. Scogin, A.J. Duncan, A.J. McWilliams

**Thrust Area**: Nuclear Materials Threat Reduction

**Project Start Date:** October 1, 2018

**Project End Date:** September 30, 2019

*The development of a stable proliferation resistant waste form for excess plutonium has long been a goal of the Department of Energy (DOE). This project sought to examine the use of liquid phase sintering as a method of preparing pellets with oxide entrainment as a waste form. The ultimate goal would be to develop and demonstrate high density stainless steel pellets or pucks containing plutonium oxide embedded within the metal matrix using a liquid phase sintering technique. Work in FY19 focused on cold testing using* $Al_2O_3$ *as a surrogate oxide, 316B stainless steel, and a nickel-boron braze alloy.*

## Objectives

- Fabrication of Liquid Phase Sintered Pellets for Oxide Entrainment.

## Introduction

The development of a stable proliferation resistant waste form for scrap plutonium has long been a goal of the Department of Energy (DOE). Principal metrics for waste forms often include proliferation resistance, plutonium loading, and stability in a variety of storage conditions. Equally important are small process footprint, simplicity of manufacture, and a robust process which can accommodate a wide variety of feed material.

The goal is to develop and demonstrate high density stainless steel pellets or pucks containing plutonium oxide embedded within the metal matrix. Using liquid phase sintering, it is possible to create metal forms without melting the base materials or using high pressures. Liquid phase sintering fuses a base material using a small amount of low melting alloy powder mixed into a base alloy powder; it can produce stable forms at temperatures which are significantly lower than the melting point of the base alloy, and in times significantly shorter than required for traditional sintering.

The waste form would offer resistance to proliferation, in that it would be difficult to selectively extract the plutonium without processing the entire waste form. The waste form should be robust enough to work even with the most impure materials, so that no additional reprocessing would be necessary with the impurities of primary concern being halide salts.

Liquid phase sintering (LPS) is a powder processing technique used to produce dense multiphase material. Commonly two powders are thoroughly mixed, pressed together into a compact or pellet, and then sintered at elevated temperatures. One powder is selected to melt at a lower temperature forming a liquid that wets the remaining solid powders. During this interaction the liquid begins to dissolve the remaining solids causing powder rearrangement and grain coarsening. Decreasing surface tension of the liquid generally increases the densification as the liquid can penetrate voids.

Reducing porosity during sintering is furthered by increasing the mass transport during the liquid phase diffusion by slightly altering the chemical composition. Adding boron to ferrous alloys creates a low melting eutectic at 1173 °C that wets the base alloy.(*1*) This research investigated AISI 316 water atomized powders with 0, 0.1, 0.2, 0.3 0.4 wt% boron additions in inter environments and pressed to 600 MPa. Sintering powders without sufficient liquid present does not sufficiently reduce the friction of particles thereby preventing rearrangement and blocks formation of liquid eutectic phase.(*1*)

The addition of oxides into the powders can lead to improved material performance as in oxide dispersion-strengthened ferritic steel that exhibits higher strength at elevated temperatures due to microstructures containing a high density of small oxide particles in the metal matrix.(*2*) It is expected that the Pu oxide and surrogate ($Al_2O_3$) will fully integrate into the sintered pellet. The elevated strength features are due to the finely dispersed oxides that are stable at high temperatures, inhibit dislocation motion, increase resistance to creep deformation, and also inhibit the recrystallization process.(*3*)

LPS has three main stages a) particle rearrangement due to surface forces, b) solution reprecipitation, c) final pore closure and grain growth. The first step is dominated by capillary forces and leads to rapid densification. This process depends on the amount of liquid present and the capillary forces, which are dependent on solubility of the solid in liquid. The mobility of the powder particles is a concern, if the compact is pressed too hard the particles are 'locked in place' resulting in both a lack of rearrangement and densification. During the second state of LPS, Ostwald ripening and coalescence increases the average grain size. During the final step pore closure is dominated by diffusion and mass transfer in the liquid phase while the grain growth occurs at a slower rate.(*4*) Boron is an effective element due to the eutectic and additional alloying elements play important roles in the LPS process and final densification. Addition of Ni to Fe-B systems can lower temperature for liquid formation and increase liquid fraction.(*5*)

The addition of Ti as particles into the preform addresses the non-wettability between metallic and ceramic phases. One issue with mixed metal composites (MMCs) is the lack of toughness and system dependence. The test samples were under vacuum ($10^{-4}$ mbar) at 1,600 °C for 4 hrs. The Ti particles were incorporated into the ceramic green body at 20 wt%. The alumina was angular-shaped particles of 158 and 31 µm and at 50-55% volume fraction for the MMCs. PMMA microbeads were added to alter the green compact density and were debonded in air at 450 °C. Steels used include tool steel CK45, hot-working steel, X38, and 316L. Impact testing was performed with Charpy impact and fracture surfaces analyzed. Absorbed impact energy increases by decreasing the brittle phases such as the $Al_2O_3$ as this increases the distance between particles resulting in the steel matrix properties dominating. Crack coalescence between fracture particles requires less energy. Fracture surfaces demonstrated crack paths intersected the $Al_2O_3$ particles, surfaces showed broken particles and little to no interfacial bonding between the ceramic and steel matrix.

The focus of this research is to demonstrate the capability of liquid phase sintering to fabricate a robust form of oxide particulates encapsulated in a stainless-steel matrix. The ideal situation is the liquid phase wets the ceramic ($PuO_2$ or $Al_2O_3$) particles and completely binds or bonds them in a 316L matrix, while the next best-case scenario is the LPS compact forms a solid shell around the ceramic particles effectively encapsulating them in a metal compact. Extraction of the ceramic particles would require significant effort of grinding and/or melting the sintered product requiring temperatures (~1,400 °C) higher than those necessary for sintering (1,000-1,200 °C) or chemical processing to completely remove the matrix. This technique of oxide entrainment has relevance for creating robust waste forms that require immiscible, high melting, or other stable materials such as ceramics and oxides to be converted to forms that are easier to handle or dispose.

## Approach

A custom CM Furnace was utilized for the cold work in this project with a programable ramp and dwell stages with multi-gas environmental control. Each powder was weighed on a calibrated balance and blended to ensure a thorough dispersion. The powders were combined into a glass jar and loaded into a manual powder mixer from Inversina and mixed for 60 seconds. The mixed powder was then loaded into a 25 mm diameter die and the pressing was completed with a manual hydraulic press from Across International with a max force of 24 metric tons.

Stainless steel 316L powder was obtained from Sandvik with an average particle size of 14.9 µm. This powder was spray atomized and spherical in shape. Due to its shape, cold pressing this powder into cohesive compacts was unsuccessful, as the pellet compacts fell apart after pressing. Stainless steel 316L flake was obtained from Novamet Specialty Products Corporation. This powder was very spongy and fell apart with a very low density even after pressing. The size was 80% +325 mesh (44 µm) with an apparent density of 0.8 g/cc, and flake thickness of 1.0 µm. Stainless steel 316B was obtained from Steward Advanced Materials Inc., with an apparent density of 2.70 g/cm$^3$, tap density 3.41 g/cm$^3$.

A chemical composition is given in Table 1 and the size distribution is shown in Table 2. This material was high pressure water atomized resulting in an irregular shaped flake particle that held together when pressed into a compact pellet.

| Element | Si | Cr | Mn | Fe | Ni | Mo |
|---|---|---|---|---|---|---|
| wt. % | 2.3 | 17.1 | 0.1 | Balance | 12.8 | 2.4 |

**Table 1.** Chemical composition for 316B powder

| Size | +180 µm | +150 µm | +125 µm | +75 µm | +63 µm | +53 µm | -53 µm |
|---|---|---|---|---|---|---|---|
| % | 2.1 | 13.5 | 19.6 | 47.5 | 13.6 | 2.9 | 0.9 |

**Table 2.** Powder size distribution for 316B powder

Nickel Boron powder, Ni-83, was obtained from Aufhauser, with a particle size of -325 mesh (<44 µm), and a chemical composition given in Table 3. The aluminum oxide powder was obtained from Buehler.

| Element | B | Cr | Fe | Si | Ni |
|---|---|---|---|---|---|
| % | 3.18 | 6.7 | 2.9 | 4.5 | Balance |

**Table 3.** Chemical composition for Ni-B powder

Powder ratios focused on two constituents: a fixed amount of ceramic, $Al_2O_3$, and a variable amount of braze alloy, Ni-B. The $Al_2O_3$ was fixed at 4 wt% to correspond to the maximum volume equivalent Pu-oxide that could be loaded into a single 40 g pellet. The Ni-B was tested at 5 wt% and 10 wt% after initial scoping tests that determined 15 wt% and 25 wt% yielded poor quality pellets after sintering. The 316B:Ni-B:$Al_2O_3$ mass ratios were nominally 36.4:2.0:4.0 g and 34.4:4.0:4.0 g respectively for 5 wt% and 10 wt% braze alloy. The pellets were massed and transferred to a glass jar and mixed for one minute before being poured into a 25 mm diameter die. The die was then loaded into the 24 metric ton press and loaded to two different pressures: 4,300 and 5,800 psi on the hydraulic fluid corresponding to a pressure on the pellet of 49,829 psi and 67,212 psi. This compares with 30,000 psi for the yield strength and 75,000 psi for the ultimate tensile strengths for stainless steel 316L.

Sintering occurred in an environmental furnace under an argon atmosphere. The temperature profile followed was a 10 °C/min ramp from ambient to a 30 minute isothermal hold at 850 °C to simulate removal of halide salts and purge oxygen and water vapor, then a 10 °C/min ramp to either 1,000 or 1,050 °C for the final isothermal hold for 60 minutes, then allowed to cool passively back to ambient overnight.

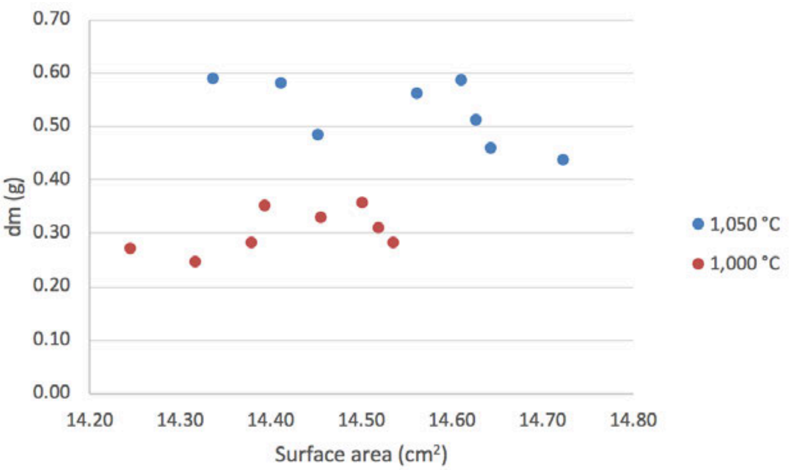

**Figure 1.** Change in pellet mass as a function of surface area for both 1,000 °C and 1,050 °C sintering temperatures

## Results/Discussion

The mass change for the pellets all increased from the as-pressed condition to as-sintered. The pellets sintered at 1,000 °C averaged a 0.76 g increase while the pellets sintered at 1,050 °C had an average increase of 1.31 g. The change in mass combined with the discoloration indicates that the increase is due to oxidation of the 316B while at elevated temperature. When the change in mass is plotted against surface area of each pellet, there does not appear to be a strong indication that the two are correlated or a function of volume. However, the batch of 1,050 °C samples were sintered first and could have baked out trapped oxygen or water vapor so the 1,000 °C started in a cleaner furnace or there may have been a small atmospheric leak.

Volume and density changes are provided in Table 4. Generally there is a small and negative change in density for the pellets due to sintering. More work needs to be done to understand the variation in density change in the 1,050 °C samples.

| P (psi) | Ni-B wt% | %ΔV 1,050 °C | %ΔV 1,000 °C | %Δρ 1,050 °C | %Δρ 1,000 °C |
|---|---|---|---|---|---|
| 67,212 | 5 | 9.86 | 1.28 | -7.93 | -0.60 |
| 67,212 | 5 | 7.96 | 1.64 | -6.36 | -1.01 |
| 67,212 | 10 | 2.97 | 2.98 | -1.48 | -2.04 |
| 67,212 | 10 | 4.09 | 2.74 | -2.77 | -1.98 |
| 49,829 | 5 | -4.43 | 1.18 | 6.18 | -0.35 |
| 49,829 | 5 | 3.04 | 1.80 | -1.71 | -1.08 |
| 49,829 | 10 | 4.10 | 2.69 | -2.53 | -1.75 |
| 49,829 | 10 | 0.80 | 2.27 | 0.60 | -1.46 |

**Table 4.** Volume and density changes for pellets at various sinter temperatures and pressing force

The pellets were section parallel to the compression direction and polished to 6 µm for microscopy characterization. The sample with Ni-B 5 wt% sample pressed at 67,000 psi and sintered at 1,050 °C is shown in Figure 2 at 20x, 100x, and 200x magnifications. These images are representative of the other pellet conditions. At 20x magnification, a thin discolored band can be seen around the diameter of the pellet and appears on all the pellets. Higher magnification of this area (not shown here) shows a slight brown discoloration that supports the slight oxidation of the powders.

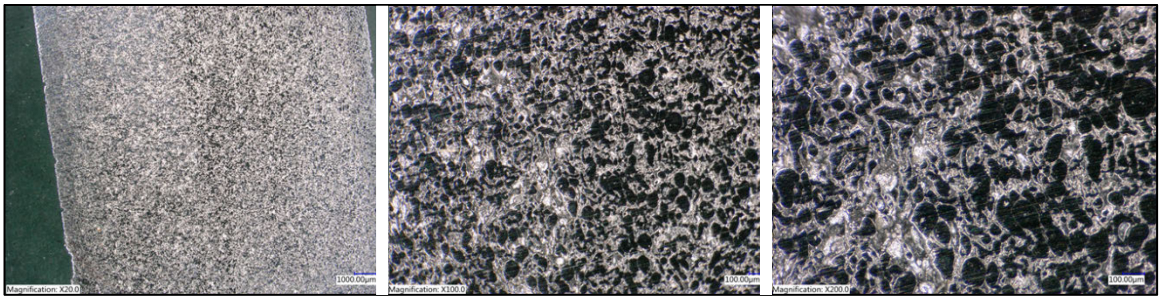

**Figure 2.** Ni-B 5 wt%, F=67,000 psi, T= 1,050 °C at 20x, 100x, and 200x magnification

Mechanical testing was performed on an Instron Model 4507 load frame with MTS-ReNew control electronics, an Instron Model 2525-801 100 kN load cell, at a cross head displacement rate of 0.125"/min at a data acquisition rate of 100 Hz. The data size was reduced by taking a 10-point average and consolidating that into a single point over the entire range. The compression data for the entire set of samples are shown in Figure 1. The data are further split to compare the different test parameters, including the sinter temperatures in Figure 4 and the braze Ni-B weight percent in Figure 5. The as pressed 316B pellet is most similar to the Ni-B 5 wt% samples for both sintering temperature and pressing force. The Ni-B 10 wt% pellets demonstrate more than double the yield strength of the 316B baseline pellet. These data indicate that the lower braze alloy loading does not have a significant impact on the strength of the sintered pellet, while increasing the braze alloy content to 10 wt% has a considerable effect.

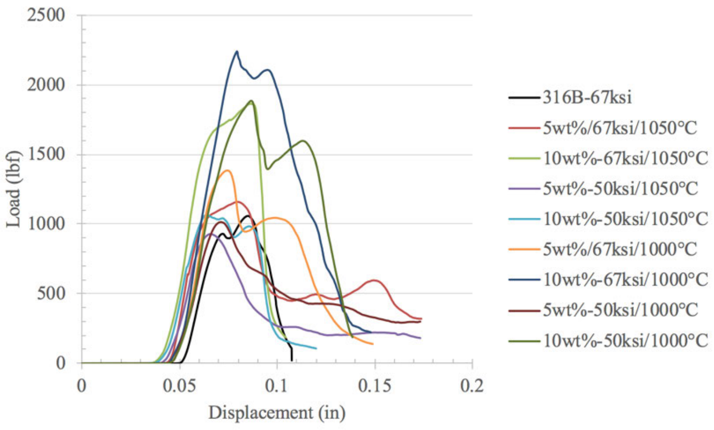

**Figure 3.** The load as a function of displacement of all 9 test conditions

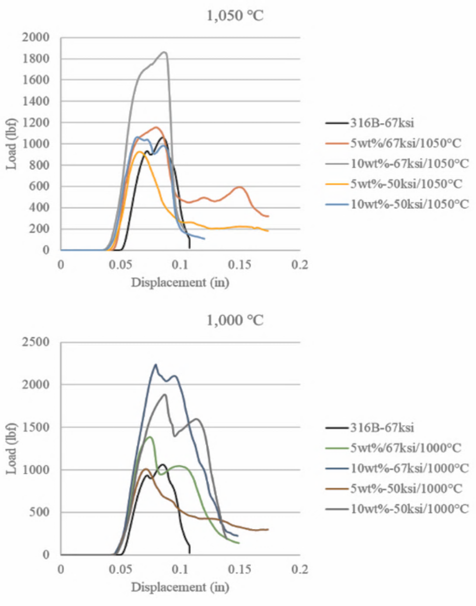

**Figure 4.** Comparison of the compression results for 4 test conditions at 1,000 °C and 1,050 °C sinter temperatures

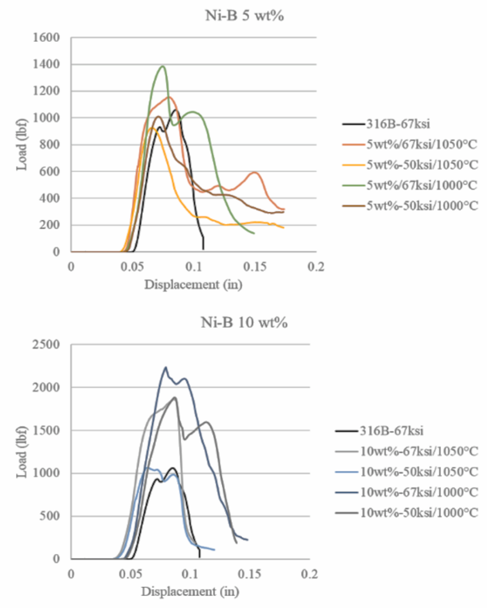

**Figure 5.** Comparison of the compression results for the 5 wt% and 10 wt% braze alloy loading content

The microscopy indicated a large number of voids and non-consolidated powder, while the thin white outline around the 316B particles is likely due to the Ni-B wetting the particles it also indicates that there was not enough liquid phase to consolidate the powder into a solid monolith. All the samples have a noticeable color differentiation around the perimeter that is attributed to a slight oxidation of the powders that would account for the small increases in volume and mass. The mechanical characterization shows that most of the pellets have a higher compressive strength than the base-line unalloyed non-sintered 316B pellet. The majority of the higher Ni-B content (10 wt%) resulted in the highest strength pellets at almost double the base-line 316B pellet. While the initial visual characterization of the pellets determined the higher Ni-B content (25 wt%) were lower quality samples, the microscopy and mechanical testing indicates that there likely was not enough liquid phase to fully fill the voids and consolidate the powders.

## FY2019 Accomplishments

- Completed experimental set up
- Procured custom environmental tube furnace
- Finished Hazard Analysis
- Identified supplier of usable stainless steel powder
- Completed Initial cold test matrix

## Future Directions

- Increase the boron-rich phase in the compacts to achieve accelerated consolidation in a reasonable time frame.
- Radiological experimental testing line will be setup in a radiological glovebox or hood.

## References

1. J. K. M. Skalon, Enhanced sintering of austenitic stainless steel powder AISI 316L through boron containing master alloy addition. Archives of Metallurgy and Materials 57, 789-797 (2012).
2. P. J. M. R.L. Klueh, I.S. Kim, L. Heatherly, D.T. Hoelzer, N. Hashimoto, E.A. Kenik, K. Miyahara, Tensile and creep properties of an oxide dispersion-strengthened ferritic steel. Journal of Nuclear Materials 307-311, 773-777 (2002).
3. E. I. C. Suryanarayana, V.V. Boldyrev, The science and technology of mechancial alloying. Materials Science and Engineering A 304-306, 151-158 (2001).
4. A. E. W. J. Patrik Persson, Steven Savage, Self-propagating high-temperature synthesis and liquid-phase sintering of TiC/Fe composites. Journal of Materials Processing Technology 127, 131-139 (2002).
5. W.-Z. C. Ming-Wei Wu, Zih-Jie Lin, Shih-Hsien Chang, Liquid phase sintering mechanism and densification behavior of boron-alloyed Fe-Ni-Mo-C-B powder metallurgy steel. Materials and Design 133, 536-548 (2017).

## Acronyms

| | | | |
|---|---|---|---|
| DOE | Department of Energy | MMC | Mixed Metal Composites |
| LPS | Liquid phasse sintering | PMMA | Polymethlmethacrylate |

# Extended UAV Flight using Alane as Hydrogen Source for Fuel Cell

**Project Team:** Henry T. Sessions Jr., Andrew Blanton, Mathius Rosenberger, Patrick Ward, Scott McWhorter, Ragaiy Zidan

**Thrust Area**: Nuclear Materials Threat Reduction

**Project Start Date:** October 1, 2018

**Project End Date:** September 30, 2019

*Small Unmanned Aerial Systems (sUAS) have experienced tremendous growth in recent years. The ability of a multi-rotor sUAS to loiter at a fixed location has proven to be a valuable surveillance tool for a variety of applications, including military and life-saving first responder missions. SRNL successfully demonstrated increased sUAS flight times compared to battery powered unmanned aerial vehicles (UAVs) of the same size and weight, by using a hydrogen fuel cell (HFC), (proton exchange membrane) with hydrogen supplied from hydride materials.*

## Objectives

- Develop lightweight vessel to withstand required temperature and pressure
- Develop removeable cartridge with heaters to house hydride material
- Design and build electronic PID (Proportional, Integral, Derivative) heater system for controlled release of hydrogen
- Test and integrate components with commercially available UAV and flight test

## Introduction

SRNL has initiated a small Unmanned Aircraft Systems (sUAS) program using commercially available remote-controlled aircraft. These aircraft are also referred to as Drones, Unmanned Aerial Vehicles (UAVs), and Birds. UAVs have evolved into useful tools for surveillance of buildings, power lines, construction sites, farm crops, orchards, application of herbicides, and assisting first responders.

A major issue with sUAS is the short flight duration, typically 20 minutes, due to battery life. An alternative to batteries is fuel cell powered sUAS using hydrogen. Hydrogen is stored in small lightweight cylinders and compressed to 7,000 to 10,000 psig to provide sufficient hydrogen for flight durations of approximately one hour. Battery powered UAVs have been in use for many years. The application of hydrogen supplied fuel cells for sUAS is just beginning and having compressed cylinders of hydrogen flying overhead is not always desirable.

An alternative to hydrogen stored in high pressure compressed gas cylinders, is hydrogen stored at low pressure on metal hydrides. SRNL has decades of experience with metal hydrides.

## Approach

Fuel cells supplied with hydrogen from metal hydrides have the potential to increase flight time of UAVs from a nominal twenty minutes, based on batteries, to several hours.

## Results/Discussion

A lightweight vessel to house the hydride material was be developed. It is to be capable of withstanding the temperature required to release hydrogen from the hydride material and containing the hydrogen pressure. It is envisioned that the hydride material will be housed in a cartridge that can be easily exchanged. An electrical/electronic heater control system for controlling the release of hydrogen from hydride material and regulating the hydrogen flow to the fuel cell was designed. This circuit functioned as a PID control and was integrated with the UAV flight controls. All of the subcomponents have been tested and integrated with a commercially available UAV and flight tested.

**Figure 1.** Photograph of successful flight with hydride material and HFC.

## FY2019 Accomplishments

- Demonstrated increased sUAS flight times compared to battery powered UAVs of the same size and weight, by using an HFC (proton exchange membrane) with hydrogen supplied from hydride materials.

## Future Directions

- Continue hydride vessel design.

### *Acronyms*

| | |
|---|---|
| **HFC** | Hydrogen Fuel Cell |
| **PID** | Proportional, Integral, Derivative |
| **sUAS** | Small Unmanned Aircraft Systems |
| **UAVs** | Unmanned Aerial Vehicles |

### *Total Number of Student Researchers*

One – Mathius Rosenberger

# Next Generation of an Advanced High Efficiency Particle Collector

**Project Team:** Eliel Villa-Aleman,
Kevin Huffman, Michael Maxwell

**Thrust Area**: Nuclear Materials
Threat Reduction

**Project Start Date:** January 7, 2019

**Project End Date:** September 30, 2019

*A new collector was designed to incorporate new housing material, flow tube, power supply, etc. The new design resulted in a reduction of the air flow (300 to 204 liters per minute (LPM)) but significantly higher collection efficiencies were attained. High collection efficiencies (>50%) were measured for particulates greater than 200 nm.*

## Objectives

- Design and build final collector using the latest technological advances tested in the laboratory.
- Develop specification sheet of particle collection efficiency with particles of different sizes to market to potential customers.

## Introduction

The successful project helped design a new collector (3 versions) with advanced features. Numerous ways were found to improve the collector. Preliminary scanning electron microscopy (SEM) analysis results from particulates deposited on silicon plates and corona wire current measurements suggest that the collectors can operate 10x better than current particle collector systems. Preliminary data also show that there is the possibility to extract the nanoparticulate fraction and provide partial size separation. A collector, based on the tests conducted with the experimental laboratory breadboard, was designed and built (ESP-EV1). The ESP-EV1 incorporated advanced features such as: **1)** high current corona wire, **2)** higher voltage, **3)** enclosures with higher dielectric, **4)** aerodynamic control, **5)** two-stage collector, and **6)** particle separation capabilities. The uniqueness of this collector will help SRNL compete for funding from NA-22. The NA-22 roadmap has already established the need for particulate collection with specific needs. Collector characterization and specification sheet will be required to demonstrate the superior performance to our customers.

## Approach

The new collector was redesigned to incorporate new housing material, flow tube, power supply, etc. The new design resulted in a reduction of the air flow (300 to 204 liters per minute (LPM)) but significantly higher collection efficiencies were attained.

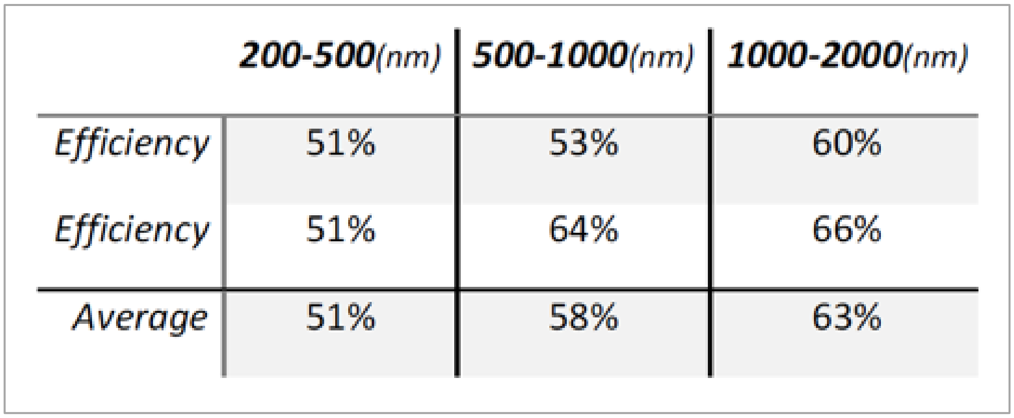

| | 200-500(nm) | 500-1000(nm) | 1000-2000(nm) |
|---|---|---|---|
| Efficiency | 51% | 53% | 60% |
| Efficiency | 51% | 64% | 66% |
| Average | 51% | 58% | 63% |

**Table 1.** Collection efficiency for particulates with different sizes.

## Results/Discussion

The two-year LDRD-2018-00012 project entitled “Smart Particle Collector with Real Time Spectroscopic Analysis” offered the opportunity to analyze the performance of the current particle collector and the variables affecting the particle collection efficiency. After several tests, it became evident that improvements could be made to improve the collector significantly. This seedling project helped design three collectors with advanced features incorporating improvements into the collector. The performance of the system with particles of different sizes was characterized. The technology will help solve current NA-22 problems and extract unique particles from environmental samples found in detonation experiments and uranium enrichment facilities. Table 1 shows the collection efficiency for particulates with different sizes. Figure 1 shows the collection plates and the size dependent particulates deposition along the length of the collection plate.

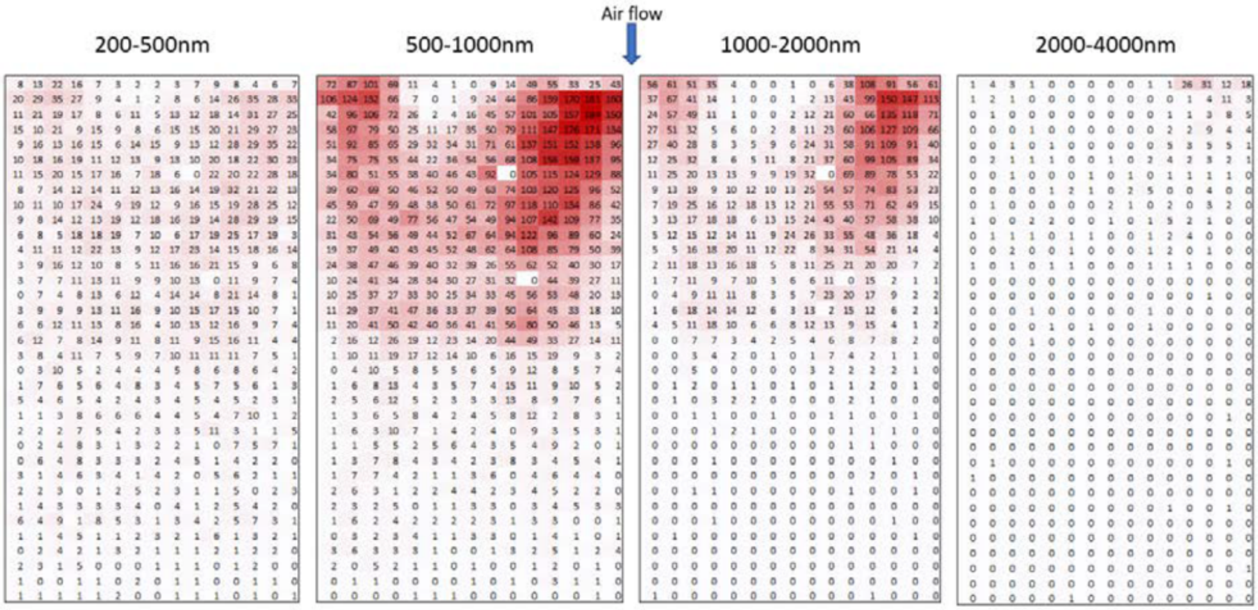

**Figure 1.** Collection plates. The coloring and numbers indicate particulate deposition along the length of the collection plate.

## FY2019 Accomplishments

- Collection efficiency measured.
- Analyses of Si collection plate imaged using scanning electron microscopy.
- The results provided a new path on the design of future particle collectors.

## Future Directions

- An invention disclosure of the new technology will be submitted.
- A new concept has been submitted to EM to remove beryllium and mercury from air.

### *Acronyms*

| | |
|---|---|
| **ESP** | Electrostatic Precipitator |

### *Intellectual Property*

Invention disclosure to be submitted

# IR Spectroscopic Investigation of Solidified $UF_6$

**Project Team:** K. A. S. Fessler (Primary), P. E. O'Rourke

**Thrust Area**: Nuclear Materials Threat Reduction

**Project Start Date:** June 27, 2019

**Project End Date:** September 30, 2019

*Gaseous diffusion uranium enrichment facilities require tools to monitor the level of enrichment to stay within the limits set for power, research, and weapons grade uranium. There is a need for field-deployable analytical methods to lessen the burden on verification laboratories, as well as reduce the sampling time, cost, and increase efficiency. The high performance infrared (HPIR) system was developed by Savannah River National Laboratory to meet this need. However, the method lacks the precision to analyze natural and depleted uranium hexafluoride ($UF_6$) samples to the International Target Values (ITVs) set by the International Atomic Energy Agency. The current method measures the shift in the broad $UF_6$ peak, because the $^{235}U$ and $^{238}U$ isotopes are not resolvable in the gas phase at room temperature due to hot band contributions. Supercooling $UF_6$ would decrease the IR band width and improve isotopic resolution, as well as increase the molecular density in the laser sampling region, thus improving signal strength and decreasing cell size.*

## Objectives

- Demonstrate proof-of-concept IR absorption measurements of solidified $UF_6$ at -50 °C (removes molecular rotations)
    - Finalize thermo-electrically cooled cell assembly and align with laser.
    - Measure $UF_6$ samples (natural, LEU, and HEU).
    - Analyze data to determine precision of enrichment predictions.

## Introduction

The project goal is to develop a field-deployable IR absorption technique and method for isotopic determination of $^{235}U$ and $^{238}U$ by solidifying uranium hexafluoride ($UF_6$) gas samples in a custom-designed cell. Previously, SRNL has demonstrated IR absorption spectroscopy using quantum cascade lasers (QCL) as a potential method for determining the isotopic ratio of uranium in gaseous $UF_6$; however, the technique was limited to monitoring low- and high-enriched samples due to IR band broadening and hot-bands prevalent in the available QCL wavelength regime. To improve the analytical method to include isotopic ratio monitoring of natural and depleted $UF_6$ samples, we propose to sharpen the IR bands by reducing hot-bands via solidification of the $UF_6$ and freezing out contributions to the IR spectrum from molecular rotations that broaden the IR bands. Solidification will also increase the molecular density of the sample, thereby reducing the required pathlength and decreasing the overall footprint of the system. A cell designed for this purpose has already been manufactured, and $UF_6$ samples are available for proof-of-concept experiments. The work would demonstrate, for the first time, IR spectra of solidified $UF_6$ without using super-sonic expansion for the cooling process, and the narrow IR bands should improve the analytical performance of the technique to allow for isotopic ratio determination for natural and depleted $UF_6$ samples at precisions closer to the International Atomic Energy Agency (IAEA) 2010 International Target Values (ITV).

## Approach

Cooling $UF_6$ to temperatures below -50 degrees Celsius should cause the gaseous sample to form a solid crystal, which would decrease the full width half maximum (FWHM) of the $UF_6$ IR band. By decreasing the IR peak FWHM, improved resolution between the $^{235}U$ and $^{238}U$ should be achievable with the same spectroscopic instrument. Thermal separation based on freezing point differences also helps purify the sample, which can reduce interferences in the observed spectrum. An IR cell specifically designed to handle the $UF_6$ and allow cooling of the sample was designed and assembled (Figure 1).

The cell was designed to hold a small volume of $UF_6$ gas that is cooled to a solid onto a gold reflective surface. The initial project task was to finalize the thermo-electrically cooled cell assembly and align with laser. After the cell alignment, a $UF_6$ sample was added to the cell as a gas and the temperature inside the cell was decreased using the thermo-electric cooler (TEC). The sample should freeze on the gold surface in a thin enough layer to allow light to pass through and reflect off the gold substrate, which is determined by the amount of sample in the cell and the thermal gradient used to cool the sample. The data was analyzed to determine precision of enrichment predictions.

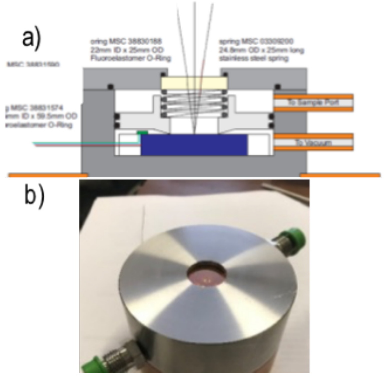

**Figure 1.** Schematic of cell design **(a)** and manufactured cell **(b).**

## Results/Discussion

The TEC was connected to the gold-coated copper sample plate inside the gas cell. After the wire ports in cell were sealed, the cell was leak-tested and the temperature control was demonstrated to reach -11 °C without a cooling mechanism for the heat sink. The cell was connected to a vacuum manifold used for $UF_6$ sampling, then aligned with the QCL (Figure 2). The signal throughput of the laser was optimized before adding any $UF_6$ to the cell. The IR spectrum of $UF_6$ was measured in the gas phase before cooling to a solid. Due to the short light-path through the gas phase sample, there was not significant signal. After the TEC was turned on and the sample began to cool, the IR signal through the cell dropped as a result of the $UF_6$ cooling on the gold surface in a mixed-phase crystalline solid. To improve throughput of the laser through the sample, the $UF_6$ needs to form a more uniform crystalline structure. Therefore, future work will attempt to cool the $UF_6$ more slowly to allow the solid to form a more structured crystal, as well as connecting the water lines to a chiller to cool the heat sink and allow for lower temperatures to be reached with the TEC.

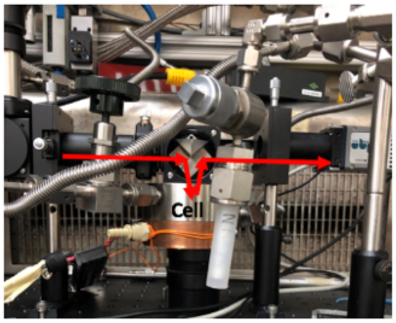

**Figure 2.** Cell aligned with laser (red arrows) and connected to $UF_6$ sampling system.

## FY2019 Accomplishments

- Connected thermo-electric cooler and thermistor to cell and reached cell temperature of -11 °C
- Aligned cell with laser and measured IR signal through the cell
- Cooled $UF_6$ onto the reflective surface and attempted to measure the signal of the solid

## Future Directions

- Connect water lines to cool TEC and reach lower temperatures, as well as slow the cooling rate to get improved crystallization
- Measure solidified $UF_6$
- Apply for additional funding

### *Acronyms*

| | |
|---|---|
| **FWHM** | Full Width Half Maximum |
| **HEU** | High-enriched Uranium |
| **IAEA** | International Atomic Energy Agency |
| **IR** | Infrared |
| **ITV** | International Target Value |
| **LEU** | Low-enriched Uranium |
| **QCL** | Quantum Cascade Laser |
| **SRNL** | Savannah River National Laboratory |
| **TEC** | Thermo-electric Cooler |
| **$UF_6$** | Uranium Hexafluoride |

# Exploring the suitability of MXenes for Sensing Applications

**Project Team:** Robert Lascola (Primary), Simona Murph, Kemryn Allen-Perry (MSIPP Intern), Fayatteville State University [FSU]), Daniel Autrey (Professor, FSU)

**Thrust Area**: Nuclear Materials Threat Reduction

**Project Start Date:** July 1, 2019

**Project End Date:** September 30, 2019

*Two-dimensional titanium carbide nanoflakes (MXenes) were synthesized by several methods and tested for use as sensing platforms via surface-enhanced Raman spectroscopy (SERS). Films made from MXenes formed by etching with LiF/HCl were successful in generating SERS signal for the test molecule Rhodamine B, with a linear relationship to concentration to at least as low as 5 x $10^{-7}$ M. Several ways to improve the reliability of the measurement were identified. MXene films hold promise for eventual development as an alternative to existing optical spectroscopy methods for trace detection of uranium species.*

## Objectives

- Determine that MXene synthesis methods likely to yield good sensing materials
- Demonstrate the viability of MXenes as sensing platforms for trace-level detection by optical methods (Raman spectroscopy, fluorescence)
- Demonstrate the use of MXenes to sense trace concentrations of uranium

## Introduction

MXenes are two-dimensional materials composed of layered transition metal carbides, nitrides, or carbonitrides. They have the general formula $M_{n+1}X_nT_x$, where M is an early transition metal, X is C and/or N, and T are surface termination groups such as -F, -OH, and -O. The most common form of these materials is $Ti_3C_2T_x$. MXenes have been used as a surface-enhanced Raman spectroscopy (SERS) substrate [1], with the SERS effect arising from both surface plasmon properties and chemisorption and charge transfer effects. MXenes have also been experimentally observed [2] and theoretically predicted [3] to strongly and selectively adsorb uranyl ion from neutral to slightly acidic (pH = 2.5-7) solutions.

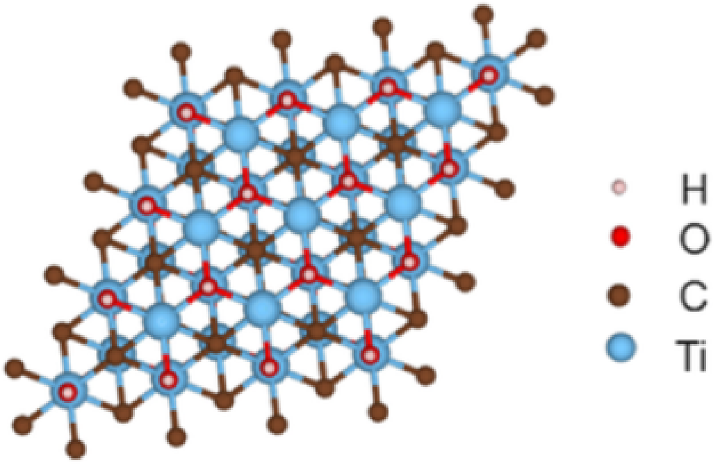

**Figure 1.** Hydroxylated $Ti_3C_2$ structure (from Reference 3)

The combined facts of SERS activity and selectivity for uranyl suggest that optical interrogation of uranyl ions attached to MXenes could be the basis of a sensitive detection method. There have not been any studies reported in the literature which examine this question. The long-term goal of the project was to study both the Raman spectroscopy and the fluorescence of adsorbed uranyl. If successful, MXene based sensing could be developed into a process/field portable alternative to kinetic phosphorescence assay (KPA) as an optical low assay U measurement.

## Approach

FSU supplied MXenes that had been synthesized from titanium aluminum carbide precursors by two different etching processes (LiF/HCl and HF). The materials were sonicated, suspended, and centrifuged to prepare solutions that were deposited drop-wise onto a substrate. The drops were characterized for elemental composition, particle size and distribution, and for use as a SERS sensor with a test analyte (Rhodamine B). If time permitted, the materials would have been exposed to uranyl and tested for detection of the latter by SERS and/or fluorescence spectroscopy.

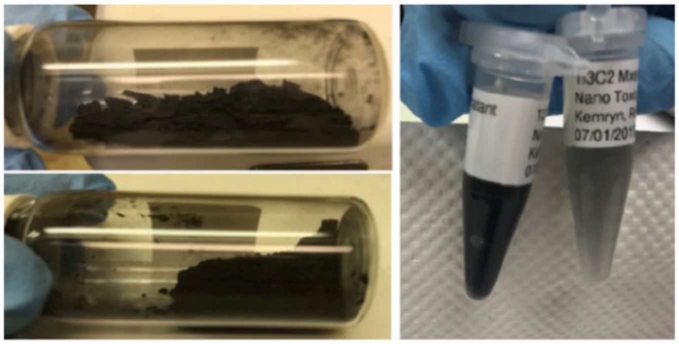

**Figure 2.** LiF/HCl- **(top left)** and HF- **(bottom left)** etched MXenes and prepared aqueous solutions **(LiF/HCl, Left; HF, right)**

## Results/Discussion

The LiF/HCl etching process resulted in larger flakes than the HF-etched material, which is consistent with the LiF/HCl being a gentler reagent. Elemental analysis revealed that more Al was present in the LiF/HCl material, meaning that the etching process was less complete. The larger LiF/HCl flakes resulted in a more concentrated suspension and thicker drop-cast film (4 L drops) than the HF-etched material. "Macroscopic" SERS spectra of Rhodamine B were obtained by drying a single 4 L drop of 0.5 – 5 M solution onto previously deposited and dried MXene drop-cast films. SERS was measured at 532 nm using a conventional fiber probe with ~100 m diameter spot size and 50 mW excitation. Spectra were observed with films made from the neat LiF/HCl material, but not from a 1:4-diluted LiF/HCl solution or from the HCl solution. For the neat LiF/HCl films, the SERS response for Rhodamine B was linear with concentration and consistent with prior literature reports [4] obtained with a different substrate. Intrinsic fluorescence of the Rhodamine B was greatly reduced for these samples compared to dried drops of neat Rhodamine B solution. Suppression of fluorescence is a characteristic of plasmonic coupling and supports the conclusion that a surface-enhancement effect is occurring. "Microscopic" SERS spectra of the LiF/HCl samples were also obtained at 532 nm through a microscope with a 20x objective and sub- W laser powers (~1 m spot resolution) . Raman spectra were highly spot-dependent. Some spectra roughly resembled the spectra obtained with the macroscopic objectives, while others corresponded to small Rhodamine B particles (with high fluorescence) or to a MXene particle of some kind. Microscopic spectra of the HF material were inconclusive. These results suggest that the SERS spectra observed for LiF/HCl etched MXene with the microscopic Raman probe are probably a spatial average of Raman-active and -inactive regions. Due to time limitations (especially with the limited tenure of the summer intern), we were not able to test the response to uranyl solutions.

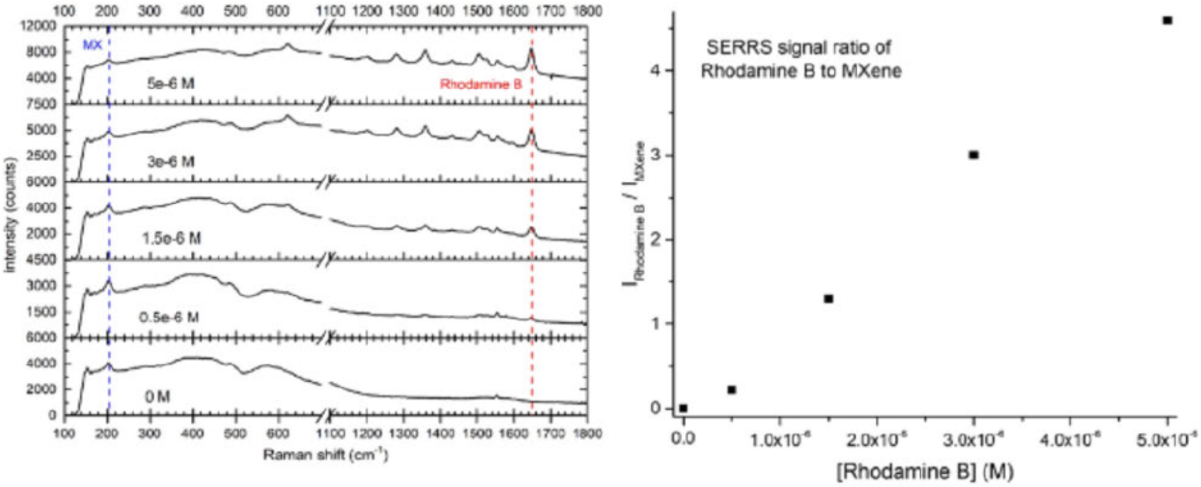

**Figure 3.** Raman spectra **(left)** and SERS enhancement signal **(right)** of Rhodamine B on LiF/HCl-etched MXene.

## FY2019 Accomplishments

- We were able to make stable MXene-based sensing films with simple procedures.
- We observed a SERS response for Rhodamine B on LiF/HCl-etched MXenes despite incomplete etching of the original material. Although HF-etched MXene has been reported to have a larger SERS enhancement than LiF/HCl-etched material, the thicker and more uniform surface coverage of the latter makes it a better candidate for subsequent SERS method development.

## Future Directions

- Revise etching conditions, especially with the LiF/HCl process, to obtain more complete removal of Al and improve the formation of MXene flakes. (Work to be done at FSU)
- Optimize sensing film formation to obtain more uniform distribution of MXenes within the drops. Develop a reproducible film formation procedure that will allow the films to be a reliable substrate for future method development. Examine utility of mixing MXene and analyte solutions prior to casting films in order to obtain more uniform results.
- Test SERS signal for uranyl solutions, and compare sensitivities to those obtained by other optical techniques (KPA).

### *Publications/Presentations*

A presentation will be made by our undergraduate student (K. Allen-Perry) at the 2020 Emerging Researchers National (ERN) Conference in STEM, Washington, D.C., in February 2020.

### *References*

1. A. Sarycheva *et al.*, *J. Phys. Chem. C* **121** 19983-19988 (2017).
2. L. Wang *et al.*, *Chem. Commun.* **53** 12084-12087 (2017).
3. Y.-J. Zhang *et al.*, *J. Hazard. Mater.* **308** 402-410 (2016).
4. L. Zhang et al., *Applied Spectroscopy* **71** 2395–2403 (2017).

### *Acronyms*

| | |
|---|---|
| **FSU** | Fayetteville State University |
| **KPA** | Kinetic Phosphorescence Assay |
| **SERS** | Surface Enhanced Raman Spectroscopy |

### *Total Number of Student Researchers*

One - MSIPP Undergraduate Summer Intern) / Work performed off-site (materials synthesis) and on-site (sample prep, materials characterization)

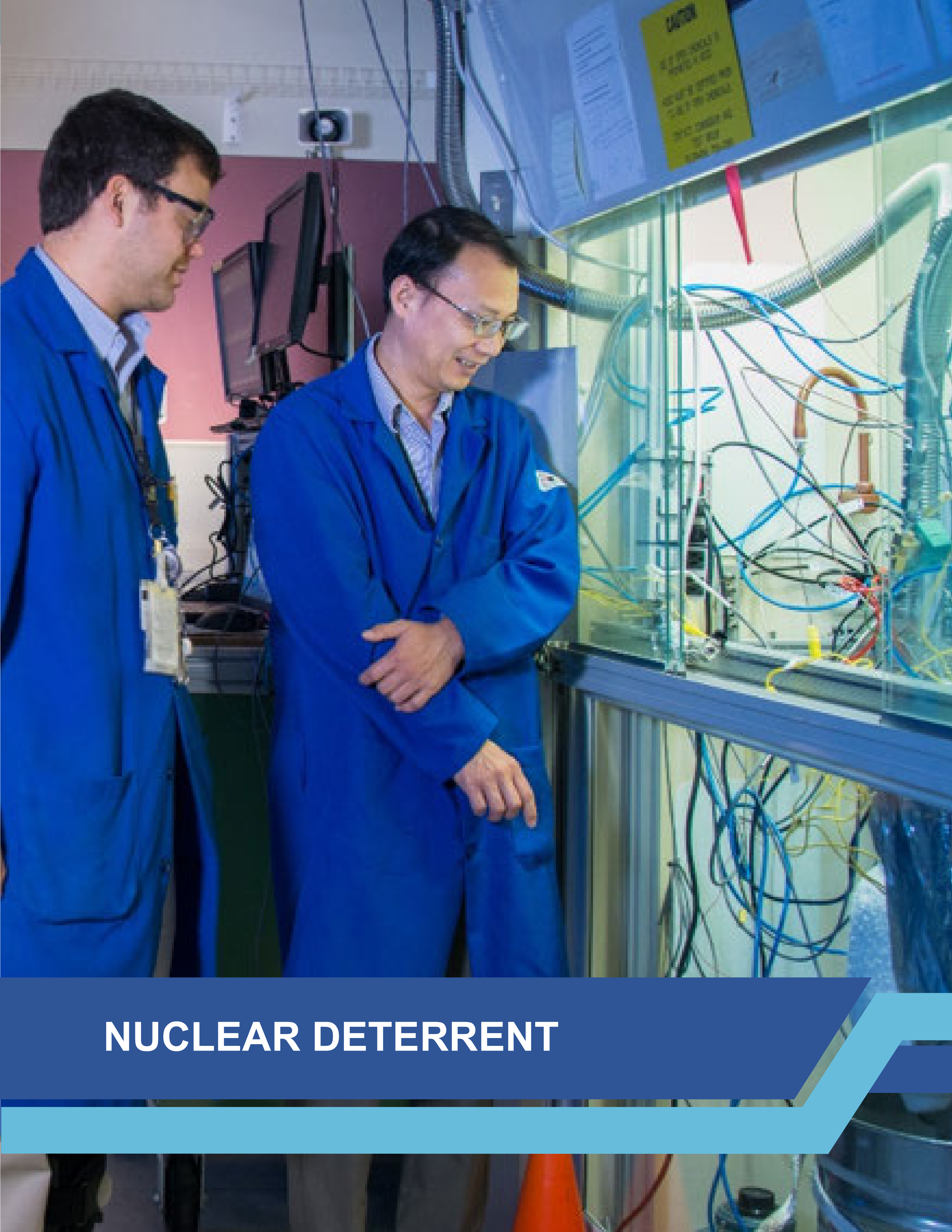

# NUCLEAR DETERRENT

# Kelvin Probe Force Microscopy for High-Resolution Imaging of Hydrogen in Steel Alloys

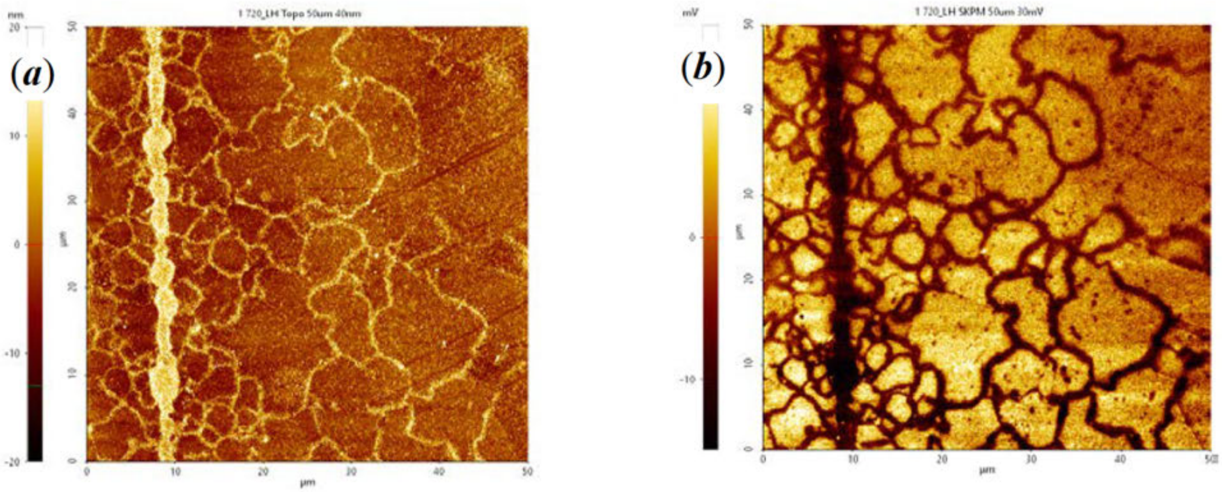

Topography **(a)** and surface potential **(b)** of pinch welded austenitic stainless steel to map grain boundaries around the weld region. In **(a),** bright lines correspond to raised grain boundaries, and in **(b),** dark lines correspond to a hydrogen induced change in the work function. Specimen was polished then hydrogen charged at 17 MPa hydrogen pressure. After charging and before imaging, specimen was kept in dry freezer to discourage hydrogen from diffusing out of the material.

**Project Team:** A. J. Duncan, J. D. McNamara (Co-PIs)

**Collaborators:** P. S. Korinko, M. J. Morgan, D. D. Dick, L. Inabinet

**Thrust Area**: Nuclear Deterrent

**Project Start Date:** October 1, 2017

**Project End Date:** September 30, 2019

*Kelvin probe force microscopy (KPFM) was used to directly image and co-locate the presence of hydrogen in stainless steel with various microstructures. Several specimens were investigated, including forged, welded, LENS® fabricated, and pinch welded materials. Each sample was examined either after being charged under hydrogen gas, or as received (i.e., uncharged) condition. H-charged forged and welded samples show an increase in the work function for regions of retained delta ferrite, and this is indicated by a decrease in the contact potential difference (CPD) voltage. LENS® fabricated samples show an increase in the CPD around the cellular regions. This is indicative of elemental variation which is confirmed by energy dispersive spectroscopy (EDS) data. Cleaned austenitic 316L fill stems were pinch welded under nitrogen using range of currents. The pinch welds were characterized by atomic force microscopy (AFM) and KPFM in the as-welded condition (with and without hydrogen) and post weld hydrogen charging. The results show the presence of hydrogen along grain boundaries in the welded region. Electron backscatter diffraction (EBSD) was used to analyze the grain size and orientation along the pinch welds. To control the introduction of hydrogen into the materials, an electrochemical cell was designed to be used while imaging in situ. The results of the electrochemical charging measurements are inconclusive, and future work is necessary.*

## Objectives

- Develop *in situ* electrochemical charging and characterize various types of metal alloys

## Introduction

Understanding the mechanism of hydrogen interactions in metal alloys is continually a topic of interest for applications which involve the long-term storage of hydrogen.[1] Atomic hydrogen segregates to regions of extended defects, such as grain and phase boundaries, and can cause stress and premature cracking through a process known as hydrogen embrittlement.[2,3,4] Advanced microstructural imaging techniques, with minimal sample preparation needs, that are capable of resolving features down to the nanometer scale are needed. Current imaging and testing technologies for understanding the effects of hydrogen in metals involve low-resolution optical microscopy and fractography after mechanical testing. Hydrogen segregated at the surface and particularly at defect sites changes the local work function of the material and can be measured by KPFM, a variant of atomic force microscopy (AFM).[5] KPFM produces surface potential (i.e., voltage) images, and is capable of measuring the local change in work function of surfaces with very high spatial resolution compared to current methods of optically imaging the microstructures. The spatial and energy resolution of KPFM is approximately 5 nm and 10 mV, respectively.[5] By locating the presence of hydrogen and its relationship with extended defects at the surface using KPFM, it may be possible to predict the long-term storage properties of a container.

The mechanism of Kelvin probe microscopy is based on establishing an electrical equilibrium between the work function of a metallized probe and the work function of a surface when the two systems are placed in electrical connection.[5] During KPFM operation, an AFM is used to bring an oscillating metallized probe very close to the sample surface. A piezo actuator mechanically drives the probe close to its resonant frequency, and, due to Van der Waals forces between the tip and surface, the resonance frequency of the probe changes as it raster scans across the surface of the sample for a predetermined scan area. In this way, topological variations can be measured. Simultaneously, the second resonant frequency of the probe is monitored while applying an AC voltage to electrostatically resonate the probe. A potential difference will develop between the sample and the probe due to differing Fermi levels and will create an electrostatic force between the two materials.[5] Using a feedback loop, a specific DC voltage is also applied to the probe such that, at any given point on the surface, the electrostatic force between the tip and the sample is nullified. In the case of vanishing electrostatic force, the applied DC voltage will be equal to the surface potential. This value is called the contact potential difference (CPD) and is defined as the change in work function between the sample and the probe:[5]

$$\mathrm{CPD} = \phi_{tip} - \phi_{sample} \ ,$$

where $\varphi_{tip}$ and $\varphi_{sample}$ are the work functions of the tip and sample, respectively. The CPD is equal in magnitude, opposite in polarity, to the backing potential that is necessary to nullify the electrostatic force between the sample and the probe. Figure 1 shows schematically how the vacuum levels of the sample and the probe become aligned as a DC voltage is

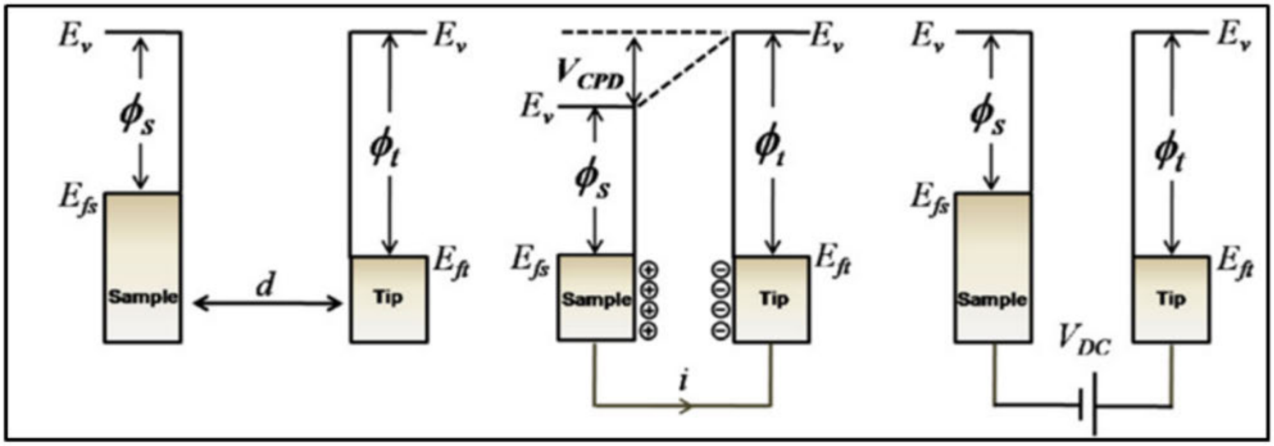

**Figure 1.** $V_{CPD}$ is the difference in work function values of the sample and the tip. This value can be measured by applying a DC voltage to nullify the electrostatic force between the sample and the tip.

applied, thereby allowing for the measurement of the CPD. Figure 2 gives an example of the topography and microstructure of 304L austenitic stainless steel after it has been electropolished. The corresponding surface potential image shows how the work functions of the grains vary which could be due to different oxidation levels or grain orientation. Using the KPFM technique allows for very localized work functions to be measured and attributed to the corresponding defects. It is important to mention that crystallographic orientation[6] and compositional variation will change the local work function as well.

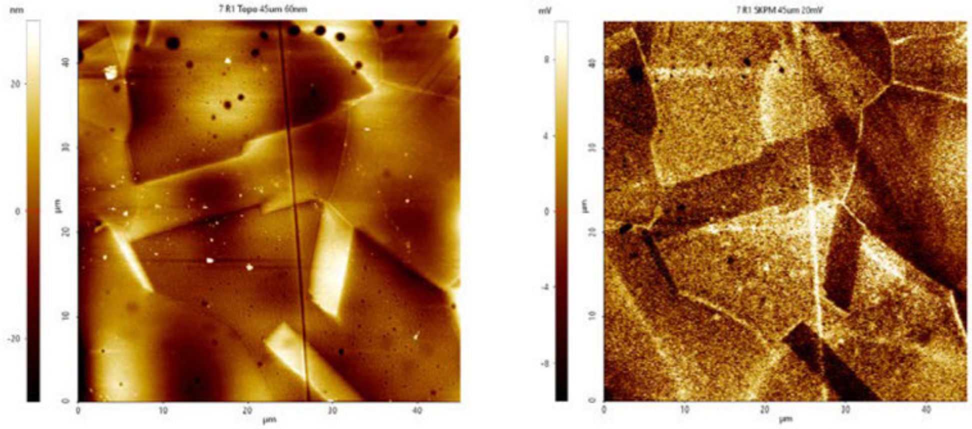

**Figure 2. (left)** The height or topography information of electropolished stainless steel; **(right)** The corresponding variation of the surface potential.

KPFM has been previously used to image hydrogen in palladium thin films, duplex stainless steel and aluminum alloys.[7-11] Duplex stainless steels were electrochemically charged with hydrogen and subsequently measured with KPFM. Since the work function of the surface is the physical quantity being monitored during these measurements, it was possible to detect the diffusion of hydrogen to the surface as it changed the local work function. The ferrite phase showed a much more drastic change in work function compared to the austenite phase with increasing time of hydrogen loading. The change in work function was attributed to changes of the surface oxide band structure due to the presence of hydrogen.[8] Studying the behavior of hydrogen at the surface of duplex steels yields interesting results due to the vastly different diffusion rates of hydrogen in ferrite and austenite phases. Hydrogen segregation was also observed at deformation twin sites in twinning-induced plasticity (TWIP) steel, where the potential images showed a decrease in CPD in the region of the deformation twin sites. For most of the research reported in the literature, samples of stainless steel are coated with palladium to reduce topological effects, as well as to desorb the hydrogen. In these instances, the samples were electrochemically charged with hydrogen using various electrochemical solutions.

Additionally, it is important to characterize and understand the capabilities of additive manufactured (AM) stainless steel components being considered for hydrogen storage. Years of research and operational experience have demonstrated the effects of tritium on traditionally fabricated hydrogen service components, but the same cannot be said for AM components. KPFM studies of the microstructural behavior of hydrogen charged AM stainless steels can provide a technique to understand and predict the long-term effects of tritium and hydrogen embrittlement on its containers.

In this work, we discuss the results of KPFM imaging of various stainless-steel samples and compare it with complimentary techniques, such as scanning electron microscopy (SEM) and electron backscatter diffraction (EBSD) measurements to understand the behavior of hydrogen segregation in stainless steel.

## Approach

Stainless steel samples which were forged, welded, pinch welded, and fabricated by the LENS® method[12] were investigated to understand their microstructures and the behavior of hydrogen within the material. Forged stainless steel samples, type 304L and welded stainless steels, with 21% Cr - 6% Ni - 9% Mn base metal, and 308L filler metal were hydrogen charged under 34 MPa hydrogen gas, at 350 °C, for 2 weeks. Fill stems which were type 304L stainless steel, machined from forgings, gun drilled and crush ground and Oakite cleaned were obtained from Kansas National Security Campus and were pinch welded at varying currents (2900-4100 A) in nitrogen. Specific pinch weld samples were then hydrogen charged under the same conditions as above. Four type 304L stainless steel (SS) samples were prepared by the directed energy deposition method of laser engineered net shaping (LENS®) at Sandia National Laboratory and Los Alamos National Laboratory. Hydrogen charging was performed on two of the samples (D and E) by pressurizing a chamber with 34 MPa of hydrogen gas at 350 °C for approximately 2 weeks. All samples which were pressure charged by hydrogen are hereafter called "H-charged" samples. After charging, samples were stored at 0 °C to prevent the unnecessary loss of hydrogen by diffusion. All samples were cut and mechanically polished for AFM imaging by standard metallographic practices. Samples were cleaned by rinsing with soap and de-ionized (DI) water, followed by rinsing with ethanol and drying with dry nitrogen or air. A light electrolytic etch was performed with 10% oxalic acid for 30 s at 10 V to reveal the microstructures for initial measurements. Once these initial measurements were performed, the samples were re-polished to return to the as-polished conditions for subsequent analysis. Before imaging, all samples were cleaned with supercritical $CO_2$ gas which acted to both dissolve organic contamination and release particulate material from the surface.

Imaging was performed using a Park Systems XE-70 AFM, in non-contact mode and the extended, electrostatic force microscopy mode coupled with a Stanford Research Systems lock-in amplifier for KPFM measurements. The AFM is contained within an environmental chamber to control the humidity levels, and dry nitrogen is flowing through the chamber during imaging. The relative humidity levels for the AFM measurements in this work were about 8%. Optical micrographs were taken on a Nikon MM-400 measuring microscope. SEM examination was conducted on a Hitachi SU823 SEM and energy dispersive spectroscopy (EDS) measurements were performed with the attached Oxford detector. EBSD measurements were performed as well. Since KPFM is a surface sensitive technique, only the behavior of hydrogen at the surface can be investigated. Additionally, imaging the samples while in a nitrogen environment reduces the thin water layer which develops on the surface of materials exposed to ambient conditions and acts as a screening potential, which is detrimental to surface potential measurements.

## Results/Discussion

### *Forged, welded, and LENS® fabricated samples*

The surface morphology of the forged, welded and LENS® fabricated stainless-steel samples were characterized by an AFM to understand the microstructural characteristics. In order to image the fine cellular grains of the LENS® fabricated samples, the samples were given a quick electrolytic etch. Figure 3 shows the microstructure for one of the LENS® samples. Typical microstructural patterns of these samples are large grain features on the order of 50 – 100 µm across, and small cellular-like regions which are on average less than 5 µm. The cells have either polygonal (sometimes circular) shapes or elongated skeletal structures and are contained within the large grains. The size of the structures is related to the heat input during melting and its corresponding solidification rate. Samples fabricated by LENS® undergo highly localized heating from the laser, followed by rapid cooling and solidification as the heat source advances.[13,14] This process creates fusion zone type microstructures very similar to those of welded samples. Each layer of the sample is melted by the laser, solidified rapidly, and followed by successive deposition and solidification of more material. The melt pools are about 500 µm to 1 mm wide, and AFM image areas are no greater than 45 µm, which allows each image to be fully contained within one melt region. LENS® materials show very fine grains compared to forged steels and have directional anisotropy depending on the build parameters.[15]

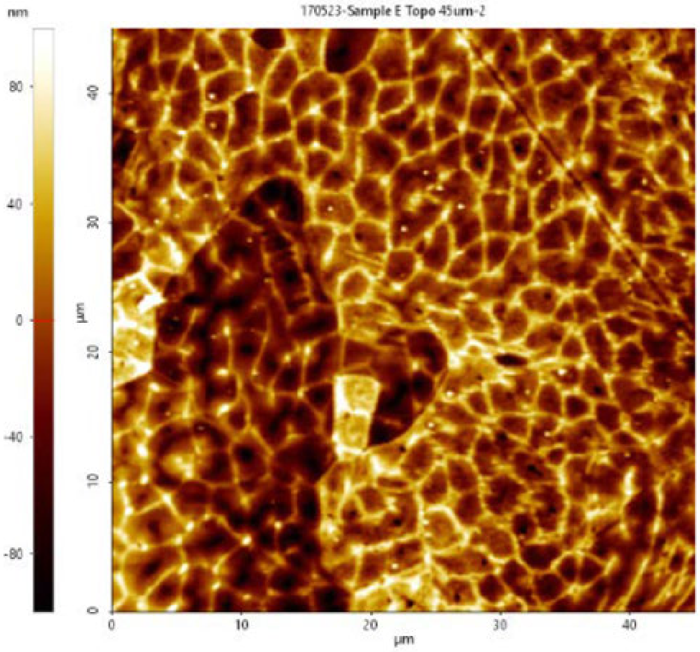

**Figure 3.** Topography as measured by the AFM for a LENS® fabricated sample after mechanical polishing a light oxalic acid etch.

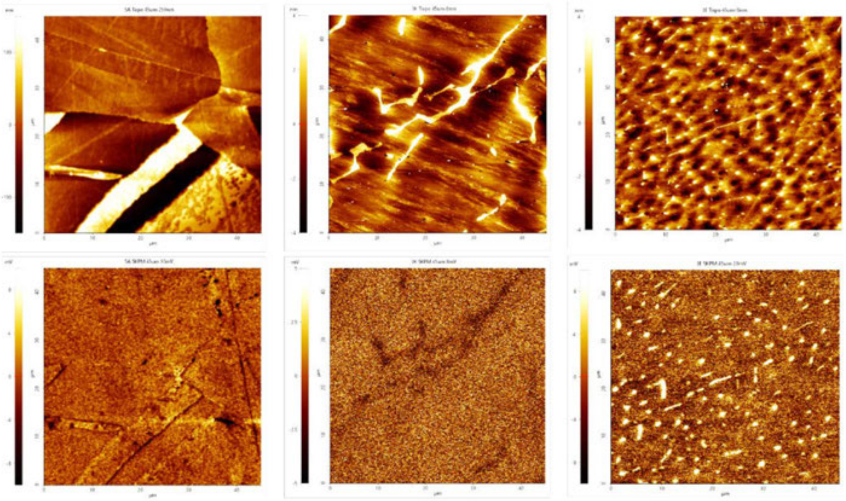

**Figure 4. (top)** topography images of forged **(left),** welded **(center),** and LENS® fabricated samples **(right)** with their corresponding surface potential maps **(bottom).**

Surface potential measurements (KPFM), with their corresponding topography images, were performed on as-polished forged, welded and LENS® samples, both H-charged and uncharged, to image the changes in the local work function and are shown in Figure 4. All the samples were hydrogen charged; however, the sign of the change in CPD was negative for the forged and welded samples, and positive for the LENS® samples. Uncharged samples, regardless of the growth conditions showed no noticeable variation in surface potential for our measurements. This leads us to conclude that the surface potential variation is a factor of elemental composition or phase variation. It is well known that welded samples have regions of retained delta ferrite which should have a different work function than the surrounding austenitic regions. For the LENS® samples, EDS data (Figure 5) show that the intercellular regions have a higher percentage of Cr content and a decrease in the Ni content. This is indicative of retained ferrite at the boundaries of the austenitic microstructures and is consistent with other studies on AM 316L stainless steel.[15] EDS measurements performed on one of the LENS® fabricated are shown in Figure 5, which is representative of the other LENS® samples. Both EDS line scans [Figures 5 (c) and 5 (d)] and maps (not shown) show an increase in the Cr content and a decrease in the Ni content at the cellular and grain boundaries. Other EDS data show that there is compositional variation in the same regions (e.g., grain boundaries)[13] which are posited to be concentrated in hydrogen. Since both charged and uncharged samples showed a change in surface potential, we must assume that the changes in the work function are due to crystallographic orientation or elemental variation for the LENS® samples.

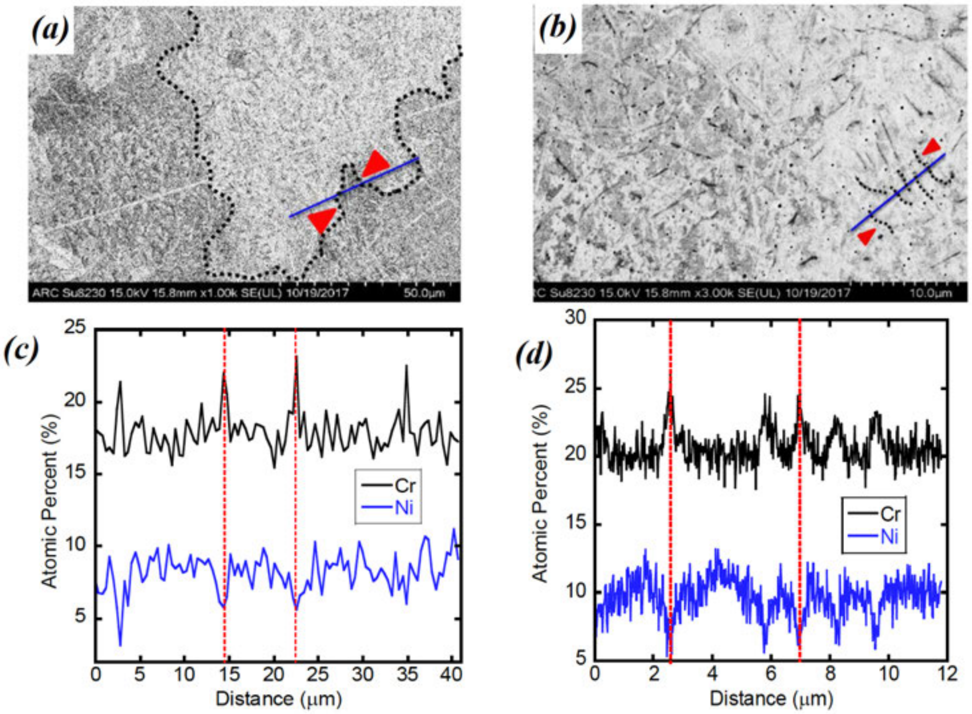

**Figure 5.** SEM micrographs and EDS line scans of a LENS® sample. The red dotted lines in **(a)** highlight the edges of a grain, and the correlating EDS line scan **(c)** shows an increase in Cr and decrease in Ni content. Similarly, **(b)** and **(d)** show an increase in Cr and decrease in Ni content at the boundaries of the rice-like structures, which are similar to cellular structures in these LENS materials.

### *Pinch welded samples*

The topography and KPFM images of 4 pinch welds shown in Figures 6 and 7 are prepared with the weld in the longitudinal orientation. On the left, the samples were measured uncharged and, on the right, the samples were measured after hydrogen charging, for both Figures 6 and 7. For Figure 6, the pinch welds were welded at 2900 A, and the weld is clearly visible in the topography images. Figure 7 shows samples that were welded at 4100 A, and the weld line is no longer visible due to continuous grain growth across the boundary. The surface potential images show drastic changes in the work function for the hydrogen charged samples (on the right in both Figures 6 and 7). The regions surrounding the grain boundaries and the weld line seem to indicate increased hydrogen content compared to the surrounding matrix. For the hydrogen charged pinch welds, care was taken to ensure that they were kept in a freezer between H-charging and imaging to inhibit hydrogen diffusion from the material.

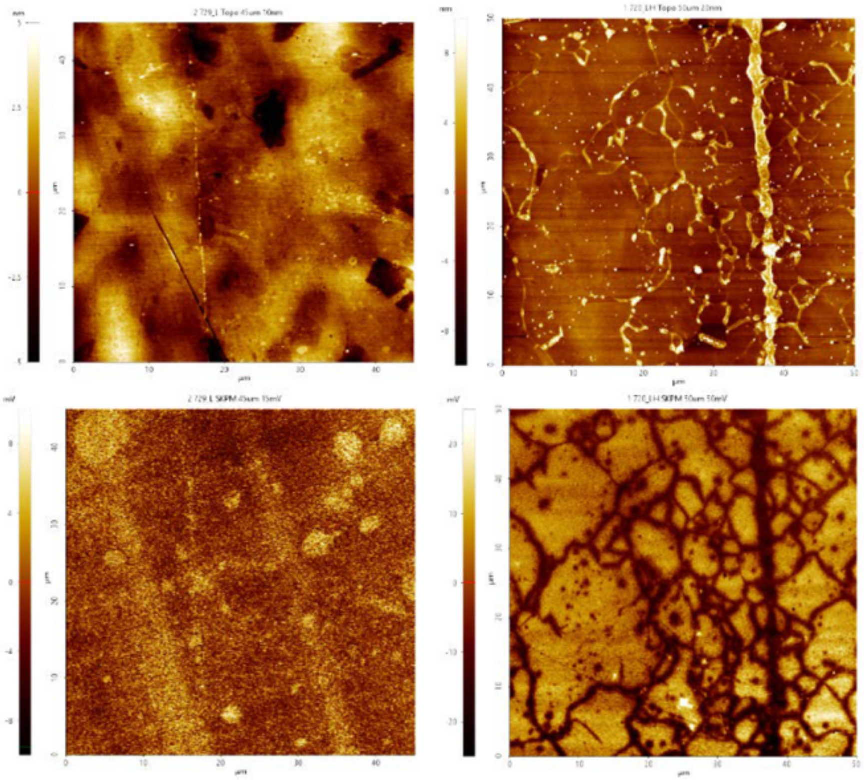

**Figure 6.** Two pinch weld samples with topography (top) and KPFM surface potential measurements (bottom) welded at 2900 A. The sample on the right was H-charged before imaging and shows clear surface potential variations around the weld line and surrounding grain boundaries.

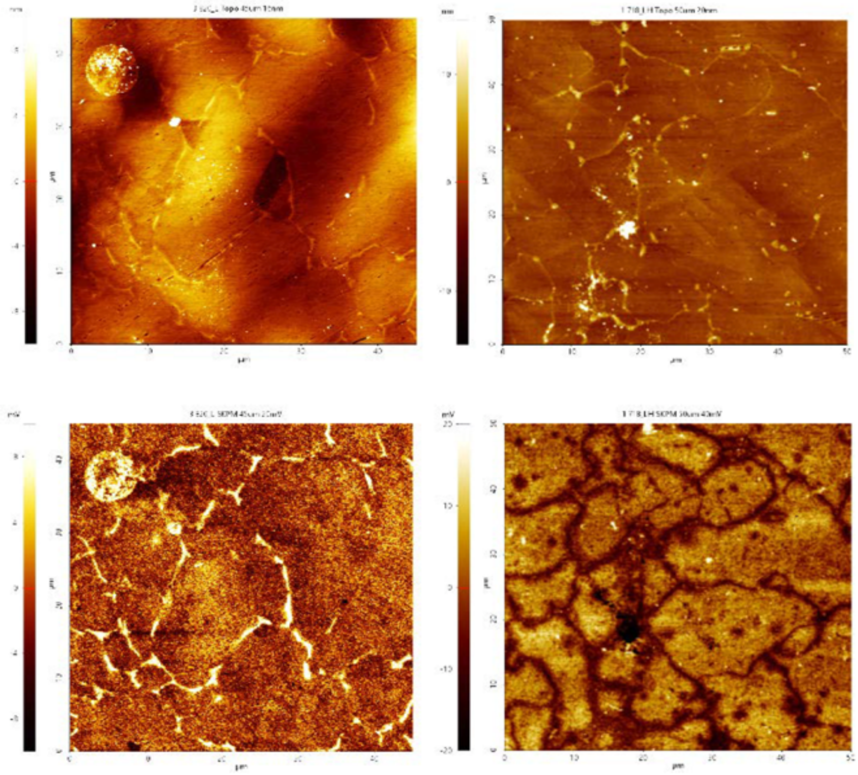

**Figure 7 (right).** Two pinch weld samples welded at 4100 A with topography **(top)** and KPFM surface potential measurements **(bottom).** The weld line is not visible as the grains grew across the boundary during the pinch process. The sample on the right was H-charged before imaging and shows clear surface potential variation around the surrounding grain boundaries.

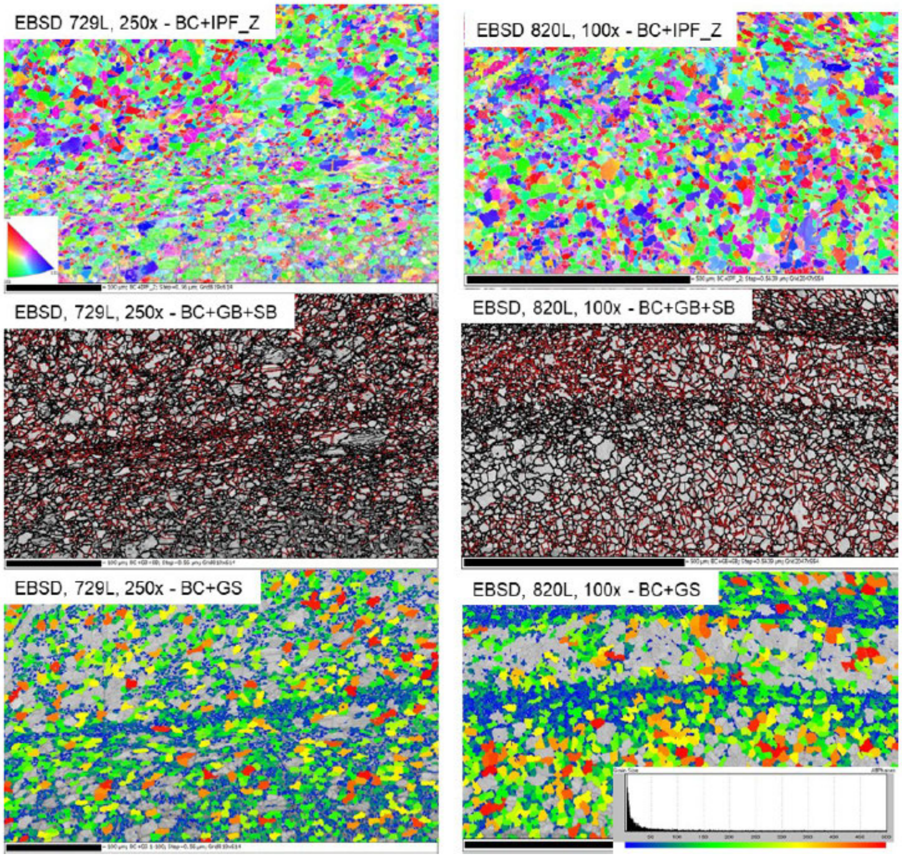

**Figure 8.** EBSD maps of a pinch weld welded at 2900 A (left) and one welded at 4100 A **(right).** Weld interface is oriented horizontally. Inverse pole figures in respect to the z direction **(top)** show the varying grain orientations along the weld; the band contrast together with grain boundaries and special boundaries **(middle BC+GB+SB)** show the outline of the grains; the grain size distribution map **(bottom)** shows the distribution of grain sizes along the weld.

Pinch welds performed at 2900 A and 4100 A were characterized using EBSD to investigate the grain size distributions and orientation with respect to the weld interface. These data are shown in Figure 8. Three types of maps were chosen to image the welds. Inverse pole figure (IPF) maps show various orientations of the grains and the many colors are representative of the grain orientation in respect to the Euler angles. The IPF maps are shown at the top of Figure 8 with the weld oriented horizontally. Band contrast (BC) images use the average intensity of the Kikuchi bands in regard to the overall intensity of the map to highlight the grain boundaries (GB) and special boundaries (SB). The GB maps are defined based on misorientation angles, and the SB are specifically oriented <111> 60° Twin boundaries, with sigma 3. These BC+GB+SB maps are shown in the middle of Figure 8. Finally, grain size (GS) maps use a color scale to indicate the sizes of grains, and these maps are shown at the bottom of Fig. 8. For the sample that was welded at a relatively low current value of 2900 A (Figure 8 left), the weld interface at the center propagating from the pinch point is clearly visible in all three maps. The IPF and GS distribution maps do not show any correlation with the growth of the grains at the weld interface. In contrast, the sample which was welded at a higher current (4100 A, Figure 8 right) displays interesting features in the EBSD maps. The band contrast image shows grains which are grouping together in bands parallel to the weld line. The GS map shows that very small grains lie close to the weld interface in a band, as shown by the blue colored grains, and in another band about 250 µm above the weld line. This behavior was observed, previously.[16] Future measurements need to be performed to understand the nature of the grain growth in respect to grain size and distribution, and to understand the changing strain fields occurring in the samples. In this manner, we hope to shed light on the segregation of hydrogen at the surface of stainless steel.

### *Electrochemical Studies*

An alternative technique for hydrogen loading is through electrochemical charging in a solution. In high pressure hydrogen charging, hydrogen gas dissociates and permeates through the surface layers of the material into the bulk at favorable temperatures and partial pressures. In electrochemical hydrogen charging, hydrogen ions are drawn to the sample surface from an electrolytic solution when the sample is held at a constant voltage or current in respect to a sacrificial anode and reference electrode. The capability of electrochemically charging the alloys *in situ* while being investigated by the AFM is currently being developed in similar fashion to a system developed by researchers at MIT.[17]

Two methods of electrochemical (EC) charging were employed during the course of study: bath solution charging and *in situ* charging. In the case of bath charging, the sample is immersed into an electrolyte and a current is applied between the sample (working electrode) and a Pt wire (counter electrode). Either the current or the voltage can be held constant, and cyclic voltammetry (CV) measurements can aid in determining the appropriate current or voltage values depending on the sample material and electrolyte resistance.

For the *in situ* method, a custom EC cell was 3D printed out of Teflon, to provide *in situ* hydrogen EC charging capabilities on our Park Systems AFM. The EC cell shown in Figure 9 allows for the bottom of a sample to be *in situ* hydrogen charged and its top surface probed for the presence of hydrogen using KPFM. Hydrogen charging is accomplished in the typical manner except that only one side of the sample is immersed in the electrolyte while the other is kept dry via an O-ring seal. The small volume (~15 mL) of this cell necessitates that the electrolyte solution be refreshed during hydrogen charging. This is accomplished by using a peristaltic pump to pump the solution from a reservoir, through the cell, and back into the reservoir; this process also vents any off-gas that is generated during the charging process. Internal spacers and notches allow for varying sample sizes. This design was motivated by recent work performed at MIT.[17]

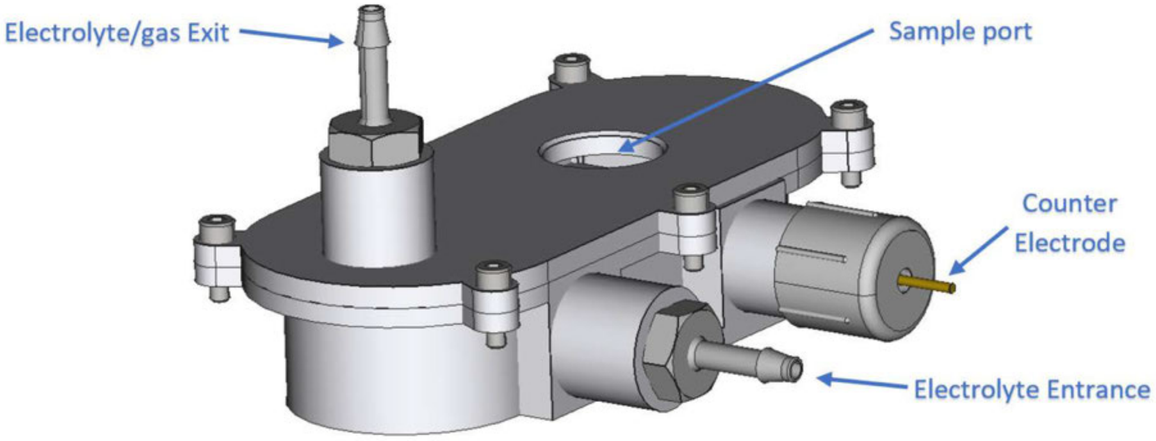

**Figure 9.** Drawing of EC cell designed specifically for our Park Systems AFM. The functions of each port are indicated.

### *Bath Hydrogen Charging*

In this work, thin specimens of Al 2219 rolled plate material were cut into coupons with dimensions of approximately 10×7×1 mm length, width, and thickness, respectively. A cursory search of the literature reveals efforts using KPFM to study other types of Al alloys, but none on Al 2219.[18-23] To cathodically charge the samples with hydrogen, the coupons were immersed in 1 M $H_2SO_4$ electrolyte at various current densities and durations. A Pt wire was used as the counter electrode, and a relative hydrogen electrode (RHE) for the reference electrode. The solution was deoxidized by bubbling nitrogen through the solution. Three runs, with a duration of 30 mins each, were conducted with 3 different coupons. The current density was varied from 0.5 mA/cm$^2$ to 2 mA/cm$^2$. The samples were subsequently polished before imaging with AFM and KPFM. These results were inconclusive, and it was decided that the samples should be polished before hydrogen loading, and that the current should be increased. After using CV measurements to determine the appropriate voltage, one pre-polished sample was held at -0.8 V for 30 minutes. The progressive appearance of bubbles at the surface of the charging face over time indicated that an initial oxygen reaction was replaced with hydrogen reduction and formation at the surface.

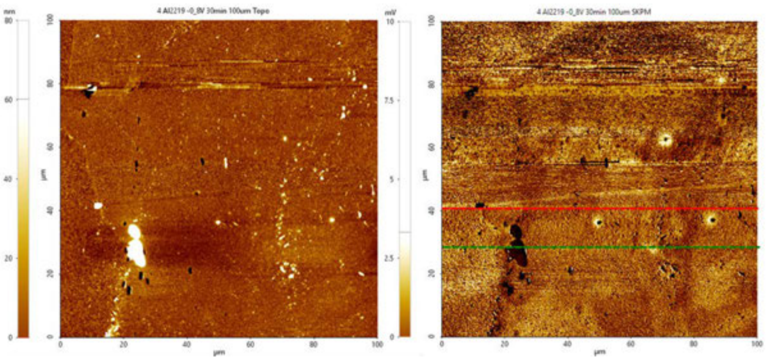

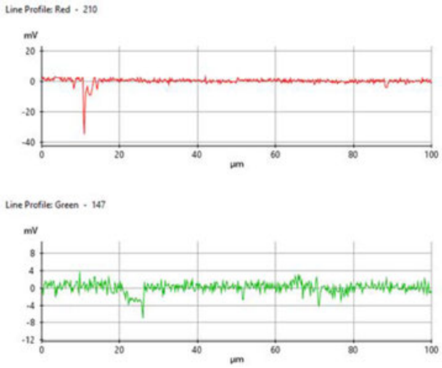

**Figure 10. (above left)** Topography of Al 2219 after hydrogen loading at -0.8 V in 1 M H2SO4 for 30 minutes **(above right)** corresponding surface potential from KPFM measurement shows change in voltage at surface defects.

*Above is surface potential line cross sections. AFM measurements were started 20 minutes after hydrogen loading and scanned from the bottom to the top.*

In no more than 20 minutes after being removed from the electrolytic solution, the sample was cleaned with high pressure CO$_2$ (known as “snow cleaning”[24]) under a blanket of nitrogen gas and loaded into the AFM environmental chamber. Figures 10 and 11 show the topography, at 100 µm$^2$ scan size, and surface potential measurements of the last sample which was kept at –0.8 V for 30 minutes. Compared to previous surface potential measurements of uncharged Al 2219, there are not significant differences between the change in surface potential for the charged and uncharged samples. The Al$_2$Cu precipitates are still showing a higher work function, which is indicated by the decrease in surface potential. In order for hydrogen effects to be observed on the surface of these materials and to clarify the role of hydrogen at surface defects, electrochemical charging conditions need to be optimized in future tests. To push the limits of resolution, 1 µm$^2$ scans were taken on the same sample 2 days after hydrogen loading and can be seen in Figure 12. The decrease in surface potential for the Al$_2$Cu precipitates is most likely due to an increased work function from the higher composition of Cu, and not likely caused by electrochemical hydrogen loading, since **(1)** the same decrease is observed in uncharged samples, and **(2)** copper is unlikely to hydride. These images are necessary, however, to show the changes due to hydrogen once conditions for electrochemical charging are optimized.

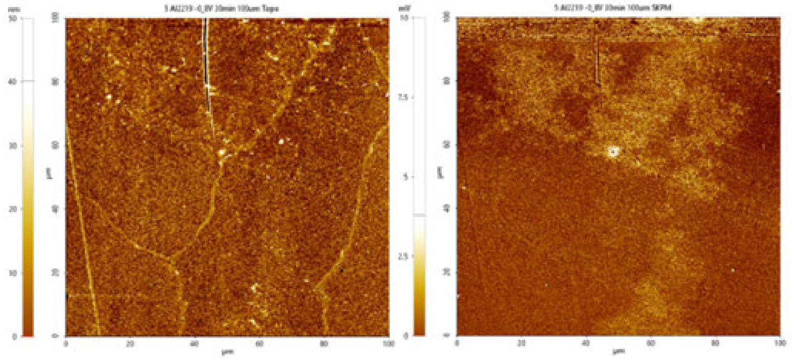

**Figure 11.** Topography **(above left)** and surface potential **(above right)** images of Al 2219 after hydrogen loading in 1 M H2SO4 at -0.8 V for 30 minutes. AFM measurements were started approximately 1 hour after hydrogen loading and scanned from the top to the bottom.

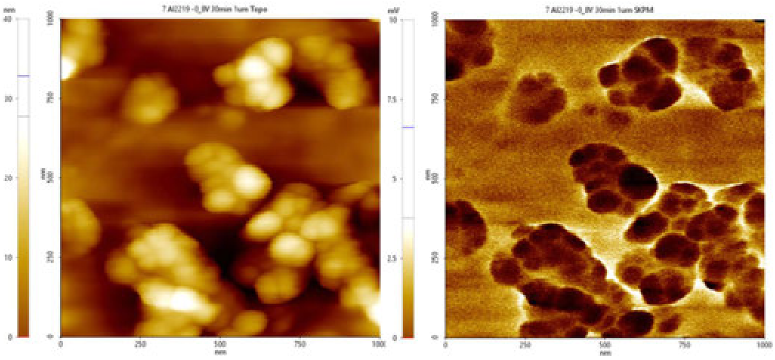

**Figure 12. (above left)** 1 µm2 topography and **(above right)** surface potential scans of Al 2219 sample 2 days after electrochemical hydrogen charging. The surface potential changes are similar to data reported on uncharged samples. The Al2Cu precipitates show an increased work function (decrease in surface potential).

### *In situ Hydrogen Charging*

Ferritic steel samples (alloy 4340 and quenched and tempered AT40) were precisely machined to thickness of approximately 0.75 mm using electric discharge machining (EDM), and lengths and widths of roughly 2.5 cm. The samples were polished to a mirror finish following standard metallographic procedures. The samples were loaded into the EC cell and sealed so that the cell was leak tight. Solutions of 0.1 M NaOH and 0.5 M $H_2SO_4$ were circulated through the cell, and various current values were used to find the optimal voltage. From CV studies, we found that current values as high as -130 mA were necessary to form hydrogen at the bottom side of the sample. Although various current values (5 – 130 mA) were applied for several lengths of time (1 – 64 hrs), the KPFM technique was unable to detect hydrogen segregating at the surface. Figure 13 shows the difference between before and after charging for both topography and surface potential images. Since the hydrogen occurred at one side of the sample, a diffusion gradient was established across the sample, and without the presence of significant trapping sites, the hydrogen species desorbed into the atmosphere on the exit side relatively quickly. The presence of hydrogen may be detected at the surface more easily if the experiment is repeated with a different material (e.g., a duplex stainless steel) or if the sample was under a gradient of residual stress intensity (i.e., notched bar).

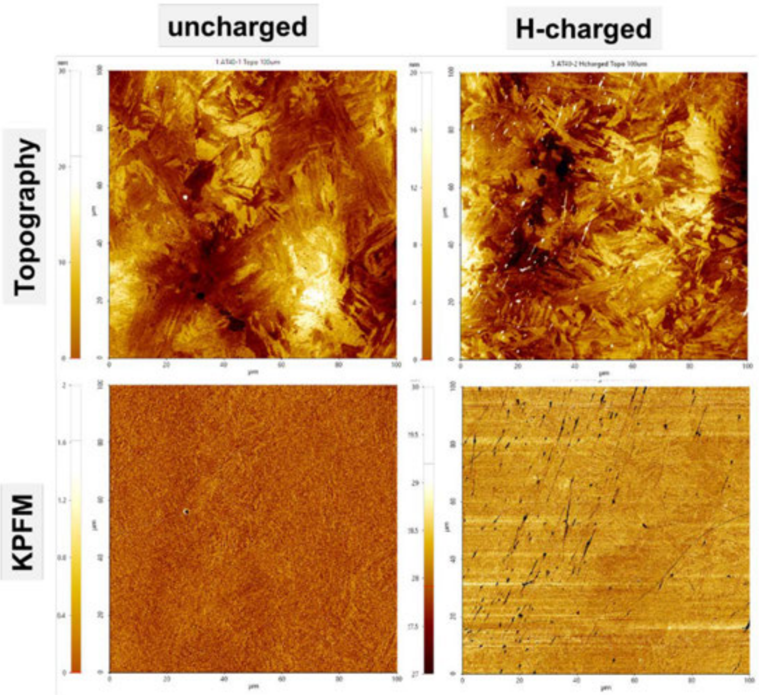

**Figure 13.** Topography **(top)** and surface potential images **(bottom)** of samples before **(left)** and after **(right)** charging. The subtle variations in surface potential is insufficient to demonstrate the presence of hydrogen trapped at the surface.

## FY2019 Accomplishments

- Characterized microstructural differences between forged, welded, LENS®, and pinch welded SS specimens.
- Developed sample prep methodology and nitrogen environment for AFM.
- Imaged hydrogen charged and uncharged samples and confirmed hydrogen segregation to grain and cell boundaries.
- Developed *in situ* electrochemical charging.

Further work is being done through a collaboration with hydrogen materials consortium to improve the electrochemical *in situ* charging conditions. Changes in the hydrogen concentration as a function of time will also be investigated with this *in situ* setup.

## Future Directions

- Incorporate electrochemical H-charging and time-resolved studies for H decay studies.
- Determine the role kinetics play in H-charging and redistribution after charging.
- Image specifically engineered defects and microstructures.
- Correlate direct imaging KPFM with indirect quantitative techniques for hydrogen studies.
- Parallel KPFM, TDS (thermal desorption spectroscopy), and magnetic force microscopy (MFM) studies.
- Develop system for deuterium/tritium work.
- Understand isotopic effects of deuterium/tritium.

## Publications/Presentations

1. J. D. McNamara, A. J. Duncan, M. J. Morgan, and P. S. Korinko, "Imaging hydrogen in stainless steel alloys by Kelvin probe force microscopy" Proc. ASME 2018 Pressure Vessels and Piping Conference, PVP2018, July 15-20, 2018, Prague, Czech Republic.
2. M. J. Morgan, D. Hitchcock, T. Krentz, J. McNamara and A. Duncan, "2017 Accomplishments – Tritium Aging Studies on Stainless Steel Weldments and Heat-Affected Zones," SRNL-STI-2018-00036, January, 2018, Savannah River National Laboratory, Savannah River Nuclear Solutions, LLC, Aiken, SC 29808
3. J. D. McNamara, A. J. Duncan, M. J. Morgan, and P. S. Korinko, "Kelvin Probe Force Microscopy for Imaging Hydrogen in Steel Alloys", AVS 64th International Symposium and Exhibition, Tampa, FL, November 2, 2017.
4. P. S. Korinko, "SRNL Welding Joining Site Update," SRNL-STI-2018-00024, welding IMOG, WAM FE, Sandia National lab, Jan 22-23, 2018.
5. P. S. Korinko, SRNL-STI-2018-00237, SRNL Welding and Joining Site Update, Wire Additive Manufacturing Focused Exchange and Welding JOWOG, May 21-25, 2018, AWE, Reading, Berkshire, England.

## Acronyms

| | |
|---|---|
| **AFM** | atomic force microscopy |
| **AM** | additive manufactured |
| **CPD** | contact potential difference |
| **EBSD** | electron backscatter diffraction |
| **EDS** | energy dispersive spectroscopy |
| **H** | hydrogen |
| **KPFM** | Kelvin probe force microscopy |
| **LENS®** | laser engineered net shaping |
| **MFM** | magnetic force microscopy |
| **PW** | pinch weld |
| **SS** | stainless steel |
| **TDS** | Thermal desorption spectroscopy |
| **TWIP** | twinning-induced plasticity |

## Total Number of Post-Doctoral Researchers

Two

## References

1. Caskey, Jr., G. R., Hirth, J. P., Oriani, R. W. and Smialowski, M., eds., Noyes Publication, Park Ridge, NJ, 1985, p. 822.
2. Koyama, M., Rohwerder, M., Tasan, C. C., Bashir, A., Akiyama, E., Takai, K., Raabe, D. and Tsuzaki, K. "Recent progress in microstructural hydrogen. Mapping in Steels: Quantification, kinetic analysis, and multi-scale characterisation," *Mater. Sci. Technol.* **33** (13), 1481 (2017).
3. Perng, T.-P. and Altstetter, C. J., "Hydrogen effects in austenitic stainless-steels," *Mater. Sci. Eng. A,* **129**(1), 99 (1990).
4. Wang, Y., Wang, X., Gong, J., Shen, L. and Dong, W., "Hydrogen embrittlement of catholically hydrogen-precharged 304L austenitic stainless steel: Effect of plastic pre-strain," *International Journal of Hydrogen Energy,* **39**(25), 13909 (2014).
5. Melitz, W., Shen, J., Kummel, A. C. and Lee, S., "Kelvin Probe Force Microscopy and Its Application," *Surf. Sci. Rep.* **66,** 1 (2011).
6. Hua, Z., An, B., Iijima, T., Gu, C. and Zheng, J. "The finding of crystallographic orientation dependence of hydrogen diffusion in austenitic stainless steel by scanning Kelvin probe force microscopy," *Scripta Mater.* **131,** 47 (2017).
7. Evers, S., Senoz, C. and Rohwerder, M., "Spatially resolved high sensitive measurement of hydrogen permeation by scanning Kelvin probe microscopy," *Electrochemica Acta* **110,** 534 (2013).
8. Senoz, C, Evers, S., Stratmann, M. and Rohwerder, M., "Scanning Kelvin Probe as a highly sensitive tool for detecting hydrogen permeation with high local resolution," *Electrochem. Commun.* **13,** 1542 (2011).
9. Evers, S., Senoz, C. and Rohwerder, M., "Hydrogen Detection in Metals: a Review and Introduction of a Kelvin Probe Approach," *Sci. Technol. Adv. Mater.* **14,** 014201 (2013).
10. Larignon, C., Alexis, J., Andrieu, E., Lacroix, L., Odemer, G. and Blanc, C., "Investigation of Kelvin Probe Force Microscopy Efficiency for the Detection of Hydrogen Ingress by Cathodic Charging in an Aluminium Alloy," *Script. Mater.* **68,** 479 (2013).
11. An, B., Hua, Z., Iijima, T., Gu, C., Zheng, J., Marchi, C. S., "Scanning Kelvin Probe Force Microsopy Study of Hydrogen Distribution and Evolution in Duplex Stainless Steel" *Proceedings from the ASME Pressure Vessels and Piping Conference*, Waikoloa, Hawaii, PVP2017-66121, (2017).
12. Korinko, P. S., Adams, T. M., Malene, S. H., Gill, D. and Smugeresky, J., "Laser Engineered Net Shaping® for Repair and Hydrogen Compatibility," *J. Welding,* **90,** 171 (2011).
13. Wang, Z., Palmer, T. A. and Beese, A. M., "Effect of processing parameters on microstructure and tensile properties of austenitic stainless steel 304L made by directed energy deposition additive manufacturing," *Acta Mater.* **110,** 226 (2016).
14. Ziętala, M., Durejko, T., Polański, M., Kunce, I., Plociński, T., Zieliński, M., Stępniowski, W., Czujko, T., Kurzydlowski, K. J., Bojar, Z., "The microstructure, mechanical properties and corrosion resistance of 316 L stainless steel fabricated using laser engineered net shaping," *Mater. Sci. Eng. A,* **677**, 1 (2010).
15. Wei, H. L., Mazumder, J. and DebRoy, T. "Evolution of solidification texture during additive manufacturing," *Sci. Rep*. **5**, 16446, (2015).
16. Korinko, P.S. and West, W.L. "Pinch Weld Evolution: A Phenomenological Model," WSRC-RP-2005-01762, September 2005, Savannah River National Laboratory, Aiken, SC 29808
17. J. Kim, and C. C. Tasan, *Int. J. Hydrogen Energy,* **44** (2019) pp. 6333-6343.
18. M. C. Lafouresse, M-L. de Bonfils-Lahovary, C. Charvillat, L. Oger, L. Laffont, C. Blanc, *J. Alloys and Compounds,* **722** (2017), pp. 760-766.
19. C. Larignon, J. Alexis, E. Andrieu, L. Lacroix, G. Odemer, C. Blanc, *Electrochim. Acta,* **110** (2013), pp. 484-490.
20. L. Oger, M. C. Lafouresse, G. Odemer, L. Peguet, C. Blanc, Mat. *Sci. Eng. A,* **706** (2017) pp. 126-135.
21. C. Larignon, J. Alexis, E. Andrieu, L. Lacroix, G. Odemer, C. Blanc, *Scripta Materialia*, **68** (2013) pp. 479-482.
22. N. Takamo, Mat. Sci. Eng. A, 483-484 (2008) pp. 336-339.
23. P. Rozenak, E. Sirois, B. Ladna, H. K. Birnbaum, and S. Spooner, *J. Alloys and Compounds*, **387** (2005) pp. 201-216.
24. R. Sherman, *Particulate Sci. Tech,* **25** (2007) pp. 37-57.

# Heat and Mass Transfer Study to Understand Thermal-Cycling Absorption Process (TCAP) Scale-Up Issues

**Project Team:** Steve Xiao, Ben Randall, Bob Rabun, Boone Thompson, Bruce Tatarchuk

**Subcontractor**: Auburn University

**Thrust Area**: Nuclear Deterrent

**Project Start Date:** October 1, 2018

**Project End Date:** September 30, 2019

*TCAP was invented by SRNL and is a world-leading technology in hydrogen isotope separation, a critical process for fusion energy development and scientific research. External interests/inquiries have been received for as high as a 1000-fold throughput increase over the currently available TCAP system. This study determined a major factor impacting TCAP column scale-up. A model derived by J. Calvin Giddings indicates that the combination of a coiled packed column and an increase in the column tube radius results in reduction of column separative performance.*

*Reevaluation of data from SRNL TCAP column testing performed in 2004 indicates that the results are consistent with the Giddings model.*

*Work with the Auburn University Center for Microfibrous Materials Manufacturing indicates that microfibrous entrapped sorbents (MFES) made from copper microfibers and Pd/K could resolve issues with channeling and improve heat transfer and cycle time in TCAP columns.*

## Objectives

Understand the fundamental physics of the efficiency losses previously noted during the 2004 HT-TCAP scale up and devise means to overcome them through the following:

- Determine the factors affecting and affected by TCAP gas mass transfer
- Determine the factors affecting and affected by TCAP heat transfer.

## Introduction

TCAP is a palladium-based chromatographic process invented by Myung Lee at SRNL in 1980 and is a world-leading technology in hydrogen isotope separation.[1,2] Hydrogen isotope separation is a critical process for fusion energy development and scientific research. External interests/inquiries have been received for as high as a 1000-fold throughput increase over the current TCAP system.

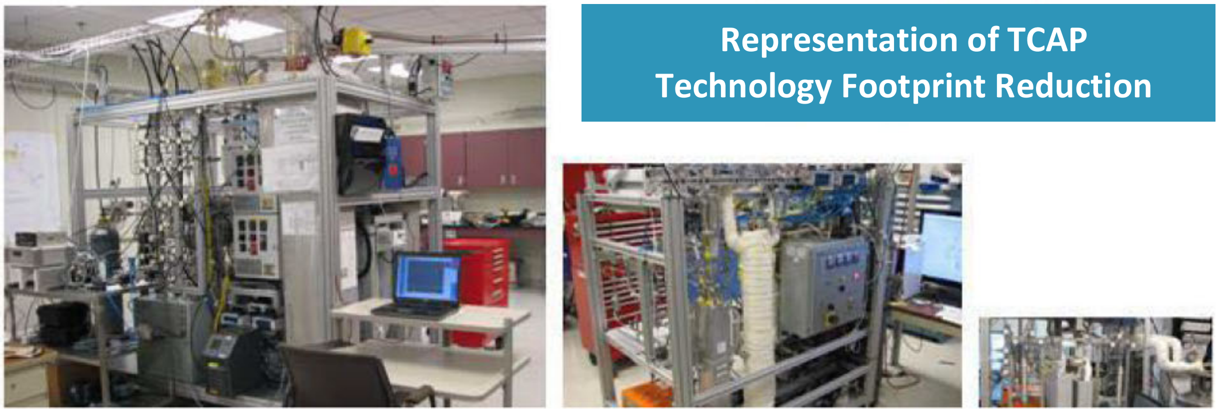

Representation of TCAP Technology Footprint Reduction

**Figure 1.** Successful Scale-down of TCAP systems

### *Success with TCAP Scale-down*

SRNL has been successful in scaling down the size of TCAP while maintaining the required capacity (Compact-TCAP, Mini-TCAP, Micro-TCAP).[3] Results from this study suggest that, among other improvements, some of the success of TCAP size-reduction efforts comes from reducing the tube diameter.

### *Issue with TCAP Scale-up*

TCAP scale-up has been more difficult. In 2004 a newly-installed, scaled-up hydrogen-tritium TCAP system (HT-TCAP) demonstrated unexpectedly low separative performance.[4,5] SRNL performed extensive testing to explain and improve HT-TCAP performance. With the results of this testing, the flowsheet and operating parameters were optimized allowing the project to be completed successfully and on time. However, though the immediate project concerns were addressed, an unexplained and substantial gap remained between the expected separation and the actual HT-TCAP performance.

This project seeks to develop a clear understanding of the issues affecting TCAP scaling and enable the application of SRNL TCAP technology to the need for very-large-scale hydrogen isotope separation infusion energy research, other nuclear applications, and environmental protection.

## Approach

- Performed an extensive review and evaluation of prior theoretical work, mathematical models, and experiments on chromatographic separation including palladium chromatography.[6-9]
- Reviewed and re-evaluated data and results from the 2004 tests in support of the HT-TCAP project.
- Worked with Auburn University to evaluate microfiber-entrapped sorbents for application to TCAP to improve heat transfer and potentially improve mass transfer.

## Results/Discussion

The review and evaluation of prior theoretical work, mathematical models, and experiments revealed that coiling of large-scale (vs. analytical scale) columns has been studied and reported by a small number of researchers. The most prolific, J. Calvin Giddings, in the 1960's, derived a mathematical model for the impact of coiled packed column dimensions on separation efficiency.[10-14] Tijssen in the 1970's also addressed coiling of chromatographic columns, but his work focused mainly on capillary and open-tube analytical columns and showed that coiling actually improved the resolution. However, both Giddings and Tijssen concluded that coiling and bending of packed columns decreases separation performance.[15-17]

The relationship developed by Giddings shows that coiling a packed column: **(1)** increases the HETP (height equivalent to a theoretical plate) of the column, reducing the number of stages and therefore reducing the efficiency, and **(2)** increases the negative impact of larger tube diameters.

$$H = \frac{7 v r_0^4}{12 R_0^2 \gamma D_g}$$

In this mathematical model, H or HETP is greatly dependent on the tube radius, $r_0$, as it is raised to the fourth power. The coil diameter, $R_0$, has an inverse and lesser effect, as it is only squared.

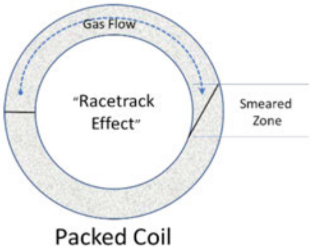

**Figure 2.** Illustration of the "Racetrack Effect" in coiled packed columns

**"Plate Theory" in Chromatography and HETP**

**In 1941,** Martin and Synge worked out a method of describing and modeling chromatographic separations using a distillation analogy and terminology (where "column" is a literal vertical column and the "height equivalent to a theoretical plate – HETP" is the height of column needed for one stage of separation). "Column", "plate", and other distillation terms are still used today to describe chromatographic systems. HETP remains a key measure of column and packing performance.

$$\text{HETP} = \frac{\textit{Total column length}}{\textit{Number of plates}}$$

**(smaller is more efficient)**

*A. J. P. Martin and R. L. M. Synge, "A Theory of Chromatography", Biochem. J. 35 (1941) pp. 1358-1364. For this and a companion work, they were awarded a Nobel prize.*

A detailed review and reanalysis of data from the 2004 testing performed during this project revealed that column geometry played a large role in TCAP separation capability.

In 2004 tests were run on straight and coiled 2" diameter columns, but the results of the two cases were not compared at that time.[18,19] Reevaluation of the data revealed that the length per stage (same as HETP) increased by almost a factor of 2.5 for the coiled column, 4.3" vs. 1.6" for the straight column.

Working with the Auburn University Center for Microfibrous Materials Manufacturing we determined that microfiber entrapped sorbents MFES made from copper microfibers (Figure 4) and Pd/K could:

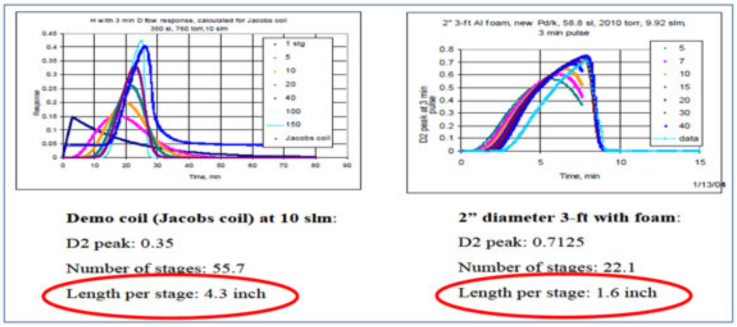

**Demo coil (Jacobs coil) at 10 slm:**
D2 peak: 0.35
Number of stages: 55.7
Length per stage: 4.3 inch

**2" diameter 3-ft with foam:**
D2 peak: 0.7125
Number of stages: 22.1
Length per stage: 1.6 inch

**Figure 3.** Comparison of coiled and straight 2" diameter column pulse tests showing an increase in HETP with coiling

- Reduce or eliminate the wall-to-packing resistance to heat transfer,
- Make the radial temperature profile of a column nearly isothermal,
- Reduce wall effects on gas velocity, and
- Reduce axial dispersion and flatten concentration profiles across the column.[20-23]

## FY2019 Accomplishments

- Discovered that coiling a packed column reduces separation efficiency compared to a straight column and amplifies the negative effect of increasing the tube diameter.

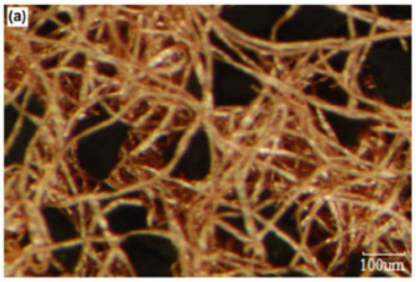

**Figure 4.** Microfibrous Entrapped Sorbent (MFES) using copper microfibers

- Determined from prior SRNL testing that the data from straight and coiled packed column testing are consistent with the model showing loss of separation efficiency with large diameter coils.
- Determined that MFES developed at Auburn University could improve TCAP performance by eliminating inhomogeneities such as channeling effects and by improving cycle time.

## Future Directions

- Apply report findings on column geometry, heat transfer, and MFES to new design of test column for scale-up testing.
- Test new concepts for reducing the negative impact of column coils and bends.

### Presentation

Presentation and paper at the April 2020 Technology of Fusion Energy (TOFE) meeting in Charleston, SC.

### References

1. M. W. Lee, "TCAP for Separation of Hydrogen Isotopes", USDOE Report DP-1660, also issued as Report No. DPST-83-82, 1983.
2. M. W. Lee, "Information on TCAP Useful to the Preparation of a Disclosure", Report No. DPST-82-1047, 1982.
3. Xin Xiao, L. Kit Heung and Henry T. Sessions, "Recent Advances in SRS on Hydrogen Isotope Separation Using Thermal Cycling Absorption Process", 2015, Fusion Science and Technology, 67:3, pp. 643-646.
4. Anita S. Poore, "HT-TCAP Protium-Deuterium (HD) Test Summary, Part I", WSRC-TR-2004-00274, May 2004.
5. Anita S. Poore, "Material and Process Characterization Testing Summary for HT-TCAP", WSRC-2004-00275, May 2004.
6. James Chadwick, "A Palladium Column for Concentrating Tritium from 2-Litre Mixtures of Tritium andHydrogen", U. K. Atomic Energy Authority Report, AERE 1/M47, 1958 .
7. E. Glueckauf and G. P. Kitt, "Gas Chromatographic Separations of Hydrogen Isotopes" in Vapour PhaseChromatography (D. H. Desty ed.), pp. 422-427, Butterworths Publications, Ltd., London, 1956.
8. E. Glueckauf and G. P. Kitt, inventors, "Improvements in or Relating to Separation of the Isotopes of Hydrogen", Patent, GB825934A, filed 1956-02-04, published 1959-10-23.
9. Carl O. Thomas and Hilton A. Smith, "Gas Chromatography with Hydrogen and Deuterium", J. Phys. Chem., 63, March 1959, pp. 427-431.
10. J. Calvin Giddings, "Coiled Columns and Resolution in Gas Chromatography", Journal of Chromatography, 3 (1960) pp. 520-523.
11. J. Calvin Giddings, "Nature of Gas Phase Mass Transfer in Gas Chromatography", Analytical Chemistry, Vol. 34, No. 10, September 1962, pp. 1186-1192.
12. J. Calvin Giddings, "Principles of Column Performance in Large Scale Gas Chromatography", Journal of Chromatographic Science, Volume 1, Issue 1, January 1963, pp. 12–21.
13. J. Calvin Giddings, "Plate Height in Coiled Columns", Journal of Chromatography, 16 (1964) pp. 444-447.
14. J. Calvin Giddings, "Practical Criterion for Minimum Coil Diameter in Gas Chromatography", Analytical Chemistry, Vol. 37, No. 12, November 1965, pp. 1580-1581.
15. R. Tijssen, "Effect of Column-Coiling on the Dispersion of Solutes in Gas Chromatography, Part I: Theory", Chromatographia, 3 (1970) pp. 525-531.
16. R. Tijssen and R. T. Wittebrood, "Effect of Column-Coiling on the Dispersion of Solutes in Gas Chromatography, Part II: Generalized Theory", 5 (1972) pp. 286-295.
17. R. Tijssen, "Axial Dispersion in Helically Coiled Open Columns for Chromatography", 1979, Technical University Delft, PhD Dissertation.
18. L.K. Heung et al, "Hydrogen Isotope Exchange Tests in Support of HT-TCAP", WSRC-TR-2004-00402, 2004, Savannah River Site.
19. L. K. Heung, G. C. Staack, J. E. Klein and W. D. Jacobs, "Tests of Isotopic Separation Efficiency of Palladium Packed Columns", Fusion Science and Technology, Vol. 54, Aug. 2008, pp. 391-394.
20. Ranjeeth Reddy Kalluri, "Microfibrous Entrapper Catalysts and Sorbents: Microstructured Heterogeneous Contacting Systems with Enhanced Efficiency", 2008, Auburn University, PhD Dissertation.
21. Min Sheng, Hongyun Yang, et. al., "Novel catalyst structures with enhanced heat transfer characteristics", Journal of Catalysis, 281, (2011), pp. 254–262.
22. Min Sheng, Hongyun Yang, "High conductivity catalyst structures for applications in exothermic reactions", Applied Catalysis A: General, 445– 446, (2012), pp. 143– 152.
23. Min Sheng, Donald R. Cahela, et. al., "Effective thermal conductivity and junction factor for sintered microfibrous materials", International Journal of Heat and Mass Transfer, 56, (2013), pp. 10–19.

### Acronyms

| | |
|---|---|
| **MFES** | MicroFibrous Entrapped Sorbents |
| **MFES** | Height Equivalent to a Theoretical Plate |
| **HT-TCAP** | Hydrogen-Tritium Thermal Cycling Absorption Process |
| **Pd/K** | Palladium coated on kieselguhr (diatomaceous earth) — the column packing material used in SRNL TCAP |
| **TCAP** | Thermal Cycling Absorption Process |

# Development of Poison Resistant Palladium Alloys for Hydrogen Processing

**Project Team:** K.L. Shanahan, S. Xiao, L. M. Angelette, A. B. Thompson, D. A. Hitchcock, M. D. Drory, G. C. Staack

**Thrust Area**: Nuclear Deterrent

**Project Start Date:** October 1, 2018

**Project End Date:** September 30, 2019

*This project successfully established SRNL synthetic capabilities for palladium binary and ternary alloys. These alloys were composed of elements that were hoped to give the material resistance to the poisoning effects of common hydrogen permeability poisons such as carbon monoxide and sulfur. Several experimental and operational difficulties were encountered and overcome during the first year of this project. The method established uses melting in a tube furnace at ~1700 °C to alloy the elements, followed by flattening and rolling the metal into thin foils. These foils were then characterized by scanning electron microscopy with energy-dispersive X-ray analysis, X-ray diffraction, and hydrogen absorption/desorption isotherm measurements.*

## Objectives

- Establish synthetic capability and/or identify external synthesis partner/subcontractor
- Synthesize representative alloys
- Characterize alloys

## Introduction

The SRNL Defense Programs Technology (DPT) Section did not have facilities to form new alloys for investigation. Therefore, an LDRD Project was proposed and accepted to establish alloy synthesis capabilities for the purpose of preparing poison-resistant palladium alloys. Synthetic capability has been achieved. Three Pd alloys have been prepared and characterized.

Palladium (Pd) alloys are formed by adding a wide variety of alloying elements to Pd. Alloys typically show altered hydrogen absorption/desorption characteristics that can have benefit to hydrogen isotope processes at the Savannah River Site (SRS). One aspect of this is poison resistance. Several gases or contaminants in gases can absorb on Pd-alloy materials and severely block hydrogen absorption or desorption properties. Two of particular interest are carbon monoxide (CO) and sulfur (S). Sulfur can be found in many gaseous compounds, but perhaps the most recognized is hydrogen sulfide ($H_2S$) or rotten-egg gas. Exposing Pd alloys to either of these two compounds results in an almost complete blocking of hydrogen absorption capability. CO can normally be removed by elevating the alloy's temperature to over 300 °C, but removal of surface S (formed by decomposition of $H_2S$) is difficult to achieve. Typically, in surface science studies the S is sputtered away with an argon ion gun or dissolved into the bulk by heating. The latter approach however, will alter the alloy characteristics in the same fashion as adding any other alloying element does.

At SRS there are two primary uses of Pd and a Pd-Ag alloy: Pd supported on kieselguhr is the base component of the TCAP process used to separate hydrogen isotopes, and Pd-23 at% Ag is the typical diffuser membrane material used to extract H isotopes from waste gas streams or from water-gas shift products. It would be advantageous to SRS (and other hydrogen purification process users) to have alloys that resist poisoning, as this allows for longer process lifetimes and the possibility of lower temperature operation (Pd-Ag membranes are typically operated at ~400 °C to prevent CO poisoning and beta-phase formation).

## Approach

After locating various potential synthetic facilities, both at SRNL and elsewhere, the most efficacious one was chosen. This turned out to be a melting process using a tube furnace located in SRNL (Figure 1). Synthetic capability was demonstrated initially by preparing a binary Pd-10% Rh alloy by melting a mixture of elements at ~1700 °C in a tube furnace. The alloy was characterized with SEM/EDX, XRD, and hydrogen isotherm determinations, and compared to prior research results obtained on foils made elsewhere. The comparison was highly favorable and thus indicated proceeding was warranted.

**Figure 1. Clockwise from upper left:** Tube Furnace, Operating Tube, Pd-Rh Alloy button, Rolled Pd-Rh foil

Subsequently, two ternary alloys were prepared, nominally $Pd_{0.86}Rh_{0.1}Y_{0.04}$ and $Pd_{0.84}Au_{0.15}Y_{0.01}$. In the first, the highly oxygen-reactive material Y was found to have picked up substantial oxygen, which formed an insoluble oxide. Procedural modification then solved this problem and the third ternary alloy was prepared. That alloy did still evidence a small oxide content. The choice of alloying elements was dictated by prior research in this area indicating Y offered CO-poisoning resistance and Au offered S-poisoning resistance if present in 15 at% or greater amount. The subsequent plan in following years was to expose these materials to the appropriate poisons and re-characterize their hydrogen isotherm characteristics to determine how much poison resistance had been conferred. Composition was to be optimized and possible other alloying elements tested to obtain maximized performance in membrane applications.

## Results/Discussion

This project was initially proposed as a multi-year project. The primary objectives of the first year were to establish alloy synthesis capability and make and test several alloys. Three alloys were synthesized and characterized in FY19; $Pd_{0.9}Rh_{0.1}$, $Pd_{0.86}Rh_{0.1}Y_{0.04}$, and $Pd_{0.84}Au_{0.15}Y_{0.01}$. The first was simply to establish that the alloy synthesis process developed under this project produced alloys of acceptable quality. This was shown by comparing to ones prepared by a University of Vermont chemist, Prof. T. Flanagan, under a prior research contract with SRNL. Figure 2a shows the Pd-Rh alloy's XRD compared to a Pd-Rh-V alloy supplied by Prof. Flanagan. Figure 3 shows the Pd-10%Rh foil's EDX elemental maps which show no chemical inhomogeneity, i.e. the alloy was fully alloyed. Figure 4 compared the 50 °C hydrogen isotherm with prior Flanagan results. The differences noted are well within normal experimental error for the synthetic process, and show the prepared alloy was of high quality.

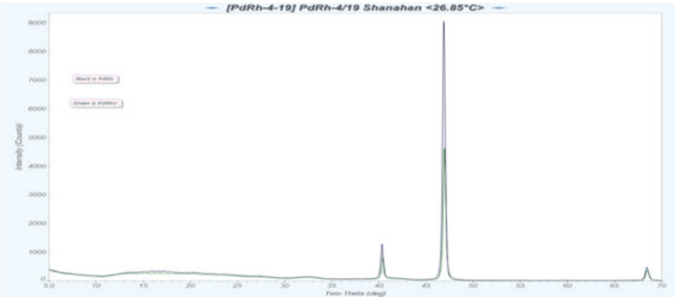

**Figure 2a.** XRD spectra from Pd-10%Rh (black) and Pd-Rh-V alloy (green)

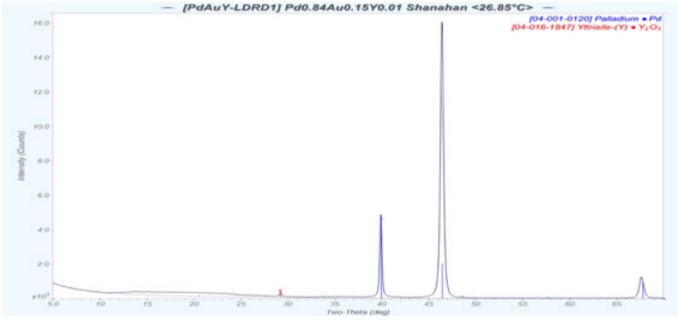

**Figure 2b.** XRD spectra from Pd-15%Au-1%Y alloy

The second alloy used a highly oxygen-reactive metal, yttrium (Y), and the synthetic procedure used did not adequately protect against this. Thus, the alloy was inhomogeneous and contained significant $Y_2O_3$. Subsequently, the procedure was altered, and the third alloy prepared. XRD results (Figure 2b) show the problem was mostly resolved with only a small oxide content being detected. Future research would include the use of a referential oxide getter in the melting furnace. Hydrogen isotherms (Figure 5) showed slightly sloping plateaux which typically indicates the need for the application of post-rolling annealing, which can also be done at SRNL.

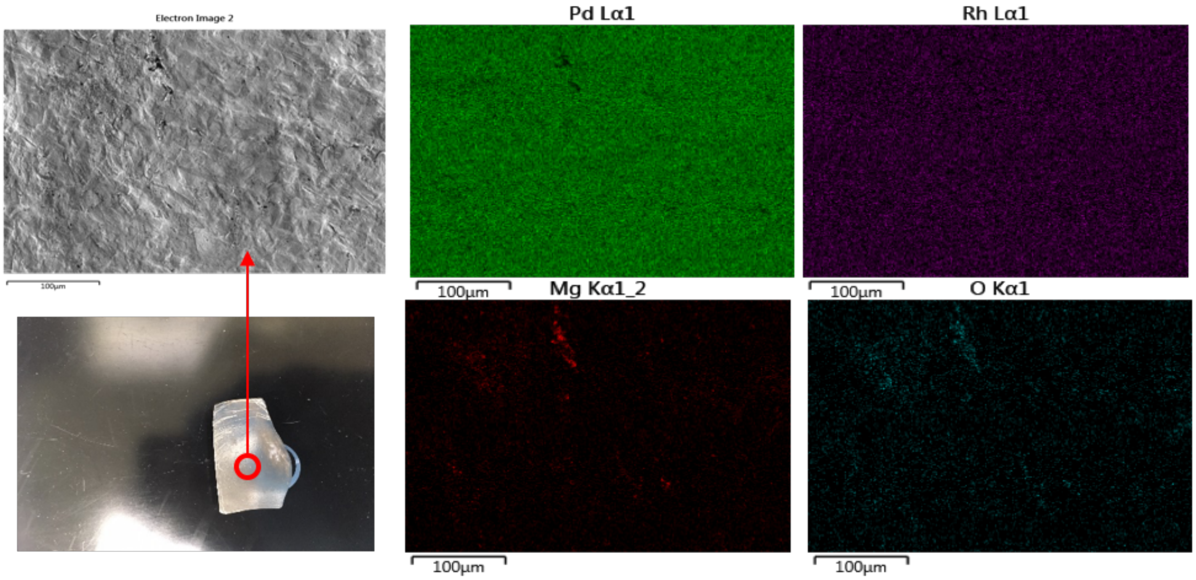

**Figure 3.** SEM/EDX analysis of indicated region of Pd—10%Rh foil **(circled on low magnification SEM photograph of the whole foil piece, lower left).** Elemental maps of Pd, Rh, Mg, and O shown. (MgO crucibles were used to prepare the alloys.)

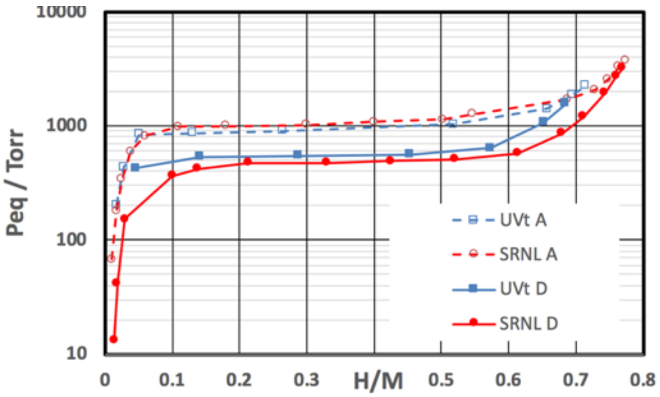

**Figure 4.** 50 °C Hydrogen Absorption/Desorption Isotherms from Pd-10%Rh alloy (Equilibrium Pressure vs. Hydrogen-to-Metal ratio). **(Red:** SRNL foil**, Blue:** U. Vermont (Ted Flanagan, UVt). **Dashed:** Absorption (A), **Solid:** Desorption (D).**)**

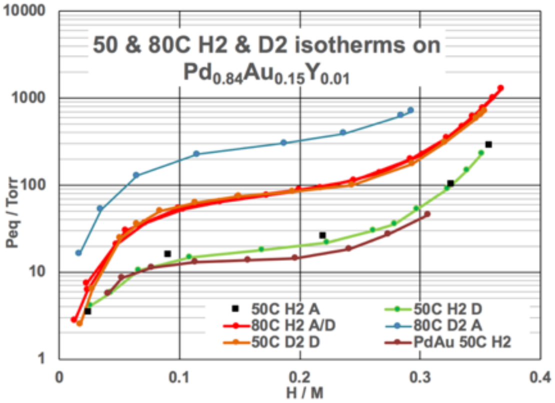

**Figure 5.** 50 and 80 °C Hydrogen and Deuterium Absorption/ Desorption Isotherms from Pd-15%Au-1%Y alloy (Equilibrium Pressure vs. Hydrogen-to-Metal ratio) compared to published Pd-15%Au (PdAu) alloy. **(Absorption (A), Desorption (D).)**

## FY2019 Accomplishments

- Identified the most efficacious way to develop SRNL alloy synthesis capability
- Prepared and characterized three alloys and resolved synthetic issues

### *Acronyms*

| | |
|---|---|
| **EDX** | Energy Dispersive X-ray (analysis) |
| **SEM** | Scanning Electron Microscopy |
| **TCAP** | Thermal Cycling Absorption Process |
| **XRD** | X-Ray Diffraction |

# Hydrogen Process Imaging

**Project Team:** G. Larsen, K. Nguyen,
K. Shanahan, M. Brown, K. Lawrence,
S. Murph

**Subcontractor**: The University of Georgia

**Thrust Area**: Nuclear Deterrent

**Project Start Date:** October 1, 2018

**Project End Date:** September 30, 2020

*The goal of this project is to develop a system that uses small magnetic fields to spatially and temporally determine the amount of hydrogen stored on a metal hydride bed within a processing facility environment. Such a capability does not currently exist – hydride beds are essentially "black boxes." Therefore, a magnetic hydrogen measurement system would be a unique tool to assess and optimize the performance of these critical hydrogen processing components. Magnetic characterization is also a promising technique for measuring hydrogen content in metal hydrides on the microscopic scale using magneto-optical techniques. The proposed research will investigate these issues to develop a hydride imaging for both bulk and microscopic scale to improve hydrogen processing.*

## Objectives

- Characterize the magnetic properties of the base metals (palladium, palladium alloys, lanthanum nickel aluminum alloys)
- Measure the changes in magnetic properties as a function of hydrogen loading in these materials
- Investigate novel hydrogen detection mechanisms via plasmonic effects
- Develop computational models to interpret experimental findings

## Introduction

Metal containers safely enclose hazardous materials and energies, but their opacity and conductivity limit the types of signals that can be used for chemical process measurement, imaging, and optimization. Magnetic fields are among the few physical phenomena that can easily penetrate through both insulating materials and metallic materials, such as stainless steel, aluminum, and others. Therefore, magnetic fields could be used to probe the contents of chemical process vessels made from such materials. For example, researchers from the University College London and the Atomic Weapons Establishment (AWE) have recently shown that is possible to collect magnetic images of conductive objects, even when fully enclosed inside of two metallic ferromagnetic containers.[1]

The degree to which a magnetic field interacts with a system depends on a number of factors, including chemical and electronic states, and this can reveal underlying chemical processes. One example is when a metal absorbs hydrogen, an electron is transferred from the absorbed hydrogen to the metal lattice. Depending on the original electronic configuration of the metal, these donated electrons will cause the metal to respond less strongly (e.g., Pd, LANA.75) or more strongly (e.g., Pu, U) to an applied magnetic field, and the response will scale with total amount of hydrogen absorbed (Figure 1).[2-5] In this way, magnetic measurements can be used to detect hydrogen content of metals, even when they are enclosed inside of containers.

Magnetic characterization is a promising method for tracking and trending hydrogen adsorption on metal hydride beds, and unlike neutron imaging,[6] it could be straightforward to adapt the technique to applications outside of the laboratory. However, additional research is needed to demonstrate the use of magnetic measurements for assessing and imaging hydrides in process environments. Additionally, in-situ measurements of hydrogen loading on the microscopic scale are challenging, and the use of magneto-optical techniques could enable localized imaging of metal-hydrogen systems that have previously escaped visualization. The goal of the proposed research is to establish the practicality of these concepts.

## Approach

The first task of this project is to establish an in-house magnetic characterization system to measure the magnetic properties of metals and metal hydrides. This will be done using AC susceptibility and a magneto-optical Kerr effect (MOKE) systems. These experimental geometries are readily adaptable to Sieverts instruments, which are commonly used for hydrogen sorption experiments. These systems, when coupled together, can then be used to examine the effects that hydrogen process variations (e.g., isotope, temperature, aging) may have on magnetic properties of metals and hydrides. Finally, the knowledge gained from these experiments will guide the development of process imaging systems that utilize changes in magnetic properties for visualization of hydrogen content.

## Results/Discussion

The objectives for this fiscal year have all been met. The magnetic susceptibilities of the base metals (Pd, LANA.75) and process metals (stainless steels) have been measured, and it was found that base metals have significant susceptibilities in comparison to the process metals. The magnetic susceptibilities of Pd and LANA.75 were measured as a function of hydrogen loading, and both were found to decrease with hydrogen content. Notably, the LANA.75 hydrogen loading experiments were done within stainless steel vessels, demonstrating that measurements can be done through opaque metal containers. MOKE measurements on Pd and Pd alloys in inert and hydrogen environments were conducted. Hydrogen absorption within PdCo alloys generated a ferromagnetic to paramagnetic transition. Plasmonic and spin transport effects of hydrogen absorption were also examined, which led to the development of new and novel hydrogen sensors. The electromagnetic behavior of the hydrogen sensors were examined computationally through finite-difference-time-domain simulations.

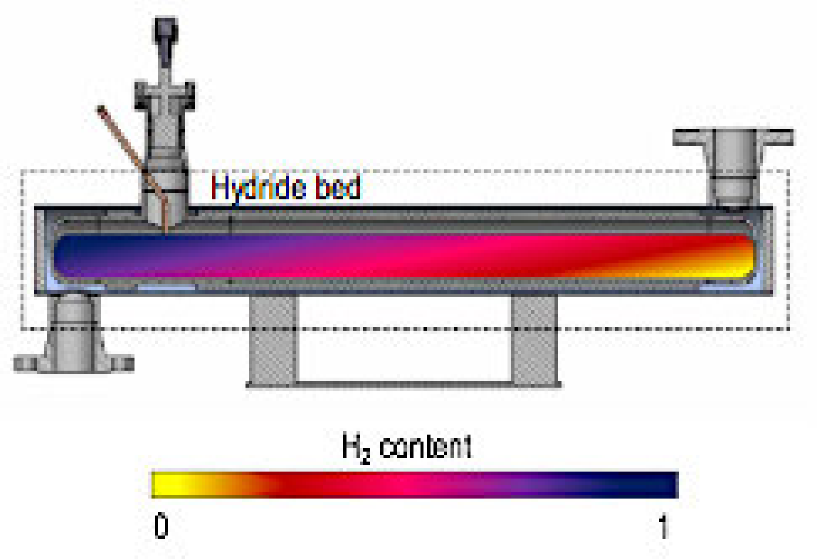

**Figure 1.** Conceptual schematic of a hydride bed imaging system

## FY2019 Accomplishments

- Demonstrated that magnetic measurements can be used to detect hydrogen in metals enclosed inside of metal vessels
- Utilized novel magneto-optical effects to measure hydrogen in metals using laser light
- Developed new optical ultrafast hydrogen sensors with a record response time of 90 ms. The previous record, reported May 2019 in *Nature Materials*, was 300 ms.

## Future Directions

- Evaluate the effects of parameter variation on magnetic measurements of hydrides
- Incorporate knowledge gained to develop an imaging system using bulk measurements and magneto-optical effects
- Continue to investigate hydrogen-induced modulation of novel phenomena

## Publications/Presentations

1. Geng, Rugang, et al. "Magnetically tunable organic semiconductors with superparamagnetic nanoparticles." Materials Horizons (2019).
2. Luong, Hoang Mai, et al. "Plasmonic sensing of hydrogen in Pd nano-hole arrays." Plasmonics: Design, Materials, Fabrication, Characterization, and Applications XVII. Vol. 11082. International Society for Optics and Photonics, 2019.
3. “Hydrogen sensing in Pd hole arrays and Pd patchy particles” *in preparation.*
4. “Ultrafast Hydrogen Sensing in PdCo patchy particles” *in preparation.*
5. G. Larsen, “Applications of Electromagnetic Fields for Tritium Processing,” IMOG meeting, Aiken, SC. May 15 2019.
6. G. Larsen, “Plasmonic and Magneto-Optical Sensing of Hydrogen in Pd Nano-hole Arrays and Pd-Co Thin Films,” SPIE Optics + Photonics, San Diego, CA. August 15 2019.
7. (*Invited*) G. Larsen, “Exploring the Interactions Between Light and Materials for Chemical Processing,” Augusta University Materials Science Research Seminar, Augusta, GA September 27, 2019.

## References

1. Darrer, B.J., et al., Magnetic Imaging: a New Tool for UK National Nuclear Security. Scientific Reports, 2015. **5**: p. 7944.
2. Termsuksawad, P., et al., Measurement of hydrogen in alloys by magnetic and electronic techniques. Journal of alloys and compounds, 2004. **373**(1): p. 86-95.
3. Akamaru, S., M. Hara, and M. Matsuyama, In situ measurement of alternating current magnetic susceptibility of Pd–hydrogen system for determination of hydrogen concentration in bulk. Review of Scientific Instruments, 2012. **83**(7): p. 075102.
4. Kim, J.W., et al., Detecting low concentrations of plutonium hydride with magnetization measurements. Journal of Applied Physics, 2015. **117**(5): p. 053905.
5. Gruen, D.M., Magnetic Properties of Uranium Hydride. The Journal of Chemical Physics, 1955. **23**(9): p. 1708-1710.
6. Jacobson, D.L., et al., Neutron imaging studies of metal-hydride storage beds. International Journal of Hydrogen Energy, 2010. **35**(23): p. 12837-12845.

## Acronyms

| | |
|---|---|
| **AWE** | Atomic Weapons Establishment |
| **LANA.75** | lanthanum nickel aluminum alloy |
| **MOKE** | magneto-optical Kerr effect |

## Intellectual Property

Two Invention Disclosures in Development

## Student Researches

Two Graduate Students — Supported at The University of Georgia

# Time Domain Thermoreflectance and Photodeflection Signatures of He Bubbles in Metal

**Project Team:** Eliel Villa-Aleman (Primary), Amanda L. Houk, Don D. Dick, Dale A. Hitchcock, Paul S. Korinko

**Thrust Area**: Nuclear Deterrent

**Project Start Date:** October 1, 2018

**Project End Date:** September 30, 2020

*The mechanical properties of the steel and weldments for different components are affected by the formation of helium bubbles as a result of tritium decay. Therefore, periodic analyses of metals exposed to tritium gas are conducted to determine structural defects and temporal damage from tritium gas decay and He precipitation. Transmission electron microscopy (TEM) and autoradiography are the current analytical methods for the evaluation of metal damage. These methods are functional after several years of damage to the crystal lattice where $^3$He bubble formation damage can be seen with TEM. New analytical methods that can assess the damage to the crystal lattice early during the exposure to tritium are highly sought to ascertain the effects of material processing and tritium interactions. Further, simple sample preparation, compared to TEM, at a significantly reduced cost is highly desirable. A pump-probe laser technique using a femtosecond laser has been demonstrated to measure the thermal diffusivity of different materials. The time domain thermoreflectance (TDTR) laser setup can provide thermal diffusivity and phonon lifetime, which can be correlated with lattice damage. This advanced nonlinear optical technique will enable measurements of nanostructure damage in the metal before and after tritium exposure within a year.*

## Objectives

- Develop a technology to measure lattice damage from He bubbles based on thermal diffusivity.
- Demonstrate that a pump-probe experiment with a high repetition rate femtosecond laser can be used to characterize the metal lattice.
- Design and build experimental breadboard for time domain thermoreflectance (TDTR).
- Design container for tritiated samples and test materials with known damage in a clean laboratory.

## Introduction

Periodic analyses of reservoirs filled with tritium are conducted at the Tritium Facility to determine the effects of tritium to the stainless steel and the temporal damage from He precipitation (Figure 1a). The mechanical properties of the walls and pinch weld of the tritium vessels are affected by the tritium decay resulting in the formation of He bubbles (Figure 1b). Transmission electron microscopy (TEM) and autoradiography are the current analytical methods for the evaluation of the reservoir metal. These methods are functional after several years of damage to the crystal lattice where $^3$He bubble formation damage can be seen with TEM (Figure 1c and d). New analytical methods that can assess the damage to the

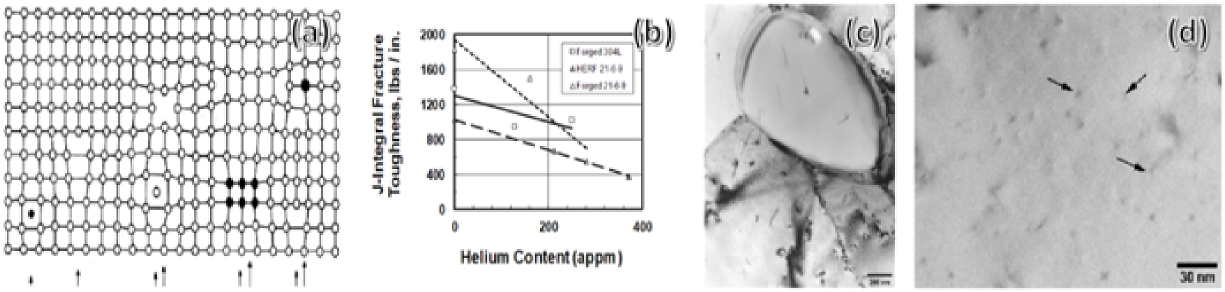

**Figure 1. (a)** Defects**, (b)** tritium damage impact on mechanical properties and **(c and d)** TEM images of the He bubbles.

crystal lattice early during the exposure are highly sought to ascertain the effects of material processing and tritium interactions. Further, simple sample preparation, compared to TEM, can be done at a significantly reduced cost. An ultrafast pump-probe laser technique is an innovative approach to this problem, where only 20 μm of material is required for analysis.

The time domain thermoreflectance (TDTR) technique will enable measurements of nanostructure damage in the metal before and after tritium exposure within a year. If this work is successful it will result in significant savings to the program (short turnaround analysis) and could help provide new directions for research on new materials, effects of processing, metal coatings and new designs for tritium storage systems. This work is also applicable to other tritium production and storage products, such as tritium-producing burnable absorber rods (TPBARS). This new technology will enhance SRNL's reputation as the leader for tritium storage research through years to come, which can result in significant funding from NNSA Weapons Programs. This report discusses current efforts in the design and development of the TDTR technique and the application to material characterization.

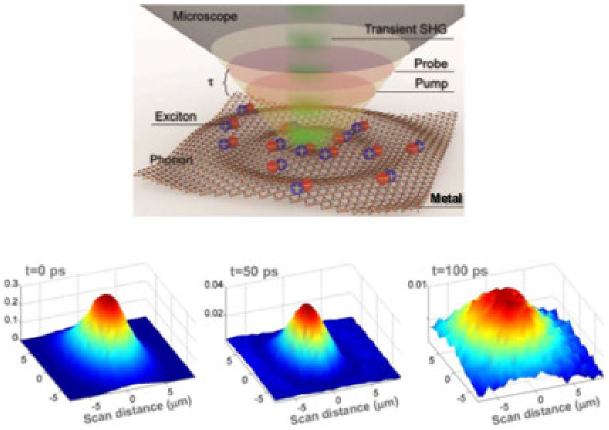

**Figure 2.** The pump-probe temporal surface dynamics

## Approach

Paddock *et al.* [1] in 1986 demonstrated for the first-time thermal diffusivity measurements from thin metal films using picosecond transient thermoreflectance to measure the thermal properties of metal films as thin as 100 nm. The thermal conductivity of the material is based on an ultrafast heating pulse inducing a change in the index of refraction of the material, and therefore a change in the optical properties. The ultrafast pump-probe technique is a two-laser beam technique that depends on one laser for heating the surface (pump), while another laser probes the heating effect on the material via reflection (Figure 2). Technology has evolved using a femtosecond laser instead of a picosecond laser, different colors for the pump and probe (better discrimination) and the optical modulation of the laser beam to enhance the signal-to-noise ratio. Additional improvements have been added with the interference of two optical beams reflected from the front surface and scattering depth. These improvements have resulted in the understanding of thermal properties of nanoparticles with dimensions less than 10 nm. Other variants include the ultrafast demagnetization of a sample while probing its recovery, such as the magneto-optical Kerr effect.

The advances in pump-probe technologies can be used to demonstrate the detection and quantification of He bubbles in steel and other metals. The beta decay of tritium results in the formation of $^3$He, which precipitates in bubbles. The $^3$He precipitates damage the metal crystal lattice producing phonon scattering points. Phonons (collective excitation in a periodic, elastic arrangement of atoms or molecules in condensed matter) produced during the laser heating pulse travels through the crystal lattice until thermalization. The presence of defects in the lattice shortens the phonon lifetime. This effect will be valuable to determine the crystal lattice damage by the beta decay and precipitation of He bubbles.

Since metals do not show Raman bands, the best option is to measure the phonon lifetime based on thermal conductivity. Previous work by Weisensee *et al.* [2] measured the effect of ion irradiation on the thermal conductivity of $UO_2$ and $U_3O_8$ using TDTR. Thermal conductivity measurements via TDTR were also used to characterize radiation-induced damage of ZIRLO [3], a low oxidation Zircaloy, and in silicon. Lattice impurities have been shown to affect the thermal conductivity of materials. For instance, oxygen impurities changed the thermal conductivity of beta-$Si_3N_4$ [4] from 120 W/m-K to 88 W/m-K.

## Results/Discussion

A TDTR setup was assembled on a laser table adjacent to the Astrella laser to take advantage of the Vitara oscillator laser (80 MHz, 35 fs) embedded within the Astrella laser system. Our TDTR setup was developed as a two-tint pump-probe technique, meaning the pump and probe wavelengths are split into two beams from a single broadband beam and the wavelengths of the two beams are only separated by ~10 nm [5]. In addition, to the assembly and alignment of the TDTR setup, programming to control the delay stage, lock-in amplifier and spectrograph is underway. Thermal code is also being written to extract thermal conductivity and capacitance information from the collected TDTR data. Figure 3a shows the schematic of our TDTR setup and Figure 3b shows a photo of our actual laboratory setup.

A sample cell tested by the SRNL/Defense Programs to transport tritiated materials in an inert, argon atmosphere has been selected as a sample holder for this program. A plan for the transfer of tritium-loaded samples to a clean laboratory was discussed with Radiological Protection and has been approved. In addition, discussions have occurred with the Tritium Facility resulting in the preparation of tritiated samples for delivery to SRNL.

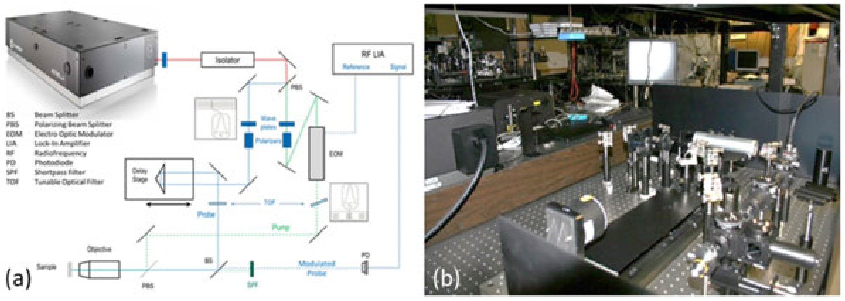

**Figure 3. (a)** Pump-probe experimental setup (TDTR) under development and **(b)** actual pump-probe TDTR experimental setup under development.

## FY2019 Accomplishments

- Different designs for a TDRD setup were evaluated for this project.
- A system based on a single broadband wavelength laser with two filters (two-tint) was chosen for this project.
- An existent optical table from another organization was moved to the Advanced Spectroscopy Laboratory (ASL) for this project.
- Components for TDRD breadboard were procured.
- The TDRD setup was assembled next to the Astrella laser to take advantage of the embedded 80 MHz, 35 fs oscillator laser.
- Initial laser beam alignment through the TDRD system completed.
- Programming to control stage, lock-in amplifier and spectrograph is underway.
- A cell tested by the SRNL/Defense Programs to transport tritiated materials in an argon atmosphere was selected as a sampler for this program.
- A plan for the transfer of tritium-loaded samples to a clean laboratory was discussed with RadCon and has been approved.
- Discussions with the Tritium Facility resulted in the preparation of samples with tritium for delivery to SRNL.

## Future Directions

- The thermal conductivity and capacitance will be measured for several materials to ensure the instrument is properly calibrated.
- Possible technical issues arising from materials held in a cell will be investigated.
- Samples with known dosage and time exposed to tritium will be investigated.
- A different TDTR setup using the 2nd harmonic of the fundamental will be investigated by inserting a doubling crystal or modifying existing equipment.

## Publication/Presentation

1. "Time Domain Thermoreflectance (TDTR) Signatures of He Bubbles in Metals", (presentation), 12th International Conference on Tritium Science & Technology, Busan, Korea, April 22-26, 2019.

## References

1. C.A. Paddock and G.L. Eesley, "Transient thermoreflectance from thin metal films", *J. Appl. Phys.,* 60 (1), **1986,** 285-290.
2. P.B. Weisensee, J.P. Feser, and D.G. Cahill, "Effect of ion irradiation on the thermal conductivity of UO2 and U3O8 epitaxial layers", *J. Nucl. Mater.,* 443, **2013,** 212-217.
3. R. Cheaito, C.S. Gorham, A. Misra, K. Hattar, and P.E. Hopkins, "Thermal conductivity measurements via time-domain thermoreflectance for the characterization of radiation induced damage", *J. Mater. Res.,* 30(09), **2015,** 1403-1412.
4. H. Yokota and M. Ibukiyama, "Effect of lattice impurities on the thermal conductivity of β-$Si_3N_4$*", J. Eur. Ceram. Soc.,* 23(1), **2003,** 55-60.
5. K. Kang, Y.K. Koh, C. Chiritescu, X. Zheng, and D.G. Cahill, "Two-tint pump-probe measurements using a femtosecond laser oscillator and sharp-edged optical filters", *Rev. Sci. Instrum.,* 79, **2008,** 114901.

## Acronyms

| | |
|---|---|
| **ASL** | Advanced Spectroscopy Laboratory |
| **He** | Helium |
| **TDTR** | Time Domain Thermoreflectance |
| **TEM** | Transmission Electron Microscopy |
| **TPBARS** | Tritium-Producing Burnable Absorber Rods |

## Total Number of Post-Doctoral Researchers

One, on-site at SRNL

# SECURE ENERGY AND MANUFACTURING

# Hybrid Thermochemical Hydrogen Production

**Project Team:** H. Colón-Mercado,
M. Gorensek, A. Thompson
SRC – M. Elvington, Prabhu Ganesan
USC – J. Weidner, J. Weiss, B. Meekins,
B. Tavakoli, J. Weiss, V. Gopal, L. Murdock

**Subcontractor**: University of South Carolina (USC); Savannah River Consulting (SRC)

**Thrust Area**: Secure Energy & Manufacturing

**Project Start Date:** October 1, 2017

**Project End Date:** September 30, 2019

*The Hybrid Sulfur (HyS) process is a promising thermochemical water-splitting cycle with global scale hydrogen production potential. The $SO_2$-depolarized electrolyzer (SDE) is a critical component of the cycle. At the core of the SDE is the membrane-electrode assembly (MEA), which consists of a polymer electrolyte membrane (PEM) sandwiched between two electrocatalyst layers. New electrocatalyst and membrane materials are being developed with the goals of improving the electrolyzer performance and extending the lifetime of the MEA. A high-throughput methodology is being developed to screen potential candidates based on Pt and Au thin films prepared through physical vapor deposition. $SO_2$ oxidation reaction kinetics are being analyzed for the novel catalysts and compared to the state-of-the-art, Pt/C. In addition, advanced polymer electrolyte membranes of polybenzimidazole (PBI) are utilized, which have shown superior performance in comparison to the state-of-the-art, Nafion®. These catalysts and membranes will be combined to produce high performance MEAs.*

## Objectives

### Electrocatalyst Development

- ○ Develop High-throughput catalyst screening methodology
- ○ Develop carbon-supported catalysts

### Membrane Development

- ○ Develop optimized membranes
- ○ Membrane testing

### Electrolyzer Performance Evaluation

- ○ Membrane electrode assembly fabrication
- ○ Evaluate material performance in electrolyzer

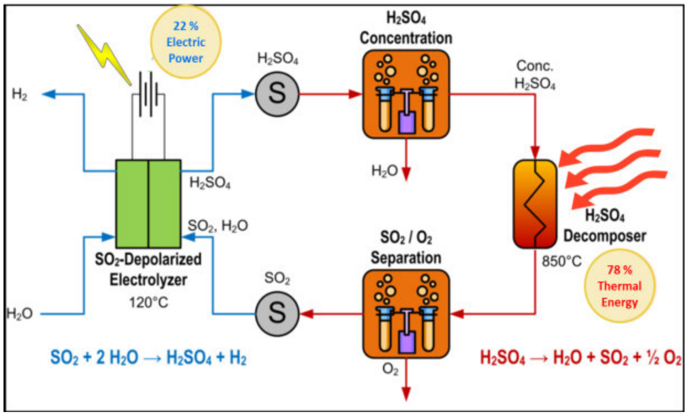

**Figure 1.** Simplified schematic of the HyS process.

## Introduction

There exists a significant and growing need for clean, efficient, and large-scale hydrogen production. Using high temperature heat, thermochemical cycles can provide an energy-efficient route for hydrogen production. The HyS process is a promising thermochemical water-splitting cycle with significant scalability. The HyS process, one of the most researched thermochemical cycles, is a sulfur-based water-splitting cycle which contains a low temperature electrolysis step, and thus can be considered an electrochemical and thermochemical hybrid process. In the HyS process, $H_2SO_4$ is thermally decomposed at high temperature (> 600 °C), producing $SO_2$ [r1]. $SO_2$ and $H_2O$ enter the SDE where $SO_2$ is oxidized to form $H_2SO_4$ and $H^+$ at the anode [r2], while at the cathode, $H^+$ is reduced to form $H_2$ [r3]. The overall electrochemical reaction consists of the production of $H_2SO_4$ and $H_2$ [r4], while the entire cycle produces $H_2$ and $O_2$ from $H_2O$ with no side products [r5]. Figure 1 shows a simplified schematic of the overall process and the main chemical reactions taking place.

| | | |
|---|---|---|
| $H_2SO_4 \rightarrow SO_2 + \frac{1}{2}O_2 + H_2O$ | Thermochemical Step | [r1] |
| $SO_2 + 2H_2O \rightarrow H_2SO_4 + 2H^+ + 2e^-$ | Anode Electrochemical Step | [r2] |
| $2H^+ + 2e^- \rightarrow H_2$ | Cathode Electrochemical Step | [r3] |
| $SO_2 + 2H_2O \rightarrow H_2SO_4 + H_2$ | Overall Electrochemical Step | [r4] |
| $2H_2O \rightarrow 2H_2 + O_2$ | Cycle Process Reaction | [r5] |

The electrolysis step must be maintained at the highest possible conversion fraction to minimize unreacted $SO_2$ and obtain high $H_2SO_4$ concentration. Unreacted $SO_2$ must be recycled, and water must be removed prior to the high temperature decomposition step. Both of these are energy intensive steps and must be minimized to keep process efficiency high. Operation of the electrolyzer at the target conditions, however, is unfeasible using the current state-of-the-art materials. Therefore, new materials will be required to achieve the electrolysis performance goals. This project is focused on the development of new electrocatalysts and membranes and their effect on process efficiency, with the goals of improving the electrolyzer performance.

## Results/Discussion

A collaborative effort between SRNL and USC was initiated to develop novel materials designed to operate under the HyS process conditions with superior performance compared to the state-of-the-art. SRNL is utilizing its expertise in catalyst development and screening, along with USC's expertise in membrane development and gas analyte stream HyS operation, in order to achieve improvements in the HyS and meet DOE-EERE's hydrogen production goals. The work is being carried out in three main tasks.

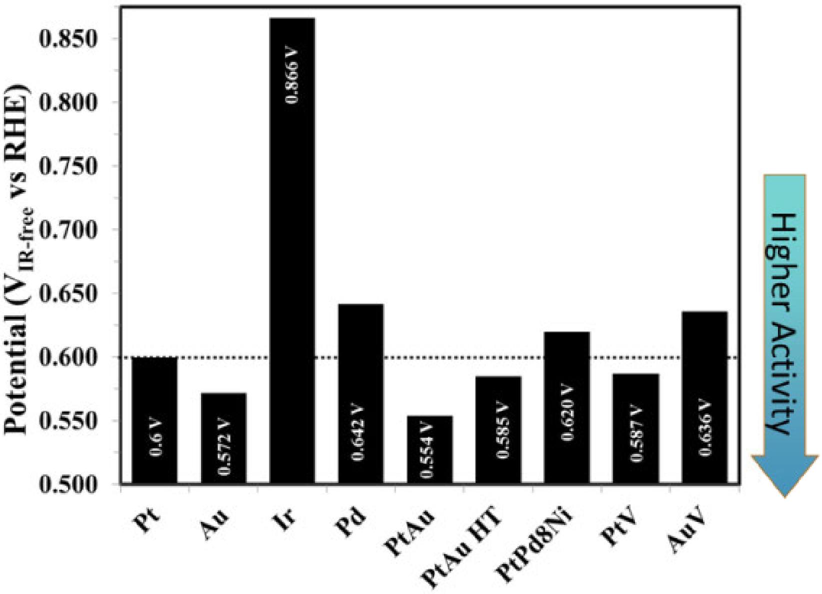

**Figure 2.** Initial catalyst screening results for the reaction [r2]. Chronopotentiometry test performed in 30 wt% $H_2SO_4$ saturated with $SO_2$.

### *Task 1-Catalyst Development*

Pt black and Pt/C have long been the state-of-the-art catalysts for PEM electrolyzers. Recently, as demonstrated in Figure 2, advances in catalyst design have demonstrated that Pt-M (M: V, Co, Fe, etc.), Au, and Au-based catalysts have improved kinetics for the $SO_2$ oxidation reaction [r2]. In order to design a catalyst for the conditions of the HyS, a high-throughput combinatorial methodology is under development that will aid in the catalyst selection. Once a catalyst composition has been identified, electrocatalyst materials will be produced in order to test them in-situ.

### *Task 2-Membrane Development*

Nafion® has long been the PEM solid electrolyte material of choice due to its stability in highly corrosive solutions (30 wt% $H_2SO_4$ saturated with $SO_2$) and at high operating temperature (80 °C), while maintaining practical ionic conductivity. However, to meet $H_2$ cost targets, membrane materials capable of operating at higher temperatures and acid concentrations are needed. At higher temperatures (>80 °C) and acid concentrations, Nafion® and many other solid electrolyte membranes become dehydrated and consequently become more resistive to ion transport. Benicewicz and Weidner's research groups at USC are currently developing membrane materials specific for the HyS process. Not only are the membranes able to operate at higher temperatures than Nafion®, they can also operate at higher acid concentrations as they do not rely on water content for their $H^+$ conductivity. Membranes developed at USC will be evaluated at SRNL and combined with newly developed catalysts to meet HyS operational targets.

### *Task 3-Electrolyzer Performance Evaluation*

SRNL modified its existing pressurized button cell test facility to evaluate the performance of new catalysts and S-PBI membranes. MEAs are being fabricated and tested for activity and stability according to SRNL's developed protocols.

## Results/Discussion

### *Combinatorial thin-film evaluation*

Combinatorial trimetallic catalyst films of Pt, Au, and V were prepared by sputtering a range of compositions onto glassy carbon plates (Figure 3). The catalyst films were mapped by scanning electrochemical microscopy (SECM) in order to determine the most active catalyst composition. In order to develop this method, a SECM was set up and tested under various conditions. A scanning droplet system (SDS) was used in the SECM to study the electrochemical activity of the films. This system was used as it is more suitable for studying irreversible reactions such as $SO_2$ oxidation. Figure 4 shows the composition results from the analysis of Au and Pt thin films. Compositions were analyzed at 0.6 V and 0.1 V vs $Ag/Ag_2SO_4$. The low and high potentials were selected to view the reaction kinetics at the regions close to the thermodynamic limited potential (0.1 V) and at the kinetically limited region (0.6 V). As observed by the results from the pure AuPt samples, an increase of activity with increasing Au content is observed. The effects of V addition are currently being evaluated.

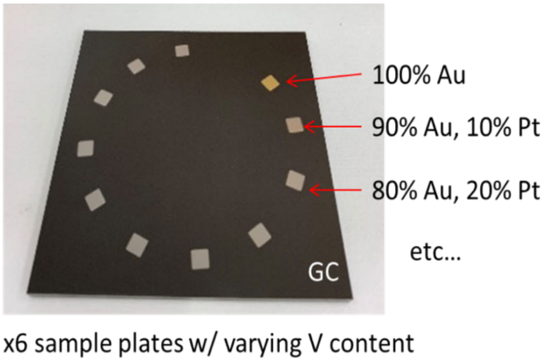

**Figure 3.** Example of combinatorial bimetallic catalyst films of Pt and Au prepared by sputter depositing a range of compositions onto glassy carbon plates.

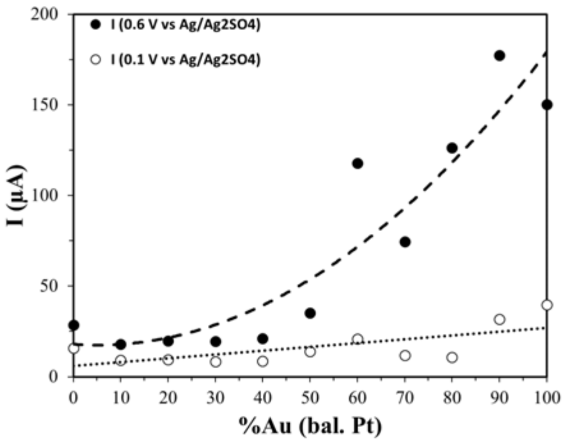

**Figure 4.** SDS-SECM combinatorial analysis of thin-film PtAu films on glassy carbon substrate.

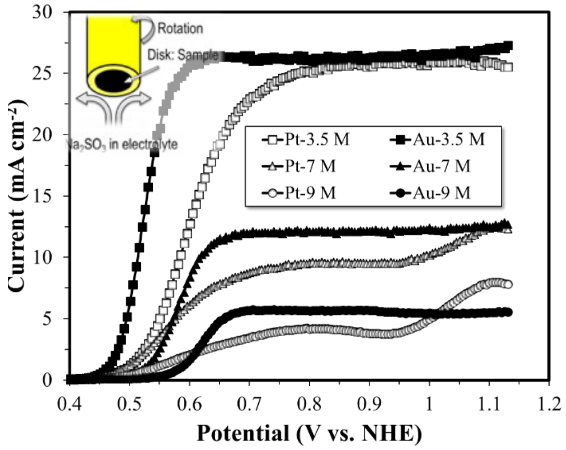

**Figure 5.** Linear sweep voltammetry measured at 400 RPM for 20% Au/C (solid symbols) and 40% Pt/C (open symbols) in 3.5 M (squares), 7 M (triangles), and 9 M (circles) sulfuric acid, all with 50 mM sulfite measured at 50 mV/s. Insert shows the simplified schematic of the rotating disc.

### *Ex-situ catalyst evaluation*

Prior literature reports have shown that acid electrolyte concentration can impact the catalysts' electrochemical activity by varying diffusion limitations. This observation was taken under consideration while evaluating the electrocatalysts via rotating disc electrode (RDE). Various concentrations of sulfuric acid solutions with 50mM sodium sulfite salt ($Na_2SO_3$) were used as well-defined surrogates instead of dissolved $SO_2$. It is important to note that during electrolyzer testing with $SO_2$, it is difficult to predict the local acid concentration at the electrode layer due to possible mass transport limitations. Therefore, understanding the effect of sulfuric acid concentration on RDE performance can help predict the environment at the catalyst layer in the electrolyzer. Once a thin layer of catalyst powder was loaded onto the RDE tip, we conducted sulfite oxidation in increasingly concentrated sulfuric acid solutions with a rotation speed of 400 rpm (Figure 5). The first noteworthy observation is that there is a significant difference in the limiting current that is dependent on the acid concentration. Although the sodium sulfite concentration is constant in all acid solutions, a continuous decrease in limiting currents is observed as the acid concentration increases. This effect is attributed to changes in the diffusion coefficient and kinematic viscosity. In the 3.5 M sulfuric acid solution, Au has a lower onset potential for the oxidation of sulfite to sulfate. The diffusion-limited currents observed for Au and Pt catalyst are similar. In 7 M sulfuric acid, Pt has a lower onset potential, but Au has a higher limiting current and outperforms Pt from about 0.57 V to approximately 1.1 V (vs. NHE). In 9 M sulfuric acid, Pt again has a slightly lower onset potential, but Au again exhibits higher limiting current and outperforms Pt from about 0.62 V until 1.0 V. Au has just one oxidation peak under all concentrations tested. Pt, however, has a second oxidation step that is observed in both 7 M and 9 M $H_2SO_4$ concentrations at approximately 0.95 V. It is possible that the second oxidation step is influenced by the formation of a Pt oxide layer. This result, using metal nanoparticles deposited on carbon black, confirms the thin film combinatorial screening performed using SDS-SECM, where Au shows better activity than Pt.

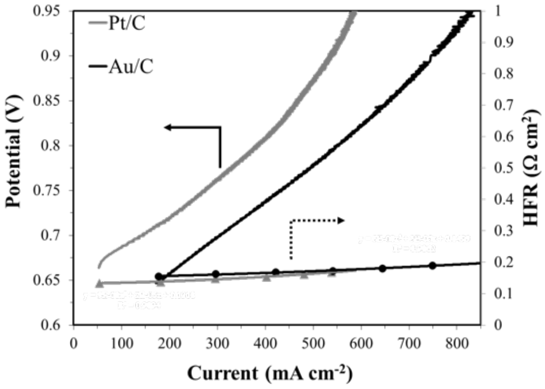

**Figure 6.** $SO_2$ performance curve for anodes with Pt/C (grey trace) and Au/C (black trace) tested at 90 °C. Metal loading is 0.1 mg $cm^{-2}$ for all cases. Nafion® 115 was used for the test.

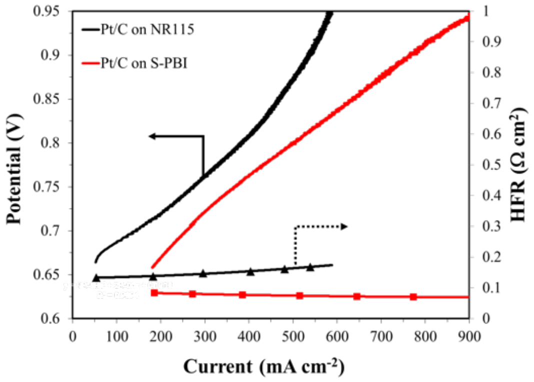

**Figure 7.** $SO_2$ performance curve for MEAs based on S-PBI and Nafion® 115. Anodes consist of Pt supported on carbon. Nafion® MEA tested at 90 °C and S-PBI tested at 110 °C.

### *In-situ material evaluation*

The electrochemical performance of Pt/C and Au/C catalysts were also evaluated in an electrolysis cell. In the present experiments, the metal loading on the anode remained the same for both Pt and Au, but a lower loading (0.1 $mg_M$ $cm^{-2}$) than typically observed in the literature (~1 $mg_M$ $cm^{-2}$) was used. The lower loadings were selected to facilitate evaluations of the kinetic limited regions of the electrolyzer performance. As observed in Figure 6, the $SO_2$ electrooxidation performance of the gold catalyst is superior to that of the Pt catalyst, confirming the RDE results. In addition, the high frequency resistance (HFR) is very similar for cells employing Pt/C and Au/C, indicating that the difference in performance is entirely due to the catalyst. The HFR increase as a function of current can be correlated to a local increase in acid concentration at the catalyst/membrane interface. The electrolyzer was not operated at potentials lower than 0.6 V to limit unreacted $SO_2$ crossover to the cathode.

High temperature operation was also evaluated with the use of sulfuric acid doped polybenzimidazole membrane (S-PBI). This membrane was prepared to meet the operation requirements in the SDE, which includes high temperature operation, high acid concentration, and low $SO_2$ crossover. Results from the testing are shown in Figure 7. As observed in the figure, S-PBI MEA shows around 150 mV improvements in the electrolyzer performance. Additionally, the high frequency resistance is much lower than that of the Nafion® based MEA. It is expected that further gains will be obtained by incorporation of the Au/C catalyst on the MEA.

## FY2019 Accomplishments

- **Goal:** Find better catalysts and membranes for the Hybrid Sulfur (HyS) process for hydrogen production from water
- **Approach:** Improve catalyst activity, improve membrane ionic conductivity, and improve catalyst/membrane stability for operation at higher temperature and higher acid concentration (faster kinetics and efficiency)
- **Progress:** Found promising new mixed-metal catalysts and better membranes for further exploration, developed new capabilities/techniques for high-throughput catalyst synthesis/testing, established new partnerships and external funding, improved performance through the use of high temperature membranes

## Future Directions

- Continue high throughput catalyst screening with ternary compositions
- Develop, characterize and test additional metal supported on carbon anode catalysts
- Continue optimization of sulfonated polybenzimidazole based membrane electrode assemblies

### Publications/Presentations

1. BH. Meekins, V. Gopal, BA. Tavakoli Mehrabadi, MC. Elvington, P. Ganesan, JC. Weiss, JW. Weidner, HR. Colón-Mercado, "In-situ and ex-situ comparison of the electrochemical oxidation of SO2 on carbon supported Pt and Au catalysts." Manuscript submitted to International Journal of Hydrogen Energy.

### Acronyms

| | |
|---|---|
| **DOE-EERE** | Department of Energy-Office of Energy Efficiency and Renewable Energy |
| **HyS** | Hybrid Sulfur |
| **MEA** | membrane electrode assembly |
| **S-PBI** | sulfuric acid doped polybenzimidazole |
| **PEM** | polymer electrolyte membrane |
| **SDE** | $SO_2$-depolarized electrolyzer |
| **SDS** | Scanning droplet system |
| **SECM** | Scanning electrochemical microscopy |
| **SRC** | Savannah River Consulting |
| **SRNL** | Savannah River National Laboratory |
| **USC** | University of South Carolina |

### Total Number of Post-Doctoral Researchers

B. Tavakoli / Post-doctoral student, USC
L. Murdock / Graduate student, USC

### Total Number of Student Researchers

J. Weiss / Undergraduate, USC
V. Gopal / Undergraduate, USC

# Embedded Hardware Solution for Cybersecurity of Industrial Control Systems

**Project Team:** R. Barnett (Primary), J. Horne, J. Kuzel, K. Burkes

**Thrust Area**: Secure Energy & Manufacturing

**Project Start Date:** October 1, 2017

**Project End Date:** September 30, 2019

*Manufacturing and utility companies utilize industrial controls systems (ICS) to automate their plants as a means of increasing efficiency and productivity. These environments consist of older ICS devices that have been networked, although they were never intended to have this functionality. To identify appropriate defensive characteristics needed to contribute to defense-in-depth of cyber-physical systems, we performed a survey of ICS environments and devices. A unique level of concern for ICS are levels one and zero (L1/L0). Devices at these levels are conducting physical activities (and thus considered cyber-physical systems). Our focus was securing network segments using a novel unidirectional modular networking device. This strategy allowed us to implement added security that was not firmware or software dependent, can control traffic flow direction, and can still accommodate a wide variety of protocols agnostically.*

## Objectives

- Deploy Core Virtualization Laboratory equipment
- Design Low Level Unidirectional Data Device
- Develop Prototype for Data Device

## Introduction

Manufacturing and utility companies utilize industrial controls systems (ICS) to automate their plants as a means of increasing efficiency and productivity. These environments consist of older ICS devices that have been networked, although they were never intended to have this functionality. More modern Industrial Internet of Things (IIOT) devices, that are rapidly developed with full suites of communication and intelligence features but not security, are also being deployed in these environments. This new interconnectedness on the production floor is being used to connect facilities across the internet to command and control centers. This state of highly interconnected computing capability leaves these systems vulnerable where once a true air-gap existed. In an unfortunate inability to learn from the general history of the internet the networking technologies for these environments are largely being developed on a model of trust. While this attitude is changing, improving ICS security it is a very slow process. The lifecycle for ICS devices can be 10-20 years in time making ICS enticing targets for adversaries looking to impact critical infrastructure [1].

A common topology of ICS networks is generalized by breaking the network into five standard levels. It starts with a Business/Enterprise center at the top (level 5) and ends with sensor or actuator devices at the bottom (level 0). Supervisory Control and Data Acquisition systems (SCADA) show up typically at level 3 in the model. It is this point in the model that communication technology transitions from Information Technology (IT) to Operations Technology (OT). With the shift in technology type comes changes in hardware and communication protocol usage. This shift in technology means there must also be changes in how security is conducted for OT systems as compared to standard IT security that accounts for the different nature of the OT environments and devices [2].

A unique level of concern for ICS are levels one and zero (L1/L0). Devices at these levels are conducting physical activities (and thus considered cyber-physical systems). These two levels are also the most different from IT in terms of behavior and considerations and suffer the most in terms of security. In order to raise the bar for security of these end devices, we have reviewed network architectures and device types, and engaged with industry to identify weaknesses and vulnerabilities which would benefit from tailored security for L1/L0 cyber-physical systems. Using this information, we have developed a plan for an ICS testbed, and the outline of a prototype device which will be developed in the second year to test security concepts for cyber-physical systems.

## Approach

To identify appropriate defensive characteristics needed to contribute to defense-in-depth of cyber-physical systems, it was necessary to begin with a survey of ICS environments and devices. Engagement with the ICS community via conferences and workshops, as well as utilization of white papers provided by SANS and E-ISACs, and conversations with Fort Gordon cyber protection team personnel were used to discover contemporary issues with control systems. The results of this discovery phase were used to develop a plan for the development of an ICS-specific cybersecurity testbed, as well as development of specifications for a device that would allow implementation of security features at this low level.

Proper network segmentation and isolation can be a major concern for lower level IT devices. A remedy for this would be a device capable of segmenting a network and allowing hardware-controlled data flow between segments. Ideally this would accommodate both ethernet carried data and ICS specific protocols and remain agnostic to the data being passed to a segment. Our approach to this problem is to design a unidirectional modular hardware unit that can accommodate typical Cat6 cable connections for ethernet based traffic as well as serial, or other data types depending on connector and pins needed.

## Results/Discussion

We had three main objectives for this project: identify vulnerabilities in the ICS environment, develop a testbed that will allow us to conduct cybersecurity research on a range of ICS environments, and develop specifications for a prototype to address one of the identified vulnerabilities. Our final prototype was a unidirectional modular communication device. This addressed the need for secure passing of data from one network segment to another without allowing data flow to a more secured portion of the network. Second, we completed the major hardware purchases and installation of the hardware for the ICS testbed. We were also able to establish a link with the University of North Carolina, Charlotte (UNCC) to deploy their network virtualization software to our testbed (this will be an ongoing task).

Initially we intended to produce a report classifying the vulnerabilities in ICS but the sheer volume proved overwhelming and ultimately distracting from the scope of this project ( [3] as an example of the volume of classifications). The most discussed problem in person and at conferences was around gateway controllers and their lack of authentication [4] [5] [6]. While this was initially explored as an avenue for research, the development of a novel form of authentication was beyond the technical capabilities of SRNL engineers at this present time and we required lower hanging fruit. The unidirectional device was an ideal target as its security could be implemented through hardware design with minimal firmware requirements. This also addressed a desire by SRNL partners to securely link end devices and databases in a manner that allows them to only pass data one way, making them secure for log extraction.

## FY2019 Accomplishments

- Completed all required purchases for the core ICS Laboratory
- Installed core hardware servers, switches, gateways, and PCs needed for the ICS laboratory
- Established an agreement with UNCC to use their Network Virtualization platform
- Designed and Prototyped the Unidirectional Modular Networking Device

## Future Directions

- Collaborate with UNCC to fully install the virtualization platform
- Test, deploy, and refine the Unidirectional Modular Networking Device

### References

1. L. Obregon, "Secure Architecture for Industrial Control Systems," 23 September 2015. [Online]. Available: https://www.sans.org/reading-room/whitepapers/ICS/secure-architecture-industrial-control-systems-36327. [Accessed 2018].
2. G. Aydell, "The Perfect ICS Storm," 15 May 2015. [Online]. Available: https://www.giac.org/paper/gcia/10551/perfect-ics-storm/141222. [Accessed 2018].
3. J. Z. Andrei Costin, "IoT Malware: Comprehensive Survey, Analysis Framerwork and Case Studies," 2018. [Online]. Available: http://i.blackhat.com/us-18/Thu-August-9/us-18-Costin-Zaddach-IoT-Malware-Comprehensive-Survey-Analysis-Framework-and-Case-Studies-wp.pdf. [Accessed 2018]
4. T. Roth, "Breaking the IIOT: Hacking Industrial Control Gateways," in *Blackhat USA 2018*, Las Vegas, 2018.
5. J. Shattuck, "Snooping on Cellular Gateways and Their Critical Role in ICS," in *BlackHat USA 2018*, Las Vegas, 2018.
6. M. P. J. S. Daniel Crowley, "Outsmarting the Smart City," August 2018. [Online]. Available: http://i.blackhat.com/us-18/Thu-August-9/us-18-Crowley-Outsmarting-The-Smart-City-wp.pdf. [Accessed 2018].

### Acronyms

| | |
|---|---|
| **ICS** | Industrial Control Systems |

### Total Number of Student Researchers

One – Ryan Cruz / Graduate Student, DOE Fellow / On-site

# HEMP Transformer Defense through Power Electronics

**Project Team:** Klaehn Burkes (Primary), Vincent Cessyens

**Subcontractor:** Clemson University

**Thrust Area**: Secure Energy & Manufacturing

**Project Start Date:** October 1, 2018

**Project End Date:** September 30, 2020

*High altitude electromagnetic pulse (HEMP) generated by an exoatmospheric nuclear burst has the ability to affect the electric power grid. The main power grid components, cables and transformers, act as large antennas that have current induced in them from the HEMP. These currents are called geomagnetically-induced currents (GIC), and they can occur during geomagnetic disturbances from HEMP or solar flares. HEMPs produce pulses with high electric field strengths that breakdown the dielectric of most electronics and, it is broken into three stages: E1 pulse with a microsecond width, E2 the falling trail of the pulse, and E3 a constant DC component. Oak Ridge National Laboratory has proven that transformers fitted with lightning arrestors do not receive damage from E1 and E2 pulses. However, the DC component of the E3 causes the transformer's core to saturate and induce rapid heating that damages the transformer. SRNL is developing a power electronic system that is connected to the neutral of the high voltage side of large power transformers (LPT). This system will inject the inverse of the DC effect from the HEMP into the primary side of the transformer canceling out the E3 waveform and protecting the transformer from half-cycle-saturation. This year SRNL successfully simulated removing the DC injected and accurately simulated saturation on the transformer.*

## Objectives

- Issue Clemson contract for developing grid support control function (2/7/2019)
- Receive Typhoon CHIL hardware (1/7/2019)
- Simulate Power Electronic System in Typhoon (7/31/2019)
- Write Paper on Power Electronic Design and Simulation (9/31/2019)

## Introduction

A high altitude electromagnetic pulse (HEMP) is generated from exoatmospheric nuclear busts that consist of three stages: E1 pulse with a microsecond width and a nanosecond rise time, E2 the falling edge of the initial pulse, and an E3 a constant DC component. This waveform is represented by Figure 1. The high electric field of the E1 pulse train is responsible for causing dielectric breakdown in traditional electronic components by causing arcing because of the high strength of the electric field. This E1 strength is not relative to the yield of the nuclear device, but from the air conductivity, the height of the burst and the line of sight to the observer on the ground [1]. Oak Ridge National Laboratory has studied the effects of E1 on distribution transformers as well as large power transformers and have dictated that using lightning arrestors transformers can be protected from this high electric field [2]. This protection comes from the E1 waveform being a double exponential pulse that is the same as a lighting pulse with just a higher electric field. Figure 1 shows the intermediate-time, E2, waveform is a much lower electric field and has the same mathematical representation as E1. E2 is not as damaging as E1 because of the lower electric field.

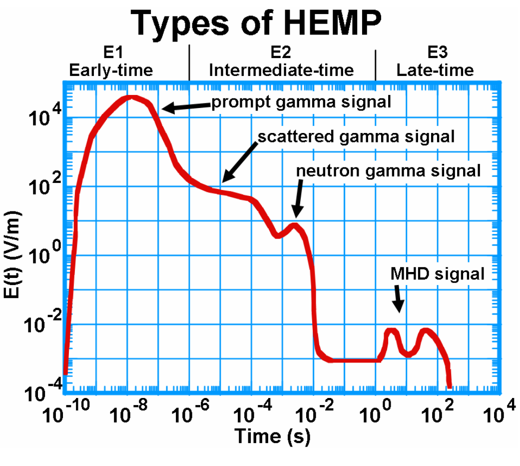

**Figure 1.** Electric Field Produced from High Altitude Electromagnetic Pulse

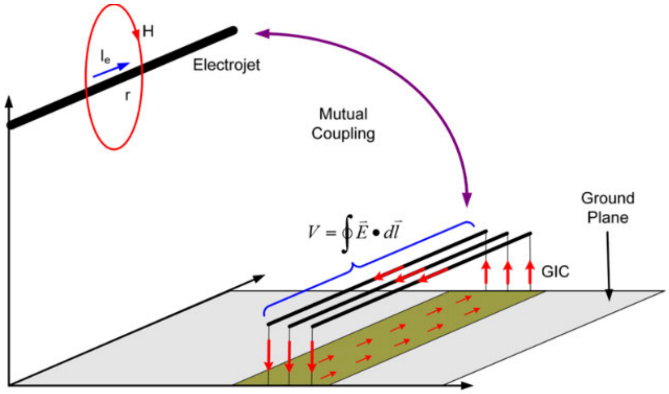

**Figure 2.** Method for E3 Coupling on Transmission Lines [3]

The late-time, E3, portion of the waveform is the longest portion of the HEMP waveform and is produced mainly from the generation of X-rays from the nuclear explosion. It consists of two components, the blast and the heave, and is attributed to the driving factor to damaging electric grid components [3]. The blast heave changes the earth's magnetic field and causes large currents to be produced in the ionosphere that are millions of amperes in magnitude. These large currents have a resulting magnetic field that is very large and can couple with conducting paths throughout the earth surface such as transmission lines, metallic pipes, telephone cable, and railways [4]. In the power system the transmission network is grounded throughout by design for paths for fault current to flow. However, this causes a circuit between the ground and the transmission network. Therefore, the mutual coupling between the transmission lines and the electrojets causes voltage differentials throughout the transmission system, which causes current to flow between the transmission lines and ground Figure 2.

The E3 of a HEMP creates GICs from the motion of the ionized bomb debris and is broken into two parts the Blast Wave and the Heave. The blast wave is created by the fire ball expansion of the explosion which expels magnetic field. This bubble of magnetic field distorts the magnetic field lines of the earth. The heave is when the blast wave causes the upper atmosphere to heat and rise. The rising creates a conductive patch that produces currents and magnetic fields on the earth's surface [3]. The result of both these are magnetic fields on the earth's surface and thus occurs electric fields in the earth's surface and long conducing paths as discussed before with geomagnetic disturbance (GMD). These electric fields now cause voltage differentials and circulating currents or GICs. And the result as with GMD is GICs circulating through the ground and the transmission system but with a different amplitude and duration than GMDs.

### *Impacts of GIC from GMD/E3 on Power Grid*

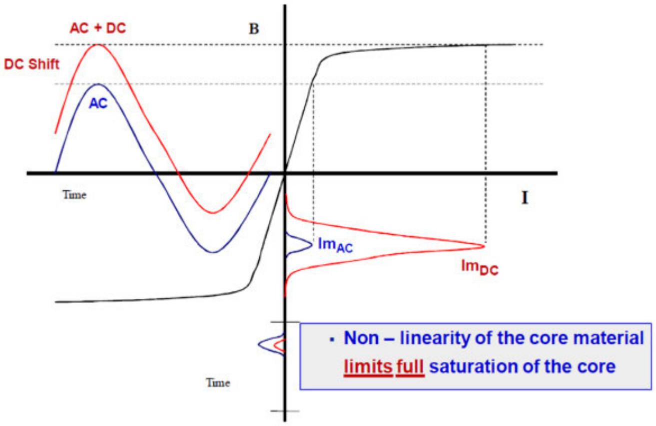

**Figure 3.** Effect of Half-Cycle Saturation [5]

The electric power grid was built to operate with 60 Hz AC power in the United States. There are mechanisms for handling harmonic currents and conversions from AC to DC, but the system was not built to handle AC and DC coupled together. This is especially true for magnetic transfer of power. Therefore, because GICs are quasi-DC meaning they are injected constant currents at different magnitudes for a small duration of time, they can cause transformers, reactors, voltage regulators, and other components to saturate and operate in a non-linear condition. This quasi-DC causes magnetic systems to undergo half-cycle saturation from the DC shift in the AC waveform and draw large amounts of magnetic current as shown in Figure 3.

The quasi-DC currents cause the core of transformers to saturate and cause internal heating. The magnetic current drawn from saturation requires massive amounts of reactive power draws which effects power system stability and power quality. There is the capability of miss operation of protective relays due to the reactive power and harmonics produced. There is also a greater chance of damage to shunt capacitors, static var compensators, and harmonic filters. Generators can experience rotor heating from saturation [6].

As discussed GICs flow through the power system through long transmission lines and back through ground by grounded neutrals on the transformers. These GICs will not flow if there is no return path to ground. The electric field magnitudes from E3 can be on the amplitude of up to 35 V/km [7] which can affect shorter length transmission and distribution. However, GMD are in the range from 1 to 6 V/km [4]. Therefore, high voltage potential difference can only be built up on longer lines, and for the power system these will be mainly be extra high voltage (EHV) transmission lines. This is because of the larger line length and lower average resistance. Therefore, the transmission lines have more DC current induced and the transformers in the EHV system will experience higher and longer saturation levels. This is critical to the power grid because the EHV system is critical in bulk power transformer [8].

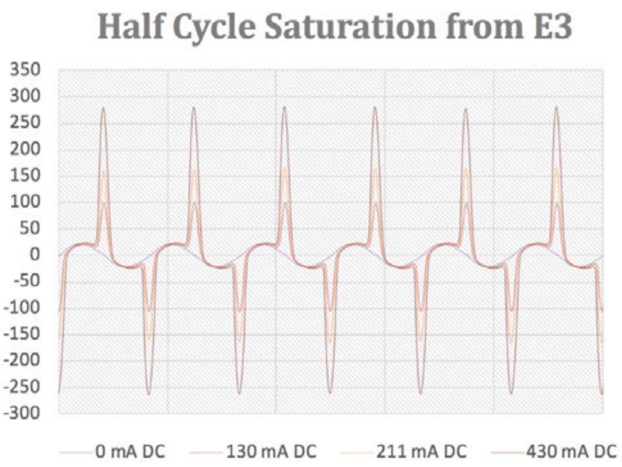

**Figure 4.** Half Cycle Saturation from E3 on Distribution Transformers [9]

The LPT in the EHV system will experience high and longer saturation levels. This means they will produce more harmonics causing miss operation of protective relays and overloading of capacitor banks. The longer saturation will allow for more heating from the magnetic flux extending beyond the core. This causes eddy currents to flow, and the transformer will experience high magnetization losses with more heating in the core. Finally, it will draw massive amounts of current from the electric power grid causing instability and blackouts. These currents can be on the magnitude of 10 times the traditional peak as seen in Figure 4.

## Approach

A passive method for protecting devices from HEMP would be to just filter the waveform out. However, when dealing with distribution or transmission components this is not possible because of the high voltage requirement of capacitors and high current requirements of reactors needed. Therefore, a series power electronic compensator was used as the design for developing the prototype. The architecture of the power electronics will be similar to an inverter on connected to the neutral of the transformer. This design will be used because it can actively regulate the voltage going into the transformer without having to control high voltages or currents. A simplified architecture is presented in Figure 5, and it operates in the following manner. A H-Bridge Converter is used as the foundation of the power electronic components and converts AC to DC and vice versus. A capacitor is placed across the DC side of the H-bridge, and a reactor is used to connect the converter to the electric grid. The H-bridge will charge up and discharge the capacitor based on the voltage difference across the reactor. By monitoring the input voltage to the transformer, the converter can change its output in order to draw current through the reactor as to control the voltage going into the transformer. This is how the compensator will be able to regulate the voltage going into the transformer and absorb the HEMP waveform.

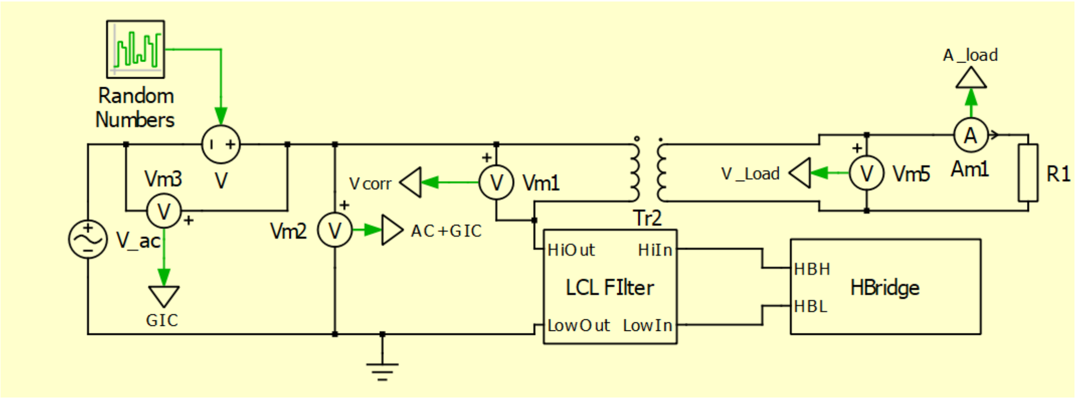

**Figure 5.** PLECS Simulation Block Diagram of GIC Mitigation

Understanding how the HEMP saturation effects the transformer is important for simulation purposes. Also, when developing a model for testing the controller hardware in the loop, accurate representation of the effect of DC on transformers is required before implementing in the laboratory. Therefore, Typhoon HIL will be used to perform controller hardware in the loop testing. The following simulation, Figure 6 was set up in Typhoon to simulate the GIC. Two transformers are placed high voltage to high voltage windings with being energized and loaded by the low voltage windings. This is because in the laboratory setting this is the safest and most accurate way of determining what is the direct effect of GIC on a transmission system.

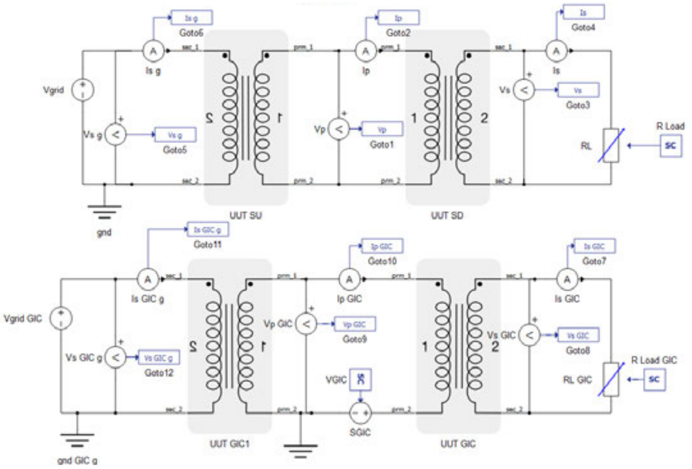

**Figure 6.** Typhoon Simulation of Test Setup for Distribution Transformers

## Results/Discussion

The simulated H-Bridge converter was able to successfully compensate and remove the DC injected from GIC to the transformer. This is shown in Figure 7. A random DC amplitude was injected into the circuit and changed every 0.1 seconds. This emulated how GMD would effect a transformer more than E3 because E3 would not vary randomly but have a defined DC. Nevertheless, the system would remove both GMD and E3 from a transformer. The grey plot is the amount of GIC voltage induced on the system. In simulation the amplitude of DC was much larger that what is seen in real life. This was done to make sure that the converter system could handle large amounts of DC with very large swings in amplitude. The blue plot is what would be the voltage to the transformer without having any DC compensation. The orange plot is what is seen by the transformer. It can be seen that there are transient spikes when the DC changes; however, it dampends out very quickly.

The reaction of the control algorithm for injecting DC to compensate for GIC is shown in Figure 8. When the DC jumps the input to the converter follows and then within about a cycle the voltage to the transformer stabilizes. This will be acceptable for the GIC compensation system because the quasi-static transients from E3 EMP/GMD are not fast transitions. Also, they will not be step changes but more exponential rises and decays. This system shows that large amounts of DC can be removed from the voltage going into the transformer by changing the reference position of the ground on the transformer. This work now moving to testing the compensation when the transformer is capable of being saturated as the next step and then performing controller hardware in the loop testing.

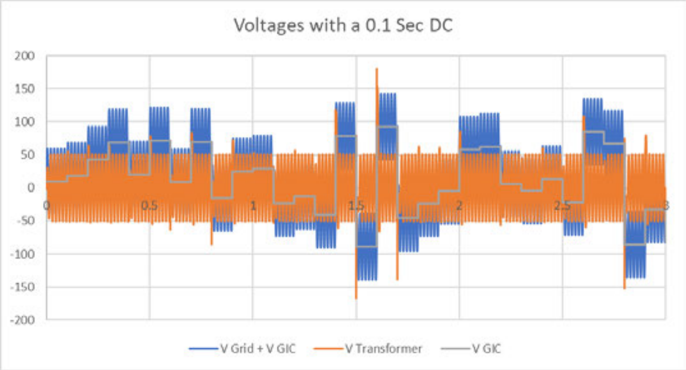

**Figure 7.** GIC Removal to Transformer

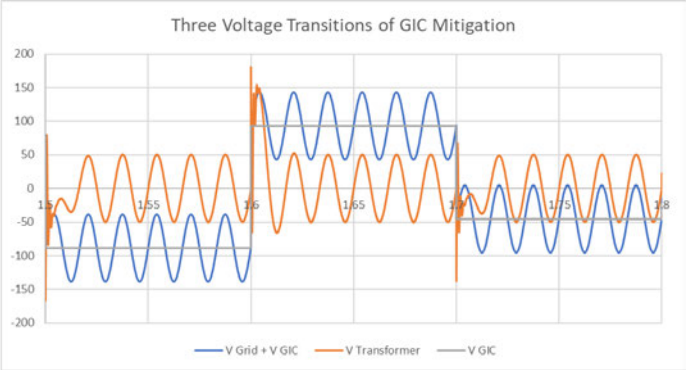

**Figure 8.** Three Transisitons of Voltage waveforms

## Accomplishments

- Submitted three conference papers on failure mechanisms from GMD and HEMP of transformers and previous research on testing GICs
- Working with Clemson professor, 2 post docs, and PhD students for developing the topology for protecting transformers
- Purchased and programming a controller hardware in the loop (Typhoon) for increasing the capability for simulation and development of power electronic systems.
- Simulated GIC effect on transformers
- Simulated DC compensation on transformer

## Future Directions

- Build Power Electronic System (PES) to test at the eGRID facility
- Integrate PES with distribution transformers for testing
- Put DC on distribution transformers neutral and monitor results
- Research detection methods to responding to GIC and E3

### Publications/Presentations

1. M. Nazir, K. Burkes, M. Babakmehr, F. Harirchi and J. H. Enslin, “Transformerless Converter-based GMD Protection for Utility Transformers,” Submitted to APEC 2020.
2. M. Nazir, K. Burkes and J. H. Enslin, “Enhanced Grid Stability through GIC elimination and Grid Support,” Submitted to ISGT 2020.
3. K. Burkes, J. Cordaro, T. Keister, J. Keister, B. Schafer, J. Enslin, “E3/GMD Effect and Testing of Quasi-DC Currents on Distribution Transformers,” Will be submitted to PES GM 2020.

### References

1. J. Cordaro, J. Dagle, G. DiPeso, C. Hanley, B. Kirkendall, C. Lawton, S. McBride, M. Rivera and A. Tarditi, "High-Altitude Electomagnetic Pulse (HEMP) and the Electric Grid: A Brief Overview,"," Mission Executuion Council, United States, March 27, 2017.
2. E. Savage, J. Gilbert and W. Radasky, "The Early-Time (E1) High-Altitude Electromagentic Pulse (HEMP) and its impact on the U.S. Power Grid," Oak Ridge National Laboratory, Oak Ridge, Tennessee, January 2010.
3. J. Gilbert, J. Kappenman, W. Radasky and E. Savage, "The Late-Time (E3) High-Altitude Electromagnetic Pulse (HEMP) and Its Impact on the U.S. Power Grid," Metatech Corporation, Goleta, CA, January 2010.
4. NERC, "Geo-Magnetic Disturbances (GMD): Monitoring, Mitigation, and Next Steps," Atlanta GA, 2011.
5. R. Girgis, Writer, Impact of GIC on Power Transformers and Power Systems. [Performance]. ABB, Febuary 2019.
6. W. B. Gish and W. E. Feero, "Rotor Heating Effects from Geomagnetic Induced Current," *IEEE Transactions on Power Delivery,* vol. 9, no. 2, April 1994.
7. R. Horton, *Perspective on Protecting the Electric Grid from an Electromagnetic Pulse or Geomagnetic Disturbance,* Washington D.C.: Hearing of the U.S. Senate Homeland Security and Governmental Affairs Committee, February 27, 2019.
8. J. Kappenman, "Geomagnetic Storms and Their Impacts on the U.S. Power Grid," Metatech Corporation, Goleta, CA, January 2010.

### Acronyms

| | |
|---|---|
| **AC** | Alternating Current |
| **DC** | Direct Current |
| **EMP** | Electromagnetic Pulse |
| **EHV** | Extra High Voltage |
| **GMD** | Geomagnetic Disturbance |
| **GIC** | Geomagnetically Induced Currents |
| **HEMP** | High Altitude Electromagnetic Pulse |
| **LPT** | Large Power Transformer |

### Intellectual Property

Invention disclosure is being submitted and as well as a Joint Intellectual Property Agreement with Clemson

### Total Number of Post-Doctoral Researcher

Two post-doctoral researchers and two PhD students worked on the project through Clemson University

# Novel Complex Hydride Flow Batteries for Grid Storage Applications

**Project Team:** Ragaiy Zidan,
Patrick Ward, Hector Colón-Mercado

**Subcontractor:** Joseph A. Teprovich Jr. (CSUN)

**Thrust Area**: Secure Energy & Manufacturing

**Project Start Date:** October 1, 2018

**Project End Date:** September 30, 2020

*A variety of complex metal hydride alanates were synthesized and investigated for their potential to develop high energy batteries in a redox flow cell configuration. Electrochemical analysis of various alkali metal and alkaline earth metal alanates were carried out with an array of differing metal hydride working electrodes and metal and graphite counter electrodes. Novel $C_{60}H_x$ anodes were also investigated for applications in lithium ion batteries. The reduced solubility of $C_{60}H_x$ versus $C_{60}$ allows for their use as anodes in lithium ion batteries. $C_{60}H_x$ with varying degrees of hydrogenation were cycled 50 times to determine the ideal degree of hydrogen content. Density functional theory (DFT) calculation were carried out to explain the experimentally observered enhancements in $C_{60}H_x$ as an anode for lithium ion batteries.*

## Objectives

- Synthesize and characterize an array of alkali and alkaline earth metal alanates as electrolytes and metal hydrides as anodes
- Evaluate various metal hydride electrodes (anodes) for compatibility with the proposed battery technology
- Carryout electrochemical analysis to determine the ideal combination of metal hydride anode, cathode material, alanate electrolyte, and electrolyte solvent
- Continue research related to $C_{60}H_x$ anodes for lithium ion batteries that was started in a previous BES funded project

## Introduction

Electrical grid resiliency and effective deployment of large-scale renewable technologies such as photovoltaics and wind power require large scale electrical storage. Flow batteries offer several advantages to traditional energy storage such as high scalability and flexibility that can be applied to a wide range of applications in a diverse grid-energy market. Our proposal idea was based on using complex hydride materials that offer a high energy density alternative to state-of-the-art materials. In addition, the proposed novel technology has the advantage of operating at a higher voltage not available with current technology. Most metal alanates are much less costly than typically used vanadium oxide in current flow batteries technology. The project seeks to develop novel complex hydride flow batteries for high energy density grid storage applications.

## Approach

A series of complex hydrides, called alanates (e.g. $LiAlH_4$, $NaAlH_4$, $KAlH_4$, $Mg(AlH_4)_2$, $Ca(AlH_4)_2$, etc.), dissolved in organic solvents such as ethers or amines will be examined to demonstrate their feasibility as an electrolyte for flow cell batteries. Previously obtained preliminary results illustrate the possibility of utilizing alanates in THF as an electrolyte. Since $AlH_3$•Adduct is an intermediate of the electrochemical reaction and the adduct is a solvent molecule, a suitable solvent or solvent combination must be carefully considered and chosen. It is well-known that the diethyl ether adduct of $AlH_3$ (alane) is not stable over long periods of time and therefore would not be an appropriate choice. Once a solvent or combination of solvents with an appropriate alane stabilization effect, high ionic conductivity, and suitable operational conditions is selected, the ex-situ effort will focus on the appropriate alanate and electrode choice. The reduction of ions such as $Li^+$, $Na^+$, $Mg^+$, $Ca^+$ and $K^+$ to metals requires different voltages depending on the metal and results in batteries with different operational voltages and differing numbers of charges transferred. In the case of $LiAlH_4$ or $NaAlH_4$ the electrolyte is ionized when potential is applied to the battery to produce a lithium or sodium ion ($Li^+$)/($Na^+$) and an alanate ion ($AlH_4^-$) at cathode and anode, respectively, as shown in equation (1) and (2). One electrode in this case is made to intercalate Li/Na based materials; the other electrode is made of metal hydride material or materials that have metal hydride embedded in it, (e.g. $AB_5$, $AB_2$, metal hydrides embedded in graphite, etc.).

$$AlH_4^- \rightarrow AlH_3{:}\ nTHF + \tfrac{1}{2} H_2 + e^- \quad \text{and} \quad Li^+ + e^- \rightarrow Li^0 \qquad (1)$$

Or

$$AlH_4^- \rightarrow AlH_3{:}\ nTHF + \tfrac{1}{2} H_2 + e^- \quad \text{and} \quad Na^+ + e^- \rightarrow Na^0 \qquad (2)$$

The charging-discharging of a $LiAlH_4$ battery of this type can be summarized in the following equations:

$$\begin{array}{rr} \mathrm{MH} + \mathrm{AlH_3} + \mathrm{e^-} \leftrightarrow \mathrm{M} + \mathrm{AlH_4^-} & 0.795\ \mathrm{V} \\ \mathrm{LiC_6} \leftrightarrow \mathrm{Li^+} + \mathrm{e^-} + \mathrm{C_6} & -3.035\ \mathrm{V} \\ \hline \mathrm{MH} + \mathrm{AlH_3} + \mathrm{LiC_6} \leftrightarrow \mathrm{Li^+} + \mathrm{AlH_4^-} + \mathrm{C_6} + \mathrm{M} & 2.24\ \mathrm{V} \end{array}$$

## Results/Discussion

Figure 1 illustrates the ability to charge and discharge a non-aqueous electrochemical cell that has an alkali metal alanate dissolved in a polar, aprotic solvent and with at least one electrode in the zero-valence state that can form a hydride. During charging, the zero-valence form of the hydride forming electrode will be the anode. At the anode, the hydride forming material will be oxidized to form the hydride and alanate anions in the electrolyte will transfer a hydride anion to the electrode and form aluminum hydride (alane) which successively forms an alane adduct that remains in the electrolyte. At the cathode, the alkali metal or alkali earth metal cations are reduced to their metallic form. During discharge, the hydride electrode (now the cathode) will be reduced to the metallic state and the hydride anion will recombine with alane to form an alanate anion. The metallic alkali metal or alkali earth metal will be oxidized to form cations that go into solution. The appropriate hydride electrode (anode during charging) will be selected from experiments with $LiAlH_4$ since there are various well-known cathodes for Li ions. Once the appropriate anode is selected, cathode (during charging) selection experiments will be carried out with each cation.

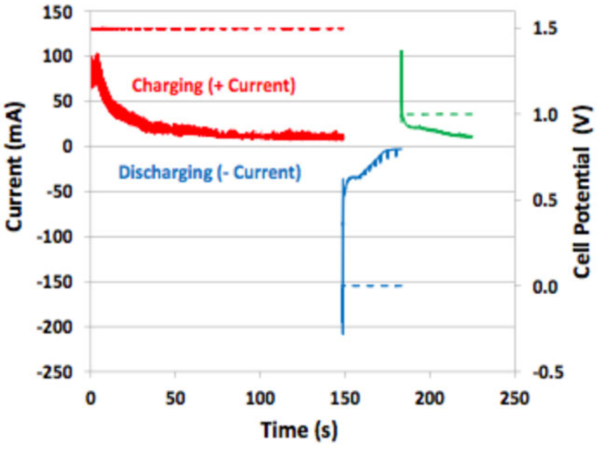

**Figure 1.** Charging and discharging curves for $LiAlH_4$ in THF

After the first phase, the 1 or 2 best combinations will be down selected, and a bench-scale flow battery system constructed. Once the full system is constructed, tested, and safety certified, various flow rates, concentrations, and slurry methods will be evaluated to maximize capacity, reduce dendrite formation, and demonstrated efficient operation. Additionally, SRNL will collaborate with Dr. Joseph Teprovich from California State University Northridge to provide expertise in the intercalation of metallic ions in novel electrodes developed in past BES funded research to be leveraged for this project.

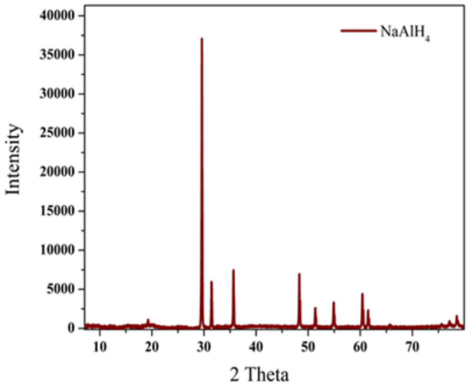

**Figure 2:** XRD pattern for pure $NaAlH_4$ produced by catalyst-free method

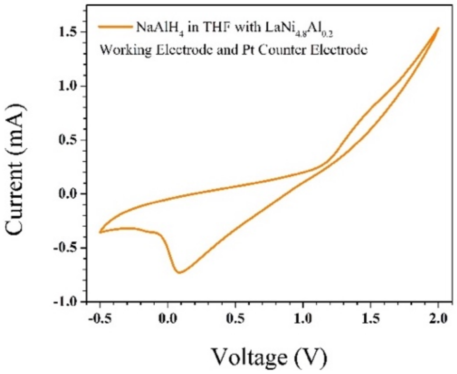

**Figure 3:** CV of 1.0 M $NaAlH_4$ in THF with $LaNi_{4.8}Al_{0.2}$ working electrode and Pt counter electrode

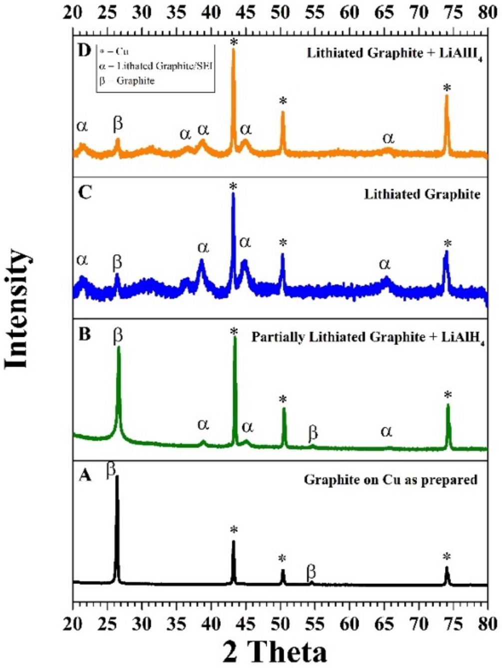

## Results/Discussion

A series of alkali metal and alkaline earth metal alanates were synthesized to provide the necessary electrolyte candidates for analysis. Previous studies found that commercially available $NaAlH_4$ (from Albemarle) was unsuccessful in producing the alane adduct needed for reversibility of the battery technology proposed. This is believed to be due to trace amounts of residual titanium catalyst used by the manufacture to produce sodium aluminum hydride. Therefore, we used a catalyst-free method, previously developed by SRNL, to produce pure $NaAlH_4$ for the studies herein. Figure 2 provides the X-ray diffraction (XRD) pattern of the $NaAlH_4$ produced by the catalyst-free method. The lack of solubility of $Mg(AlH_4)_2$ in ethers limited the practicality of this particular alanate. $Ca(AlH_4)_2$ was produced which exists in the adduct form of $Ca(AlH_4)_2$•4THF when synthesized using THF as the solvent. Preliminary cyclic voltammetry experiments with this electrolyte in THF using a metal hydride working electrode and a platinum counter electrode displayed no apparent reactions on the working electrode. The current hypothesis is the calcium alanate is not fully dissociating into ions in solution which prevents this material from behaving as a suitable electrolyte. Further investigation is still required for the calcium alanate material. Cycling voltammetry experiments carried out on $NaAlH_4$ in THF clearly display an oxidation and reduction feature as shown in Figure 3.

When using pure alkali metal electrodes as counter and reference electrodes when employing alkali metal alanates, it was discovered that a chemical reaction between the alkali metal and alkali metal alanate would result in the formation of the hexahydride version of the alanate ($M_3AlH_6$). Therefore, methods to prevent the reaction between the electrolyte and the plated alkali metal of that electrolyte were investigated. Graphite counter electrodes were employed to intercalate the alkali metal (lithium, sodium, or potassium) to prevent reaction with the alanate electrolyte. In typically lithium ion batteries, a solid electrolyte interphase (SEI) is formed from the carbonate-based solvents in the electrolyte. This formation generates an insoluble (in carbonate solvents) layer which protects from further electrolyte decomposition and facilitates the transport of lithium ions. [1] Therefore, graphite electrodes were first lithiated using a 1 M $LiBF_4$ in dimethyl carbonate/propylene carbonate electrolyte to form the SEI. XRD patterns of the graphite electrode before and after SEI formation are shown in Figure 4. These lithiated electrodes were then washed with THF and exposed to lithium aluminum hydride to evaluate the stability of intercalated lithium with the electrolyte proposed for this work. No evidence of $Li_3AlH_6$ was observed in the XRD patterns.

**Figure 4:** XRD patterns of graphite on carbon A) as prepared B) partially lithiated and exposed to $LiAlH_4$ in THF C) Fully lithiated without $LiAlH_4$ exposure D) Fully lithated with $LiAlH_4$ exposure in THF.

Additionally, $C_{60}H_x$ was investigated as an anode material for lithium ion batteries. $C_{60}$ is not suitable as an anode material due to its solubility in most solvents, but hydrogenating this fullerene reduces its solubility in typical solvents used for lithium ion batteries and expands the crystal lattice to allow for more efficient lithium diffusion. Figure 5 shows the cycling of $C_{60}H_x$ with differing amounts of hydrogen chemically bound to the fullerene cage. The overall hydrogen content of the $C_{60}$ was controlled by hydrogenation times.

For the rest of this study, $C_{60}H_x$ hydrogenated for 48 hours was focused on due to its favorable cycling stability. This anode material was then cycled 650 times and various charging rates were evaluated as shown in Figure 6. The capacity of this anodes steadily increases after a long activation period then plateaus around 588 mAh/g. DFT calculations to understand the underlying enhancement mechanisms and additional experimental details were reported in the literature.[2]

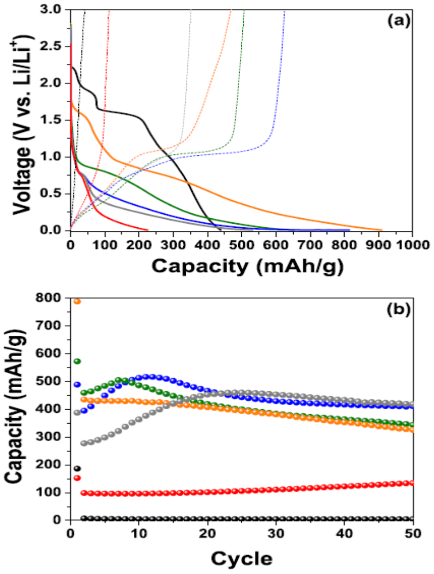

**Figure 5: (a)** First lithiation (solid line)/delithiation (dashed line) cycle of the $C_{60}H_x$ anodes at a current density of 0.025 mA/g and five different hydrogenation times (black: pure $C_{60}$; orange: 6 h = 0.66 wt. %; green: 12 h = 0.94 wt. %; blue: 24 h = 2.05 wt. %; gray: 48 h = 2.5 wt. %; red: 72 h = 3.44 wt. %). **(b)** Capacity as a function of cycle number for $C_{60}H_x$ with five different hydrogenation times performed at a current density of 0.05 A/g between 0.005 and 3.000 V vs lithium.

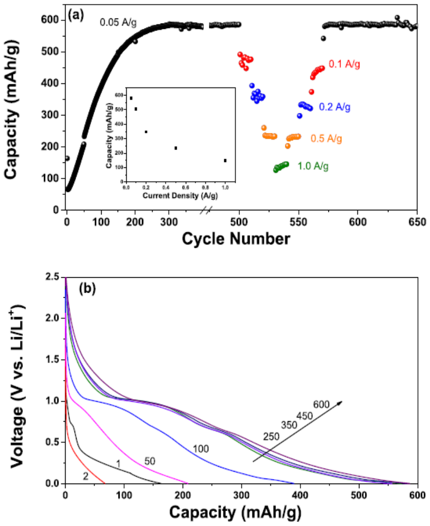

**Figure 6: (a)** Capacity vs cycle number for a $C_{60}H_x$ (48 h) anode on a Cu current collector. The current densities are listed for the cycles. Cycling was performed at a current density of 0.05, 0.1, 0.2, 0.5, and 1.0 A/g between 0.005 and 3.000 V vs lithium. Inset shows the average capacity as a function of current density. **(b)** Galvanostatic delithiation profile for selected cycles from the extended cycling study at 0.05 A/g.

## Accomplishments

- Synthesized and characterized a series of alkali and alkaline earth metal alanates for potential electrolytes
- Evaluated a series of metal hydrides for their suitability as anode materials
- Investigated various cathode materials for viability
- Carried out electrochemical testing include cyclic voltammetry and charge/discharge curves on promising candidate material configurations
- Published a peer reviewed paper in ACS Applied Energy Materials

## Future Directions

- Carryout long-term cycling of most promising candidate material configurations
- Design and construct flow cell battery testing apparatus
- Carryout testing of alanate based flow cell batteries

## References

1. Wang, L.; Menakath, A.; Han, F.; Wang, Y.; Zavalij, P. Y.; Gaskell, K. J; et. al. Identifying the components of the solid-electrolyte interphase in Li-ion batteries. *Nature Chemistry*, **2019**, *11*, 789-796.
2. Teprovich, J. A. Jr.; Weeks, J. A.; Ward, P. A.; Tinkey, S. C.; Huang, C.; Zhou, J.; Zidan, R.; Jena, P. Hydrogenated $C_{60}$ as High-Capacity Stable Anode Materials for Li Ion Batteries. *ACS Appl. Energy Mater.* **2019**, *2*, (*9*), 6453-6460.

## Acronyms

| | |
|---|---|
| **BES** | Basic Energy Sciences |
| **CSUN** | California State University, Northridge |
| **CV** | Cyclic Voltammetry |
| **DFT** | Density Functional Theory |
| **SEI** | Solid Electrolyte Interphase |
| **XRD** | X-ray Diffraction |

# Electrolytic Generation of Transportation Fuels in Molten Hydride Eutectic Electrolytes

**Project Team:** Patrick Ward, Ragaiy Zidan, Brenda García-Díaz

**Subcontractor:** Prabhu Ganesan (SRC)

**Thrust Area**: Secure Energy & Manufacturing

**Project Start Date:** January 30, 2019

**Project End Date:** September 30, 2020

*Molten alkali metal hydride and amide eutectic mixtures were evaluated for their potential to electrochemically produce value added energy carrier products. This preliminary seedling project demonstrated that methane could be generated from a eutectic mixture of alkali metal hydrides when graphite electrodes were employed. Electrochemical production of ammonia was also demonstrated in a $LiNH_2$-KH eutectic. Most importantly, the electrochemical dehydrogenation of alkali metal eutectics was confirmed demonstrating the feasibility of producing mobile hydride ions in the molten phase.*

## Objectives

- Design and construct a high temperature and pressure electrochemical cell compatible with molten metal hydrides
- Evaluate eutectic mixtures of metal hydrides and alkali metal amides to achieve lower operational temperatures for electrochemical conversion processes
- Demonstrate electrochemical conversion of precursors to desirable value-added products using molten metal hydride eutectic mixtures as electrolytes

## Introduction

Ammonia is currently produced by the Haber-Bosch process utilizing hydrogen (produced from steam reformed methane) and nitrogen. The Haber-Bosch reaction is performed at temperatures between 400 - 600 °C and at pressures of 150-200 bar. To be economical, these ammonia production plants need to be large and operate continuously. In the Haber-Bosch process, $H_2$ is obtained from fossil fuels at high temperature and pressure, resulting in a high capital cost (consumes ~1% of the worlds energy) and significant greenhouse gas emissions. Creating an electrochemical process could allow for smaller, more efficient ammonia plants that can run intermittently and take advantage of low-cost electricity from renewable energy resources to create ammonia. Most of the electrochemical methods, suggested in the past, utilize water and nitrogen. However, these methods suffered from a parasitic loss of efficiency and limited range of operating temperatures.

Another area of interest is the production of hydrocarbons from renewable resources. The Sabatier process which converts carbon dioxide or carbon monoxide into methane using hydrogen is a well-known process which has been extensively studied and modified. [1] This process uses a nickel catalyst at ~400 °C to produce methane and water from $CO_x$ and hydrogen. In order to provide an economically feasible alternative, lower temperatures and a reduction in processing steps is required.

## Approach

In the case of pure alkali metal hydrides, the incorporation of lithium is anticipated to be ideal due to the reactivity with nitrogen gas to form the nitride which can then be hydrogenated to form the amide and hydride according to equations **1** and **2** below.

1. $6\ Li + N_2 \rightarrow 2\ Li_3N$
2. $Li_3N + 2\ H_2 \rightarrow LiNH_2 + 2\ LiH$

From the lithium amide product ($LiNH_2$), electrochemical ammonia evolution could be achieved. The lithium hydride would be converted into lithium metal and hydrogen gas and the cycle would continue in this fashion to convert nitrogen and hydrogen into ammonia. The molten state of the hydride is necessary to provide the high ionic conductivity necessary for the practical electrochemical production of the desired products. Since the melting point of lithium hydride is 692 °C at atmospheric pressure [2], eutectic mixtures with other alkali metals are needed to lower the operational temperature and therefore reduce the cost of electrochemical product generation.

For hydrocarbon production, the use of low melting point metal hydrides to electrochemically convert graphite carbon electrodes directly into hydrocarbons is desired. Much like the Hall's process which converts aluminum oxide into aluminum by producing $CO_2$ at the graphite electrodes, this process would instead produce methane and the corresponding metal. This would lower the operational temperature required for methane production from a carbon source and eliminate the need for conversion to $CO_x$ as required by the Sabatier process.

## Results/Discussion

A series of metal hydrides and metal amides were investigated to determine eutectic mixtures in which a significant reduction in the melting point could be achieved. Lithium containing hydrides were a primary focus due to the ability for lithium to directly react with nitrogen and subsequently react with hydrogen to form lithium amide. Preliminary resistance measurements of KH:NaH (1:1 wt. ratio) mixtures demonstrated a melting point of ~ 200 °C. A 1:1:1 wt. ratio (5.3 : 1.7 : 1.0 mole ratio) of LiH:NaH:KH was used to prepare an eutectic which melted over the range of 320-340 °C. This demonstrates a substantial melting temperature reduction compared to the melting point of 692 °C for pure lithium hydride. Figure 1 shows the resistance measured in the electrochemical cell of the LiH-NaH-KH mixture during a heating ramp to 340 °C. The melting point of this eutectic mixture was also confirmed using High Pressure Differential Scanning Calorimetry (HP-DSC) as shown in Figure 2. A large endothermic peak at 340 °C is observed as the temperature was increased (illustrated by the red line) and a large exothermic peak observed at 320 °C during cooling (blue). These peaks are associated with the melting of the eutectic which is consistent with the resistance measurements. The HP-DCS measurements also reveal a broad exothermic peak at 428 °C observed during the temperature ramp and a corresponding endothermic peak at 414 °C during cooling. It is hypothesized that this is likely the heat of dissolution of one of the components that was in excess for this mixture.

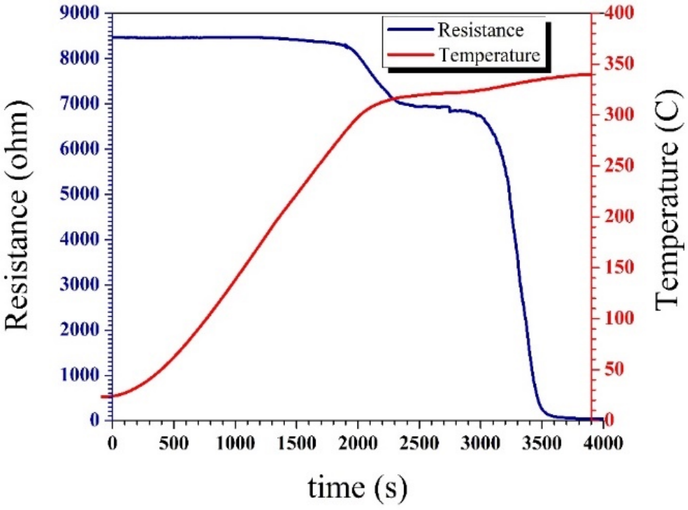

**Figure 1.** Resistance versus time during heating ramp for the electrochemical cell loaded with 10 g of LiH:NaH:KH (1:1:1 wt. ratio)

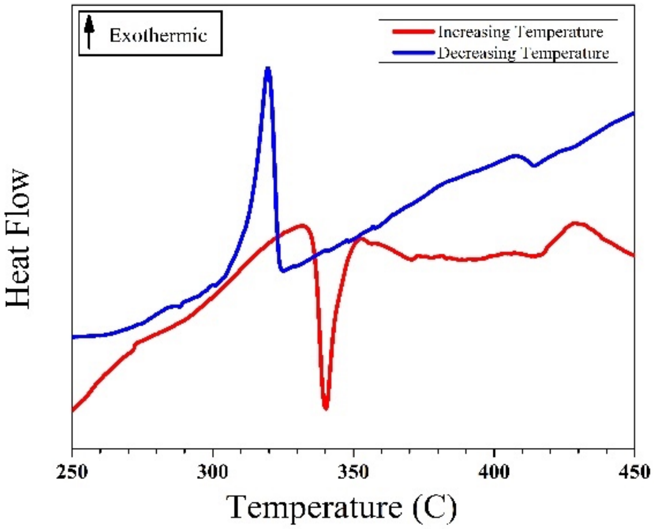

**Figure 2.** HP-DSC of LiH:KH:NaH (1:1:1 wt. ratio). Heating ramp at 5 °C/min. Cooling ramp at 10 °C/min. Constant hydrogen pressure of 60 bar $H_2$.

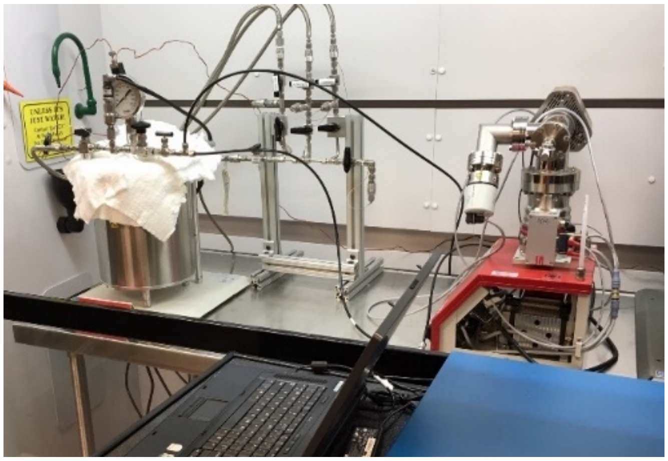

**Figure 3:** Electrochemical Testing Configuration

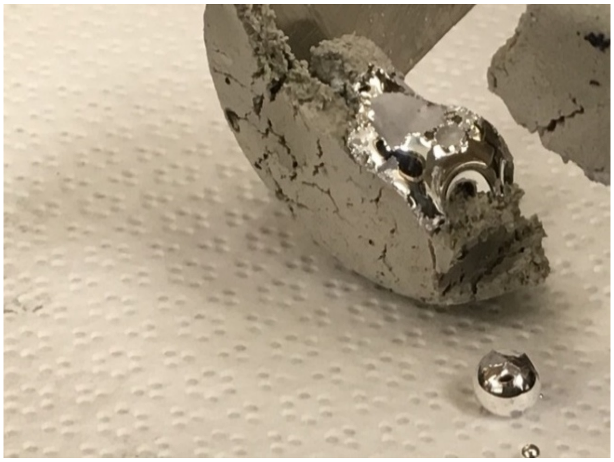

**Figure 4:** LiH-NaH-KH eutectic mixture after electrochemical

Preliminary electrochemical testing to produce ammonia from the LiH-NaH-KH mixture was performed in a custom-built electrochemical cell loaded with 10 grams of the metal hydride mixture in a pyrolytic boron nitride crucible. Nickel 200 electrodes were used as both anode and cathode. This vessel was charged with 113 psi of $N_2$ and 814 psi of $H_2$ gas then heated to 340 °C while measuring resistance, time, and temperature. A constant voltage 0.5 V was applied across the electrodes for 5 minutes and the resulting current measured using a potentiostat. The voltage was increased in 0.5 V increments and held for 5 minutes for each applied voltage. Small aliquots of the reaction mixture gas were analyzed by residual gas analysis (RGA) after each applied voltage. The experimental testing shown in Figure 3. No ammonia was observed for in the LiH-NaH-KH system, but dehydrogenation of the material was observed (Figure 4) leading to the formation of a Na-K alloy which is known to have a melting point below room temperature. [3]

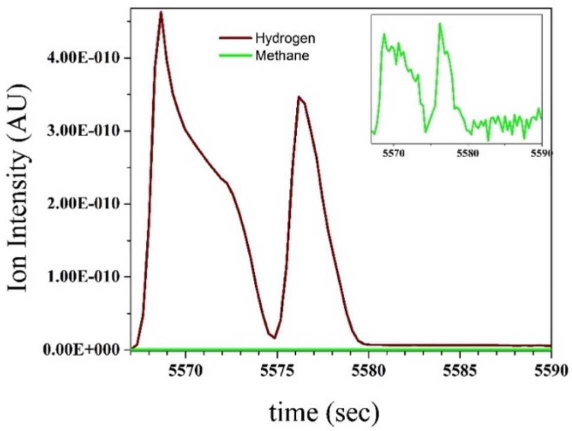

**Figure 5:** RGA spectra of gases present after applied voltage of 2.5 V to graphite electrodes in LiH:KH:NaH (1:1:1 wt. ratio)

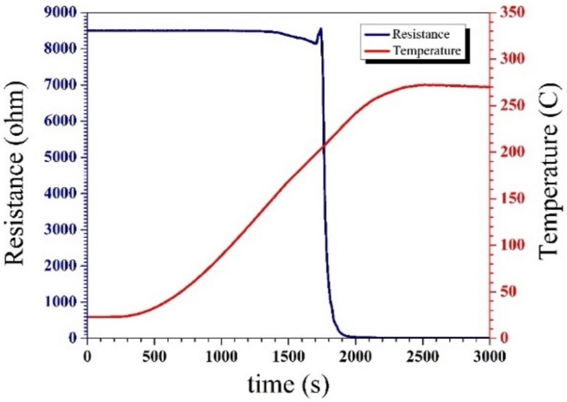

**Figure 6:** Resistance of $LiNH_2$-KH (1:1 molar ratio) eutectic during heating ramp

The feasibility of hydrocarbon production from the LiH-NaH-KH eutectic was evaluated using graphite electrodes. A 1:1:1 wt. ratio of LiH:NaH:KH was pressurized with 566 psi of $H_2$ gas and heated to 360 °C. Resistance measurements were used to confirm a molten state of the eutectic and a range of constant voltages were applied for 5 minutes while measuring the resulting current using a potentiostat. RGA analysis of the head gas confirmed the presence of methane gas after applying a 2.5 V potential difference for 5 minutes. No methane gas was observed by RGA before applying a voltage. Figure 5 shows a trace amount of methane detected after introducing two small aliquots of gas from the electrochemical cell to the RGA. Considering the large volume of the electrochemical cell (250 mL) and the high hydrogen overpressure, it is expected to have considerably more hydrogen than methane gas.

A eutectic of LiNH$_2$-KH in a 1:1 molar ratio was evaluated for it's potential to electrochemically generate ammonia. A significant drop in the resistance was observed at ~ 205 °C as shown in Figure 6. This significant decrease in resistance corresponds to the melting point of the eutectic. The gas in the electrochemical cell was analyzed after maintaining a constant voltage for 5 minutes over a series of voltages. After application of 5 V, ammonia was detected in trace amounts as shown in Figure 7. Due to the significant over pressure of hydrogen and nitrogen, 504 psi and 109 psi at room temperature respectively, the relatively small signal for ammonia is not unexpected. Furthermore, it is well-known that ammonia reacts with lithium hydride to form lithium amide and hydrogen. [4] Since this short-term study was intended for "proof of concept" analyses, a static electrochemical cell was produced and utilized. Ideally the pressurized gas would be cycled through a cooling loop to remove ammonia as it is produced to prevent reaction with the hydride to reform the amide. No hydrazine was detected in the product gas during the experiments. Metallic species were observed in the LiNH$_2$-KH melt after electrochemical studies were performed as shown in Figure 8. This also confirms the mobility of NH$_2^-$ or H$^-$ in this eutectic since no metallic species were observed for LiNH$_2$-KH melts that were held at the same operational conditions without an applied voltage.

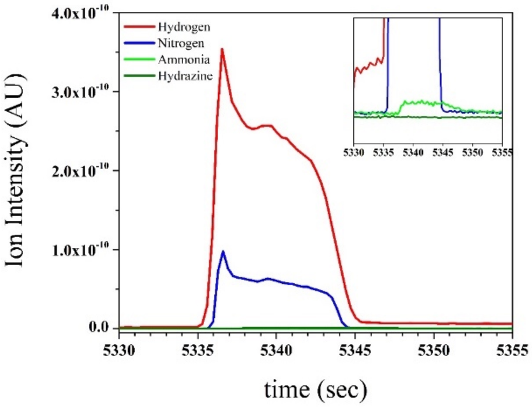

**Figure 7:** RGA spectra of product gases after an applied voltage of 5 V to the LiNH$_2$-KH eutectic

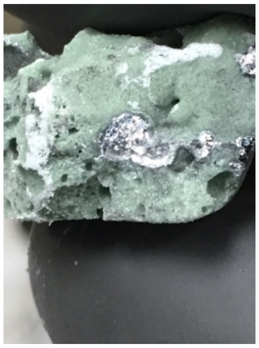

**Figure 8:** LiNH$_2$-KH (1:1 molar ratio) eutectic mixture after electrochemical testing

Although the quantities of ammonia and methane production from the LiH-KH-NaH and LiNH$_2$-KH eutectics are not substantial, this work provides preliminary data to substantiate further investigation. Of significant importance is the demonstration of dehydrogenation and deamination of the alkali metal hydrides and amines respectively. This confirms the mobility of these species in the molten state when a potential difference is applied and provides potential pathways for the electrochemical production of value-added chemicals.

## Accomplishments

- Designed and constructed a high pressure and temperature electrochemical cell compatible with molten metal hydrides and amides
- Demonstrated significantly reduced melting temperatures of alkali metal hydride and metal amide eutectic mixtures
- Demonstrated electrochemical production of methane from graphite using molten hydride electrolyte
- Demonstrated electrochemical ammonia production from LiNH$_2$-KH eutectic

## Future Directions

- Optimize electrochemical cell design to maximize nitrogen contact at the anode and develop methods for ammonia isolation once it is formed
- Evaluate additional eutectic mixtures to find optimal metal hydride composition based on melting point and performance
- Further develop carbon electrodes for the electrochemical production of methane using molten metal hydrides

### References

1. Ronsch, S.; Schneider, J.; Matthischke, S.; Schluter, M.; Gotz, M.; Lefebvre, J.; Prabhakaran, P.; Bajohr, S. Review on methanation- From fundamentals to current projects. *Fuel*, **2016**, *166*, 276-296.
2. Messer, C. E.; Levy, I. S. Systems of Lithium Hydride with Alkaline Earth and Rare Earth Hydrides. *Inorganic Chemistry*, **1965**, *4*, (*4*), 543-548.
3. Feinauer, A.; Majer, G. Diffusion of $^{23}$Na and $^{39}$K in the eutectic melt Na$_{0.32}$K$_{0.68}$. *Physical Reviews B*, **2001**, *64*, 134302-4.
4. Hu, Y. H.; Ruckenstein, E. Ultrafast Reaction between LiH and NH$_3$ during H$_2$ Storage in Li$_3$N. *Journal of Physical Chemistry A*, **2003**, *107*, (*46*), 9737-9739.
5. Impacts on the U.S. Power Grid," Metatech Corporation, Goleta, CA, January 2010.

### Acronyms

| | |
|---|---|
| **HP-DSC** | High Pressure Differential Scanning Calorimetry |
| **RGA** | Residual Gas Analysis |
| **SRC** | Savannah River Consulting |

# Toward Nano-Additive Manufacturing

**Project Team:** Simona Murph (Primary), Tommy Sessions

**Subcontractor**:
Savannah River Consulting , LLC

**Thrust Area**: Secure Energy & Manufacturing

**Project Start Date:** June 1, 2019

**Project End Date:** September 30, 2019

*We designed and demonstrate the construction and operation of a simple automated flow-throughput domain process, based on small-scale fluidics concept, that enables a uniform reaction environment for production of high-quality materials in large quantities. Nanomaterials were subsequently printed on various surfaces through reliable surface functionalization approaches.*

## Objectives

- Design and purchase the parts, components, and materials needed to build the automated flow-throughput domain process (AFTDP) technology.
- Assemble and build the AFTDP technology.
- Demonstrate precise fabrication and surface functionalization of nanomaterials via AFTDP technology.

## Introduction

The design and controlled fabrication of colloidal materials with functional properties has flourished over the last few decades. The beauty and distinctiveness of nanoscale materials is rooted in their unique properties that emerge at the 1–100 nm scale. In this transitional regime, a material's physical, chemical, and biological properties may differ in fundamental ways from the properties of both bulk matter and the constituent atoms or molecules.[1]

Metallic nanoparticles (NPs) are particularly attractive materials because they can be easily synthesized and chemically transformed. They are significantly different from the same materials in the bulk because as their size decreases, they exhibit quantum size effects. Metallic NPs interact strongly with light waves, even though the wavelength of the light may be much larger than the particle. In metal NPs, "plasma oscillations" driven by external electromagnetic fields are localized and lead to strong resonances at specific wavelengths that are dependent on the particle size, shape and the local dielectric environment.[1] Plasmonic properties of metallic nanoparticles find applications in plasmon-enhanced spectroscopy, near-field imaging, sensing, and nanophotonic devices. The plasmon band of gold and silver nanoparticles is tunable throughout the visible and near-infrared region of the spectrum as a function of particle shape, size and the local refractive index of the medium. Anisotropic metal NPs can absorb and scatter light along multiple axes; therefore, metal nanorods and nanowires display both longitudinal and transverse plasmon bands. In the case of nanorods, two plasmon bands emerge, corresponding to light being absorbed (and scattered) along the short axis (the transverse plasmon band) and the long axis (the longitudinal plasmon band). [2]

For decades, a staggering amount of research has focused on the creation of novel nanomaterials and the elucidation of their unique property-structure correlations. Highly reliable bottom-up and top-down synthetic routes that produce increasingly complex nanomaterials with highly ordered and complex geometries have been developed. Complications in scaling up and uniformity have hampered widespread application of nanomaterials. While some of these shortcomings have been addressed to some extent, small variations of the operational parameters, such as the rates of reagent additions, times, stirring rates, uneven temperatures, etc. can still have a strong negative effect on the final product. Ultimately, the quality of the nanomaterials obtained can vary greatly from one batch to the next.

Here, we propose the construction and operation of a simple automated flow-throughput domain process (AFTDP), based on a unique small-scale fluidics concept, that enables a uniform reaction environment for production of high-quality materials in large quantities. Nanomaterials were used as "ink" and "printed" on various surfaces through reliable surface functionalization techniques.

## Approach

Nanomaterials of various sizes, shapes and compositions were prepared through solution chemistry, through the reduction of molecular precursors in the presence of surfactants, and capping agents. The reduction rates of the metal precursors, reductant-to-precursor ratio, ligands and strength of reductant were all used to manipulate the final product and have an effect on the shape, size, and crystallinity, which affect the optical and physical properties. The ligands on the surface are used to stabilize the NPs and change the surface energy at certain facets through preferential adsorption to achieve shape control. By automatically varying the amount, volumetric flow rates, timing, location, size of the capillaries/tubings, etc. of the injected reagents, highly reliable and uniform nanomaterials can be produced. Continuous operation of the system will allow production of nanomaterials in large quantities. Once produced, nanomaterials could be printed by drop casting or by chemically binding on various supports.

## Results/Discussion

The route for the bottom-up manufacturing of metallic NPs employed here is based on the reduction of molecular precursors. We found that the NP's size and optical properties can be tuned by simply changing the reaction rate, flow rate and the $M^{n+}$/reducing agent ratio.

One interesting finding observed during the operation of the AFTDP is that the small reaction volumes enable reactions to be performed with higher yields than can typically be achieved with conventional reactors. It is possible that the applied stress (stress-induced crystallization) increases of the interaction among nano-objects, nucleation density makes the NPs prone to enhanced structural arrangements and crystallization.

To create uniquely shaped morphologies, anisotropic growth of NPs of interest was investigated. Crystalline symmetry was broken through the use of shape directing ions and/or facet specific binding coordinating compounds. Nanostars and nanotriangles were successfully produced.

Bimetallic NPs are of long-standing interest because they can exhibit catalytic, electronic, and optical properties distinct from either of their constituent monometallic NPs. The importance of the relative surface alloying or layering arrangements of metals on single-crystal substrates has been recognized, including the "near surface alloy" model of metal adlayer on metal substrate.[3] By using a co-precipitation approach, metallic NPs of various compositions were produced. Once produced, nanomaterials were subsequently printed on various surfaces through reliable surface functionalization approaches.

## FY2019 Accomplishments

- Demonstrated the construction and operation of a simple automated flow-throughput concentric capillaries processing technology (based on unique small-scale fluidics concept), that enables a uniform reaction environment for production of high-quality materials
    - Large volumes of nanomaterials could be produced under continuous operations
    - Demonstrated the production of structures of various compositions and morphologies
- Created isotropic and anisotropic nanoscale structures in solution and on various supports.
    - The metallic NP's size and optical properties can be tuned by changing the reaction rate, and the $M^{n+}$/reducing agent ratios
- The small reaction volumes enable reactions to be performed with higher yields than can typically be achieved with conventional reactors.

## Future Directions

- Nanomaterial's fabrication optimization and production of uniquely shape size and composition nanostructures via AFTDP technology; Patterning with nanomaterials via the 3D Nano-Additive Printing technologies.

---

### References

1. Hunyadi Murph, S.E.; et. al. "Anisotropic and Shape-Selective Nanomaterials: Structure-Property Relationships", Nanostructure Science and Technology series, Springer Publisher, 2017, 1-470.
2. Hunyadi Murph, S.E.; et. al. "Metallic and Hybrid Nanostructures: Fundamentals and Applications", in Applications of Nanomaterials, 2012, Series ISBN: 1-62699-000-X, Vol.4, Studium Press LLC, USA.

Savannah River
National Laboratory®

OPERATED BY SAVANNAH RIVER NUCLEAR SOLUTIONS